

---

# BASEMENT CONTROL ON VOLCANIC EDIFICE STABILITY: APPLICATION TO MOUNT ETNA

---

Thesis submitted for the degree of Doctor of Philosophy at  
the University of Leicester

by  
Castagna Angela

Department of Geology  
School of Geography, Geology and the Environment  
University of Leicester

October 2020

---

***Basement Control on Volcanic Edifice Stability: Application to Mount Etna***  
***Angela Castagna***

---

**ABSTRACT**

Instability in volcanic edifices is consequence of several factors, e.g. growth and load of the edifice, magmatic intrusions and related processes, such as stress field changes, fluid circulation, earthquakes. Nonetheless, the presence of a sedimentary basement is a key control factor for instability and Mount Etna is falling into this category: it is a stratovolcano lying on top of a sedimentary basement and presenting flank instability in its eastern-southern sector. It is a well-monitored volcano because of its threat on the surrounding cities, and the wealth of multidisciplinary data collected so far helps to better constrain the dynamic of the flank. However, the deformation mechanisms are still matter of debates. Many factors can contribute to lowering the mechanical resistance of the basement, and sedimentary rocks are particularly sensitive to: a) presence of water, b) pressure, c) temperature. In this thesis, the experimental approach aims to characterize the mechanical strength of the Etnean rocks, monitoring the evolution of their behaviour from fracture nucleation to sliding under relevant conditions of P, T and pore fluid pressure, mimicking natural conditions. The study focuses on the influence of a thermal gradient induced by dyke intrusions into the host rock. Further, the development of a new piece of equipment for triaxial apparatus allows collecting additional data on the frictional resistance of Etnean gouges. Results demonstrate that rocks in the basement are transitioning from brittle to ductile behaviour in relative shallow conditions (i.e. 1-2 km), and mixtures of synthetic gouges show stable sliding with the friction coefficient sensitive to clay content. These results can help to explain the particular seismic-aseismic behaviour of the easternmost fault system bordering the sliding flank (e.g. Pernicana Fault System). Further, this experimental approach is well applicable to other volcanoes showing similar conditions.

---

## *Acknowledgment*

---

I think it would not be possible to arrive to finish my thesis if it wasn't for the full support I had from my family, my supervisors and my friends. PhD projects take a lot of time, patience, passion, dedication. Sometimes they can be really a tough time. It is possible to get lost, to feel frustrated and 'not good enough'. It is possible to lose motivation. My PhD was a tough time indeed. The joy of being abroad making this new experience, learning a new language and being able to do what I like, was jeopardized by intrinsic difficulties encountered during the project and by life events: the sadness of the loss of my mother, the indescribable joy of the arrival of my son. I really think that it could not be possible to arrive to an end without all the support I have received during these long years. For this reason, I want firstly to thank my family, Stefano and Eliseo Kári in primis. Stefano for being that sensitive, supportive, magic partner, always by my side and allowing me to work on the thesis looking after the little Eliseo Kári, especially in these last few crazy months. I do love you a lot. My brother Alberto with his Ariannna, Carlo and Gabriella and all the Cacioppo and Castagna relatives. I want to thank my supervisors: Phil to be the one that pushed me to make the Comiso experiments and get published the paper when I was literally lost in the project; Richard for being a supportive supervisor and a spokesperson; Audrey for being my mentor in the lab, following me step by step and helping me in every aspect of the project and for being a great friend. My friend, Tom, for being that kind of friend always present for chats, beers, for discussing about science, life and much more. Thanks to Marco, helping me a lot with the experiments, to listen to all my complaining and me but always giving a good advice and a place to stay in Portsmouth. All my colleagues in uni: Tara, Alodie, Takky, Michael, Vlad, Greg, Phil...it was always good to have you all around and doing some fieldwork with some of you! Thanks to Michele and Stefano to host me in Manchester and to help me out with MatLab. Thanks to all my English and Italian friends to be by my side when I was in need of a chat and support during these long years: Vale, Cinzia, Francesca, Massi, Laura and Nick, Rachel, Peter.

I would not be where I am without all of you.

Thanks, Angie.

## Table of Content

<b>Abstract .....</b>	<b>i</b>
<b>Acknowledgement.....</b>	<b>ii</b>
<b>Table of Content .....</b>	<b>iii</b>
<b>Chapter 1: The Mount Etna Case.....</b>	<b>1</b>
1.1 Introduction .....	1
1.2 Building Mount Etna .....	3
1.2.1 Geological setting of Eastern Sicily .....	3
1.2.2 Mount Etna growth and volcanic phases.....	7
1.2.3 Mount Etna: the unstable flank and its seismic/aseismic sliding .....	10
1.3 Faulted and intact rocks: experimental overview.....	14
1.4 Insights from Laboratories .....	20
1.5 Rationale of the Thesis .....	26
1.6 Thesis Structure.....	28
<b>Chapter 2 Fieldwork &amp; Material Characterization .....</b>	<b>29</b>
2.1 Introduction .....	29
2.2 Lithological characterization of Mount Etna's basement.....	29
2.3 Description of lithologies .....	31
2.3.1 Appenninic-Maghrebian Chain (AMC).....	33
2.3.2 Hyblean Plateau Foreland.....	38
2.3.3 Gela-Catania Foredeep.....	39
2.3.4 Volcano edifice.....	41
2.3.5 The Pernicana Fault System and the NE-Rift overview .....	42
<b>Chapter 3 Methods: From the Fieldwork to the Laboratory .....</b>	<b>43</b>
3.1 Introduction .....	43



3.2	Fieldwork: samples collection and <i>in situ</i> measurement .....	43
3.3	In the Laboratory: Samples Selection and Preparation .....	44
3.3.1	X-Ray Powder Diffraction .....	45
3.3.2	X-Ray Fluorescence .....	52
3.3.3	Synthetic Gouges Selection .....	53
3.3.4	Synthetic Gouge Preparation .....	56
3.4	High Temperature Thermal Apparatus for Thermal Cracking on Intact Rocks .....	56
3.5	Deformation experiments on intact rocks: Sanchez Triaxial Apparatus .....	57
3.5.1	Acoustic Emission (AEs) and Ultrasonic Surveys .....	60
3.5.2	Preparation of samples for testing, preliminary tests and experimental procedure .....	62
3.6	Frictional Experiment on Synthetic Gouges: MTS 815 - Mechanics Testing System .....	67
3.6.1	Designing the Direct Shear Sliding Holder .....	68
3.6.2	Calibration tests .....	73
3.6.3	Procedure for the final assemblage .....	82
3.6.4	Experimental procedures .....	85
3.7	Discussion: Advantages and Limitations .....	90
<b>Chapter 4 Results of Thermal Damage and Pore Pressure Effects on Comiso Limestone .....</b>		<b>93</b>
4.1	Introduction .....	93
4.2	Results of the Thermal Treatment with High Temperature Furnace: Acoustic Emission and Ultrasonic Wave Velocities .....	93
4.2.1	Triaxial test: dry conditions on ‘as collected’ specimens .....	95
4.2.2	Triaxial test: drained saturated conditions on ‘as collected’ specimens .....	98
4.2.3	Triaxial tests: dry conditions on thermally treated specimens .....	100

4.2.4	Triaxial tests: drained saturated conditions on thermally treated specimens	102
4.3	Discussion	104
4.3.1	Mechanical behaviour of dry and saturated specimens ‘as collected’	104
4.3.2	Effects of thermal treatment on Comiso Limestone strength	106
4.3.3	Brittle-ductile transition	110
4.3.4	Application of results to the Etna basement	112
<b>Chapter 5</b>	<b>Frictional Properties of the Etnean Gouges: Results</b>	<b>117</b>
5.1	Introduction	117
5.2	Results for Constant Sliding Velocity: end-members	117
5.2.1	Quartz-sand Synthetic Gouge	118
5.2.1	Quaternary Clay Synthetic Gouge	119
5.2.1	Limestone Synthetic Gouge	120
5.3	Results for Constant Sliding Velocity: Binary Mixtures	121
5.4	Results for Dynamic Sliding Velocity: End-members	123
5.4.1	Clay Synthetic Gouge	123
5.4.2	Limestone Synthetic Gouge	124
5.5	Results for Dynamic Sliding Velocities: Binary Mixtures	124
5.5	Discussion	126
<b>Chapter 6</b>	<b>Conclusions</b>	<b>132</b>
6.1	Conclusions	132
6.2	Concluding remarks	135
6.3	Future developments	135
<b>Appendix A</b>	<b>Fiumefreddo Quaternary Clay – XRF Investigation</b>	<b>139</b>
<b>Appendix B</b>	<b>Calibration procedure</b>	<b>140</b>
<b>Appendix C</b>	<b>RsFit3000</b>	<b>142</b>

**Appendix D. Published paper.....147**

**Bibliography .....148**

---

## *Chapter 1: The Mount Etna Case*

---

### 1.1 Introduction

Instability of a volcanic edifice means that the edifice is somehow weakening, due to interconnected factors that play together with different strength, depending on the case: the weight of the growing edifice is influencing the mechanical strength of the edifice and that of the basement (i.e. [De Vries and Borgia, 1996](#)), magmatic intrusion via dykes and sills or emplacement of larger magma bodies results in damage growth during emplacement (i.e. [Voight and Elsworth, 1997](#)), changes to the stress state during and following magmatism (e.g. [Aloisi et al., 2011](#), [Bonaccorso et al., 2010](#)), and high temperature gradients (e.g. [Bonaccorso et al., 2010](#)). In this last example, transient temperature variation may lead to the generation of permanent changes to the hosting material, owing to heat-induced mineralogical transitions, hydrothermal alteration, and intrusion-induced fractures. Extreme cases of thermal alteration and weakening can enhance catastrophic flank collapses (e.g. [Voight and Elsworth, 1997](#); [Day, 1996](#); [Elsworth and Day, 1999](#); [Reid et al., 2001](#); [Dieterich, 1988](#)). Most studies of such effects focused on the volcanic edifice rocks (e.g. [Reid et al., 2001](#)), or on rocks composing the basement (e.g. [Elsworth and Voight, 1992](#); [Delaney and Pollard, 1982](#); [Heap et al., 2013](#); [Bakker et al., 2015](#)).

Basement rocks typically host some type of pore fluid (water, brine, hydrothermal fluids: e.g. [Day, 1996](#), [Mattia et al., 2015](#), [Dautriat et al., 2011](#)), and owing to the distribution of intrusions in sub-volcanic systems, much of the sub-edifice basement is likely to be subject to lower – but still elevated – temperatures (i.e.  $<600\text{ }^{\circ}\text{C}$ ). The presence of a sedimentary substratum showed to be one of the factor contributing to the development of flank instability, as reported by [Van Wyk De Vries and Borgia, 1996](#), and Mount Etna is falling into this category. (e.g. [Van Wyk De Vries and Borgia, 1996](#) [Mattia et al., 2015](#)).

Mount Etna is the highest elevation volcano (3200 m.a.s.l.) in Europe and one of the most active. The volcanic edifice grew in a relatively short time (e.g. 500.000 yrs) on top of a sedimentary basement. Nowadays, the edifice has a basal circumference of 140 km elongated in the N-S direction, meaning that it has an elliptical shape. The presence of the Appenninic-Maghrebien Chain in the N-W section acts as a structural buttress for those

flanks, while the S-E side is free to slide towards the Ionian Sea: this morphology, decoupled with the regional stress fields counting compression in N-S direction and little extension in E-W direction, works to facilitate the eastern sliding of the flank.

Many volcanoes around the world are close to populous cities, and edifice weakening is therefore a direct threat for the population. Indeed, Mount Etna dominates the landscape of the densely inhabited city of Catania at its southern sector. It is one of the most monitored volcanoes in the World, listed amongst the ‘Decade Volcanoes’, a list of the sixteen potentially most dangerous volcanoes as compiled by IAVCEI (International Association of Volcanology and Chemistry of the Earth’s Interior). The necessity to build a strong knowledge on the behaviour of these dangerous volcanoes, besides the intrinsic scientific interest, is useful in the attempt to attain a forecast model for eruptions and/or catastrophic flank collapses. Many volcanoes present flank instability linked to their structural and geodynamical setting, the role of magma intrusions, and the role of the basement (e.g. [Mathieu et al., 2011](#); [Poland et al., 2017](#); [Walter et al., 2005](#); [Munn et al., 2006](#)). The macro-scale approach studies the structural control exerted by the presence of fault systems or other tectonic controls, by seismic monitoring and GPS monitoring, and by geophysical and geochemical investigations. In the case of Mount Etna, the wealth of data collected so far allows a better understanding of the volcanic dynamics and it is fundamental to better constrain its flank dynamic, which is still matter of debates. However, micro-scale investigations cannot be ignored (e.g. [Bakker et al., 2013](#); [Bakker et al., 2015](#); [Harnett et al., 2018](#); [Heap et al., 2009](#)). For this reason, this thesis presents an experimental approach aimed to characterize the mechanical and frictional strength of the rocks composing Mount Etna’s basement. The data collected shed light on the role played by temperature and water in degrading the Etnean rocks, therefore contributing to the deformation that is triggering the flank motion. This research focuses on Mount Etna because of the open questions about its instability and because it is object of studies since many years. The multidisciplinary approaches used until now to detect and monitor Mount Etna’s behaviour and evolution make it as one of the best candidate to apply a systematic experimental approach. Nonetheless, the approach here used can extend to other volcanoes showing edifice instability, being the strength of the rocks a major player for instability, and being mechanical characterization procedures easily accessible in laboratory.

## 1.2 Building Mount Etna

Mount Etna volcano sits atop a structurally complex sedimentary basement dominated by formations consisting of sandstone, limestone, and clay that are part of the wider Appenninic-Maghrebian Chain (AMC). The AMC chain is part of the accretionary wedge that lies above a thick carbonate plateau, which is part of the African plate. The following paragraphs detail the geological background of Mount Etna.

### 1.2.1 Geological setting of Eastern Sicily

Three domains describe the complex tectonic and structural configuration of the eastern part of Sicily (i.e. [Lentini et al., 2006](#); [Lentini, 2014](#)): (i) the foreland domain; (ii) the orogenic belt; (iii) the hinterland domain. The foreland domain, (i) comprises the continental areas of the Pelagian block and the Ionian basin. The orogenic domain (ii) sees the superimposition of three tectonic belts: in order from the top, the Kabilo-Calabride Chain (KCC) over-thrusted onto the units of the Appenninic-Maghrebian Chain (AMC), the latter in turn over-thrusted on top of the External Thrust System (ETS), which involves carbonate units belonging to the foreland domain. Finally, the Sardinia and Corsica blocks, together with the Tyrrhenian basin, are part of the hinterland domain (iii) (Fig. 1.1). The volcano edifice lies on the complex multilayer basement of orogenic belt, deposited during the Neogene Africa-Europe collision. This large event piled up Mesozoic-Cenozoic continental and marine sedimentary units belonging either to the European margin, to the Tethydean Ocean and to the African plate, transporting and re-arranging them into an accretionary wedge (e.g. [Gardu et al., 1997](#); [Roure et al., 1990](#); [Branca et al., 2011](#)) (Fig. 1.1 E and F). Non-deformed carbonate sequences outcropping in south Sicily dominate the foreland domain, known as the Hyblean Plateau (HP). The HP gently dip northward below the orogenic belt, from  $1^{\circ}$ - $2^{\circ}$  in the HP to  $4^{\circ}$ - $6^{\circ}$  below the AMC (e.g. [Doglioni et al., 2001](#)). It consists of 25-35 km thick continental crust (e.g. [Scarascia et al., 2000](#)) underlying approximately 6-7 km thickness of Mesozoic-Cenozoic carbonate sequences. At the front of the thrust belt, towards the AMC, the Gela-Catania foredeep's sin- and post-deposition sedimentary units cover the HP. To the west, the HP is bounded by north-south oriented structures with vertical down-throw, and to the east by the Malta Escarpment, a trans-tensional fault system running into the Ionian Sea (e.g. [Branca et al., 2011](#); [Doglioni et al., 2001](#); [Lentini et al., 2006](#)).

The units composing the AMC itself derive from the late Oligocene-early Miocene transport of sedimentary sequences detached from the oceanic and continental crust, in turn over-thrusted on top of the ETS (Fig. 1.1 and 1.2) (e.g. [Lentini et al., 2006](#)). These allochthonous units propagate in sequences of '*piggy-back style*' showing a *flat-ramp-flat* geometry, via a series of SSE verging thrusts. During the last convergence phase, the subducting African plate starts to flex under the weight of the developing chain trending NE-SW across the Gela-Catania foredeep. This episode created space for the deposition of quaternary sin-sedimentary deposits characterized by clayish-sandy units.

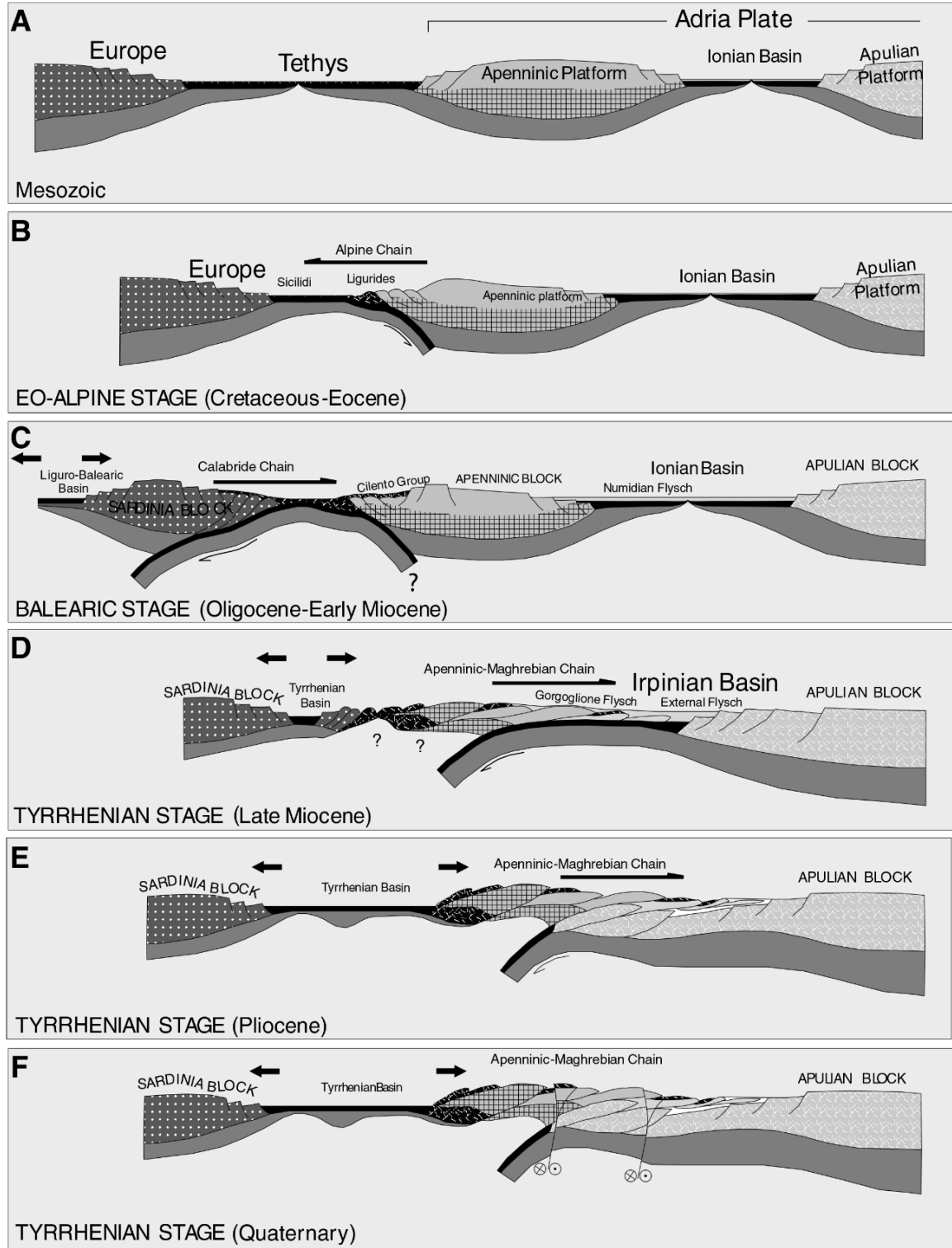


**Figure 1.1.** From A to F: simplified geodynamics of the central Mediterranean area, to highlight the formation of the Apenninic-Maghrebian Chain (adapted from [Lentini et al., 2006](#)). After early stages of compression (A, B and C), the Tyrrhenian Basin starts to open (D), pushing and piling up the marine and flyschoid units into the ramp-and-flat geometry of the accretionary wedge. The final stages of the construction of the AMC are reported in E and F.



The architecture of this orogenic belt is that of an accretionary wedge (e.g. [Lentini et al., 2006](#)). Geophysical investigations highlight the geometry and position of the lithologies (e.g. [Finetti, 1984](#); [Finetti et al., 2005](#); [Cristofolini, 1979](#); [Accaino et al., 2011](#)) (Fig 1.2).

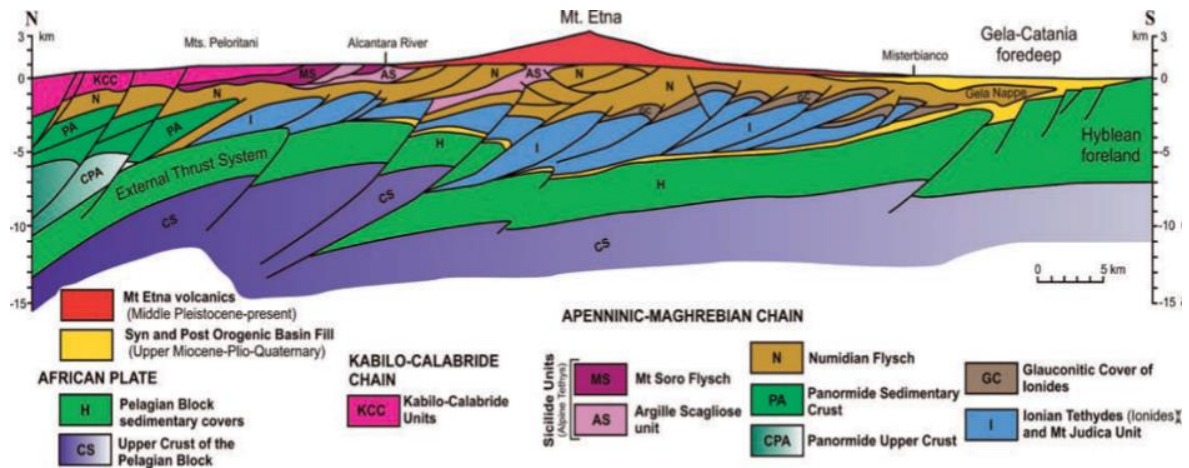


**Figure 1.2.** North to South cross section, showing the relationship amongst the main domains composing the Sicilian crust below Mount Etna (from [Branca et al., 2011](#)).

Mount Etna's edifice develops on top of the accretionary wedge, in a position that, being on the hinge of the subduction zone, is regarded as anomalous for a volcano (e.g. [Doglioni et al., 2001](#)). Compressional regional deformation in this part of Sicily occurs mostly in the north-south direction (e.g. [Doglioni et al., 2001](#); [Cocina et al., 1997](#)), whereas little extension occurs in the east-west direction (or right lateral transfer) due to the influence of the Malta Escarpment (e.g. [Doglioni et al., 2001](#)) (Figure 1.3, the red line in the right side of the picture, crossing the Ionian Sea and north Sicily). This particular tectonic setting, with the right-lateral trans-tensional movement of the Malta Escarpment, creates a sort of 'window' permitting the magma to rise through the basement, forming the volcanic edifice (e.g. [Doglioni et al., 2001](#)).

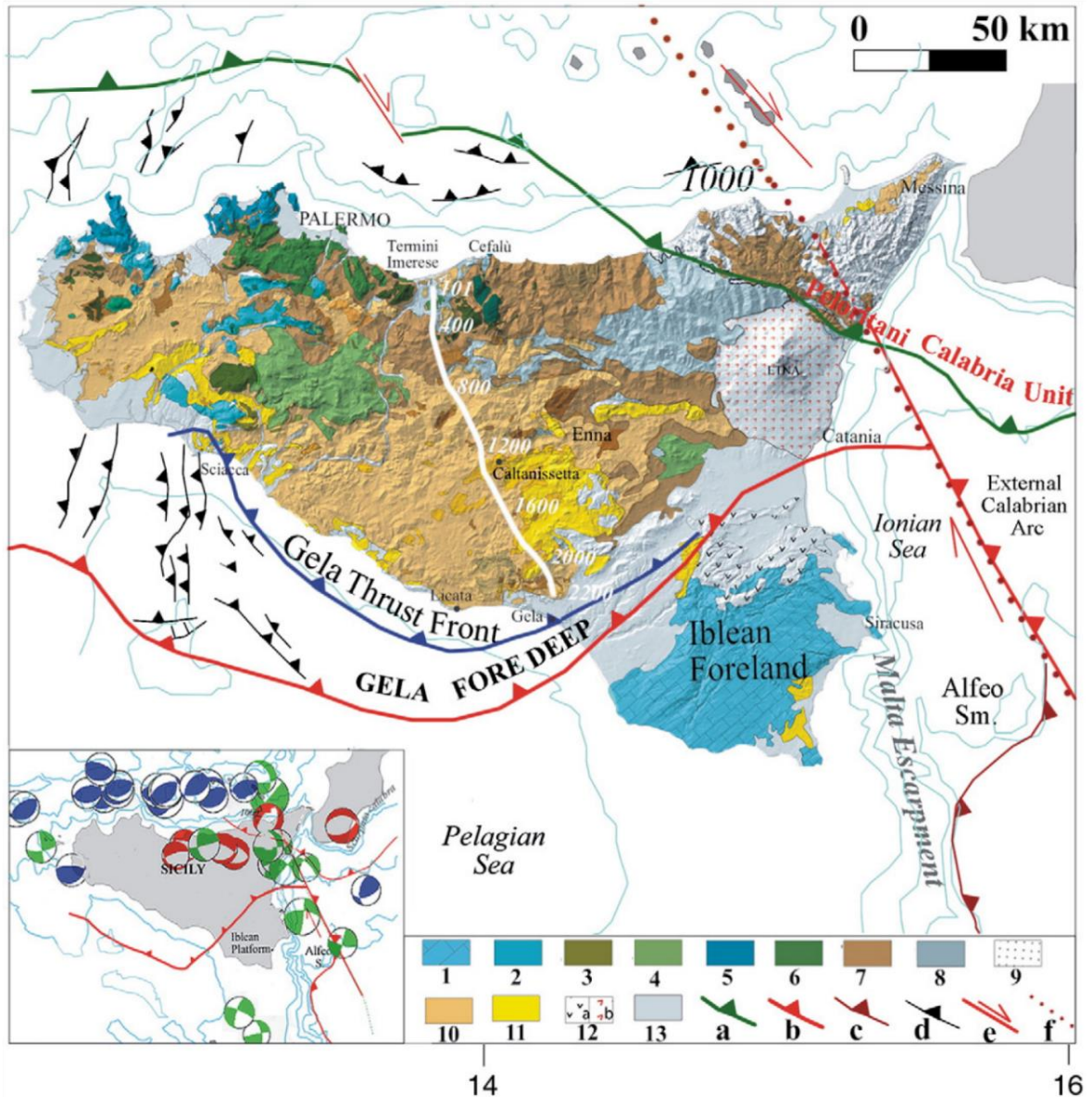


**Figure 1.3.** From [Accaino et al., 2011](#): Structural map of Sicily. It is of interest for this thesis: 1) The Hyblean Units; 4), 7), 8) and 11) carbonate and flyschoid formations composing the Appenninic-Maghrebian Chain; 12) Plio-quaternary volcanic rocks; 13) Pleistocene deposits; a) Kablylian-Calabrian Thrust Front; b) Maghrebian-Sicilian Thrust Front; e) faults with strike-slip movement, in this case the Malta Escarpment to the east.

### 1.2.2 Mount Etna growth and volcanic phases

Approximately 500,000 years ago, the area currently occupied by Mount Etna was a gulf in which marine sediments, including clays and sand, were widely deposited (e.g. [Rittmann, 1973](#)). Approximately 220,000 years ago, the volcanic activity started to migrate towards North in form of basaltic eruptions from submarine fissures (e.g. [Rittmann, 1973](#);

[Branca et al., 2007](#)) encapsulating the current active area, now testified by the presence of spilitized pillow lava (i.e. albitization of basalt during alteration) as well as hyaloclastites along the coast. The volcanism becomes subaerial around 130,000 yrs ago because of a tectonic uplift of Sicily, and it started to build the modern edifice of Mount Etna, as we know it today (Figure 1.4). Evidence for this uplift comes from outcrops of Sicilian clays at an altitude of 800 m a.s.l. along the volcano's eastern flank (e.g. [Rittmann, 1973](#)).

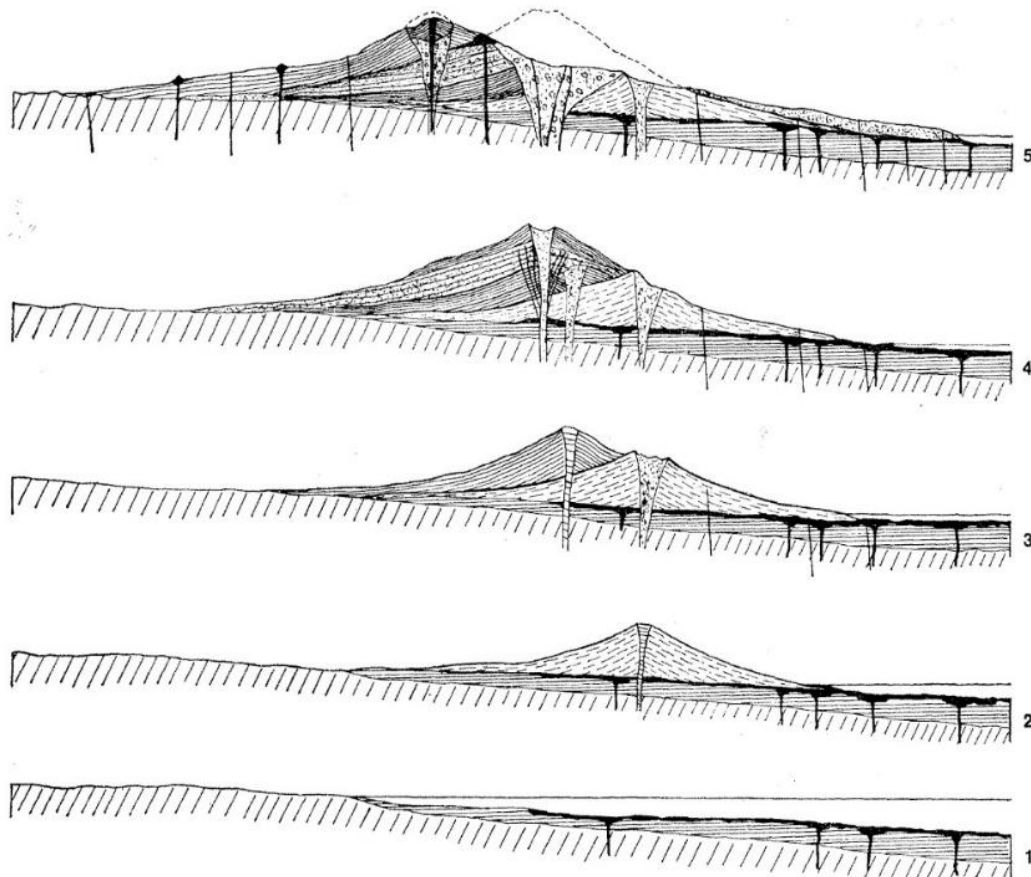


**Figure 1.4.** From the bottom to the top: initial and subsequent phases of the growth of Mount Etna volcano after [Rittmann \(1973\)](#). 1) Marine eruptive fissures; 2) Volcanism became sub-aerial; 3) and 4) Migration of the central edifice forming new central craters; 5) The actual stratovolcano.

Several authors studied and classified the history of Mount Etna (e.g. [Rittmann, 1973](#); [Chester et al., 1987](#); [Branca et al., 2004](#)). [Branca et al., \(2007\)](#) provide a good summary of Etna's activity based on geochronological and stratigraphic data, which divides the growth of the volcano into four main phases (Fig. 1.5):

Synthetic unit		Lithosomatic Unit
Stratovolcano Supersynthem	Il Piano Synthem	Mongibello volcano
	Concazze Synthem	Ellittico volcano
Valle del Bove Supersynthem	Zappini Synthem	Cuvigghiuni volcano
		Salifizio volcano
		Giannicola volcano
		Monte Cerasa volcano
	Croce Menza Synthem	Trifoglietto Volcano
		Rocche volcano
		Tarderìa volcano
Timpe Supersynthem	S. Alfio Synthem	
	Acireale Synthem	
Basal Tholeiitic Supersynthem	Adrano Synthem	
	Aci Trezza Synthem	

Basal Tholeiitic (BT): these submarine fissure-type eruptions started 500,000 years ago. Outcrops of this early stage are found along the Ionian coast. The first and oldest deposits of subaerial volcanism, found along the Simeto River, belong to this unit.

Timpe (TI): From 220,000 years ago fissure-type eruptions occurred mainly located along the Ionian coast, with a variation from tholeiitic towards alkaline lava products.

Valle del Bove (VB): This event commenced around 120,000 years ago. The feeder system stabilized in the Valle del Bove area.

Stratovolcano (SV): The final stabilization of the plumbing system occurred about 60,000 years ago, forming the Ellittico volcano which is the bulk of the current edifice. In the last 15,000 years, the volcanic activity built the Mongibello volcano and its volcanic products have extended their coverage to some 85% of the actual volcano surface.

**Figure 1.5.** From [Branca et al., 2007](#). This scheme reports the main sequences and sub-sequences, grouped by lithosomatic units, composing Mount Etna's edifice, from ancient (bottom) to recent (top).

During historical times, Mount Etna remained mainly a basaltic volcano, characterized by effusive activity with intermitted explosive trend (i.e. Plinian and sub-Plinian eruptions), with magmatic compositions ranging from tholeiitic to alkaline basalts (e.g. [Doglioni et al.](#),



2001). This intermittent explosive activity takes place in flank eruptions, and it is referred as more dangerous than the almost continuous summit activity (e.g. Allard et al., 2006; Branca et al., 2007).

### 1.2.3 Mount Etna: the unstable flank and its seismic/aseismic sliding

As specified previously, a common feature for composite volcanoes edifices is an inherent flank instability (e.g. De Vries and Borgia, 1996; De Vries and Francis, 1997; Doglioni et al., 2001; Ruch et al., 2012; Ruch et al., 2013; Elsworth and Day, 1999). In the case of Mount Etna, the SE movement towards the Ionian Sea is extremely well monitored using GPS, strain meters, and seismic methods (Fig. 1.6). Seismicity occurs mainly on the eastern sector of the edifice, with 80% of the events occurring at very shallow depths (<5 km) and with variable energy (e.g. Azzaro et al., 2013; Mattia et al., 2015; Patane' et al., 2011).

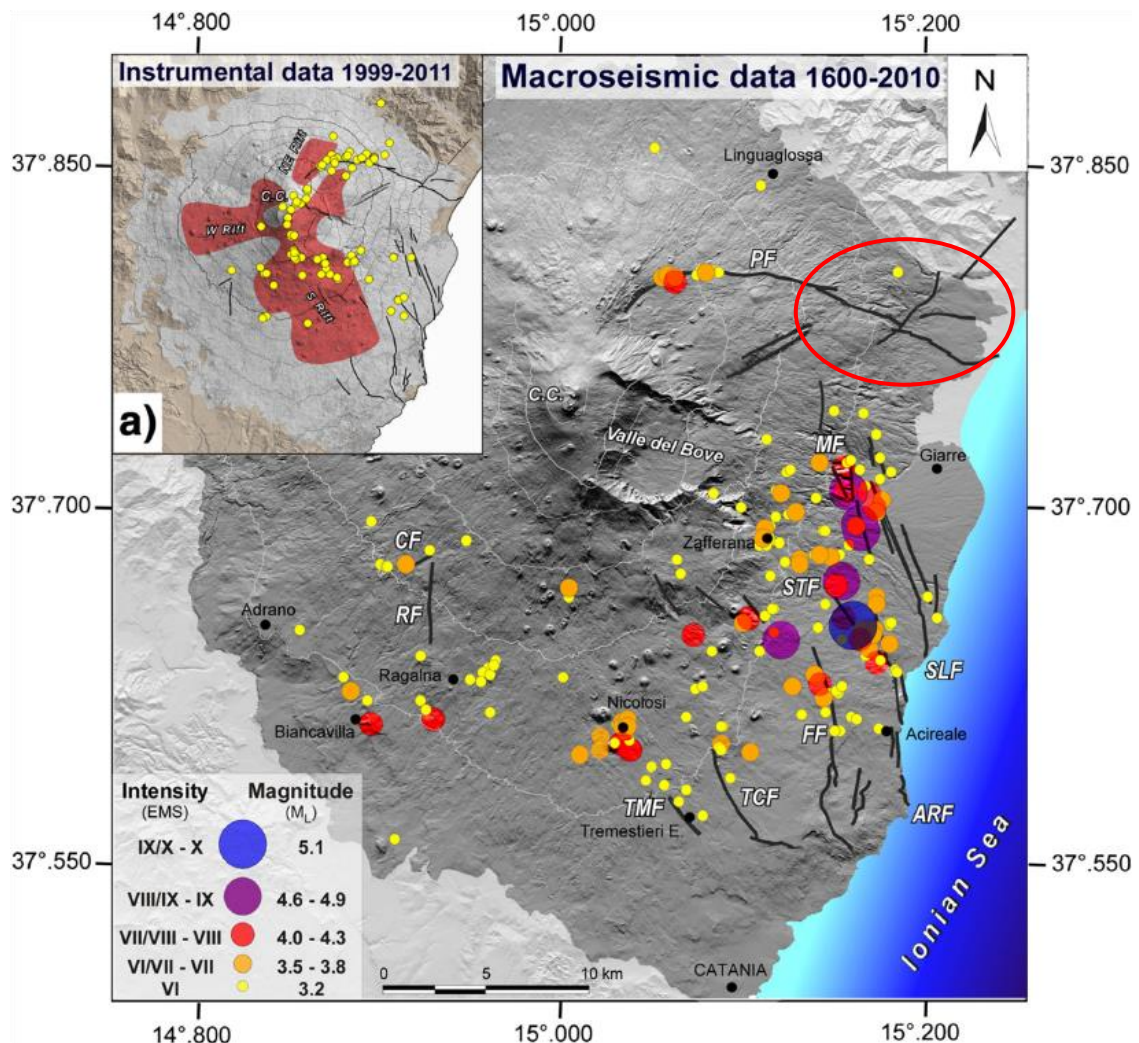


**Figure 1.6.** Map of the historical seismicity (1600-2010) showing that seismic events are located mainly along the fault systems bordering the southern-eastern flank of Mount Etna. In clockwise order, the faults' abbreviations: PF, Pernicana; MF, Moscarello; STF, Santa Tecla; SLF, San Leonardello; FF, Fiandanca; ARF, Acireale; TCF, Trecastagni; TMF, Tremestieri; RF, Ragalna; CF, Calcerana. The majority of the events are located in the eastern sector characterized by a series of normal faults, called Timpe, here divided in MF, STF, SLF, FF, ARF (from [Azzaro et al., 2013](#)). It is worthy to not the lack of seismicity along the lower sector of the PF, highlighted by the red circle.

[Borgia et al., 1992](#) first documented that the flank is sliding over its clay-rich substratum driven by gravity, starting from some 300k years ago and still active. Since then, several approaches such as GPS monitoring, field mapping, seismic investigations, and geophysical investigations studied the south-eastward spreading (e.g. [Bonforte and Puglisi, 2006](#); [Azzaro et al., 2013](#); [Acocella et al., 2013](#); [Alparone et al., 2013](#); [Azzaro et al., 2012](#); [Groppelli, 2011](#); [Mattia et al., 2015](#); [Ruch et al., 2010](#); [Ruch et al., 2013](#); [Siniscalchi et al., 2012](#)). Fault systems delimit the flank from north-east with the Pernicana Fault System (i.e. PFS), to the south with the Ragalna Faults (i.e. RF). To the east, it is present a series of normal faults with consistent eastward downthrow (i.e. up to 200 m), called Timpe Fault System, which permits the flank to slide into the un-buttressed side facing the Ionian Sea (e.g. [Borgia et al., 1992](#); [Acocella et al., 2013](#); [Chiocci et al., 2011](#); [Bonforte and Puglisi, 2006](#)). All together, these fault systems dissect the flank into five different domains, each one moving at a different rate (i.e. [Azzaro et al., 2013](#)), and delineating a complex structural and geodynamic interaction.

[Azzaro et al., 2013](#) divide the five domains in the following areas (Fig. 1.7): (i), the NE block, delimited to the north by the PFS and presenting the highest deformation velocities (2-3 up to 5 cm/y in concomitance with eruptions), with velocities diminishing towards south (i.e. light blue in Figure 1.7); ii) a central block delimited by the MF and STF, located in the Timpe Fault System (i.e. light blue block); iii) the Giarre wedge positioned to the east of the Timpe system (i.e. red block); iv) the medium-E block, delimited by the STF and TCF (i.e. green block); and v) the SE block to the south, that shows the least activity (i.e. yellow block).

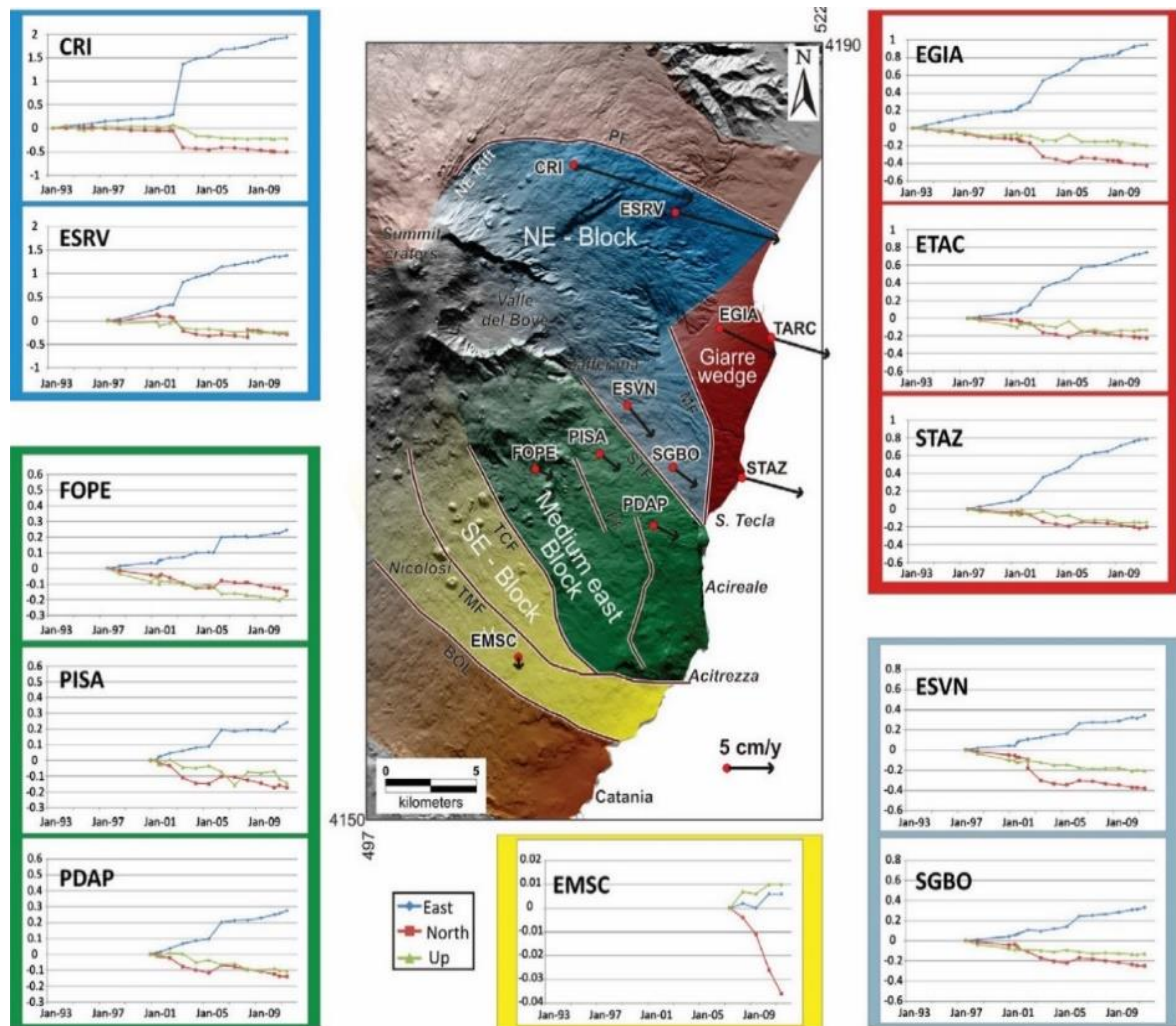


**Figure 1.7.** From [Azzaro et al., 2013](#). Division of the eastern flank in five main blocks, according to GPS measurements in combination with SAR (i.e. Synthetic Aperture Radar) velocities, where each block shows a certain direction and velocity. Starting from top left in blue are reported data for 1) the NE block, delimited by the PFS, showing the highest velocities; part of this block are 2) the stations reported in light blue at the right bottom, and located in the map at the centre of the sliding flank; 3) top right in red are reported data for the Giarre Wedge; 4) in green at the left bottom data for the Medium East Block; 5) in yellow at the bottom the velocities for the SE block, reporting the slowest deformation velocities.

Ground motion movement is monitored by GPS since 1988 (e.g. [Puglisi et al., 2004](#); [Azzaro et al., 2013](#)) highlighting that the deformation rate cannot be the result of only magmatic source or of gravity: a concomitance of factors leads the movement. Several subsequent studies used different approaches, including seismic, geophysical, geological,

and GPS (Global Positioning System) data in order to unravel which mechanism and/or mechanisms are active in promoting the sliding.

[Mattia et al., 2015](#) reviewed the three primary models proposed in literature to explain the sliding. Firstly, the ‘deep-seated spreading model’, in which spreading is related to magma inflation processes and it is mainly concentrated along a low-angle thrust at 5 km depth. Amongst the reasons why this hypothesis is not satisfactory, is the lack of clear morpho-structural evidences of a thrust at the foot of the edifice or offshore, where only extensional structures are detected, as well as the lack of typical compressional seismic events. Secondly the ‘shallow sliding model’, in which the sliding is located at shallow depth, along an arcuate structure and the mobile flank is dissected into minor blocks moving eastward under their own weight. This second hypothesis is not satisfactory because according to FEM model proposed if the sliding is deep should be blocked by the overburden even if closer to magmatic source, while if shallow, the load is less but magmatic sources such as dike intrusions have not enough force to trigger the sliding. Thirdly, the ‘tectonic blocks model’, where sliding is from individual blocks delimited by normal and strike-slip faults. According to this interpretation, the tectonic structures merge at depth (10-15 km). Based on these three models and integrating new data, [Mattia et al., 2015](#) presented geodetic data obtained by Continuous GPS (CGPS), seismic data, seismic tomographic data, fluid geochemistry, and groundwater chemistry between years 2008-2013 to investigate the sliding of the flank. They find that, ultimately, several factors cause the movement: gas emissions may be indicative of fluid pressure variations in the system, thus pressure changes are one of the cause of instability.

The importance of deep fluids interaction with tectonic systems is further provided by the regular seismic signals (e.g. [Day, 1996](#); [Fazio et al., 2017](#); [Gambino et al., 2016](#)). These findings also highlight the evidence of fluid circulation and its interactions with tectonic features along with the presence of a clay substratum. In particular, [Siniscalchi et al., 2010](#) well detected fluid circulation in Mount Etna’s basement, reporting the presence of ascending hydrothermal fluids and descending meteoric waters, both infiltrating along the numerous fault systems that dissect the flank. The circulation of hot magmatic fluids can induce fracturing and alteration of large portion of rocks and locally, in circumstances where pore fluid pressure can build up (e.g. presence of clay or faults), the overall strength can diminish and sliding is promoted. Fluid overpressure can cause micro-fracturing, and in



presence of soils with low permeability, hydro-fracturing driven by deep magmatic and hydrothermal fluids is particularly efficient because pressure can build up to levels higher than the overburden. This fluid circulation is further affected by the changes in strain causing transfer of thermal fluids, which in turn cause further degradation of rocks.

A characteristic feature at Mount Etna is the lack of a clear seismicity related to the movement of the easternmost sector of the flank, in correspondence of the PFS, despite its high sliding rate (e.g. [Azzaro R., 2001](#); [Ruch et al., 2013](#); [Obrizzo, 2001](#)). As highlighted in Fig. 1.6, the 80% of the events are located mostly within 5 km depth along the system of normal faults called Timpe Fault System (i.e. [Azzaro et al., 2013](#)). The PFS consists of two segments: the first part starts from the NE-Rift descending towards east, showing clear seismicity related to magmatic events, changes to the static stress fields and sliding. The second part, descending towards the Ionian Sea is showing a near continuous sliding with lack of seismic events (e.g. [Azzaro R., 2001](#)) (Fig 1.6, inside the red circle). The latter can be due to the interplay of different factors: the presence of lithologies that lower the frictional strength resulting in stable behaviour and the presence of fluids that contribute to lower the overall strength. [Mattia et al., \(2015\)](#) concluded that the interaction of magmatic fluids with groundwater and aquifers in the presence of an impermeable layer of quaternary clays is a key factor for flank instability at Mount Etna.

To date, the majority of the results accounting for the feasible mechanisms operating in the Etnean basement lowering the strength and promoting the sliding are mostly obtained from macro-scale approaches. For this reason, few recent studies using Etnean samples started to question what are the leading factors contributing to such an extent to the degradation of these rocks' mechanical strength. Various experimental approaches used P, T and pore fluid pressure at relevant conditions to shed light on the mechanisms activated during deformation, as reported in section 1.3.

### 1.3 Faulted and intact rocks: experimental overview

Faulted and intact rocks are matter of study since many years. Understanding how and why rocks deform under certain laboratory conditions, often chosen to represent as close as possible the natural conditions, helps to constrain in a controlled manner the physical, chemical, mechanical processes that rocks experience during deformation. What is the definition of strength of a rock? 'Qualitatively, *strength* can be defined as the resistance to

permanent deformation by flow or fracture. In a more precise, quantitative sense, strength is the stress level that is required to produce a certain type of permanent deformation, fracture or flow, under well-defined experimental conditions' (i.e. [Chapple, 1987](#)). Amongst the numerous technique used to assess rocks strength, which their description goes beyond the scope of this thesis, triaxial deformation using specific experimental apparatus is one of the most used technique. Triaxial apparatus apply differential pressures that can resemble those present in depth, for instance in the upper crust: the three axis of principal stresses are therefore non-zero. Stress is the unit force per area, in geology expressed in MPa and for definition  $\sigma_1$  is the maximum effective stress,  $\sigma_2$  the intermediate stress and  $\sigma_3$  the minimum effective stress, and compressive stress is considered positive (i.e. [Paterson and Wong, 2005](#)) (Fig. 1.8).

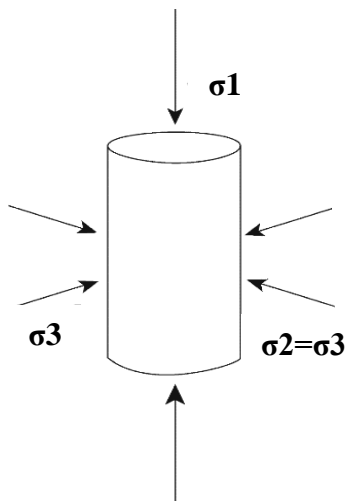


**Figure 1.8.** Stresses representation in triaxial configuration, modified after [Paterson and Wong, 2005](#).  $\sigma_1$  is considered positive and it is applied axially,  $\sigma_2 = \sigma_3$  with  $\sigma_3$  being the confining

The volume of rock, in cylindrical shape, is firstly loaded in hydrostatic conditions with confining pressure until the desired pressure is reached, such as that  $\sigma_1 = \sigma_2 = \sigma_3$ . Then an axial pressure is applied through a loading piston in contact with the sample, such as  $\sigma_1 \neq \sigma_2 = \sigma_3$  with  $\sigma_1 > \sigma_2 = \sigma_3$  until deformation (e.g. strain) occurs, and differential stress is recorded ( $\sigma_1 - \sigma_3$ ). Pore fluid pressure is usually applied, as fluids has great influence in rock deformation, and in this case the effective stress is recorded  $\sigma = \sigma_1 - P$  with  $P$  as pore fluid pressure (MPa) (e.g. [Paterson and Wong, 2005](#); [Baud et al., 2000b](#); [Rutter, 1972](#); [Rutter, 1974](#)).

Triaxial apparatus allow to record many parameters (i.e. load displacement, pore fluid pressure, confining pressure, temperature), and data are graphically represented in the force/displacement or stress/strain space (Fig. 1.9).

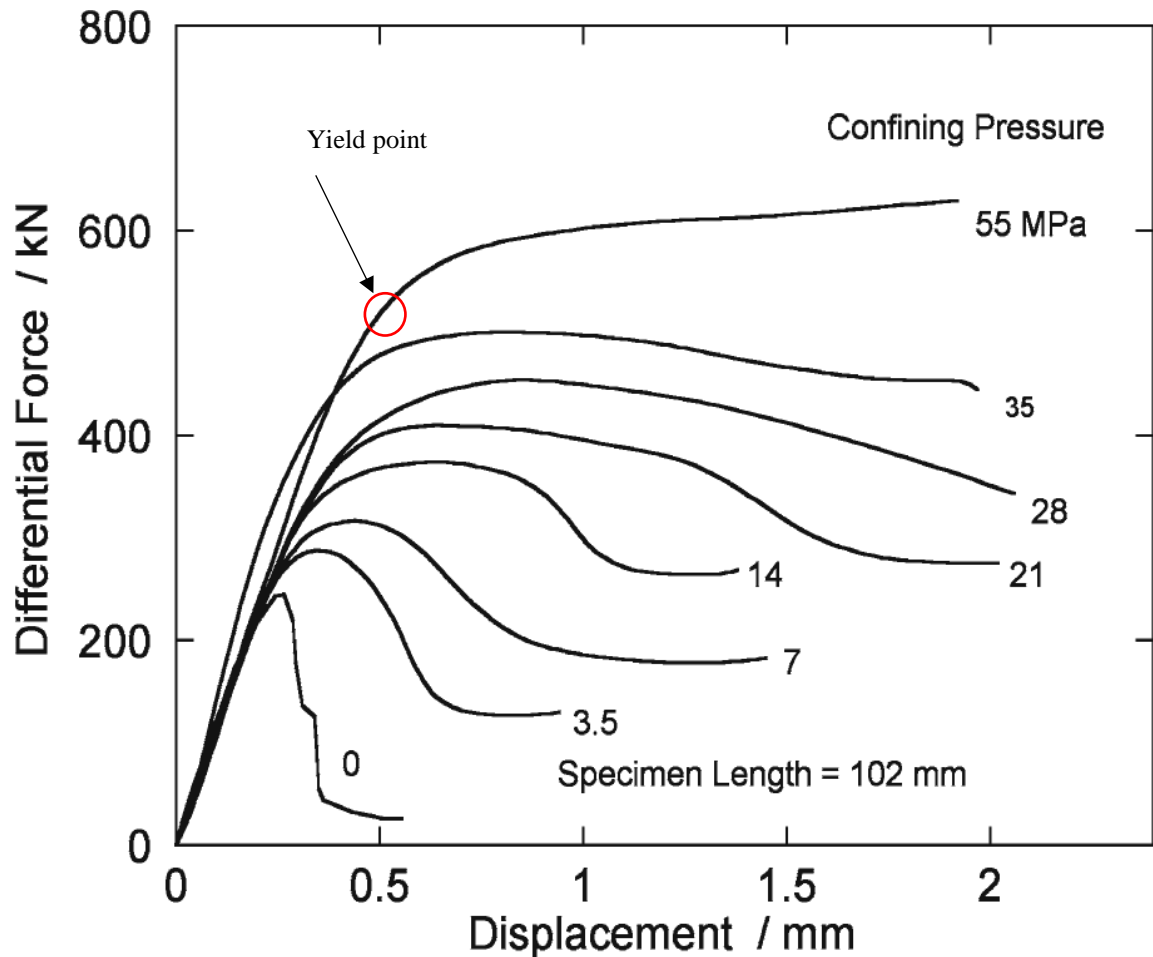


**Figure 1.9.** Modified after [Paterson and Wong, 2005](#). General example of the evolution of the mechanical behaviour of Tennessee marble at increasing confining pressure (reported in MPa close to each curve). The red circle highlights the Yield point, at which the deformation moves from elastic to inelastic.

As reported in Fig. 1.9, the data obtained are useful to study the mechanical behaviour of rocks when exposed to increasing confining pressure and axial load, resembling natural conditions at depth. The mechanical approach allows recording and monitoring closely the evolution of deformation that rocks are experiencing, otherwise difficult or even impossible to retain with *in situ* measurements. In the example reported in figure 1.9, the first part of the curve shows a linear behaviour defined as the elastic behaviour. In this section it is possible to measure the Young Modulus (i.e. the elastic stiffness of the rock), expressed as

the ratio of the axial stress over the strain  $E = \frac{\sigma}{\epsilon}$ . Inelastic behaviour follows, starting at the yield point (i.e. the limit between elastic behaviour and the onset of inelastic behaviour, or plastic behaviour. Red circle in figure 1.9): from this point onward, depending the type of rock and the conditions applied, the rock can deform by localized shear fracture, or by ductile behaviour. The Coulomb failure criterion describes the development of brittle failure in intact rocks (1.1):

$$|\tau| = c + \mu_i \sigma_n \quad (1.1)$$

with  $\tau$  shear stress and  $\sigma_n$  normal stress respectively acting on the newly formed fault plane,  $c$  is cohesion, and  $\mu_i$  is the coefficient of internal friction (e.g. [Lockner and Beeler, 2002](#)). Brittle behaviour implies the formation of a macroscopic fracture, here described following the standard definition that failure is a sudden loss of strength (i.e. [Lockner and Beeler, 2002](#)). When the fracture takes form, the frictional strength of the material filling the voids between the surfaces of the fracture dictate the strength of the system. Amontonow's law (1.2) describes the frictional resistance as:

$$|\tau| = \mu_f \sigma_n \quad (1.2)$$

with  $\mu_f$  being the friction coefficient.

Several experimental studies highlight the importance of many parameters influencing the strength of both intact rocks and fractured rocks (i.e. [Lockner and Beeler, 2002](#)), for instance mineralogy, porosity, surface roughness, temperature, pore fluid pressure. After several friction coefficient measurements, [Byerlee, 1978](#) found that below the threshold of 200 MPa normal stress, the majority of rocks follow a linear equation for friction, such as that  $\tau = 0.85\sigma_n$ , and for  $200 < \sigma_n < 1700$  MPa is  $\tau = 0.50\text{MPa} + 0.6\sigma_n$ . Despite its empirical nature, eq. (2) is often referred as the Byerlee's rule. For certain type of rocks, such as carbonate, the ductile behaviour is easily achieved in laboratory, when relevant conditions of temperature, pressures and pore fluid pressures are applied (e.g. [Baud et al., 2000a](#); [Rutter, 1974](#)). Pore fluid pressures has a direct effect on the rock strength, reducing the effective stress according to the law (1.3):

$$\sigma_{n,\text{eff}} = \sigma_n - \alpha p \quad (1.3)$$

with  $\alpha$  being the pore geometry constant, and  $\alpha=1$  for well-connected porosity rocks (e.g. [Walsh and Brace, 1984](#)). Temperature, the other parameter here considered, has a renowned effect in reducing rock strength already in the brittle regime, promoting thermal cracking (e.g. [Rutter, 1972, 1974](#); [Siegesmund S., 2000](#) [Lockner 2002](#) and references therein).

The ductile behaviour is the capacity of the sample to sustain an increasing axial displacement without the formation of a macroscopic failure or loss of strength (e.g. [Paterson and Wong, 2005a](#); [Bakker et al., 2015](#)) (in fig. 1.9 the experiment at 55 MPa confining pressure is showing ductile behaviour). The brittle-ductile transition (BDT) is not a sharp transition: indeed rocks often show a transitional behaviour called semi-brittle flow or cataclastic flow (e.g. [Baud et al., 2000a](#)), in which the rock is showing a macroscopic ductile behaviour but micro-fracturing is present at the grain scale. The BDT plays a paramount part in the fluid transport capacity of rocks (e.g. [Violay et al., 2012](#)). It has been seen that the cataclastic flow regime activates two end-members, depending on the nature of the rock, its porosity and grain size, and the stress field. The first end-member, dilation, is usually present when porosity is low and circulation of fluid is promoted and the permeability is increasing until the brittle failure is reached. The second end-member, compaction, is present when porosity is higher and pores collapse as deformation is continuing, and permeability is suppressed (e.g. [Baud et al., 2000a](#)). Dilation and compaction, or an interplay of the two, may therefore promote or prevent fluid circulation (e.g. [Violay et al., 2012](#)).

Laboratory measurements at increasing P and T conditions allow estimations of the mechanical strength of rocks composing the Earth's crust and their transition from the brittle to the plastic regime, and data are used to create strength profiles of, for instance, the oceanic and continental lithosphere (i.e. [Kohlstedt et al., 1995](#)). In the case of this study, it is helpful to identify the region at which the deformation mechanisms are activating dilation or compaction. The general transition from brittle to semi-brittle, and from semi-brittle to ductile deformation is reported by [Kohlstedt et al., 1995](#) in figure 1.10 showing the fracture strength (i.e. solid black line) behaviour at increasing strength and pressure, defining the transition at BDT and BPT (i.e. semi-brittle to plastic flow).

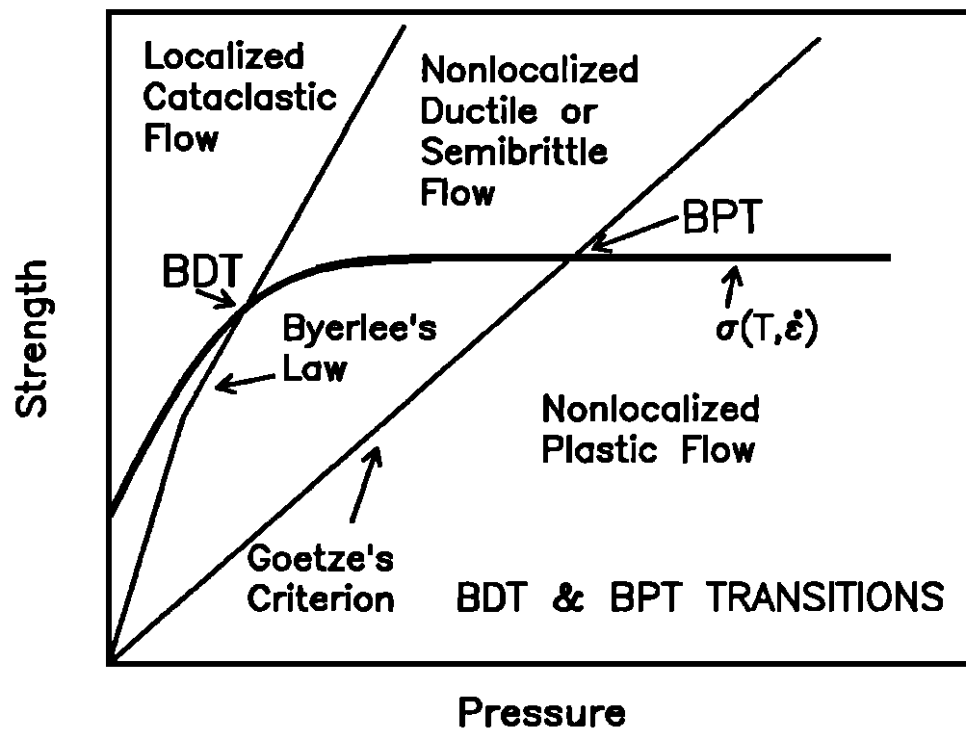


**Figure 1.10.** From [Kohlstedt et al., 1995](#). Representation of the transition from the brittle deformation to the semi-brittle flow (BDT transition), and the transition from semi-brittle deformation to plastic flow (BPT transition). The Byerlee's Law and the Goetze's Criterion are reported as reference.

The Goetze's Criterion identifies the region where the stress necessary to activate the plastic flow is about equivalent to the confining pressure.

Nucleation and development of a macroscopic fracture under applied stress-strain conditions involves micro-cracks growth, oriented according to the stress field applied, and stages pre-, during, and post-failure are often accompanied by emission of 'noise' or Acoustic Emissions (AE) and release of energy or elastic wave velocities (i.e. micro-seismic events) well recorded by the mean of ultrasonic piezoelectric transducers (PTZs). The ongoing brittle deformation causes damage inside the sample creates elastic anisotropy. Seismic waves travelling through the sample are sensitive to the elastic anisotropy, and its measurement allow the estimation of the seismic anisotropy, which is an index of the internal damage. In particular, faults nucleation and growth have been extensively studied through AEs emission, showing to have different frequency responses at ongoing stages of deformation (i.e. [Onhaka and Mogi 1982](#)). Nowadays, PTZs allows the recording of AEs

together with their spatial location: it is possible to graphically position these signals to get an image of the deformation (e.g. [Scholz, 1968a](#); [Benson et al., 2007](#)). AEs, being the expression of brittle deformations, are sensitive to the transition to semi-brittle and ductile deformations, in which they tend to diminish in frequency and rate.

Finally and generally speaking, when the fracture is formed, the frictional properties of the fault surfaces and fault gouges control the overall strength of the system. Investigation about frictional properties of rocks and gouges and mechanisms active during sliding is also a long story. In the broad spectrum of fault slip, the response of rocks to movements along pre-existing planes (e.g. faults) determines the seismogenic or non seismogenic nature of the fault, which is a rapid slip with generation of an earthquake or aseismic slow slip or creep, respectively (e.g. [Byerlee, 1978](#);). Friction along fault planes can vary according to many, diverse parameters: roughness of the contact surfaces, presence of fluids, composition of fluids, pressures, state of stresses before-during-after the movement, temperature, , filling materials (fault gouges), mineralogy of the gouges, particle size and angularity, fabric of fault zones just to cite few (e.g. [Byerlee and Brace, 1968](#); [Byerlee, 1978](#); [Scholz, 1998](#); [Di Toro et al., 2011](#); [De Paola et al., 2010](#); [Lockner and Beeler, 2002](#); [Kanamori, 1994](#)).

Fault gouges vary in composition, grain size and thickness depending on the nature of parent rocks, as well as on the geological setting and for chemical and/or mechanical alteration (e.g. [Byerlee, 1978](#); [Anthony, 2005](#); [Scholz, 1987](#)). Along active faults, slip accumulates through timescales that can vary from seconds to centuries (i.e. [Kanamori, 1994](#)), evolving from a state of new formation to progressively a mature fault zone, hence they can present variable thicknesses. The dominant mechanical behaviour along a fault plane, either stick slip or stable sliding, is determined by the nature of gouges, as gouges accommodate strain through comminution, dilation and/or compaction, sliding, rolling and shear localization is favoured with increment of displacement (e.g. [Anthony, 2005](#); [Marone, 1998](#); [Marone et al., 1992](#); [Scholz, 1987](#)).

#### 1.4 Insights from Laboratories

Investigations from macro-scale (e.g. field surveys, GPS, geophysical) to micro-scale (e.g. laboratory experiments) are of paramount importance to unravel the mechanisms active at Mount Etna. Laboratory experiments provide a robust approach to investigate how rock mechanical and physical properties vary depending on the large spectrum of subsurface

conditions. They enable to directly control and monitor several environmental conditions (e.g. pressure, stress, temperature, strain) whilst investigating the evolution of some samples properties in presence of conditions similar to those in volcanic basements. Previous studies have therefore taken advantages of this well controlled environment to clarify our understanding of the mechanisms supporting the instability of volcanic edifices.

Basalt is often used as representative for the volcanic edifice in order to explore such mechanisms. For instance, [Benson et al., 2007](#) provides a very detailed study on how acoustic emission (AE) and AE events locations can be used to imaging the failure of the basalt subjected to deformation in triaxial apparatus. [Fazio et al., 2017](#) mimics the transition of a hot fluid through hollowed cylinders of basalt in order to detect seismic signal driven by the passage of the fluid. [Browning et al., 2016](#) records AE emissions during heating and cooling phases of basalt samples, finding that during cooling phases the AE rate and energy are much higher than during heating, indicating higher rate of thermal cracking. [Bubeck et al., 2017](#) explores the variability of strength in porous basalts containing pores with various curvatures, showing how the strength of the basalt change accordingly to shape and elongation of the pores respect to the applied stress.

Most studies focus on rocks composing the basement (e.g. [Elsworth and Voight, 1992](#); [Delaney and Pollard, 1982](#); [Heap et al., 2013](#); [Bakker et al., 2015](#)). As highlighted before, the basement of Mount Etna is the result of a series of complex tectonic interactions involving sedimentary successions composed mainly of sandstone, claystone and limestone, with the presence of an impermeable layer of quaternary clays on top of which rests the volcano edifice. Because of this heterogeneous composition, it is not an easy task to obtain detailed physical, chemical and mechanical information encompassing all the constituent lithologies. For this reason, the primary focus here is on few representative lithologies, such as carbonate rocks.

To explore this effect in a logical and consistent manner, the evolution of rock's mechanical properties both in presence of magmatic fluids or transient high/low temperature patterns is studied. Transient temperature variation may lead to the generation of permanent changes to the hosting material, owing to heat-induced mineralogical transitions, hydrothermal alteration, and intrusion-induced fractures. Basement rocks typically host some type of pore fluid (water, brine, hydrothermal fluids: e.g. [Day, 1996](#), [Mattia et al.,](#)



2015, Dautriat et al., 2011), and owing to the distribution of intrusions in sub-volcanic systems, much of the sub-edifice basement is likely to be subject to lower – but still elevated – temperatures (i.e.  $<600\text{ }^{\circ}\text{C}$ ). Recently, new data extended this knowledge to investigate the effect of high temperatures on triggering physical and chemical reactions via decarbonisation (e.g. Heap et al., 2013; Mollo et al., 2011; Bakker et al., 2015b). In one of these studies the physical and mechanical properties of two limestone units (i.e. Climiti and Thala units, Heap et al., 2013) were investigated in uniaxial and at *in situ* elevated temperature conditions. Both materials underwent decarbonisation reactions, with a total mass loss of 45 % occurring between  $560\text{--}900^{\circ}\text{C}$ , which accompanied a drastic change of the limestone physical properties. Increasing temperature and pressure resulted in a change in peak stresses in the brittle field, up to  $500\text{ }^{\circ}\text{C}$ , above which ductility was promoted (i.e. Bakker et al., 2015), as the specimens started to ‘flow’ in an aseismic manner, with a strong dependence of flow stress on temperature (i.e. decreasing in dry elastic moduli, seismic velocities, and acoustic emission rate). It was suggested that such processes may be responsible for the large-scale deformation present at Mount Etna. This hypothesis is further reinforced by observations of clay dehydroxylation (i.e. Mollo et al., 2011), along with a decreased strength that is likely to further promote flank instability and explain low seismicity zones, as well as the high local  $\text{CO}_2$  overpressures. However, the limitation of these experiments is that they were conducted at ambient pressure conditions, rather than pressures that simulate burial depth. Nicolas et al., 2016 explored the brittle and semi-brittle behaviour of a 14.7 % porosity,  $\sim 100\%$  calcite Tavel limestone and compared the results with CL in dry and saturated conditions, also using low *in-situ* temperature in an additional series of dry tests. Tavel limestone showed a brittle behaviour up to 55 MPa followed by a semi-brittle behaviour over 55 MPa. Water had a relatively small impact on the strength of Tavel limestone (i.e. Nicolas et al., 2016). In addition, recent triaxial experiments performed on CL by Bakker et al., 2015 used representative shallow subsurface volcanic pressure conditions (specifically 50 and 100 MPa representative of 2 and 4 km depth). Collectively, these studies support the hypothesis that both elevated temperature and pressure have significant effect on the mechanical strength of carbonate rocks. Confining pressure limit the decarbonation reactions as a result of the decreased porosity due to increasing pressures, as well as the increased  $\text{CO}_2$  fugacity, which has a major role in controlling the decarbonation process (i.e. Mollo et al., 2011). They identify that the brittle-ductile mechanical transition occurs at temperatures of approximately  $350\text{ }^{\circ}\text{C}$ , with 50 MPa confining pressure and constant strain rate at  $10^{-5}\text{ s}^{-1}$ . In

addition to these investigations of induced damage at high temperatures, micro-crack damage is also inferred to occur during heating and cooling (i.e. [Browning et al., 2016](#)). This latter effect is important as the injection of dykes and sills clearly expose the country rock to significant temperature gradients. Indeed, the increasing and decreasing amount of heat radiated by an intrusion into a body of country rock very likely play an important role on the rock's temperature-dependent properties and processes, such as decarbonation in limestone, potentially further reflected in the overall deformation observed at the surface.

[Heap et al., 2013](#) performed high temperature, uniaxial compressive strengths experiments on samples from two carbonate rock layers modelled to be present in the basement. The results show how increasing temperature further promote deformation in the ductile regime strongly suggesting this to be a key factor in promoting flank instability. [Mollo et al., 2011](#) reported dehydroxylation and decarbonation reactions of clay minerals and carbonate terms respectively belonging to the Etnean basement. In this case, the *in situ* high temperature together with the chemical reactions degraded the mechanical strength of the rocks reinforcing that temperature plays a crucial role for instability. Finally, other studies (e.g. [Bakker et al., 2013](#) ; [Wiesmaier et al., 2015](#); [Bakker et al., 2015](#)) focused on microstructural, physical, and mechanical/seismic properties, and how they evolve under a series of different conditions (e.g. uniaxial and triaxial deformation, high and low confining pressures, high and low temperature, drained/undrained saturated or dry conditions).

Since the 70's, a systematic experimental and theoretical investigation was carried on with the aim of reproducing observed conditions in faults, to unravel and constrain the mechanical, physical and chemical processes acting during sliding (e.g. [Lockner and Beeler, 2002](#)). Specific apparatus designed to run experiments on bare rocks surfaces with or without the presence of gouge layers have allowed to contribute enormously to the body of knowledge of frictional mechanics in fault zone: triaxial experiments using metal or rock saw-cut cylinder geometry, with or without the presence of a gouge layer (e.g. [Rutter et al., 1986](#); [Byerlee and Brace, 1968](#); [Faulkner et al., 2011](#); [Logan and Rauenzahn, 1987](#)); double-direct shear configuration (e.g. [Collettini et al., 2009](#); [Ikari et al., 2011](#); [Marone and Kilgore, 1993](#); [Marone et al., 1990](#)); slow to high velocity apparatus or rotary shear (e.g. [De Paola, 2013](#); [De Paola et al., 2010](#); [Di Toro et al., 2011](#)).

In previous studies of granular mechanics grain size, grain angularity, mineralogy, layer thickness, and boundary surface roughness resulted to be all factors influencing sliding behaviour (e.g. [Anthony, 2005](#)). Angularity can promote stable sliding, at least for quartz gouges and carbonate gouges (e.g. [Mair et al., 2002](#); [Chen and Spiers, 2016](#)). Mineralogical content influences the sliding behaviour of gouges (e.g. [Ikari et al., 2018](#)). [Tembe et al., \(2010\)](#) combined mixtures of quartz, illite and montmorillonite showing how the friction coefficient is dependent of clay content: the friction coefficient of the samples containing variable amounts of clay fall inside the two end-members of pure quartz and pure clays. Also [Logan et al., \(1987\)](#) investigated the frictional behaviour of quartz combined with montmorillonite, finding that the presence of clays decreased the friction coefficient. [Anthony, \(2005\)](#) conducted experiments on simulated gouges both with angular and spherical grains, with rough and with smooth boundary surfaces, and with varying layer thicknesses. They found that the presence of rough surfaces along with layers of angular grains consistently increased the friction coefficient. They also showed that thin layers (i.e. 2 mm) have a higher friction coefficient relative to thicker layers (i.e. 8 mm).

Changes in the friction coefficient depend also from sliding velocity. To describe how friction coefficient  $\mu$  is dependent from velocity ( $v$ ) perturbations and other internal variables  $\theta_i$  (e.g. [Skarbek and Savage, 2019](#); [Marone, 1998](#)), [Dieterich, 1979](#) and [Ruina, 1983](#) introduced the rate and state friction law. In particular,  $a$  and  $b$  express the direct and evolution effect that is happening when the velocity is changed, hence how the friction coefficient responds to the change ( $a$ ) and how is the evolution towards a new steady state ( $b$ ), and  $D_c$  is the slip distance needed to attain this new steady state. Hence the friction coefficient is:

$$\mu = \mu_0 + a \ln (v/v_0) + \sum_i b_i \ln(\frac{v_0 \theta_i}{d_{ci}}) \quad (1.4)$$

To describe the evolution of the state variable, two equations are usually used. The aging law ([Dieterich, 1979](#)):

$$\frac{\delta \theta_i}{\delta t} = 1 - \frac{v \theta_i}{d_{ci}} \quad (1.5)$$

and the slip law (Ruina, 1983):

$$\frac{\delta \theta_i}{\delta t} = -\frac{v \theta_i}{d_{ci}} \ln\left(\frac{v \theta_i}{d_{ci}}\right) \quad (1.6)$$

By resolving the rate and state friction law, it is possible to obtain information about the friction properties of the material tested. If  $(a-b) > 0$ , then the material is velocity strengthening, that is the strength of the material is increased and the sliding is stable. If  $(a-b) < 0$ , then the frictional resistance decrease and the material is considered velocity weakening, presenting unstable sliding.

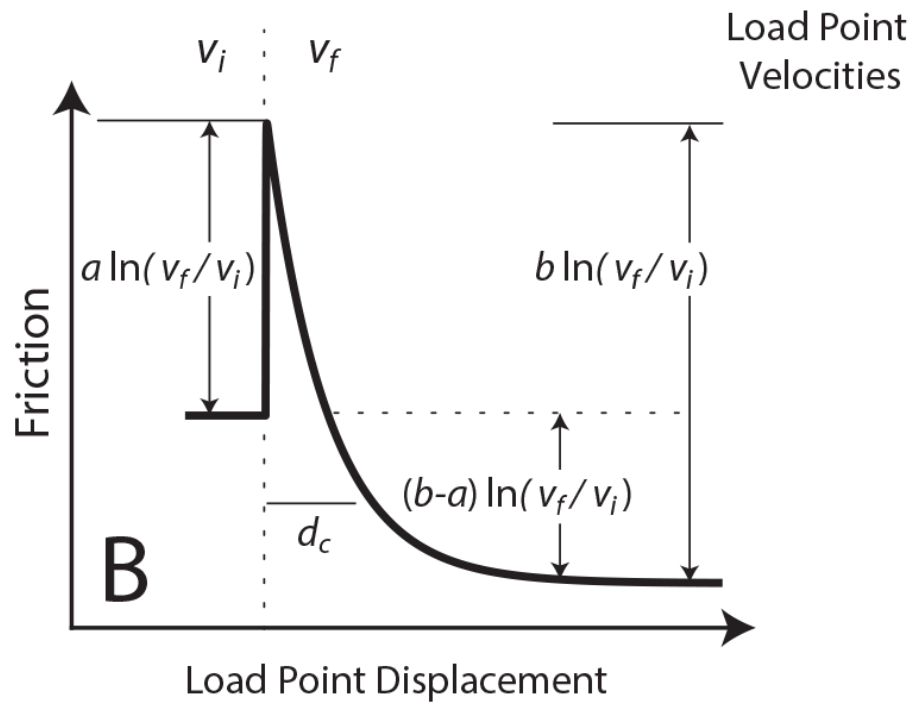


**Figure 4.25.** Example of a velocity step event (from Skarbek and Savage, 2019). The velocity change from  $V_i$  to  $V_f$  is causing an abrupt increase in friction coefficient, followed by a new steady state after a critical distance  $d_c$ . In the example reported,  $(a-b) < 0$  hence is velocity-weakening.

Samuelson and Spiers, (2012) recently introduced the so-called direct shear setup, in which triaxial friction tests are conducted by the means of two L-shaped half cylinders with a layer of synthetic gouge between them. As reported by the authors, it builds on and improve the precedent technique as it allows maintaining a constant normal stress on the sample throughout the test, avoiding continuous stress changes and recalculations pertaining to the saw-cut configuration. The technique has then been consequently used in other studies, with

the aim of further explore fault gouges properties (e.g. [Faulkner et al., 2018](#); [Leclere et al., 2016](#); [Verberne et al., 2013](#); [Pluymakers et al., 2014](#); [Hunfeld et al., 2017](#)). In this study, we designed and created our own sliding holders to accommodate more initial materials and shear displacement than is available in these other existing versions to support the research investigation.

### 1.5 Rationale of the Thesis

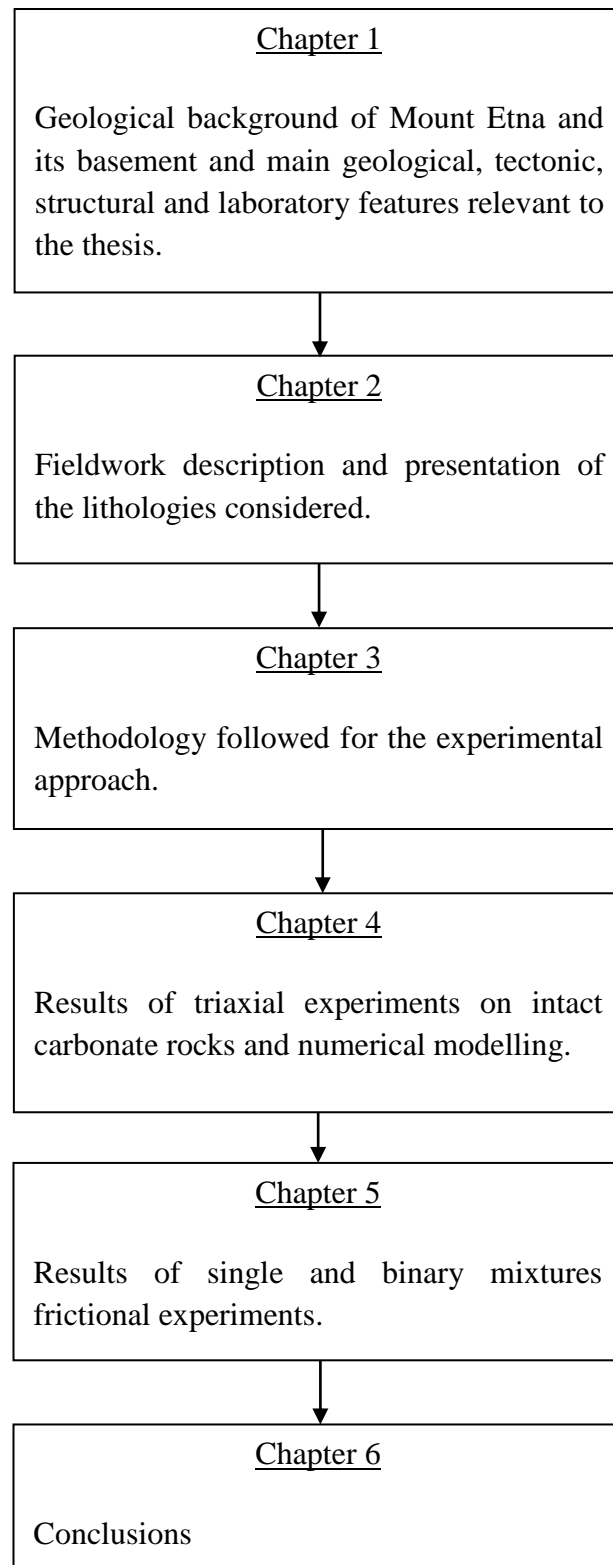
The main aim is to study how the application of differential pressures on intact carbonate rocks, thermally treated to mimic a distant dike intrusion, as well as the influence of pore fluid pressure alter the strength of these rocks, here considered as representative being one of the most abundant rock type present at Mount Etna's basement. Intrusions and magma emplacement (e.g. dike intrusions) repeatedly interest the volcano and its basement and they are consequently subjected to temperature gradients. Dyke emplacement increases temperature locally and rapidly in the hosted layers. Once inactive, the temperature naturally decreases to the regional ambient conditions. It is therefore very natural to question 'how such a heating and cooling event affects the Etnean carbonate rock properties present in the basement? How temperature and pressure influence these thermally degraded rocks promoting the transition from brittle to ductile deformation? How deformations can influence fluid transportation in the basement?'. At Mount Etna's basement, the presence of weak carbonate rocks prone to brittle-ductile transition at low depth (e.g.  $< 2$  km) brings important effects on fluid circulation due to the alternation between dilatant or compactant fracture modes. When fluids cannot circulate, and stress changes bring to an increase of the local pore fluid pressure, important consequences such as a decreased strength of the host rocks may contribute to the instability of the edifice. The presence of the impermeable layer of quaternary clay as well as the clayish lithologies composing the basement are other factors contributing to the limitation of fluids circulation.

The triaxial investigations on intact rocks brings new highlights on the role of transient temperature in Etnean rocks, determining the mechanical strength related to heating and cooling phases. Along with temperature, the presence of water is used to investigate the mechanical variations. Finally, a model reproducing two different dyke sizes (e.g. 1 and 10 m thickness) projects the results to estimate the indicative distance at which such temperatures are active in degrading the selected lithology,.

The study then expands the investigation on the frictional properties of Etnean rocks. Previous studies have also highlighted the presence of tectonic features such as normal and reverse faults, forming complex fault systems bordering the entire unstable flank and dipping at various and not certain depths into the basement (e.g. [Branca et al., 2011](#); [Borgia et al., 1992](#); [Puglisi et al., 2004](#); [Ruch et al., 2010](#)). In light of this research, it is timely to consider that these tectonic features are juxtaposing different lithological units, being the basement composed by such a great variety of lithologies. Furthermore, quaternary clays are present at the bottom of the volcanic edifice and clayish terms are part of the chaotic flyschoid formations of the basement, contributing with their presence in lowering frictional strength of faults and promoting flank instability. Clays significantly diminish the strength resistance on a fault plane, and as reported before in this chapter, they act as an impermeable layer able to raise significantly the local pore pressure and therefore decreasing significantly the local strength. Considering that these fault systems are active in a scale of thousands of year with considerable displacements, they are mature faults able to produce considerable fault gouges (e.g. [Tibaldi and Groppelli, 2002](#)). This hypothesis implies that flank instability also directly relates to the frictional strength of the gouge material. So the other question addressed here is: 'What is the frictional strength of Etnean gouges?'.

The second part of this PhD project hence focused on the investigation of the frictional strength of representative Etnean gouges. Building on a technique that [Samuelson and Spiers, 2012](#) used previously, a new laboratory apparatus for direct shear is first designed and implemented to allow for performing the relevant tests. The study presented here has the aim to record the variation of friction coefficient due to the presence of clays through experimental studies of binary mixtures of Etnean synthetic gouges under increasing confining pressures. Stable sliding or aseismic creep are characterizing the eastern sector of the sliding flank, and the results presented here highlight that at least one of the representative lithology (i.e. carbonate gouges) behave in a ductile manner already at shallow pressure condition (i.e.  $< 2$  km depth) and are strongly influenced by pore fluid pressure and temperature. The investigation of frictional sliding also highlighted that Etnean rocks, for the boundary conditions here investigated, show stable sliding for those mixtures combining carbonate and clay gouges. This is strongly in agreement with the hypothesis that flank sliding is located in the shallow part of the basement, if not at the edifice-basement interface where quaternary clays are abundant.

## 1.6 Thesis Structure



---

## *Chapter 2 Fieldwork & Material Characterization*

---

### 2.1 Introduction

This chapter presents an extensive description of the geological characteristics of the units collected, reporting qualitative and quantitative analyses to characterize mineralogical composition of the samples, density and particle size measurements.

### 2.2 Lithological characterization of Mount Etna's basement

Three weeks of intensive fieldwork allowed the collection of the main lithologies present in Mt. Etna's basement. The fieldwork took place between September and October 2015. Outcrops for sampling are targeted to match previous studies (i.e. [Weismaier et al, 2015](#)), and others have been added to build a broader sample set. This study focuses mainly on the units belonging to the Appenninic-Maghrebian Chain (AMC), but carbonate rocks belonging to the Hyblean Plateau (HP) foreland and a sample of blue-grey clay belonging to the Gela-Catania foredeep are added to the collection. Figure 2.1 shows the outcrops from [Weismaier et al, 2015](#) (i.e. green stars), while white stars indicate the outcrops of this fieldwork (i.e. white stars). A short description of each site follows.



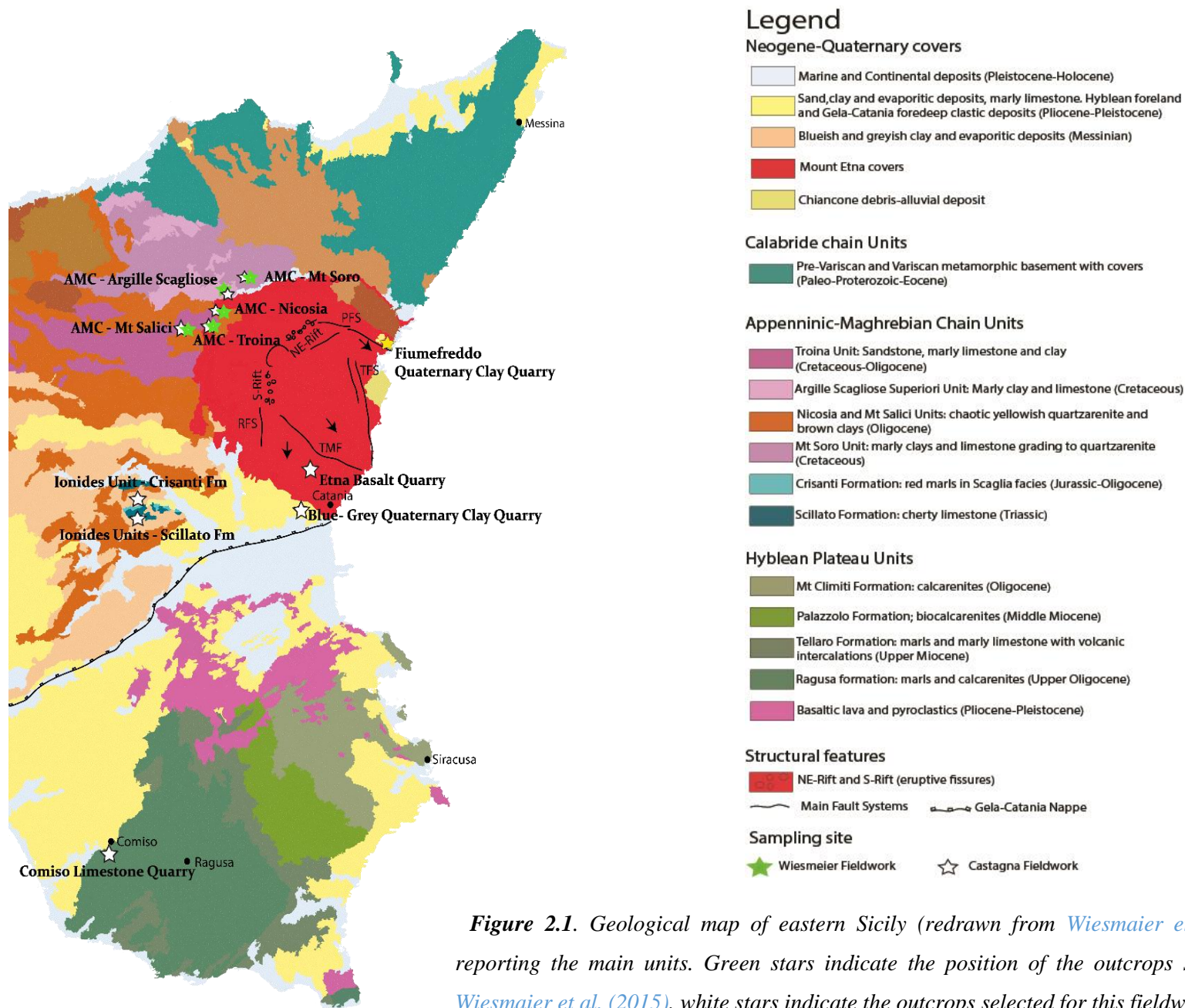


**Figure 2.1.** Geological map of eastern Sicily (redrawn from Wiesmaier et al, 2015) reporting the main units. Green stars indicate the position of the outcrops selected by Wiesmaier et al. (2015), white stars indicate the outcrops selected for this fieldwork.

### 2.3 Description of lithologies

The following section presents the lithologies collected during the fieldwork. As follow in this paragraph, a short description and the *in situ* mechanical data are listed along with the results of Uniaxial Strength by [Wiesmaier et al. \(2015\)](#), reported here as average USC obtained using their results. In Table 2.1 are summarized the main characteristic of the lithologies, explained in details in the following sections.

**Table 2.1.** Short description and mechanical analyses of the selected lithologies.

	Units	Formations	Description at the outcrop	Grain size (mm)	Colour	Schmidt Hammer	UCS Average (from Wiesmaier et al, 2015)
<b>Appenninic Maghrebian Chain</b>	Gela-Catania Foredeep	Quaternary Clay	Silt-clay	Very fine	Blue-Gray	N/A	N/A
	Sicilide	Mt Salici Flysch	Quartz-sandstone, massive	0.5 - 4	Yellow	27.1 - Weak	N/A
		Mt Soro Flysch	Quartz-sandstone, intensively fractured, fractures filled in fine material	0.5-4	Grey-Yellow	N/A	104.6 MPa
		Nicosia Unit	Sandstone, fractured,	0.5-5	Yellow	26.1 and 18.2 - Medium weak	17.49 MPa
		Troina Unit	Mica-bearing sandstone, intensively fractured	0.5-4	Grey-Yellow	19.3 - Weak	87.06 MPa
	Ionides Unit	Crisanti Fm	Limestone, intensively fractured, clayish interlayers	Very fine	Red-Green	17.6 - Weak	231 MPa
		Scillato Fm	Limestone, intensively fractured	Very fine	Yellow-White	30 - Medium weak	120.75 MPa
<b>African Plate</b>	Hyblean Plateau	Ragusa Fm	Massive layers of limestone	Very fine	White	23.95 - Medium weak	34.4 MPa (Priolo Fm)

### 2.3.1 Appenninic-Maghrebian Chain (AMC)

#### AMC - Mt Salici Units (Numidian Flysch)

Monte Salici Flysh: Mainly composed of Oligo-Miocene-age (e.g. [Carbone et al., 2009](#); [Monaco, 2012](#)) alternating claystone, sandstone, and conglomerate. It is a monotonous alternation between dark claystone and quartz-bearing sandstone. The overall thickness of the units is 200 m (e.g. [Carbone et al., 2009](#); [Monaco, 2012](#)).

The unit at the outcrop is massive, with no visible bedding or laminations and minor fractures. The samples collected are mainly quartz-bearing sandstone, grain size varying from medium sand to very fine gravel at sight investigation, yellowish in colour (Figure 2.2 a and b).

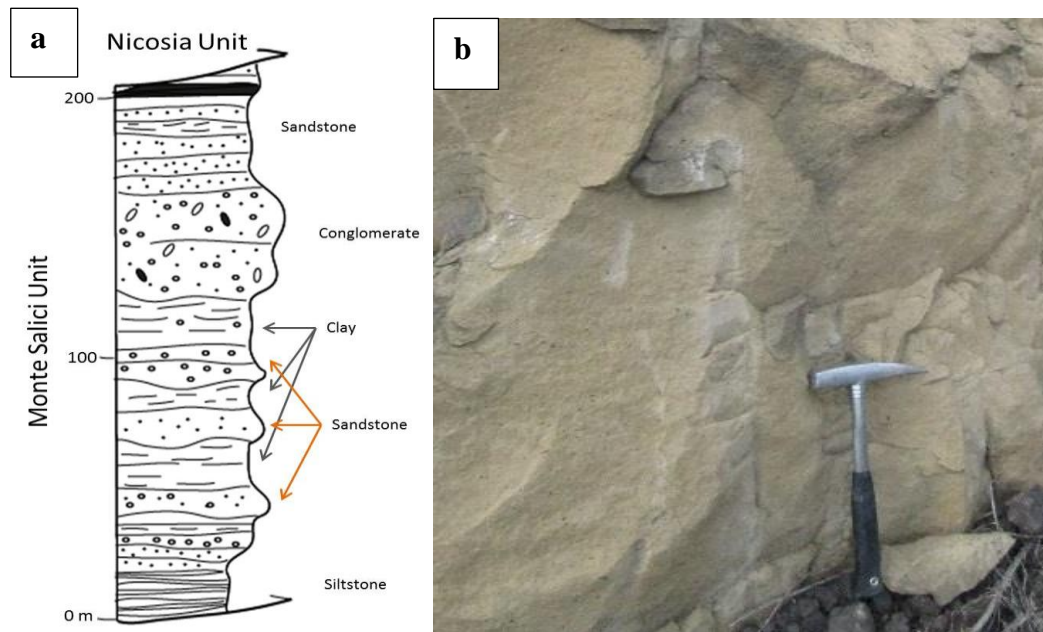


**Figure 2.2.** a) Schematic stratigraphic sequence from [Carbone et al., 2009](#); [Monaco, 2012](#), and b) the outcrop of Monte Salici Unit. Hammer (28 x 2.5 x 19 cm) used as scale.

HS= 24-24-25-25-27-27-28-29-30-32 Mean=27.1 Median= 27

UCS<sub>av</sub> = N/A

## AMC - Mt Soro Units

*Monte Soro Flysh*: primarily composed of a Cretaceous turbiditic sequence (e.g. [Carbone et al., 2009](#); [Monaco, 2012](#)), with calcareous claystone present at the top and the bottom of the sequence, separated by quartz-bearing sandstone. The basal sequence is composed of layered marly claystone that alternates with marly limestone. The median sequence is a turbiditic deposit of sandstone interlayered with clay that becomes a more massive sandstone upwards. The thickness of this unit is thought to be around 500-600 m (Figure 2.3 a and b) (e.g. [Carbone et al., 2009](#); [Monaco, 2012](#)).

At the outcrop, the quartz-bearing sandstone was well exposed and suitable to collection. Fractures filled of silt-bearing loose material separate layers of massive quartz-sandstone up to 15 cm height, as possible to see in Figure 2.3 b. The sandstone found in the outcrop should belong to the median sequence of the deposit, where the turbiditic sequence is becoming massive sandstone towards the end. At the outcrop, only a small part is visible, not suitable to detect any particular feature to describe this portion of the turbiditic sequence according the Bouma sequence characterization (e.g. [Shanmugam, 1997](#)).

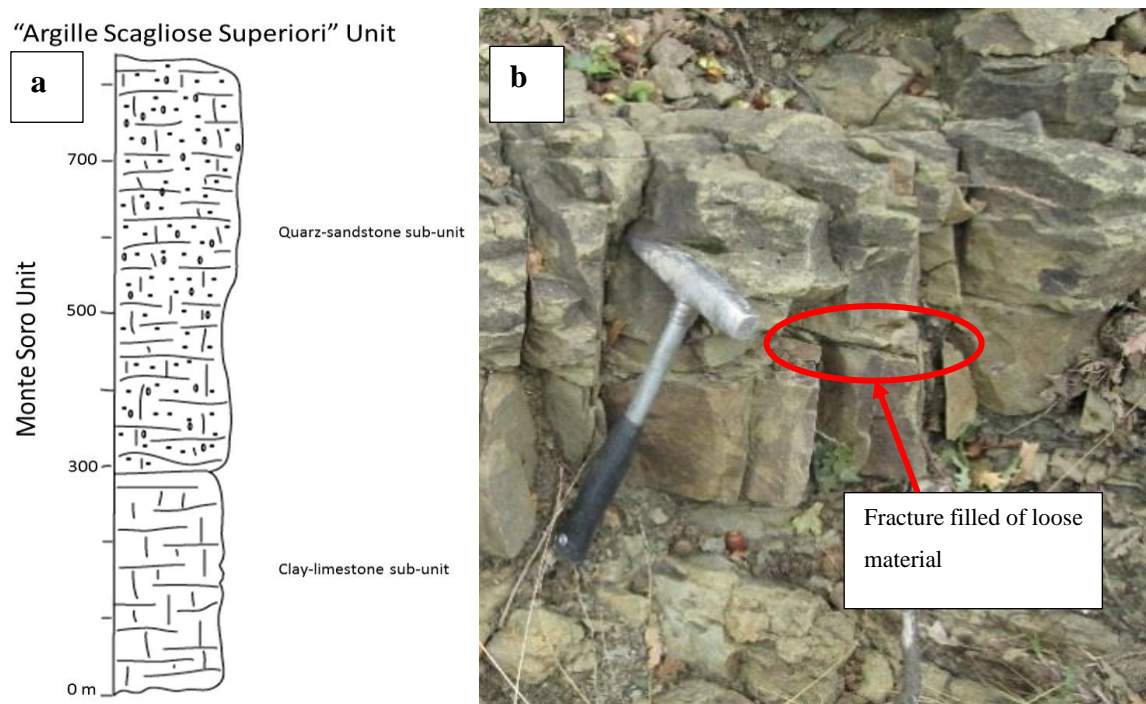


**Figure 2.3.** a) Schematic stratigraphic sequence from [Carbone et al., 2009](#); [Monaco, 2012](#) and b) the outcrop of Monte Soro Unit. Hammer used as scale. In red is highlighted the pervasive fractures filled in loose material.



HS= N/A

$UCS_{av} = 104.6 \text{ Mpa}$

### AMC - Nicosia Unit

Nicosia Flysch: The sequence is dated as upper Cretaceous-Eocene (e.g. [Carbone et al., 2009](#); [Monaco, 2012](#)), and divided in a basal part composed mainly by clay sequences (*Argille varicolori di Nicosia* = multicolour claystones) and a top part belonging to a turbiditic deposit. The sandstones are mainly quartz-bearing, becoming mica-bearing upwards. Towards the top there is a change to marly limestone. The sample collected is a quartz-bearing sandstone and shows coarse grain size (Figure 2.4 a and b) (e.g. [Carbone et al., 2009](#); [Monaco, 2012](#)).

At the outcrop, Nicosia Unit is a sandstone varying from fine ( $\sim 2 \text{ mm}$ ) to coarse ( $>5 \text{ mm}$ ) grain size, divided in visible layers. In the layers with coarse grain size it is possible to identify individual minerals (i.e. 2-4 mm), while in the layer composed by fine grain size there are clear laminations (Figure 2.4 b).

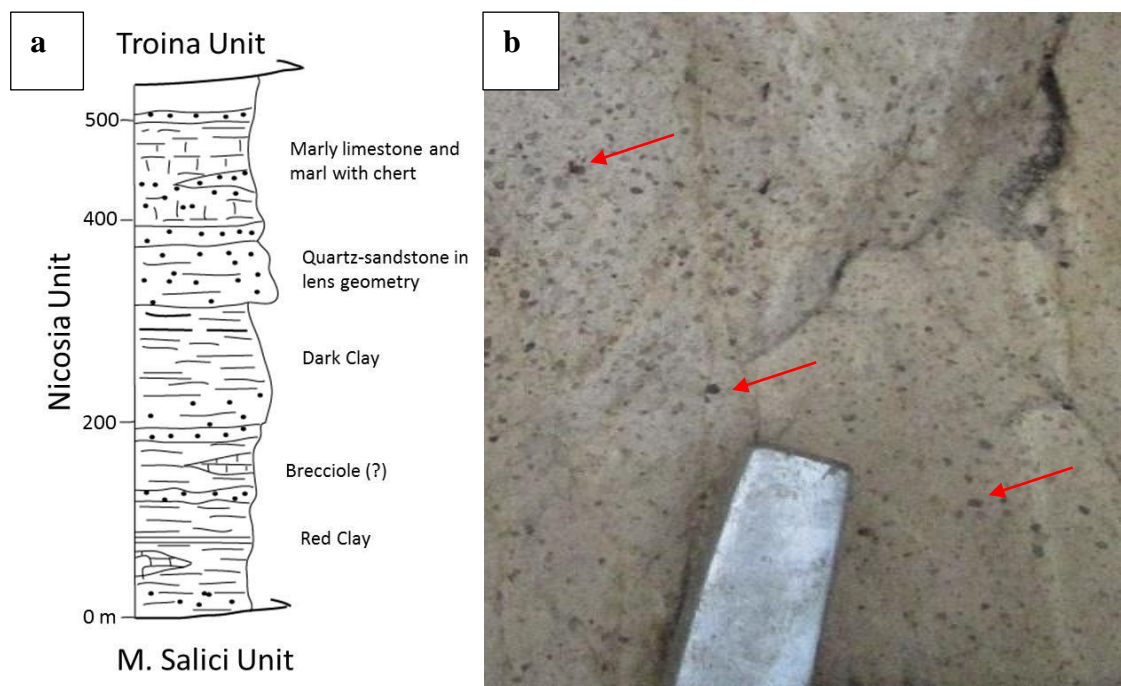


**Figure 2.4.** a) Schematic stratigraphic sequence from [Carbone et al., 2009](#); [Monaco, 2012](#) and b) the outcrop of Nicosia Unit. Coarse minerals are highlighted with red arrows. Hammer used as scale.

HS<sub>fine grain size</sub> = 19-22-24-25-26-27-28-29-30-31. Mean = 26.1 Median = 26.5

HS<sub>coarse grain size</sub> = 11-11-13-19-23-24-20-20-20-21. Mean = 18.2 Median = 23.5

UCS<sub>av</sub> = 17.49 MPa

### AMC - Troina Unit

Flysh Troina-Tusa: Composed by the Miocene age flyshoid units. They are grey marl interlayered with marly limestone in thick layers (Figure 2.5 a and b). (e.g. [Carbone et al., 2009](#); [Monaco, 2012](#)).

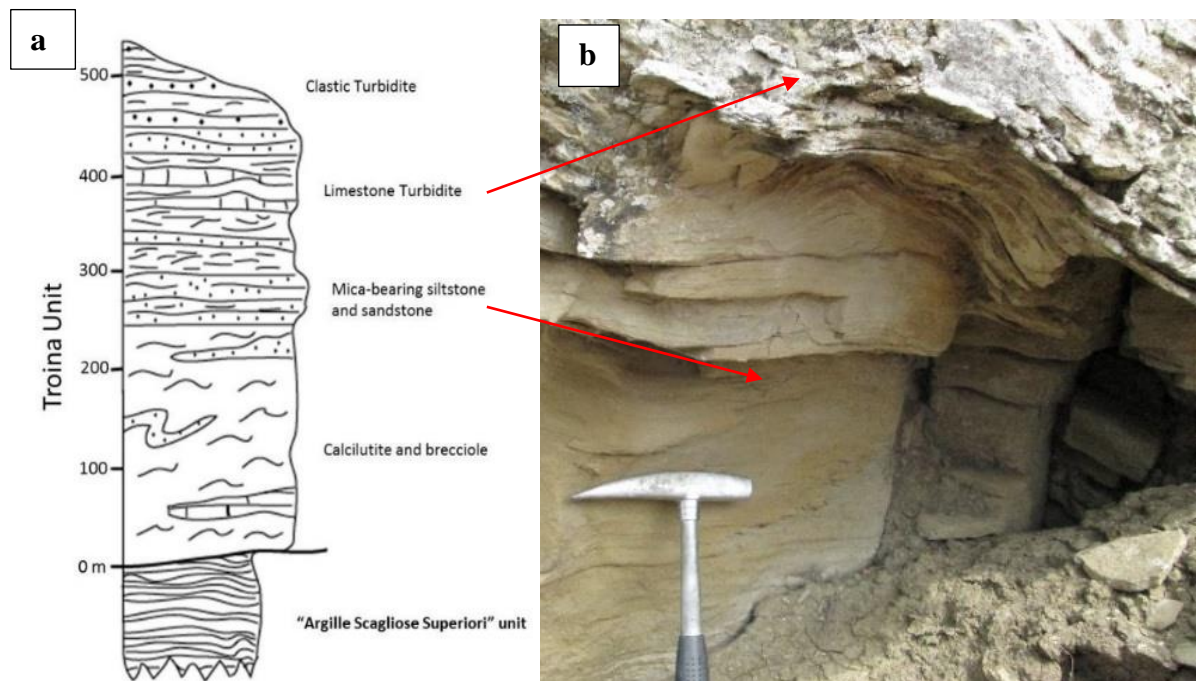


**Figure 2.5.** a) Schematic stratigraphic sequence from [Carbone et al., 2009](#); [Monaco, 2012](#) and b) particular of the outcrop of Troina Unit, with focus on the transition from laminated sandstones to the limestone turbidite, as highlighted with the arrows. Hammer for scale.

Troina Unit is a mica-bearing sandstone that is visibly laminated presenting at the top a clear transition to siltstone characterized by water transport structures. The samples collected are from the sandstones' layers, which are intensively fractured and with a strong presence of calcite veins. The sandstone is fine to coarse grain size (Figure 2.5 b).

HS = 9-9-9-14-19-20-22-27-28-36. Mean = 19.3 Median = 19.5

$$UCS_{av} = 87.066 \text{ MPa}$$

### Ionides Unit - Crisanti Fm

This unit comprises massive limestone beds, interbedded with clay-bearing strata. Limestone layers presents several fractures and degradation due to alteration, resulting fragile. The colour is reddish to greyish. Limestone beds present variable thickness from 3 to 20 cm (i.e. green arrow in fig. 2.6), while unconsolidated interlayers varies from 1 to 15 cm (i.e. red arrow in fig. 2.6). Along some fractures are present whitish halos probably due to fluid alteration (Figure 2.6).

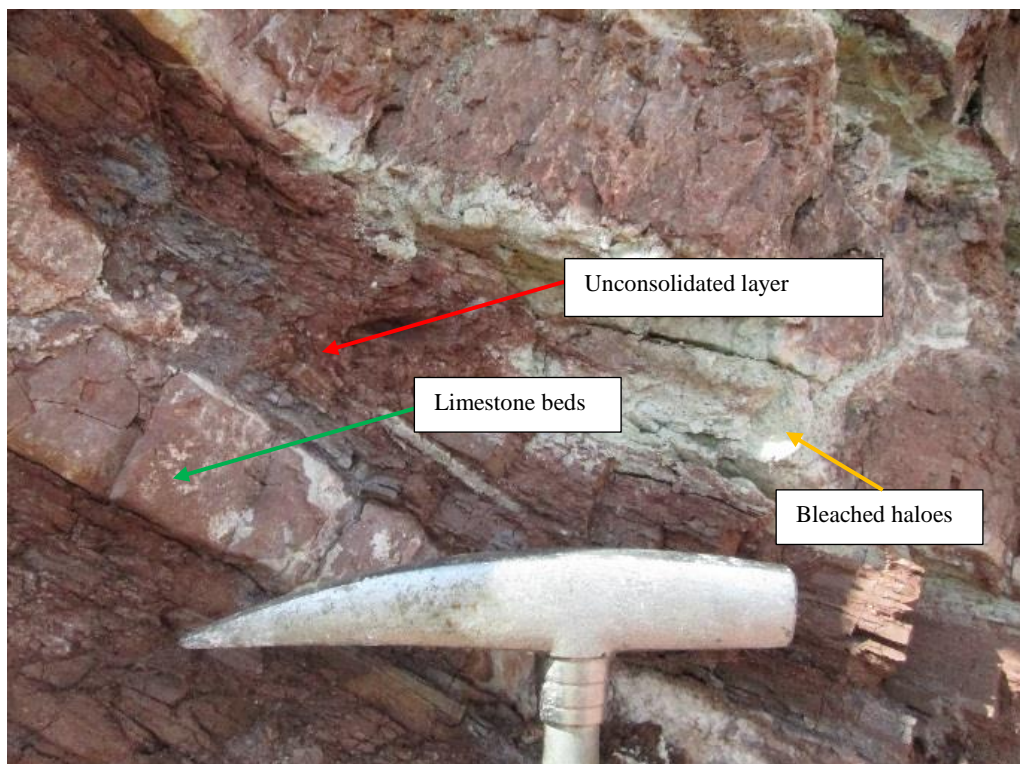


**Figure 2.6.** Formation at the outcrop. Highly fractured layers with variable thickness are highlighted with a green arrow, while the interlayers presenting mostly fine and unconsolidated material are highlighted with red arrow. Bleached haloes due to hydrothermal alteration are highlighted with the yellow arrow. Hammer for scale.

$$HS = 9-10-15-15-16-19-20-22-24-26. \text{ Mean} = 17.6 \text{ Median} = 17.5$$

$$UCS_{av} = 231 \text{ MPa}$$



### Ionides Unit - Scillato Fm

At the outcrop, this limestone shows fine grain size, whitish to yellowish in colour, with lenticular flints embedded. The outcrop is highly fractured, from closed fractures, to > 5 cm opening (Figure 2.7).



**Figure 2.7.** Scillato Formation is highly fractured, with fractures varying in aperture from few centimetres up to 15-20 cm. Not available scale for this picture.

HS = 20-21-23-25-33-33-34-36-38-40. Mean= 30 Median= 33

$UCS_{av} = 120.75 \text{ MPa}$

#### 2.3.2 Hyblean Plateau Foreland

##### Comiso Limestone (Ragusa Fm)

The Hyblean Plateau (HP) is mostly characterized by a thick Mesozoic-Tertiary carbonate sequence (e.g. [Carbone et al., 2009](#); [Monaco, 2012](#)). Comiso is a small village near Ragusa, where Comiso Limestone (Fig. 2.1, white star labelled as Comiso Limestone Quarry) belonging to the Ragusa Formation, is extracted and carved (Figure 2.8). The limestone presents a series of monotonic layers with thickness consistently in the range 50-

60 cm; interlayers of a fine grained material are observed also. The colour is whitish/yellowish. The overall bedding dip is  $335^{\circ}/16^{\circ}$ . A number of five blocks has been purchased at the quarry, as this limestone has been used in previous experiments (e.g. Bakker et al., 2015; Bakker et al., 2016; Barbera et al., 2014; Bakker et al., 2013) and therefore it is a good comparison for further mechanical tests. These carbonate samples are mainly composed of calcarenites (i.e. >50 % carbonate grains with a grain size ranging between 0.06 mm to 2 mm) and marls (i.e. carbonate-rich soft mudstone with grain size < 0.06 mm) of Lower Oligocene age (e.g. Lentini and Carbone, 2014). Carbonate rocks within the formation are generally either a combination of calcite (i.e.  $\text{CaCO}_3$ ) and dolomite (i.e.  $\text{CaMg}(\text{CO}_3)_2$ ), or occasionally a pure calcite. At the intralayer scale, the fabric is isotropic and CL is treated as an essentially homogeneous material.



**Figure 2.8.** The Comiso quarry. It is possible to note the sequence of monotonic layers of limestone dipping gently towards North.

HS = 11-14-18-21-22-22-22-22-22-23-23-23-25-25-28-28-28-30-31-32-33.

Mean= 23.95 Median= 23

$\text{UCS}_{\text{av}}$  (Priolo Fm – Hyblean Foreland) = 34.4 MPa

### 2.3.3 Gela-Catania Foredeep

#### Blue-grey quaternary clay (Misterbianco Quarry)

The foredeep basin started to form in the Miocene (e.g. [Carbone et al., 2009](#); [Monaco, 2012](#)). The sediment filling the basin show a regressive sequence of blue-grey clay, sand, and gravel. The blue-grey clays are concomitant to the submarine volcanic phases. Part of the foredeep is buried by the frontal part of the AMC, but deposition was still active during the compressive phases, so part of the sedimentary cover lies on the top of the AMC (yellow in Figure 1.2, Chapter 1; yellow in Fig. 2.1, this chapter) (e.g. [Carbone et al., 2009](#); [Monaco, 2012](#)).

To collect this lithology the best site is in the Misterbianco Quarry, where continuous excavations expose the fresh wall (Figure 2.9). At the time of the collection, the clays were dry due to prolonged hot weather (varying between 30°C and > 35°C in summer). The shallower layers of clay were dry and hard, hence unsuitable to be collected as cylinders for triaxial soil tests, which requires samples of nearly 10 cm of diameter and 20 cm length. However, an entire block of clay is collected to be used for triaxial experiments on powder.



**Figure 2.9.** *The wall of blue-grey clays in Misterbianco quarry. Depositional layers are very clear. It is possible to note as the colour turned into yellow from the usual blue-grey colour due to hot weather.*

### Blue-grey clay in Fiumefreddo

In the geological map (i.e. yellow star labelled Fiumefreddo Quaternary Clays in Figure 2.1, this chapter), a small outcrop of quaternary clay is found close to the village of Fiumefreddo, which is close to the Pernicana Fault System (PFS). Conglomerates and volcanics cover the quaternary clays in this portion, with variable depth ranging from -120 m to -9 m (e.g. [Groppelli and Tibaldi, 1999](#)). Close to the villages of Vena, Presa and Fiumefreddo, clays locally crop out (i.e. [Groppelli and Tibaldi, 1999](#)). Samples are collected to be analysed by XRPD and XRF and confirm that they are matching in composition the blue-grey clay of the Misterbianco quarry (additional information can be found in Appendix E). The presence of clay below the volcanic covers are particularly important in relationship with the behaviour of the sliding flank, as explained in Chapter 1.

#### 2.3.4 Volcano edifice

##### Etna Basalt Quarry

‘Etna Basalt’ is a specific basalt lava extracted from a quarry in Camporotondo Etneo (Catania) (Figure 2.10 a and b). This basalt is largely used as representative to characterize the mechanical properties of the units composing the edifice (e.g. [Vinciguerra et al., 2005](#), [Fazio et al., 2017](#), [Benson et al., 2010](#), [Benson et al., 2007](#), [Fortin et al., 2011](#), [Heap et al., 2009](#)), though it should be noted that the intact lava represents, probably, the strongest material forming the edifice. Unfortunately, we were not allowed to get closer to the quarry wall for safety reasons and take *in situ* measurements. The basalt looks massive, with low porosity as highlighted from permeability tests run by [Fortin et al., 2011](#). It can be interpreted as a middle section of a lava flow, exhibiting few vesicles, and a wide-spaced vertical (cooling) joint system.





**Figure 2.10.** a) and b) Panoramic view of the basalt quarry located in Camporotondo Etneo (Catania – Sicily).

### 2.3.5 The Pernicana Fault System and the NE-Rift overview

#### Piano Provenzana and Pineta di Linguaglossa

The Pernicana Fault System is playing a crucial role in the sliding movement of the flank, and for this reason, a visit was mandatory during the fieldwork. Accompanied by M. Neri from the INGV (Istituto Nazionale di Geofisica e Vulcanologia – Sezione Catania), the visit took us along the trace of the PFS. Near the summit of the volcano, the NE-Rift is visible in Piano Provenzana, where several paths allow hiking the various cinder cones and the recent lavas deposited during the 2002-2003 eruptions and after. Touristic facilities are spread in the area, such as ski lifts (in function during winter season), bars and info points. The 2002-2003 eruptions in concomitance of the developing of the NE-rift destroyed the facilities that have been subsequently re-built. From the NE-Rift starts the Pernicana Fault System (PFS): as explained during this overview, unfortunately the PFS doesn't present a clear and visible fault plane, but rather it is visible in few locations as volcanic material with some dislocation. For instance, in Pineta of Linguaglossa (in east direction respect the summit), it is possible to walk into woodland and observe a rare spot where the PFS is visible: a little hill of 4-5 m height is indicating the passage of the fault. Others indications of the fault movement, besides the GPS data, are given to the dislocation of street floor and small walls, as they cross the fault plane.

---

## Chapter 3 Methods: From the Fieldwork to the Laboratory

---

### 3.1 Introduction

The experiments presented in this thesis involved sample preparation and testing at different laboratories: the Rock Mechanics Laboratory (RML) at UCL, the Rock Mechanics Laboratory (RML) at Portsmouth University and the Rock Mechanics and Physics Laboratory (RMPL) at the British Geological Survey in Nottingham, plus a series of *in situ* measurements performed during the fieldwork. Due to the intrinsic nature of the rocks collected, experiments are carried out in two stages: an initial intact rock triaxial testing to define the influence of temperature and water conducted at the RML in Portsmouth, and a second stage to carry out triaxial frictional experiments to investigate the properties of simulated fault gouges conducted at the RMPL in Nottingham. This chapter summarizes the procedure followed from the fieldwork, to the selection of the relevant samples for the triaxial testing and the sample preparations itself. It gives technical specifications of the two triaxial apparatus used and particular focus in the development of the sliding holder tools, specifically designed and built to suit the triaxial machine at the BGS' RMPL laboratory. A detailed description of the calibration procedure to validate the new tool is presented, together with a discussion of the quality of this approach.

### 3.2 Fieldwork: samples collection and *in situ* measurement

At the outcrops, specimens were collected registering their spatial coordinates in case of visible layers, beddings, grain size variation and distribution, pores and fractures, because internal variabilities can influence the strength of the sample (e.g. [Roknuzzaman et al., 2017](#); [Bubeck et al., 2017](#)). After the collections, *in situ* measurements using a Schmidt hammer type L suitable for rock testing have been taken to gain a more complete overview of the *rock mass* mechanical properties. The Schmidt Hammer, or Rebound or Impact Hammer (HS hereafter) is a non-destructive technique developed to evaluate rock quality, obtained by reading the amount of rebound which is an index of surface hardness related to the uniaxial compressive strength of that rock mass (e.g. [Aydin and Basu, 2005](#)). Hardness is an indication of material behaviour rather than a fundamental material property, as it depends on the type of test employed to measure it (e.g. indentation, rebound or scratch tests).

Hardness here depends on the properties of the surface investigated, according to the definition that is the measure of the material resistance to surface deformations. In this case, the hammer is provided with an internal spring and a piston. When loaded perpendicularly against the surface, the spring is released and the piston hits the surface at a known energy. The amount of rebound gives a value of surface hardness (Fig. 3.1). As this technique provides only an index of hardness, it is usually accompanied by other tests to evaluate the compressive strength (e.g. [Roknuzzaman et al., 2017](#)).

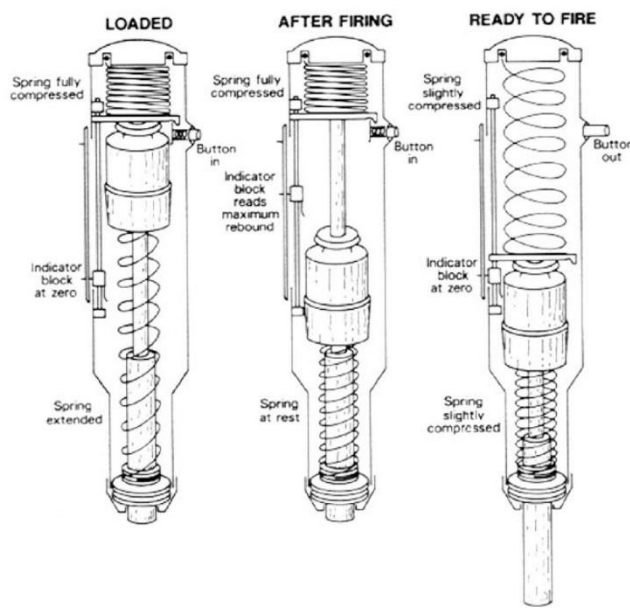


**Figure 3.1.** Illustration of how a Schmidt Hammer measures material elastic properties: the piston moves from ‘ready to fire’ to ‘loaded’. In this way the internal mass is pushed back in a loading position. When released, the loaded mass will hit the surface at a certain amount of energy, and the rebound, which depends on the hardness of the surface, is measured (‘after firing’ position) (From [McCarroll, 1994](#)).

The scale is between 10 and 100, where 10 identifies weak surfaces and 100 means strong and hard surfaces. Several factors influence the hardness, such as smoothness of the surface, age of the rock, superficial and internal moisture, particle size (e.g. [Roknuzzaman et al., 2017](#)). For these reasons, a series of tests performed onto samples presenting different orientations of layering or fractures (e.g. measurements taken perpendicular and parallel to the layering or bedding) allowed to get a first broad strength measurement, which is reported in Chapter 2, section 2.3 as average value for each lithology.

### 3.3 In the Laboratory: Samples Selection and Preparation

At the facility based at the BGS (Keyworth) is possible to prepare and core the samples. The minimum size required by the triaxial apparatus at the RMPL is a cylinder of 54 mm diameter per 120 mm length, for the triaxial machine at the RML in Portsmouth is

40 mm diameter and 100 mm length. Initial attempts to core samples highlighted that the presence of internal fractures, flaws, layers and beddings or other weaknesses in the rocks make the core process impossible to attain. Only the Comiso Limestone (CL) showed to be strong enough to be cored at the appropriate size and therefore it is selected for tests on intact rocks.

The other lithologies, being poorly consolidated sandstone, claystone, or a highly fractured quartz-arenite, failed during the initial coring process. Hence, they were manually or mechanically crushed and sieved to obtain powders to be analysed. Quantitative and qualitative chemical analyses are mandatory to obtain precise results on the mineralogical composition and results are presented here along with the main relevant results.

### 3.3.1 X-Ray Powder Diffraction

X-ray powder diffraction (XRPD) is an analytical technique used to identify the mineralogical composition of rocks (e.g. [Jenkins and Snyder, 1996](#)). By crushing the rocks into powder and by the use of X-Ray it is possible to evaluate which minerals are composing the whole sample. Minerals' lattice is a fingerprint, as the array of atoms and their distance is unique for each one. Powdered samples allow to have a random orientation of all the minerals' lattices, and therefore all possible diffraction directions of the lattices will be analysed (isotropic case) (e.g. [Jenkins and Snyder, 1996](#)). When investigated by X-Ray, the scattered patterns are collected by a detector and analysed, and according to their diffraction angle (given by the atom-atom distance) and intensity (all the peaks collected in a certain direction) is possible to recognize to which mineral they correspond, as peaks are unique for each mineral (e.g. [Jenkins and Snyder, 1996](#)). In this case, knowing the exact mineralogical composition of the rocks collected is fundamental, as mineralogical composition influences the mechanical properties. X-Ray powder diffraction is used to analyse all the samples collected and the results for each lithology is reported below.

#### Monte Salici Unit

XRPD for Mt. Salici Unit revealed that it is mainly composed of quartz, as highlighted by the red peaks, which are characteristic for quartz. Presence of calcite (blue peaks) is detected (Figure 3.2).



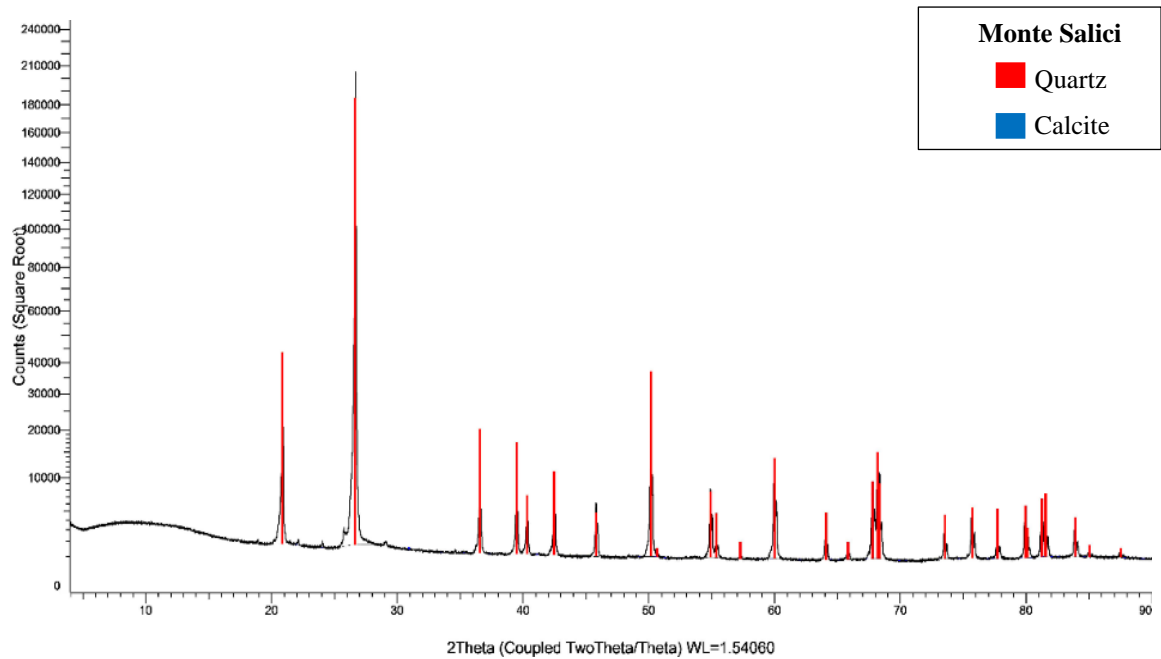


**Figure 3.2.** The XRPD analyses for Mt Salici Unit highlight the presence of mainly quartz (red peaks) and calcite (blue peaks).

### Monte Soro Unit

XRPD for Monte Soro Unit showed that this lithology is composed by quartz (red peaks), chlorite (green peaks), muscovite (pink peaks) and plagioclase phases (blue peaks). Plagioclase here is reported as phase and not as end terms Albite and Anorthite, being not relevant for the investigation (Figure 3.3).

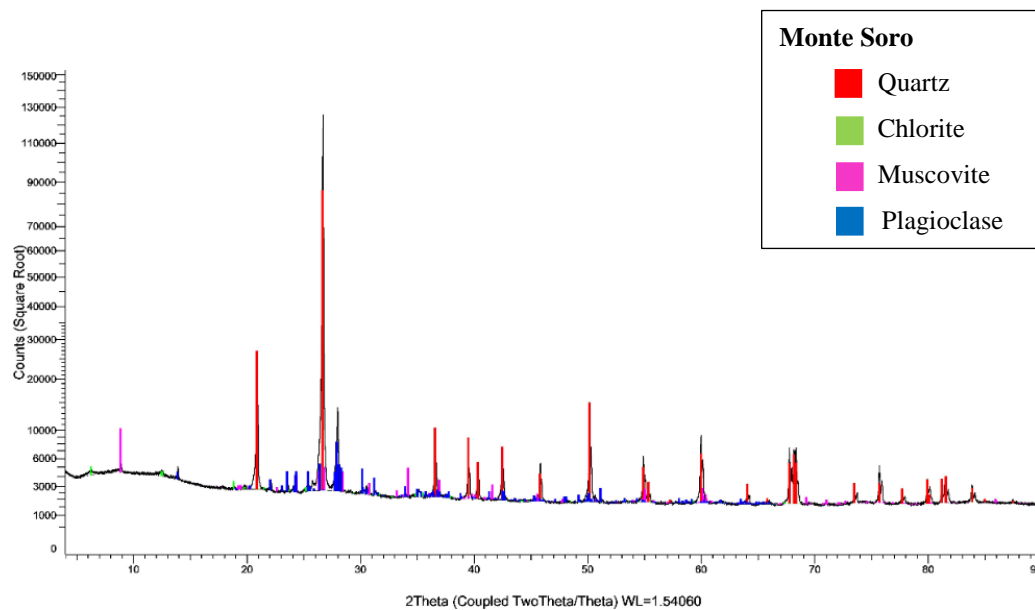


**Figure 3.3.** The XRPD analyses for Mt Soro Unit. Peaks positions highlight the presence of quartz (red), Chlorite (green), muscovite (pink), plagioclase phases (blue).

### Nicosia Unit

XRPD for Nicosia unit showed that this lithology is composed by quartz (red peaks), clays minerals such as kaolinite (blue peaks) and illite (pink peaks) and plagioclase phases (green peaks) (Figure 3.4).

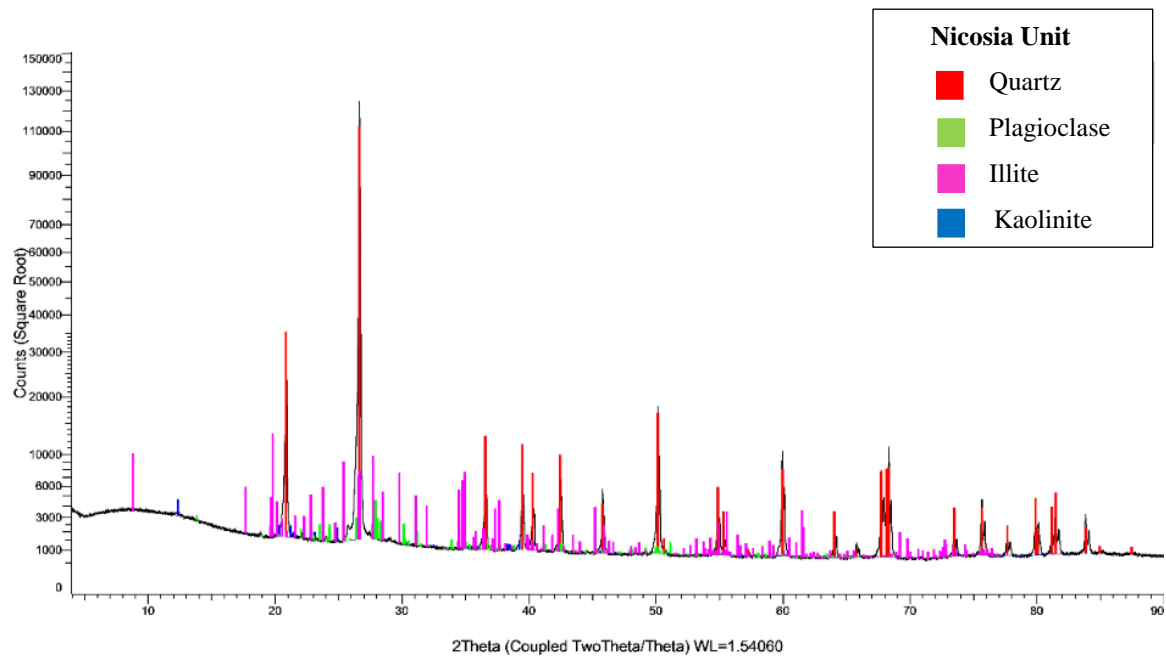


**Figure 3.4.** XRPD peaks for Mt Nicosia Unit shows presence of quartz (red), kaolinite (blue), plagioclase (green) and illite (pink).

## Troina Unit

Composition of Troina unit shows the presence of calcite (red peaks), quartz (blue peaks), chlorite (green peaks) and muscovite (pink peaks) minerals (Figure 3.5).

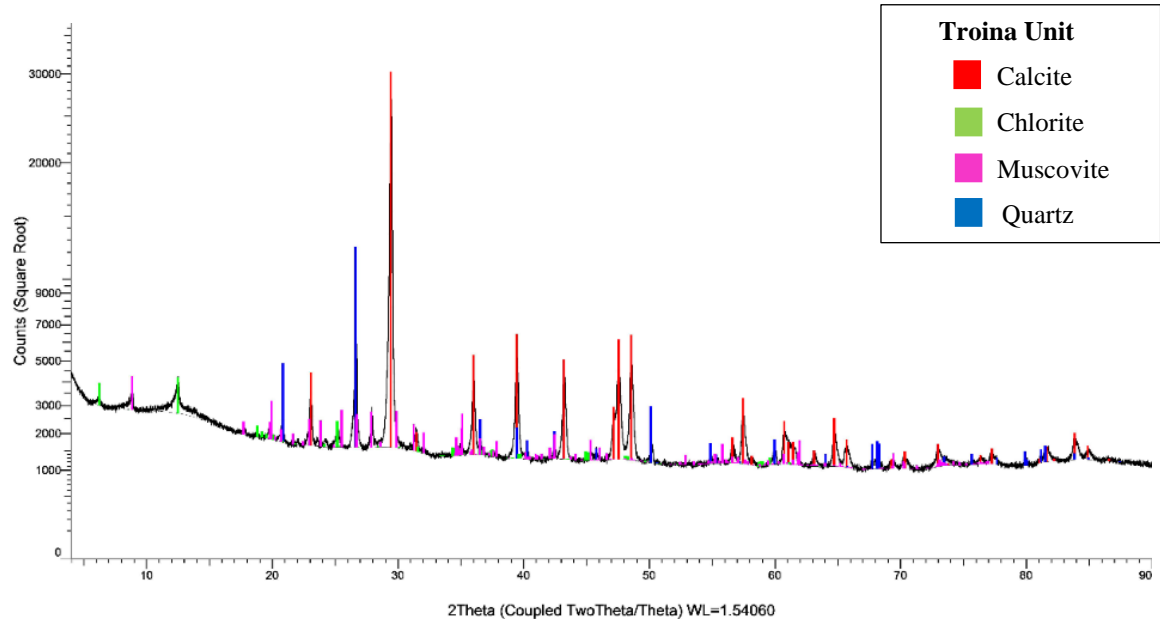


**Figure 3.5.** Analyses for Troina Unit highlight the presence of calcite (red), quartz (blue), chlorite (green) and muscovite (pink).

## Comiso Limestone

CL's XRPD analyses showed a composition of mainly calcite (red peaks) and quartz (blue peaks) (Figure 3.6).

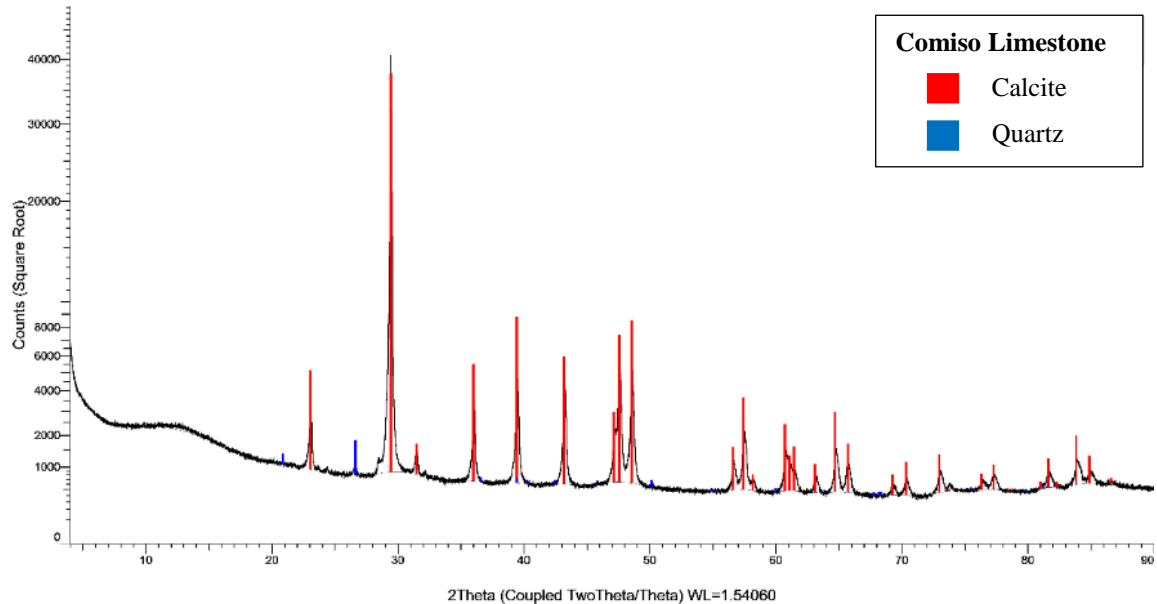


**Figure 3.6.** In Comiso Limestone are present only calcite (red) and quartz (blue).

## Blue-Grey Clay

The steps for analysing clays with XRPD technique are different from the previous samples. Clays need to be crushed and milled to separate them as much as possible from other mineral phases, but the procedure has to be done manually, to avoid the destruction of the clay mineral lattice. Therefore, the procedure is to crush the clay samples using a flying press and further diminishing their size by the use of a mortar and pestle. In terms of size, clays minerals fall between 0.001-0.004 mm, and it is therefore important to select only the right fraction for the analyses. Hence, when the samples is properly disaggregated, it needs to be added to a certain quantity of distilled water along with a deflocculant (i.e. dispersant - to avoid particle re-aggregation) and left to settle for 16 hours (i.e. decantation). According to the Stokes' law, heavy particles will precipitate, while clays will remain in suspension. After initial separation, smaller containers are filled with water containing clay in suspension without disturbing the sediment at the bottom. After being centrifuged, the clays contained in the water are deposited at the bottom of each container and they are ready to be collected, dried and tested for the first 'whole rock' X-Ray investigation. One of the major feature to

be detected within clays is the presence of swelling clays, such as smectite or illite minerals. The first step is glycollation, using the Ethylene Glycol Solvation procedure, in which clays are saturated with ethylene glycol (i.e.  $C_2H_6O_2$ ) to make them swell. After an overnight exposure in the glycollator at  $60^\circ C$ , the samples are ready for the X-ray investigation, and if swelling clays are present, they will be detected at this stage. The subsequent steps are to expose the samples both at low temperature (i.e.  $330^\circ C$ ) and high temperature (i.e.  $550^\circ C$ ), as some clays group are sensitive to temperature changes and it is easier to detect them. The treatment is set at constant heating and cooling rate, with a dwelling time of 1 hr to allow the sample to equilibrate at the target temperature. When cooled, the samples are ready for the X-ray investigation.

Whole rock (AD): Air-Dried analyses for these samples showed the presence of quartz, calcite, k-feldspar and muscovite and amongst the clay minerals the presence of chlorite, and kaolinite (Figure 3.7).

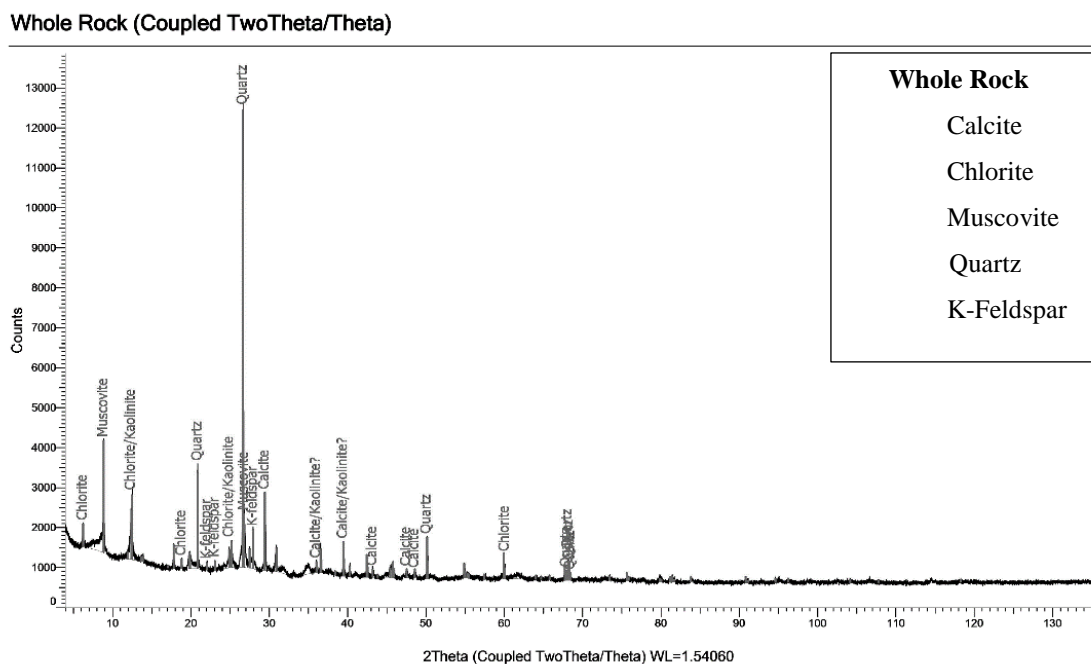


**Figure 3.7.** Results for the XRPD analyses on bulk rock.

Glycollation (GY): after the treatment with the glycollator, it is possible to reveal the presence of swelling clays, otherwise not visible. Figure 3.8 shows the results up to  $30^\circ$  of 2-theta, as this is the portion where most of the peaks for clay minerals are detected. As it is possible to note, from the AD analyses in green to the GY analyses in pink, there is a shift

in the peak from 7 to 5 along the 2 Theta axis confirming the presence of smectite (e.g. Tomás et al., 2016). One of the most common mineral inside the smectite family is montmorillonite, a swelling clay.

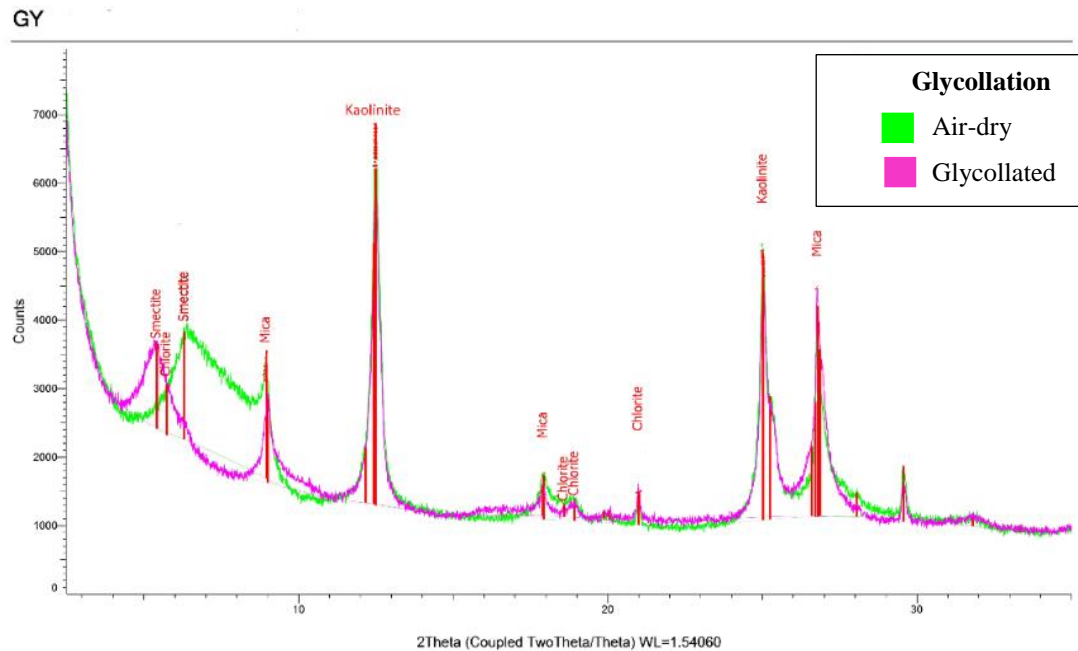


**Figure 3.8.** Results for the XRPD analyses on the sample after the glycollation procedure. It is possible to note the swift in the peaks from AD (green) to GY (pink) at 6 degrees 2 theta, highlighting the presence of smectite.

Low Temperature (i.e. LT - 350° C) and High Temperature (HT - 550° C) treatments are reported together to highlight changes for minerals sensitive to temperature. Peaks for smectite compared with GY are not present already at LT treatment, as very sensitive to temperature. Kaolinite is destroyed with HT as demonstrated by the absence of the 2 distinctive peaks (blue line) compared to the LT treatment (red line). Mica and Chlorite minerals are insensitive to temperature and their peaks remain present (Figure 3.9).

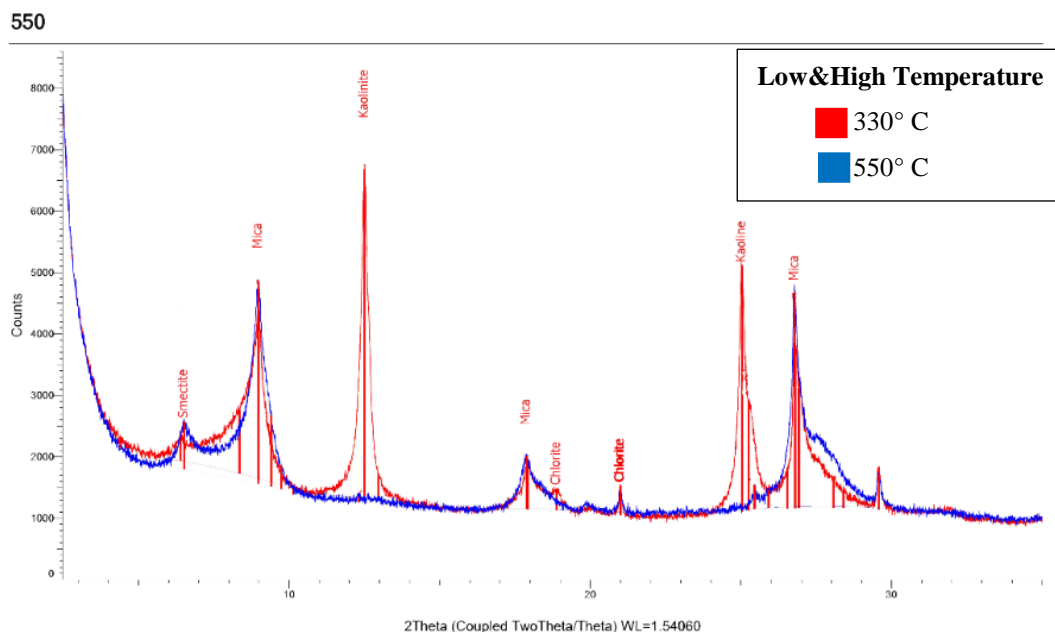


**Figure 3.9.** Results for the XRPD analyses on the sample after the LT and HT treatment. It is possible to note that the peaks highlighting the presence of kaolinite (red) are absent after the HT treatment (blue), as kaolinite is sensitive to high temperature.

### 3.3.2 X-Ray Fluorescence

Combination of XRPD results with X-Ray Fluorescence results gives the possibility to obtain the mineralogical phases present in the rocks along with the abundance of their chemical compounds reported in weight percentage (i.e. wt %). The table below reports the results of the X-Ray Fluorescence (XRF). XRF is another useful analytic technique to obtain, in this case, quantitative data of the bulk composition of the samples (e.g. [Beckhoff et al., 2007](#)). This technique takes in consideration the amount and the wavelengths of x-ray released by the components of a crystal when invested by an external source of x-rays. The sample is prepared by crushing the rock into powder and then fused and cooled into chips. This allows to have a complete selection of the major and minor elements composing the rock, the total counting also those elements that cannot survive the heating (i.e. LOI=Loss of Ignition). When the chips is analysed, the x-ray beam excites the electrons positioned into the inner orbitals removing them, and electrons coming from the outer orbitals fill the vacancies. This ‘jump’ to an inner position is happening through the release of energy in form of x-rays with a characteristic wavelength unique for each element, (qualitative analyses). A counter collects the diffracted x-ray and their final intensities give a quantitative

amount of each element. Combined with the LOI, it is possible to obtain the bulk composition of the rock. Regarding carbonates,  $\text{CaCO}_3$  is not surviving the ignition, then the total count is obtained from the LOI. In Table 3.1, the XRF results for the Etnean samples are reported.

**Table 3.1.** X-Ray Fluorescence results for the selected lithologies.

Name	Bead	SiO <sub>2</sub>	TiO <sub>2</sub>	Al <sub>2</sub> O <sub>3</sub>	Fe <sub>2</sub> O <sub>3</sub>	MnO	MgO	CaO	Na <sub>2</sub> O	K <sub>2</sub> O	P <sub>2</sub> O <sub>5</sub>	SO <sub>3</sub>	LOI	Total
<b>Mt. Salici</b>	LF41513	99.50	0.06	0.41	0.51	0.005	0.08	0.06	0.06	0.032	0.016	<0.002	0.44	101.18
<b>Mt. Soro</b>	LF41510	89.49	0.31	4.93	2.70	0.066	0.48	0.13	1.04	0.449	0.038	<0.002	1.47	101.12
<b>Nicosia</b>	LF41506	99.11	0.23	0.86	0.08	0.000	0.01	0.01	0.08	0.194	0.023	<0.002	0.37	100.97
<b>Troina</b>	LF41509	19.95	0.30	5.39	3.78	0.147	1.19	35.38	0.38	0.913	0.076	<0.002	31.59	99.09
<b>Comiso</b>	LF41516	2.29	0.04	0.22	0.13	0.007	0.91	53.30	0.02	0.047	0.051	0.040	42.57	99.63
<b>Grey-Blue Clay</b>	LF40341	52.70	0.80	15.15	6.06	0.09	2.84	6.80	1.12	2.26	0.15	0.49	11.42	99.88

Notable is the high percentage of SiO<sub>2</sub> in Mt. Salici and Nicosia Units, matching the XRPD and indicating the presence of almost only quartz in both of the samples. Another relevant result belongs to Comiso Unit, showing the 53% of CaO that combined with the 42.57% in LOI (Loss Of Ignition), reveals that Comiso Unit is almost a pure carbonate, with a minimum amount of quartz. Mt Soro presents a high quantity of quartz, a relevant percentage of aluminium and iron, and a minimum amount of sodium that combined with XRPD confirm the presence of Plagioclase, Chlorite and Muscovite. Troina unit sample results high in calcite, with a good amount of quartz and minor amounts of aluminium, iron and magnesium. The Quaternary clays show significant amounts of silica, aluminium, iron, magnesium, sodium, potassium, and LOI; according to the minerals indicated in XRPD, this corresponds to the presence of quartz, calcite, k-feldspar, muscovite, chlorite, kaolinite and smectite.

### 3.3.3 Synthetic Gouges Selection

After the detailed results obtained from XRPD and XRF presented before, it is evident that the mineralogical composition showed important variations in the selected lithologies. From the lithological point of view, four intercalated materials are mainly composing the basement: sandstone, claystone, carbonates, and clays. The purest units are the Comiso Limestone (98% calcite) and the Mt. Salici sandstone (99% quartz) (see Table 3.1).



For the triaxial friction tests, these two lithologies were selected as representative, mainly to avoid the occurrence of mechanical phenomena due to the presence of different minerals. This choice was important also for the calibration of the new piece of equipment, as mineralogical variations can induce mechanisms that were difficult to detect during the tests, and finally the choice of pure gouges found good comparisons in literature. To represent the presence of a significant clay-dominated formation within the basement, the blue-grey quaternary clay were employed to construct binary mixtures of clay-quartz and clay-limestone.

### 3.3.3.1 Specific gravity – Density bottle method (BS 1377:1975)

This method provides an accurate measurement of specific gravity of particles heavier than distilled water. The particles need to be quartered and riffled in three equal parts (i.e. 30 g each) to ensure a homogeneous distribution of the grains. The weight of the bottles together with the dry powders is taken. Then, de-aired and distilled water is added into the bottle until the specimen is covered (half bottle) paying attention to not add air or disturb the specimen itself, and the bottles are placed in a vacuum chamber until all the trapped air is removed. The powders are then stirred with a spatula and the entire procedure is repeated. When soil is no more releasing air, the bottles are removed from the chamber, filled up with de-aired water, put in a constant-temperature bath (i.e. 28°C) and left for at least 1 hour. When the bottles have reached the water temperature they are weighed again (bottle+soil+liquid). To calculate the specific gravity  $G = G_L (m_2 - m_1)/(m_4 - m_1) - (m_3 - m_2)$ , where  $G_L$  is the specific gravity of the water at constant temperature (i.e. assumed to be equal to 1000 in the case of distilled water);  $m_1$  is the mass of the bottles;  $m_2$  is the mass of the bottle+dry soil;  $m_3$  mass of bottle+soil+liquid;  $m_4$  is mass of bottle+liquid. Tables 3.2 below shows the specific gravity of the selected gouges used for the tests.

**Table 3.2.** *Results of the density particle method for the selected lithologies.*

Method	Specimen Reference	Particle Density Average (g/m <sup>3</sup> )
Pycnometer	Mt Salici	2.5
	Blue-grey quaternary clay	2.73
	Comiso Limestone	2.73

### 3.3.3.2 Grain size distribution of the Blue-Grey Quaternary clay

Determination of grain size distribution of blue-grey quaternary clays allowed understanding of the quantity of clay and silt in the sample. Initial sieving allowed separating the coarse fraction, while X-Ray sedigraph was used to investigate the fine fraction (Fig. 3.10).

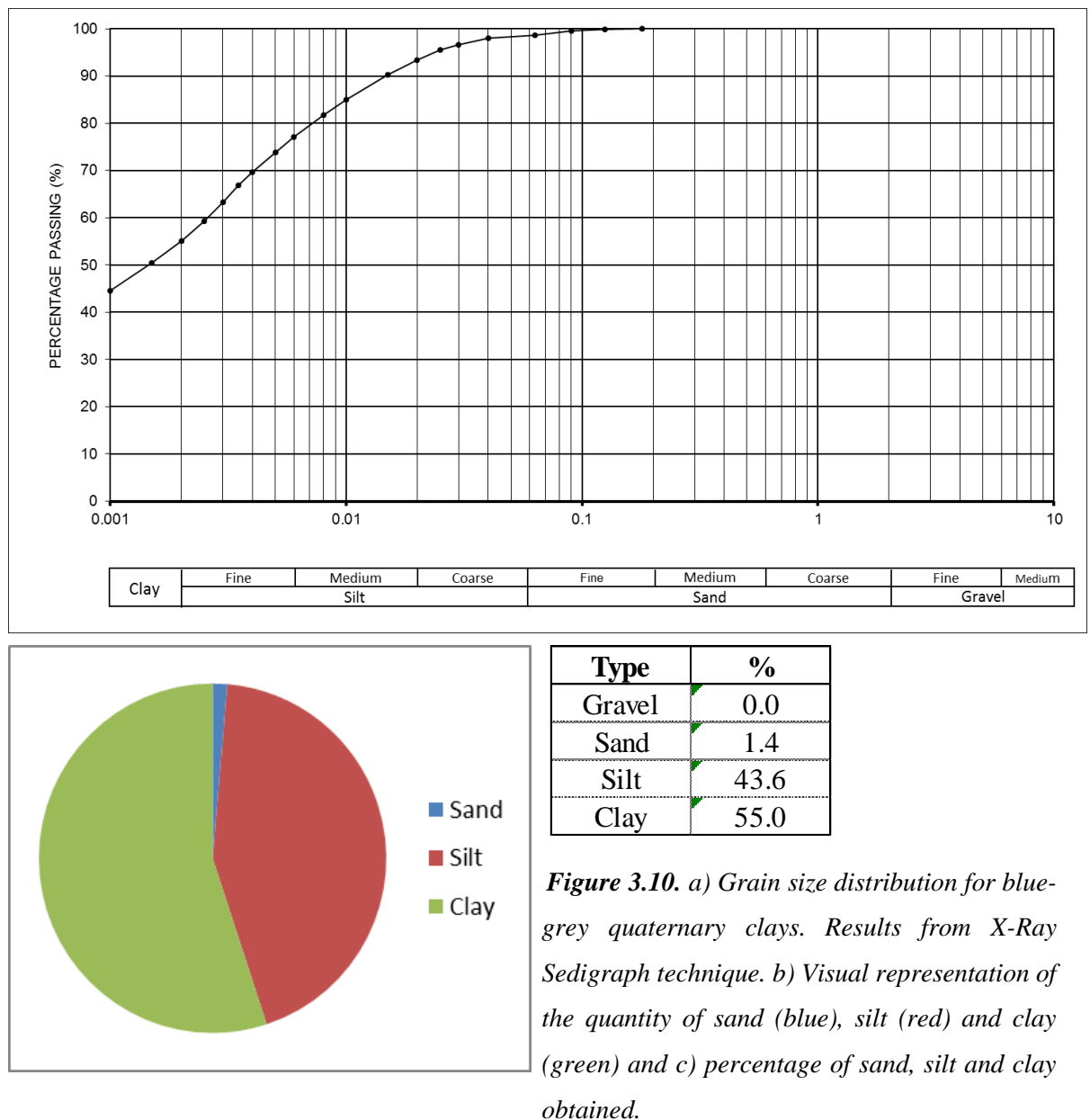


**Figure 3.10.** a) Grain size distribution for blue-grey quaternary clays. Results from X-Ray Sedigraph technique. b) Visual representation of the quantity of sand (blue), silt (red) and clay (green) and c) percentage of sand, silt and clay obtained.

### 3.3.4 Synthetic Gouge Preparation

The limestone and quartz-sandstone were crushed using a flying press and milled with a Retsch PM400 planetary mill. Because these procedures can cause destruction of clay minerals, they were manually crushed. Then, to represent the natural variability of fault gouges, the first two were mechanically sieved to reach a grain size between  $<180\text{ }\mu\text{m}$  and  $>63\text{ }\mu\text{m}$  (e.g. [Engelder, 1974](#)). For clays, the smallest diameter allowed was  $<40\text{ }\mu\text{m}$ , manually obtained. A possible procedure to separate the fine silt fraction from the clay was to immerse the sample in water. Allowing enough time (i.e. 24 hrs), silt will deposit at the bottom of the container while the clay fraction will remain in suspension. From the water containing the clay, it was possible to separate clay fraction using a centrifuge. Once the clays were collected, they need a certain time (i.e. depending on type of clay minerals present) to completely dry at room temperature. However, the total time to obtain a quantity of few grams was at least one week and unfortunately, because of the large amount of powder necessary in the new experimental set-up, this procedure was not considered as valuable.

### 3.4 High Temperature Thermal Apparatus for Thermal Cracking on Intact Rocks

Thermal treatment was applied on samples of CL to investigate the effects of thermal stressing, using a high temperature Carbolite CTF12/75/700 tube furnace (Figure 3.11) (i.e. [Browning et al., 2016](#)). Temperature range was between  $150\text{ }^{\circ}\text{C}$  and  $600\text{ }^{\circ}\text{C}$  to induce varying amounts of micro-fracture damage and allowed to cool prior to triaxial deformation tests. The specimens were held within a  $\sim 1\text{ m}$  length purpose-built steel jig comprised of rods and springs providing the specimen with a constant end load within the central section of the tube furnace. A series of thermocouples mounted immediately adjacent to the specimen surface controlled and monitored the temperature. In all tests, a controlled heating rate of  $1^{\circ}\text{C}/\text{minute}$  was applied, keeping the specimen at the desired maximum temperature for 30 minutes to allow complete temperature equilibration followed by natural cooling (i.e. generally less than  $<1^{\circ}\text{C}/\text{minute}$ ).

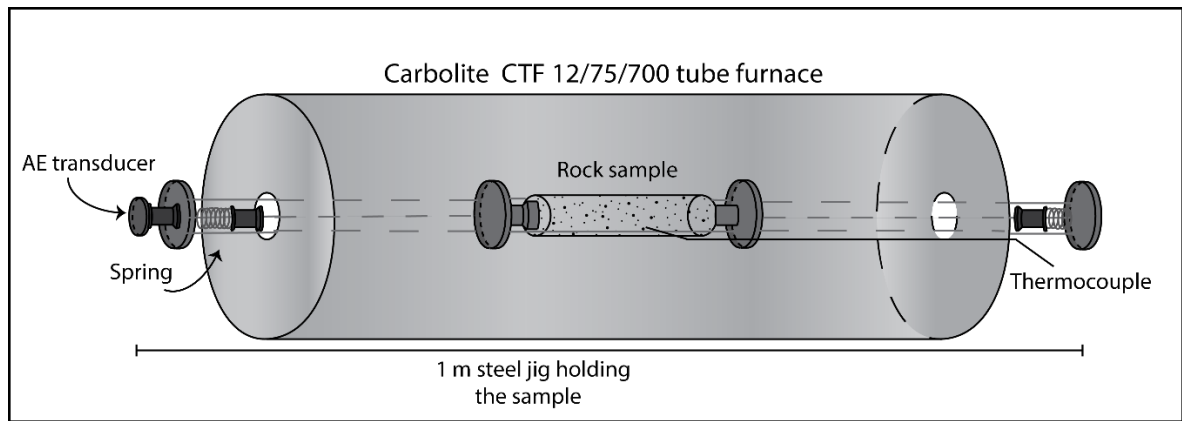


**Figure 3.11.** Schematic view of the Carbolite furnace used for thermal treatment, in use at the Rock Mechanics Laboratory at UCL: the specimens is held within the centre of the tube, where the temperature remains constant. The two springs at the end of the jig allow contraction and expansion, registered by a transducer for AE record.

AE output was recorded contemporaneously during each test on heating to, and cooling from 150 °C, 300 °C, 450 °C, and 600 °C. AEs were recorded by using the central rods to act as acoustic waveguides with one Panametrics V103 piezoelectric P-wave transducer located at the end of the waveguide. The AEs hits were used as a proxy for the rate and relative amounts of induced crack damage which included indistinctively nucleation, coalescence and propagation of newly-formed micro-cracks (i.e. assumed to be the most likely source here) as well as other microstructural processes susceptible to produce AE (e.g. friction between pre-existing micro-crack's surfaces; Griffiths et al., 2018). A threshold of 35 dB was imposed on the recorded AE amplitude to avoid background noise (i.e. Browning et al., 2016). All tests were conducted at ambient pressure (1 atm). Complementary ultrasonic P-wave and S-wave velocity measurements were recorded on the starting material prior to heating and on the cooled material following each thermal stressing test.

### 3.5 Deformation experiments on intact rocks: Sanchez Triaxial Apparatus

The Sanchez Triaxial Apparatus installed at the RML in Portsmouth is a conventional, servo-controlled triaxial apparatus capable to host specimens of 100 mm length and 40 mm diameter (e.g. Fazio et al., 2017). The machine presents an external furnace capable of heating up to 200°C. The confining medium is a high-flash point oil (i.e. 270°C) driven via direct pumps, capable to reach a confining pressure (i.e.  $P_c = \sigma_2 = \sigma_3$ ) of up to 100 MPa.

The axial piston is providing an axial stress up to 100 MPa via a precision piston of 70 mm diameter fitted on top of a hydraulic booster (Figure 3.12). The axial load is transferred to a smaller piston of 40 mm diameter fitted below the hydraulic booster and in contact with the sample. The transition from the top bigger piston to the smaller piston amplifies the axial stress of a factor x6, reaching a maximum capacity of axial stress of 680 MPa across a 40 mm diameter cylindrical specimen (Figure 3.12).

An independent pore fluid system allows injections of various pore fluids, but for the purposes of this study, distilled water is used. The pore fluid system is connected to the cell via precision piston pumps and it is capable of pressures up to 100 MPa (e.g. [Fazio et al., 2017](#)).

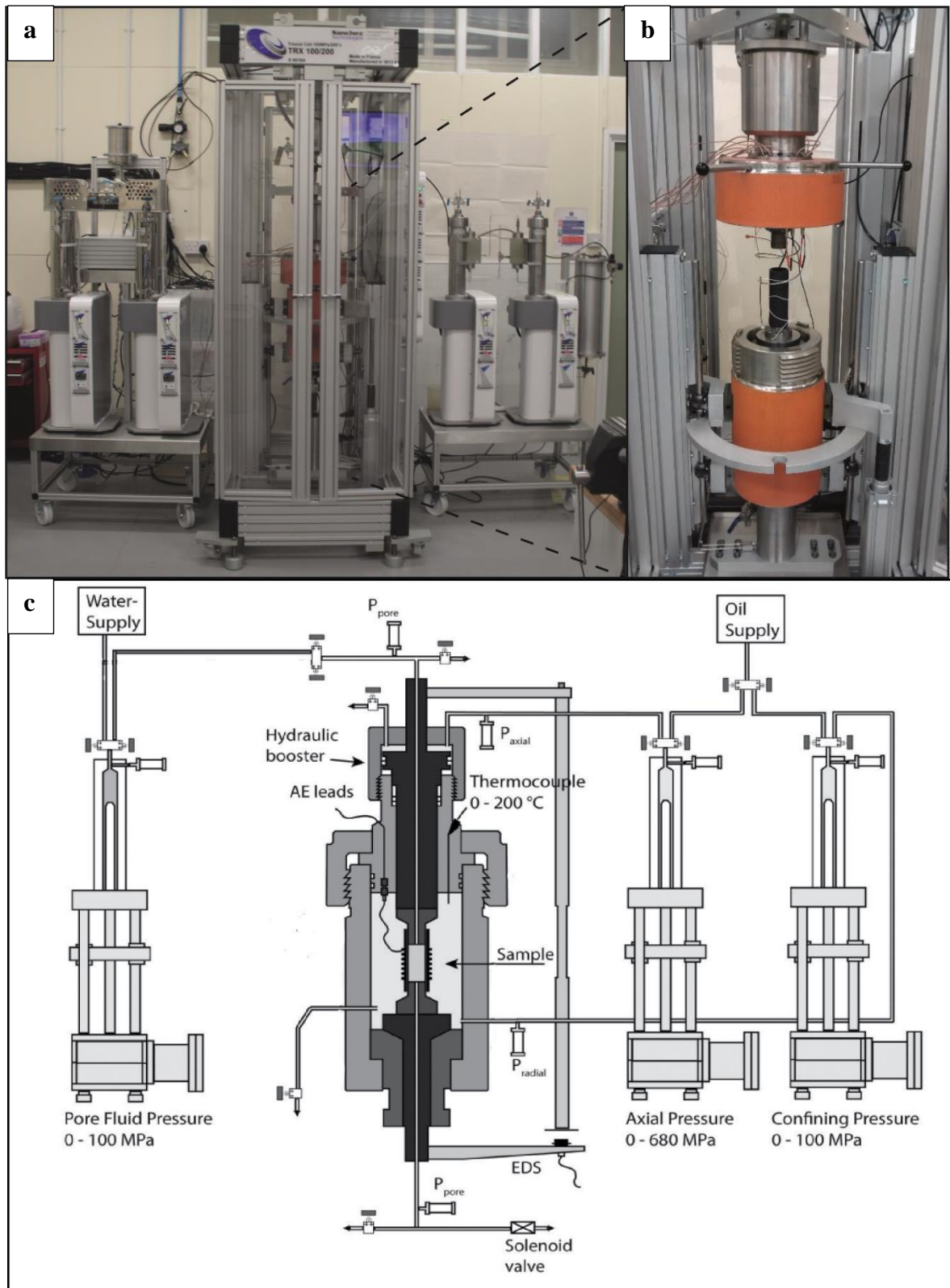


**Figure 3.12.** From *M. Fazio, PhD thesis*. a) The Sanchez triaxial machine installed at the RML in Portsmouth and b) the pressure vessel hosting the sample. c) Schematic view of the apparatus, with reported the pore fluid system and the two different precision pumps providing axial and confining

pressures. The hydraulic booster placed along with the thermocouples providing external heating to the vessel through pads. AEs cables are fitted to provide precision measurements during tests.

The machine measures the axial displacement and strain via an Eddy Displacement System (EDS) consisting of three transducers fixed to the vessel, measuring the change in distance between them and a steel target connected to the top piston. The transducers are creating an electric field and they are using the magnetic fields changes as measures of the axial displacement: measures are averaged and logged by a control computer at 1 Hz with a sub-micron precision, giving the measure of strain corrected for the length of the sample. The final data of axial strain are corrected for the stiffness of the apparatus to give a correct strain value. All the data recorded by the machine during the test (i.e. stress, strain, pore pressure and confining pressure) are transmitted to a PC provided with the proprietary control software ‘Falcon’, recording mechanical data at a rate of 1 sample/second. Separate units allow recording passive and active AEs.

### 3.5.1 Acoustic Emission (AEs) and Ultrasonic Surveys

An array of 12 piezoelectric lead zirconate titanate (PZTs) sensors embedded in an engineered nitrile jacket (i.e. [Sammonds, 1999](#)) record the emission of AEs during deformation, both passive (AEs) and active triggered ultrasonic surveys (Figure 3.13).

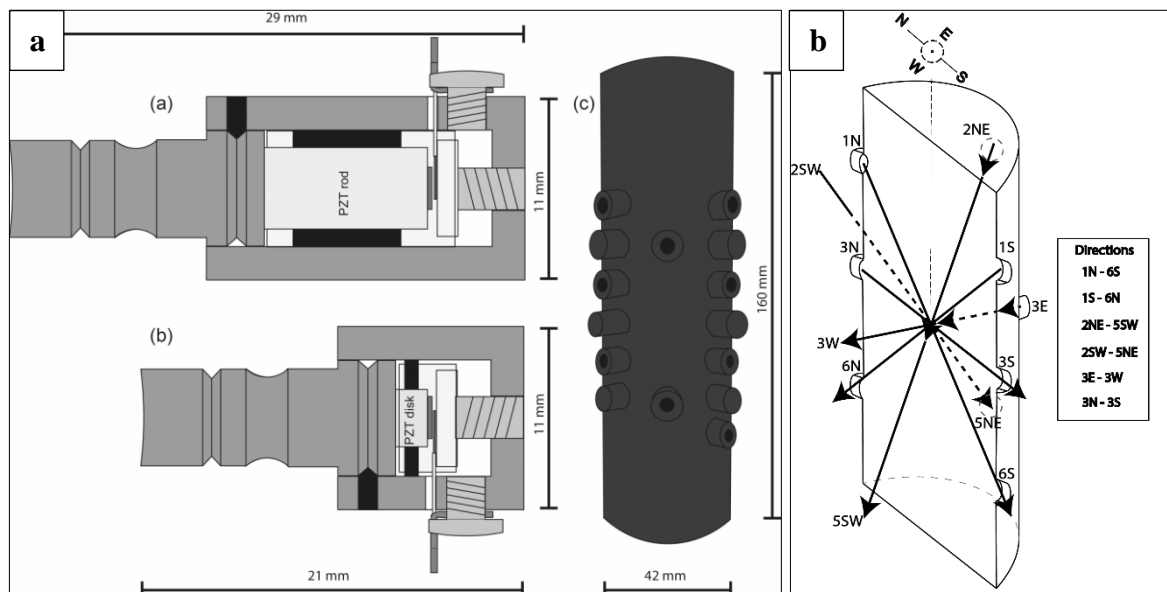




**Figure 3.13.** a) and b) show the PZT sensors at 200 kHz and 600 kHz and c) shows the rubber jacket designed to hold the 12 PZT and the sample (from [M. Fazio PhD Thesis](#)). c) the travel directions of the ultrasonic surveys according to the PZT array.

These sensors are sensitive to transient fracture events (i.e. micro seismicity) across a frequency range of approximately 80 kHz to 800 kHz. The sensors connect to the recording system through 12 Pulser Amplifier Desktop (PADs) units, which work to amplify the signal by 60 dB before being split between two different recording systems: the ‘triggered’ data and the ‘continuous’ data stream. The ‘triggered’ data, are collected in the Milne unit, and they are activated when a series of parameters are satisfied, (e.g. sensors output, threshold amplitude, number of channel). In positive case, the full waveform travelling through the sample is recorded by the 12 sensors and stored as a single event in a BSF file (a proprietary format, Binary Storage File). During an experiment, thousands of events are triggered and potentially recorded. However, interferences or not-satisfied parameters are downing the number of events of 50%. Further, the Milne unit is able to capture a certain number of events, and beyond that threshold, the recording stops. This could be an issue especially during pre- and brittle failure, when the number of AEs is usually high. For this reason, to avoid lack of data, also a ‘continuous’ data stream. In addition, each PAD sensor can be excited in sequence with a 200 V pulse, recording the travelling signal on the remaining 11 sensors to deduce the elastic P-wave velocity structure (i.e. seismic anisotropy) of the specimen during deformation, namely a *velocity survey*. Active P-wave velocity surveys are processed using the known location of each sensor (i.e. 3 sensors along a selected north direction, 3 sensors along south, 2 at north-west and 2 at south-west, for a total of 12; Fig. 3.13 b), and the signal travel time from the source to each receiver (e.g. [Benson et al., 2007](#), [Fazio et al., 2017](#)).

#### 3.5.1.1 AEs and Ultrasonic Surveys Data Elaboration

All ultrasonic data (i.e. passive AEs events and active velocity survey) were processed using the proprietary InSite-Lab<sup>TM</sup> software. Either AEs events were graphically returned from the software as pictures presenting Frequency versus Time or as a HCD file (Hit Count Data) containing the cumulative series of events. In this work, the AEs events were reported in the graphs as cumulative events.

The active survey counted for 144 BSF files (i.e. 12 receivers x 12 pulsers, one survey every 1-2 minute), and In-Site Lab converted them into an ESF format. At the end of this initial conversion, the ESF folder contained all the surveys performed during the test, and each survey contained 12 ESF files carrying the information of the waveforms. Of the 11 ESF file carrying the information (i.e. 11 waveforms, as one is the transmitter), it was mandatory to deactivate those surveys containing signals from the same side of the samples where the pulser was, as they were at a wrong angle to receive a correct waveform. This means that the final total files used to obtain the seismic model were 96 over 144. At this point, after a manual picking of the first 96 arrival times, the software allowed cross-correlation of all the other files, meaning that based on the selected criteria for the first events, all the other should be automatically picked. However, it might be that the software was not recognizing automatically the right first arrival and a manual check of each ESF file was mandatory. Once all the times and velocities were corrected, it was possible to extract the velocity model reporting the velocities' variation during the test. In-Site Lab created an excel file reporting all the useful information (i.e. Time, Velocities, Sensors) from which another excel file was created reporting the seismic anisotropy.

### 3.5.2 Preparation of samples for testing, preliminary tests and experimental procedure

Samples were prepared as conventional solid cylinders of 40 mm ( $\pm 0.03$  mm) diameter and 100 mm ( $\pm 0.5$  mm) length, respecting the ratio of 2.5 between length and diameter according to the ISRM recommendations by [Ulusay and Hudson, 2007](#). To minimize the occurrence of natural variations and heterogeneities, the same block of CL was used performing identical coring techniques. A procedure using a diamond coring drill, and a lathe fitted with a cross-cutting wheel assured parallelism to 0.01mm or better for a total of 14 cylindrical specimens.

Preliminary tests on the rocks used in this study showed an average porosity of 10.1 % (measured with a helium pycnometer) and density of 2.47 g/cm<sup>3</sup>. [Bakker et al., 2015](#) reported an average porosity of 8.7 %, and density of 2.47 g/cm<sup>3</sup> obtained on CL samples carved at the same quarry.

For dry tests, specimens achieved dry conditions in an oven at approximately 85 °C for 12 hours to avoid the presence of interstitial water, followed by cooling in a desiccator

for 1 hour. Specimens achieved saturated conditions by immersion in distilled water under vacuum for 24 hours.

A range of confining pressures ( $P_c$ : 7 MPa, 15 MPa, 30 MPa, and 54 MPa) simulated depths of 290 m, 620 m, 1.2 km, and 2.0 km respectively, assuming an average density of the overburden of 2470 kg/m<sup>3</sup> (see Table 2.2). Pore fluid pressures ( $P_f$ ) were calculated accordingly to represent the same depths and assuming drained conditions:  $P_f$  = 5 MPa, 10 MPa, 20 MPa, and 34 MPa, respectively. To compare the dry and saturated data, we therefore maintained the same effective pressures applying a simple effective pressure law where the poroelastic constant  $\alpha$  is assumed to be equal to unity ( $P_{eff} = P_c - \alpha P_f$ ; [Guéguen and Palciauskas, 1994](#)). In that common frame, a dry test at  $P_c = P_{eff} = 7$  MPa corresponded to a water saturated test where  $P_c=12$  MPa,  $P_f=5$  MPa and consequently  $P_{eff} = 7$  MPa. To investigate and isolate the role of temperature treatment,  $P_{eff}=15$  MPa was maintained in all tests using thermally-treated specimens.

The sample embedded in the rubber jacket was mounted inside the vessel of the triaxial machine (Figure 3.12), and all the AEs sensors were fitted according to the spatial array chosen inside the rubber jacket (see figure 3.13). All the samples were initially hydrostatically pressurised (i.e.  $P_c=\sigma_1=\sigma_2=\sigma_3$ ) at room temperature. For drained saturated tests, the pore pressure was applied on the vacuum-saturated samples and then increased up to the chosen value. The effective pressure was maintained constant before the beginning of the standard triaxial test, and axial stress was applied at a constant strain rate of  $10^{-5} \text{ s}^{-1}$  until failure. At the end of the experiment, the axial stress was removed to hydrostatic conditions to avoid any movement on the newly formed fracture due to differential stress.

**Table 3.3.** Summary of the experimental conditions used for the tests on CL and basic mechanical parameters, including values of stress and strain at peak differential stress, and values of differential stress and strain at specimen failure. The Young's moduli were calculated from best fit to the linear elastic section between 0.1-0.2 % axial strain. Presence of localized failure and non localized doformation are reported in the last column.

Experiment name	P <sub>conf</sub> (MPa)	P <sub>f</sub> (MPa)	Depth (m) average density of 2470 kg/m <sup>3</sup>	Thermal treatment (°C)	Peak differential stress (MPa)	Strain at peak differential stress (%)	Young Modulus (GPa)	Stress at failure (MPa)	Strain at failure (MPa)	Presence of failure
1 Dry	7		290	No	116.23	0.52	28.69	108.88	0.58	Localized
1 Sat	12	5	495	No	105.09	0.76	20.02	105.09	0.76	Localized
2 Dry	15		620	No	160.59	0.73	32.27	160.59	0.73	Localized
2 Sat	25	10	1035	No	133.49	1.01	32.43	120.97	1.57	Localized
3 Dry	15		620	150	161.73	0.68	35.65	161.73	0.68	Localized
3 Sat	25	10	1035	150	135.65	0.97	28.96	127.66	1.32	Localized
4 Dry	15		620	300	162.89	0.57	44.66	160.74	0.63	Localized
4 Sat	25	10	1035	300	132.48	0.94	27.24	122.07	1.37	Localized
5 Dry	15		620	450	164.37	0.94	28.08	159.44	1.1	Localized
5 Sat	25	10	1035	450	132.05	1.22	20.69	128.81	1.45	Localized
6 Dry	15		620	600	134.9	1.22	12.97	133.31	1.31	Localized
6 Sat	25	10	1035	600	103.19	1.1	11.69	100.96	1.2	Localized
7 Dry	30		1240	No	184.41	1.26	30.45	180.94	1.44	Localized
7 Sat	50	20	2065	No	127.25	1.44	20.78	127.25	1.44	Localized
8 Dry	50		2065	No	Ductile		35.32	Ductile		Non-localized
8 Sat	84	34	3465	No	Ductile		25.37	Ductile		Non-localized

### 3.6 Frictional Experiment on Synthetic Gouges: MTS 815 - Mechanics Testing System

The apparatus used to perform the direct shear test is the MTS 815 Rock Testing System installed at RMPL at the BGS in Nottingham (Figure 3.14).

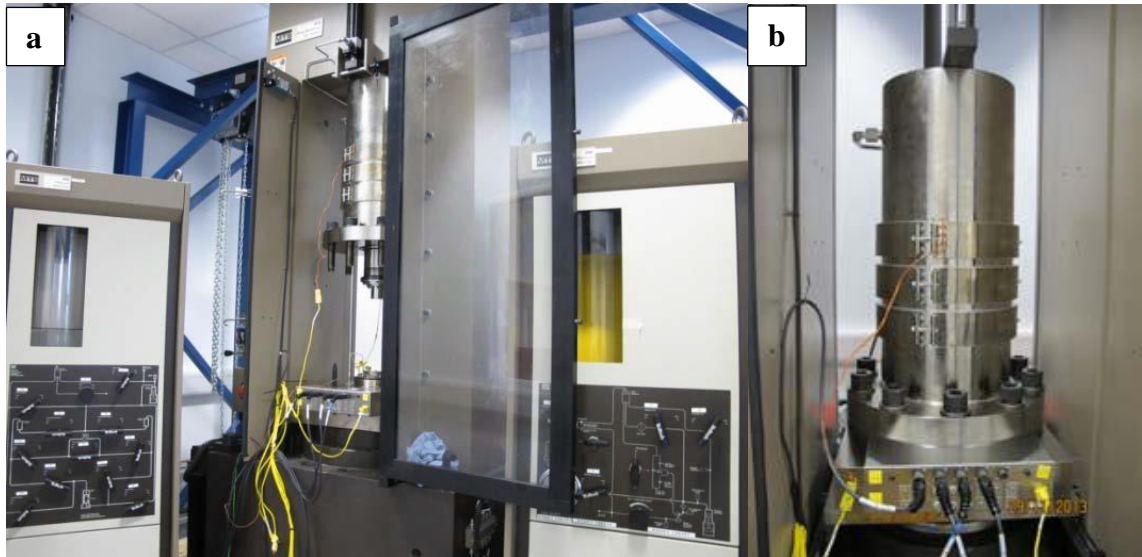


**Figure 3.14** Courtesy of the RMPL at the BGS (Nottingham). In a) from left to right is possible to see the pore pressure intensifier, the open vessel and on the right the confining pressure intensifier. b) is the closed vessel performing a triaxial experiment.

The apparatus performs uniaxial, triaxial and indirect tensile strength (Brazilian) tests. MTS is a close loop computer-controlled and servo-controlled (PID controlled or three-term controller) compression machine, consisting of a stiff load frame capable of maximum axial loads up to 4600 kN, fitted with a confining pressure vessel capable of applying confining pressures up to 140MPa (Figure 3.15). High temperature conditions are possible (although not used in this study) with external heater bands fitted to the confining cell utilising cascade control from an internal thermocouple fitted directly next to the sample and an external thermocouple fitted to a heater band (accurate to  $\pm 0.5$  °C). Mineral oil is used as the confining medium. A 2600 kN capacity force transducer (accurate to 0.32% of the load) is used to measure the axial load. A spherical seated platen is used between the specimen and the capacity force transducer to prevent eccentric loading. The parameters monitored, controlled and recorded during test are: time, axial displacement, axial load, confining pressure, confining displacement, and temperature.

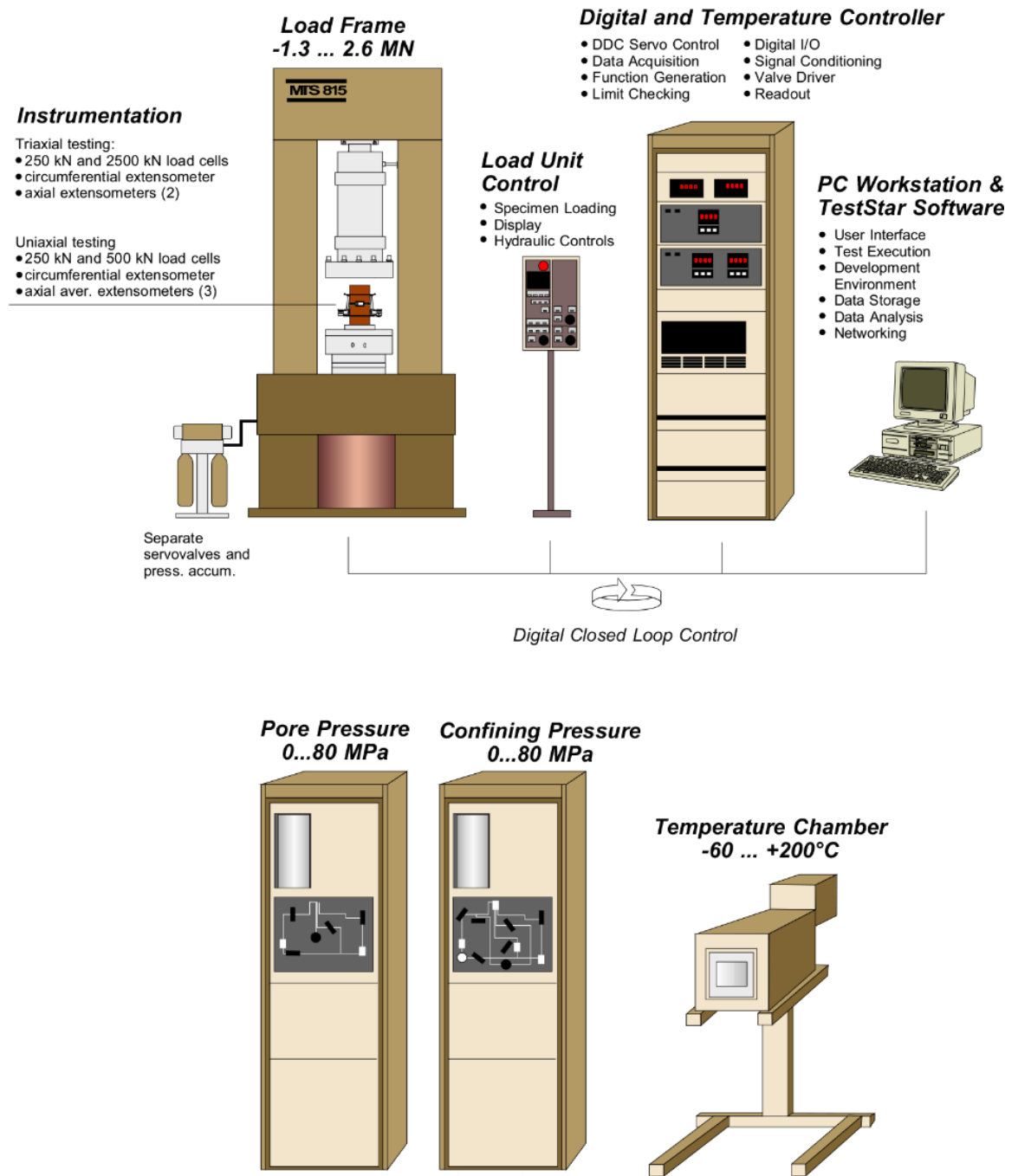


**Figure 3.15.** Courtesy of BGS Nottingham. MTS 815 Rock Mechanics Testing System used for triaxial tests in this project.

### 3.6.1 Designing the Direct Shear Sliding Holder

The aim of this part of the project was to design a sliding holder capable to fit the size of MTS 815 MTS. As proposed by Samuelson and Spiers, 2012, the direct shear setting consists in two L-shaped halves of a cylinder in juxtaposition one against the other, that when closed together they form a full cylinder (Figure 3.16). The sample is



hosted between the two half cylinder. Therefore with this orientation the applied normal load ( $\sigma_N$ ), perpendicular to the area of interest, equals the confining pressure ( $\sigma_2=\sigma_3$ ), and remains constant on the gouge layer throughout the entire experiment. The two sliding surfaces remain fully in contact until the end of shear displacement, avoiding any loss of surface. Finally, no sharp edges are in contact with the jacket, avoiding correlated failures, sometimes common in other techniques.

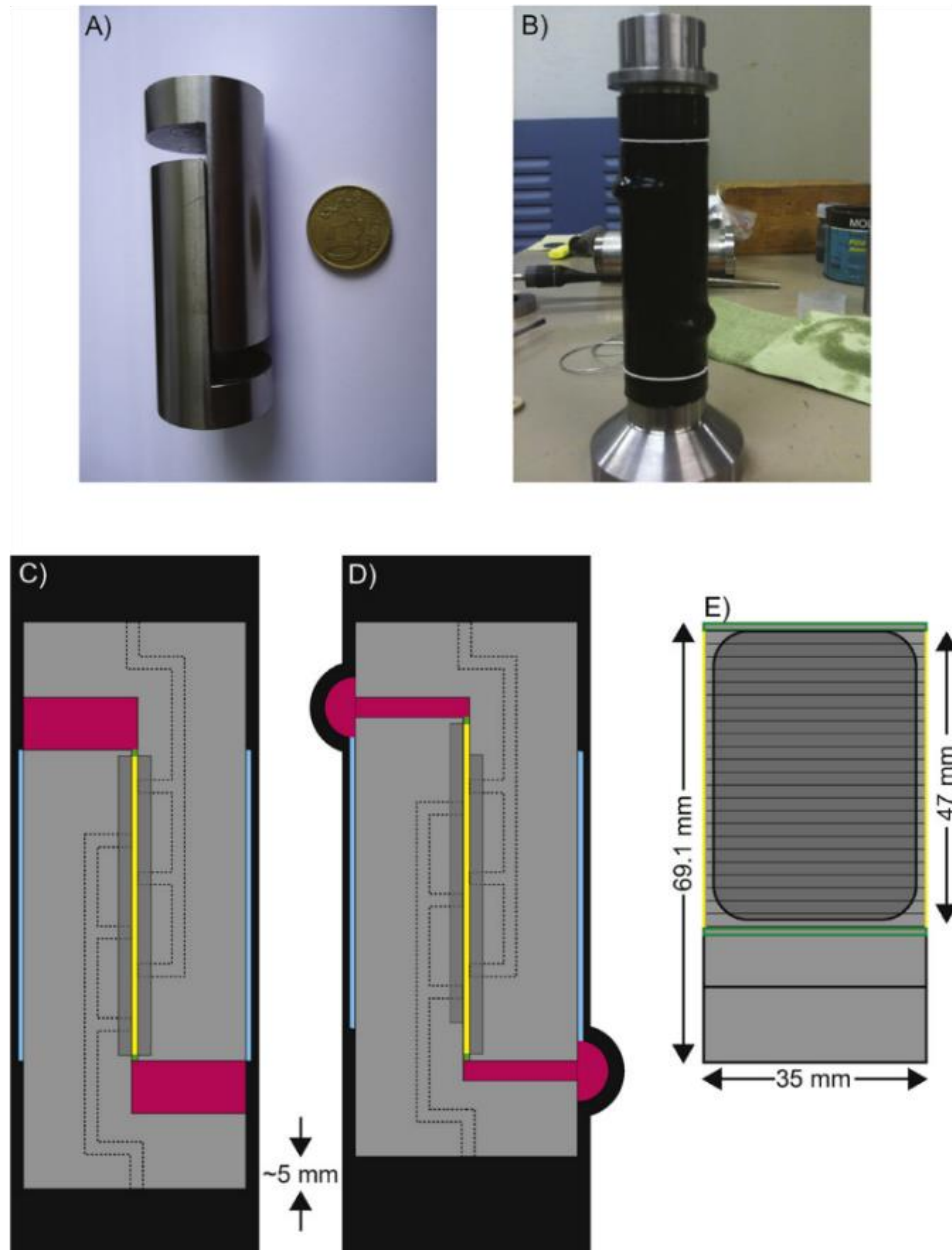


**Figure 3.16.** From [Samuelson and Spiers, 2012](#). Details of the direct shear configuration. A) The two half cylinders. B) The equipment jacketed after a test, as it is possible to see from the bulges in correspondence of the stoppers. C) and D) before and after, respectively, the test to show the behaviour of the stoppers. E) Measures of one side of the slider.

Following this procedure, a new-brand sliding holder was fabricated at the BGS' workshop. The sliding holder has full-cylinder bases and half-cylinder in the remaining length, with a total length of 210 mm and a diameter of 53.92 mm. The holders has a surface capable to host samples of 53.92 mm of diameter and 98 mm length (Fig. 3.17). The gouge-holder contact surface presents triangular grooves perpendicular to the shear direction (i.e. 0.71x0.71x1 mm side length) to avoid the occurring of shear displacement at the gouge-holder interface instead of within the gouge layer (e.g. [Marone and Kilgore, 1993](#)). The total contact area when the two half cylinder are juxtaposed, is of 5284.16 mm<sup>2</sup>. In comparison, at the actual knowledge, the other direct shear experiments using this configuration were carried on smaller equipment (e.g. about 35 mm diameter per 47 mm length contact area, as in [Samuelson and Spiers, 2012](#)).

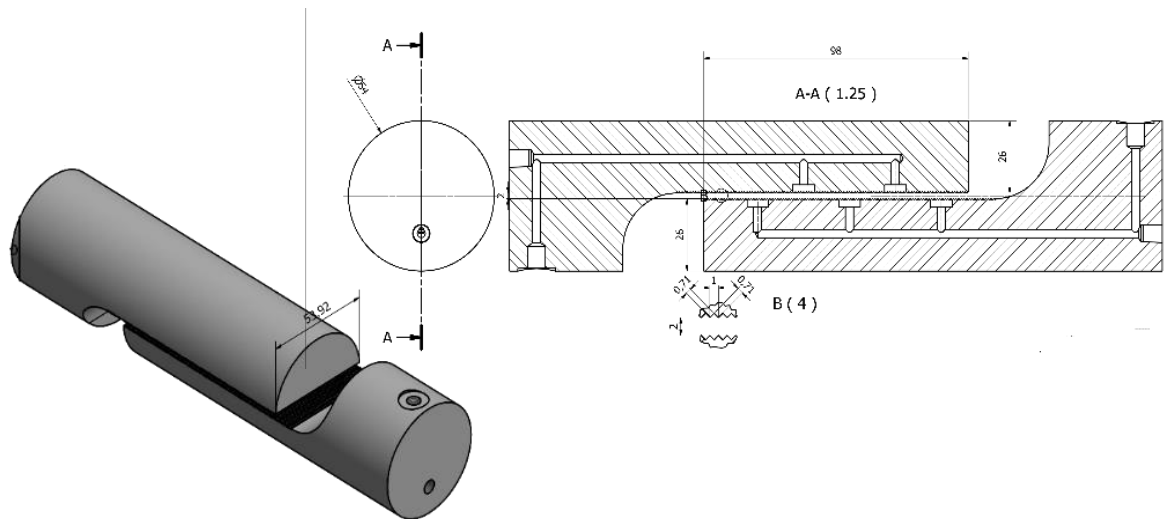


**Figure 3.17.** Sketch of the sliding holder designed for the MTS Triaxial apparatus. The diameter is 53.92 mm and the overlapping surfaces are 98 mm.

Although it might sound a straightforward process, the development of these holders involved three generations of holders before the right specifications for all the components were achieved.

#### 3.6.1.1 Sliding holder #1

The first sliding holder generation employed A 316L stainless steel. The material has a very high corrosion resistance, with a yield strength of 300 MPa. It was provided with inner conduits to allow the injection of fluids for test with pore fluid pressure

(Figure 3.18) The conduits ended at different lengths across the sliders to provide a homogeneous distribution of the fluid while testing with pore fluid pressures. In this first generation of holders, the triangular grooves were machined with their bases at the same height of the outer border, protruding from the basal level. The holders took 6 months from the design itself to the product delivery. Once the holder was finished, a series of calibration tests were carried on to check the strength and the behaviour of the final assemblage, with the sliding holder completely jacketed.

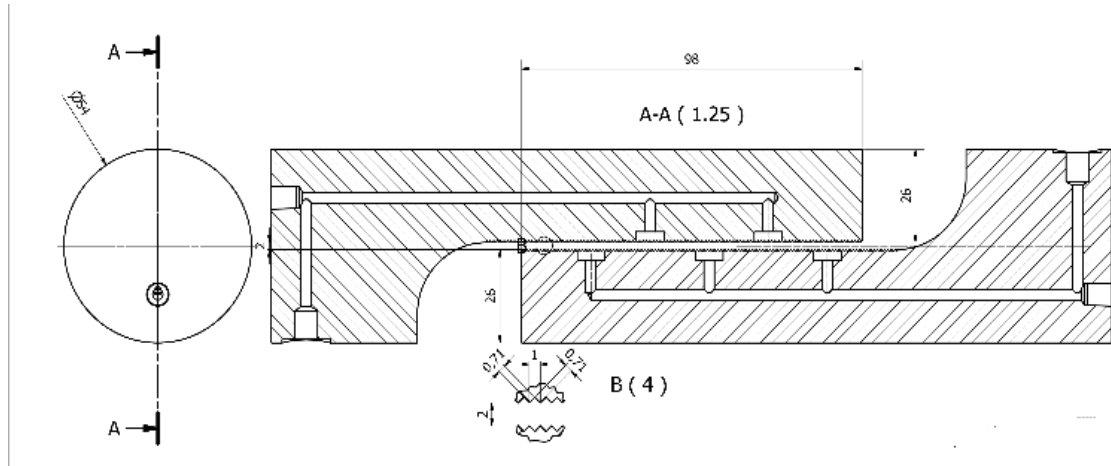


**Figure 3.18.** First generation of sliding holder. In this generation, the A316L stainless steel was used to fabricate the half cylinders. The contact surface was grooved with a series of triangular grooves, in this case with their base at the same level of the outer border, hence the grooves resulted higher than the border. The inner pore fluid conduit crossed the holders reaching the contact surface at different lengths to assure a homogeneous fluid distribution.

#### 3.6.1.1.1 Bending

After the first series of calibration tests (further described in this chapter), the first sliding holder resulted bent. A close inspection revealed that during the test the grooves interlocked in a point where stoppers moved from their original positions, creating a point of stress exceeding 100 kN in axial stress (Fig. 3.19a). A simple numerical model projecting the interlocking of the grooves to simulate the increase of stress in the holder showed that an increase in stress in the platens up to 200 kN (Fig. 3.19b) very likely occurred. Therefore, the interlocking produced stresses overcoming the yield strength of the stainless steel.

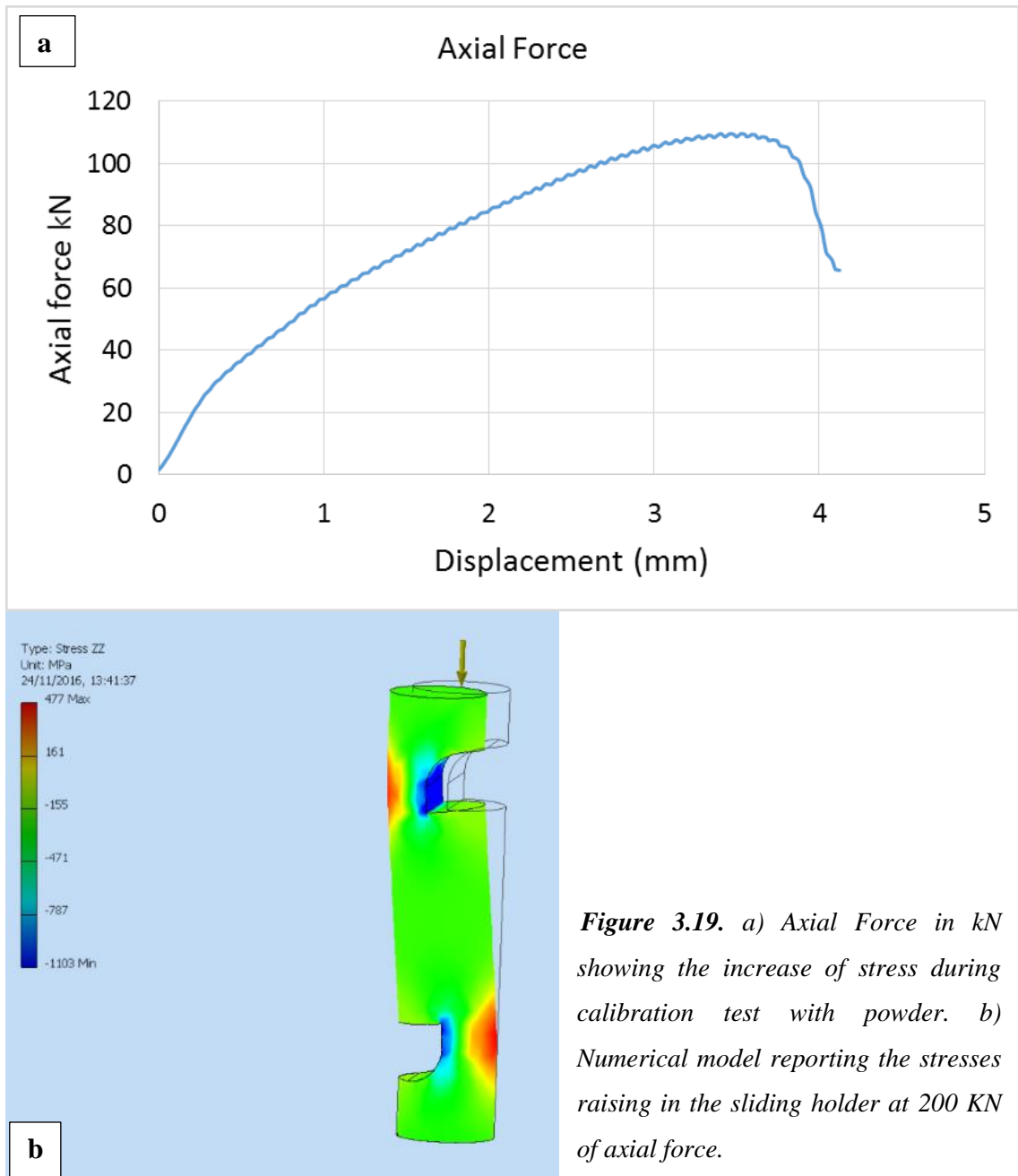


**Figure 3.19.** a) Axial Force in kN showing the increase of stress during calibration test with powder. b) Numerical model reporting the stresses raising in the sliding holder at 200 kN of axial force.

The sliding holders were subsequently repaired and inspected for any bending after each of the experiment done with this assemblage.

#### 3.6.1.2 Sliding Holder #2

The design of a second generation of sliding holders started soon after the issue encountered with the first one, knowing that the building procedure is particularly time-consuming. For this second attempt, alloy 17-4PH was used being a higher resistant material. The alloy is a stainless steel with Cu and Nb/Cb additions, providing a greater yield strength (1100-1300 MPa). A better pore fluid distribution system was also

implemented allowing the fluid to flow and saturate the gouges in a more efficiently way: on the contact surface, a sintered disk carved as a mesh was positioned to cover the conduits and to avoid gouges to go in and block the water flow. This second sliding holder was tested to see the response with simulated gouges, but unfortunately the sintered disk showed to be not strong enough to resist the friction strength created by the powder. This generation of holders was therefore discarded.

#### 3.6.1.3 Sliding Holder #3

To obviate all the inconveniences encountered with generation #1 and #2, a third (and last holder generation!), was built in alloy 17-4PH but without the presence of a pore fluid system. Here, the grooves were machined with their bases lower than the outer border, in such a way they were not protruding higher and so to avoid any interlocking issue. This latter holder proved that alloy 17-4PH was a better and resistant material with respect to the previous alloy used.

#### 3.6.2 Calibration tests

Calibration tests were required to evaluate the response of all the components of the sliding holders (e.g. end stoppers and jacketing materials, as well as the sliding holders themselves) to the applied axial load and confinement pressure, and their possible impact onto the measurements of the friction properties of the material investigated. It was particularly important to check the properties of the stoppers to quantify any shear resistance.

Stoppers were positioned at the end of each sliding holder and were used to prevent collision of the sliders. The ideal material should be elastic, with full elastic recovery after application of load and soft enough to not add any resistance to the shear. To fit the requirements of being reusable, easy to prepare and not too expensive, three materials were chosen for the tests: two rubbers and a silicon.

**Belzona 2131:** Two components rubber, short cure time (few days) depending on ambient conditions. Recovery after compression is 24 % in 30 minute. Shore durometer test: 90 (hard material).

**Belzona 2221:** Two components rubber, with high flexibility when dry and tough. Short cure time (few days) depending on ambient conditions. Recovery after compression is 16% after six hours. Shore durometer test 69 (hard material).

**Silicone:** Adshead Ratcliffe, one component high modulus silicone ISO 11600-F/G-20 HM. Long cure time (2 mm in 24 hours). Shore durometer test 20 (soft material).

The calibration cycles involved axial displacement up to the total length allowed, in two rounds: 1) cycle 1 was from 0 to 5 mm and 2) cycle 2 from 5 to 10 mm displacement. Between cycle 1 and cycle 2, the axial load was removed but the displacement was maintained. In this case, the stoppers were tested in uniaxial conditions. Cycle 3 was a repetition of cycle 1 and 2, but with an applied confining pressure of 15 MPa. All the cycles were thought to test if the stoppers presented a sort of 'rebound' (i.e. recovery) when the applied stress was removed, and mainly their mechanical behaviour (i.e. stiffness) under increasing axial pressure. Cycle 4 was a preliminary test with synthetic powders, where the axial load was constantly increasing at a fixed rate up to the maximum displacement, to obtain data reproducing a real experiment and to test the functioning of all the components. This test was run with an applied confining pressure  $\sigma_3=15$  MPa. In this case, it was also possible to extrapolate the final values of  $\mu$ , friction coefficient.

#### 3.6.2.1 Calibration procedure

As mentioned before, the direct shear configuration implies a calculation of the stresses applied on the contact surfaces that differs from previous standard triaxial techniques. In the direct shear configuration the contact area containing the sample is positioned parallel to the axial load, and perpendicular to the confining pressure. Therefore, the minimum principal stress  $\sigma_3$  equals the normal stress  $\sigma_N$ , and the maximum principal stress  $\sigma_1$  (axial stress) equals the shear stress,  $\tau$ .

Cycle 1 and 2 were run in uniaxial condition, hence with  $\sigma_3=0$ . The assembly was mounted in the load cell and the axial hydraulic actuator piston was first raised to engage with the base plate at the bottom of the pressure vessel using a manual controller. Then the base plate was raised too so the assembly was brought within 1mm of contact with the load cell at the top. As the PC was connected to the machine

registering the axial displacement during the sample preparation and positioning, the recording of the measurement began when digits of axial force became positive, hence this point was chosen as zero or starting point (i.e. when the piston is contacting with the assembly and shear was starting). All the parameters recorded (i.e. time, axial force, and axial displacement) during the ongoing preparation were subsequently zeroed accordingly. This procedure allowed also a better control in general, avoiding the unfortunate case that, if displacement at the beginning was giving a wrong digit, the safety threshold for the total displacement imposed in the procedure was stopping the experiment before the necessary.

Cycle 3 and 4 were run in standard triaxial conditions, therefore confining pressure was applied (i.e.  $\sigma_3 \neq 0$ ). When the assembly was ready after following the same initial procedure of cycle 1 and 2, the pressure vessel was lowered and sealed shut. The pressure vessel was filled with confining oil before confining pressure was hydrostatically applied to the samples at a rate of 0.04 MPa/s. Once the hydrostatic pressure reached the chosen value, the standard triaxial test began with application of differential axial load. The test terminated once the maximum allowed displacement was reached, or earlier if any issue was identified. Load was finally removed at the same rate of constant axial displacement.

Throughout the experiments, the contact area was changing continuously as the displacement increased and accurate calculations of the area were necessary to obtain valuable data on friction (i.e. [Samuelson and Spiers, 2012](#)). In this case, the total area considered was the area comprising the grooves, which means 98 mm x 53.925 mm = 5284.16 mm<sup>2</sup>. At the beginning of the experiment the contact area created by the two half cylinders it was not overlapped, as the stopper were created to allow 10 mm of displacement, and therefore they were pushing the two sliders away. During the experiment, as the piston was applying load, the two contact areas were sliding one against the other until they completely overlapped. Following this procedure, the initial area was the result of the subtraction of the true amount of area displaced from the total area, based on the time interval and the calculated area increment in millimetres (e.g. displacement in function of time). With this calculation, the value of the final area was coincident with the total area, but the area increment allowed obtaining accurate values of stress at any moment during the experiment. For uniaxial conditions, the calculation



of the shear stress was obtained dividing the axial force by the area increment; regarding the experiments run in triaxial conditions, the friction coefficient was obtained dividing  $\tau$  by  $\sigma_1$  (i.e. equal to  $\sigma_3$ ).

### 3.6.2.2 Calibration results for Belzona 2131

During cycles 1 and 2, Belzona 2131 showed to reach an axial pressure of 1.4 MPa and 1.5 MPa, respectively and a shear stress of 0.60 and 0.63, respectively. The trend was showing an increased stiffness, even if moderate, when loaded during the second cycle (Figure 3.20). The chart reports both the axial pressure and the shear stress.

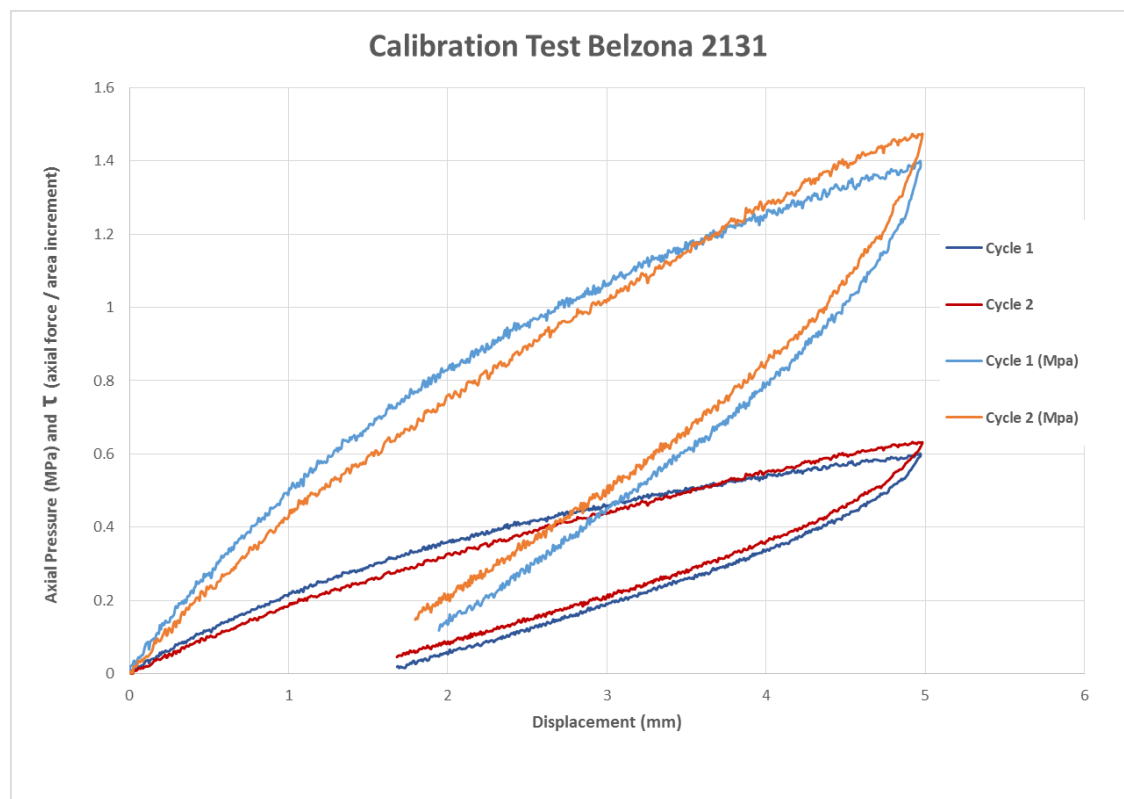


**Figure 3.20.** Increasing axial load (light blue and orange lines) and increasing  $\tau$  (purple and blue lines) for cycles 1 and 2 of Belzona 2131.

As highlighted in the chart, Belzona 2131 was opposing some resistance to shear and in particular, the extrusion of the material at the end of the experiment was severe: the Teflon jacket is heavily stretched. In cycle 3 with an applied confining pressure of 15 MPa (Figure 3.21), Belzona 2131 showed an initial hardness with the differential axial stress increasing from zero to 4 MPa after only 0.12 mm displacement. The trend

continued increasing steadily reaching a peak of 6 MPa already at 2.7 mm of axial displacement. For this reason, the test was stopped to check the Teflon jacked conditions.

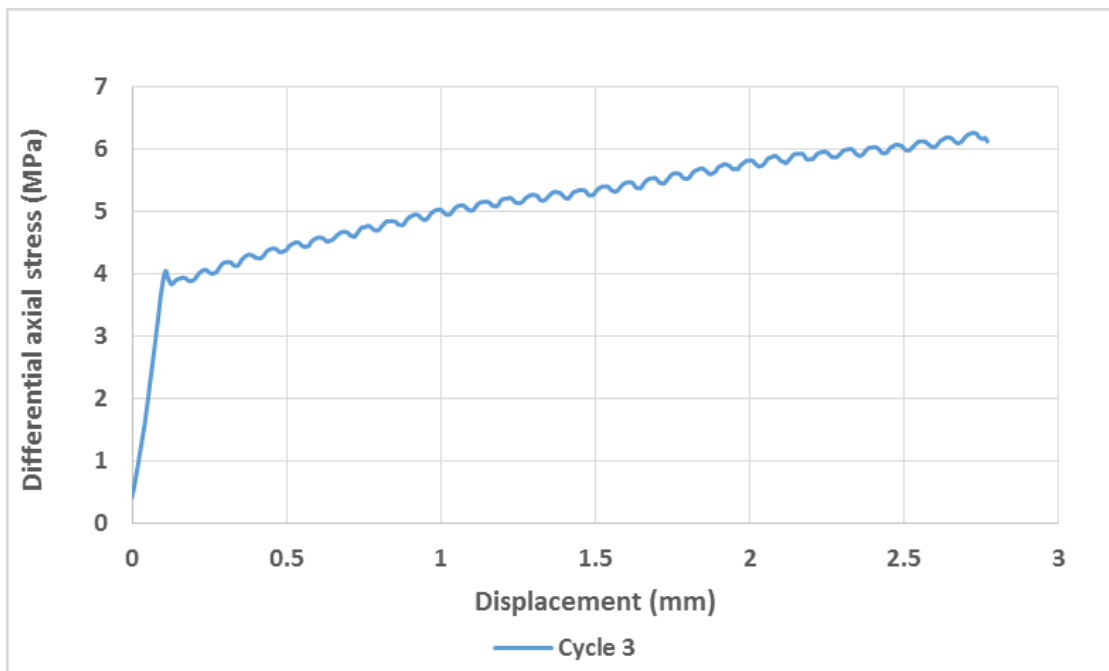


**Figure 3.21.** Behaviour of Belzona 2131 with  $P_c=15$  MPa applied. The axial stress showed a dramatic increase up to 4 MPa after 0.12 mm of displacement and consequently a lower but steady increase until the experiment was stopped.

As expected, the extrusion was really severe, and along the contact between the two sliders the Teflon jacket started to show failure, due to intense stretching caused by the extrusion. For these reasons, Belzona 2131 was discharged.

### 3.6.2.3 Calibration results for Belzona 2221

Belzona 2221 was characterized by softer properties than Belzona 2131, as reported in section 3.6.2, this chapter. In cycle 1 and 2 it reached a peak of 0.75 MPa and 0.85 MPa axial pressure, respectively and 0.33 and 0.37 of shear stress, respectively. In addition, the rubber started to behave in a stiffer manner during the second cycle of applied stress (Figure 3.22).

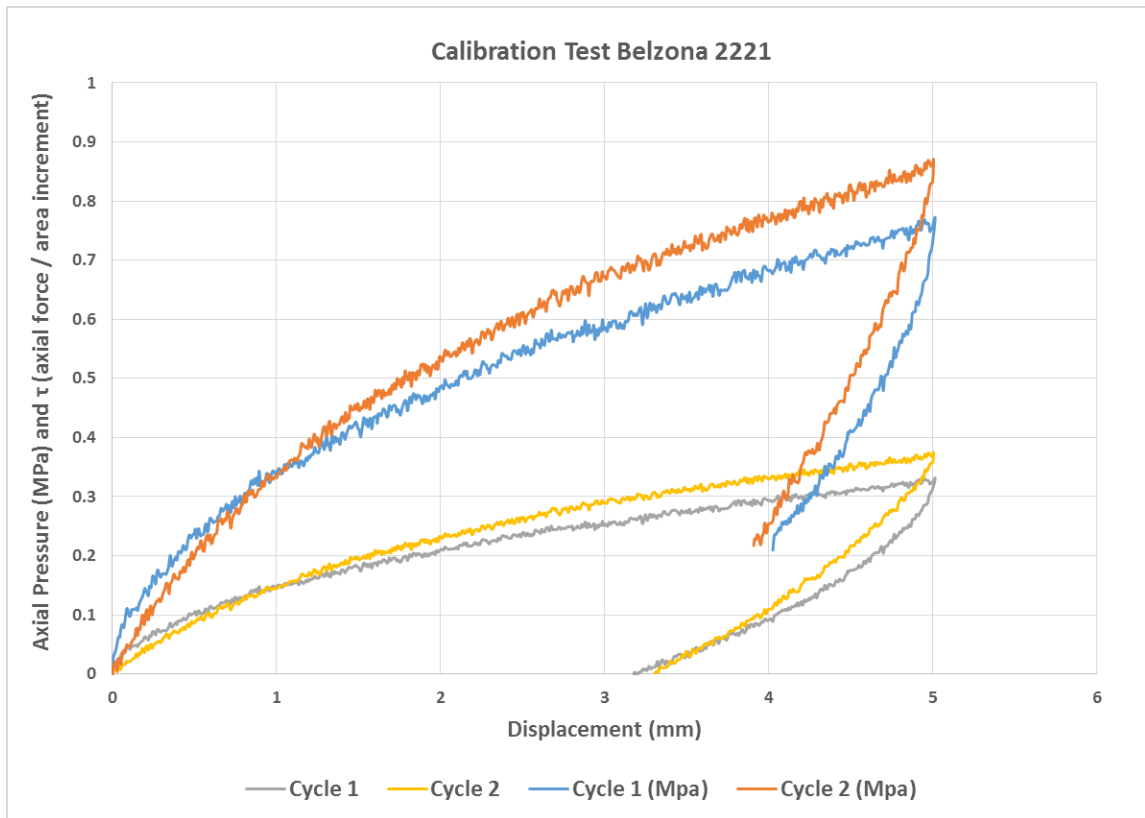


**Figure 3.22.** Axial pressure increasing at 0.75 MPa (light blue line) and 0.85 MPa (orange line) and increasing  $\tau$  (grey and yellow lines) at 0.33 and 0.37 for cycles 1 and 2 of Belzona 2131.

Despite the lower peak stress reached compared to Belzona 2131, the extrusion was even more severe (Figure 3.23, a and b) and , even if the Teflon jacket didn't break, it was heavily stretched (Figure 3.23, a and b) and therefore the experiment with confining pressure applied it was not performed. Belzona 2221 was not selected.

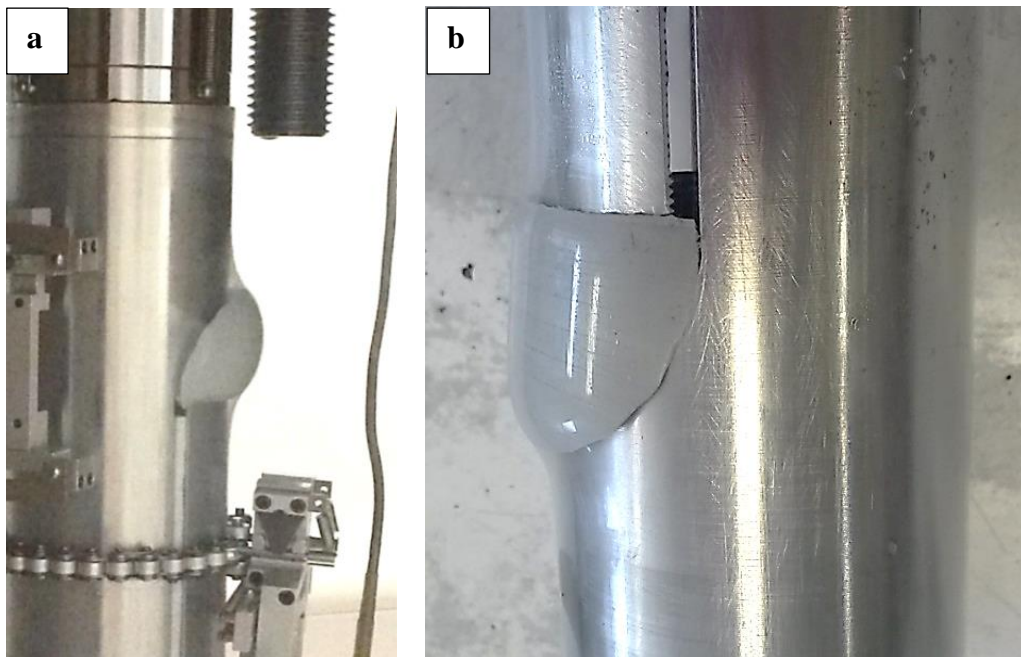


**Figure 3.23.** a) and b) Belzona 2221 extrusion after cycle 1 and cycle 2 of calibration test.

#### 3.6.2.4 Calibration results for Silicone

The series of calibration tests for silicon showed that this material had the softest properties amongst the materials tested (Figure 3.24).

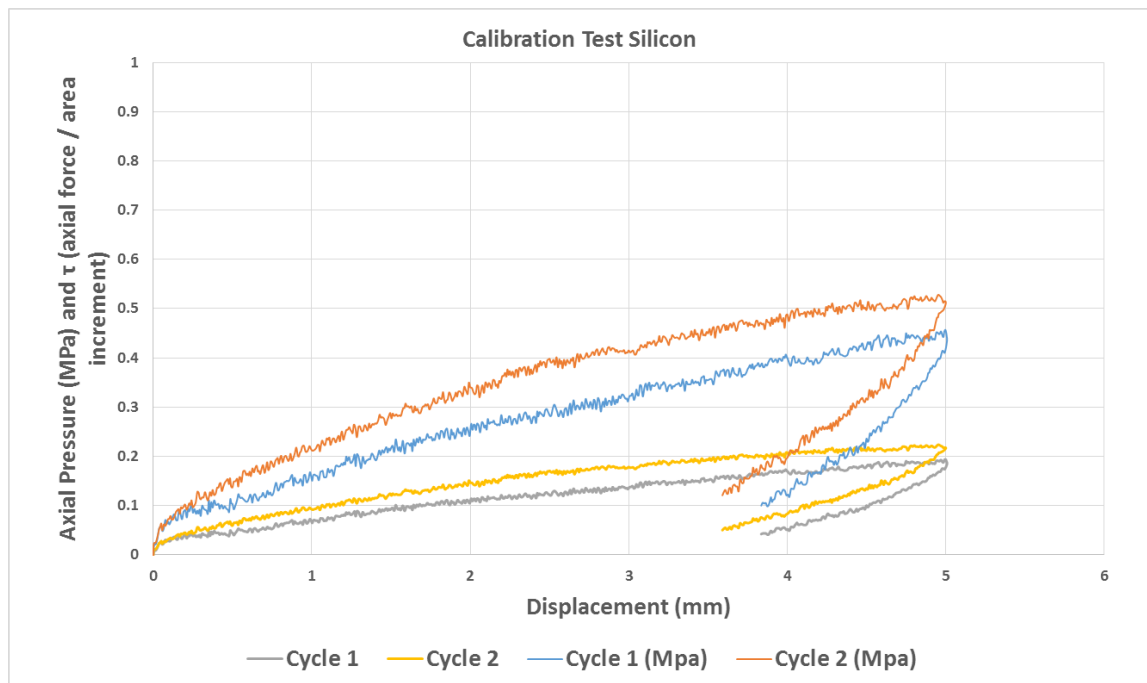


**Figure 3.24.** Axial pressure (blue and orange lines) and shear stress (grey and yellow lines) results for silicone. The shear stress showed the lowest values respect to the other materials used for calibration, with a peak of 0.19 and 0.21 for cycle 1 and 2, respectively.

The axial stress reached a peak of 0.44 MPa and 0.51 MPa during the two loading stages and when calculated as shear stress, it gave values of 0.19 and 0.21, respectively. Despite the material showed an increasing stiffness during the second cycle, it remained moderate. During the experiment, the extrusion of the stoppers is modest, hence the Teflon jacket was not heavy stretched. Regarding the values of shear stress, the positive values indicated that some resistance is somehow created inside the holder, for instance as contribution of the external layer or jackets or the inner Teflon used as layer. After an accurate check at the end of the experiments, it is clear that the Teflon sheet were the cause of the resistance registered. A single sheet of Teflon was used as layer between the holders and being a soft material, it was affected by the presence of the grooves that indented it.

When this calibration test was repeated for sliding holder #3, two Teflon sheets were put in contact with an applied confining pressure of 15 MPa. Final values of friction coefficient,  $\mu$ , were obtained (Figure 3.25). Cycle 1 showed an increase up to 0.03  $\mu$ , before the stop at 4.70 mm displacement, then cycle 2 started and the friction coefficient reached a maximum value of 0.065  $\mu$  at 6.63 mm displacement. In this case, more reliable results of friction coefficient were obtained.

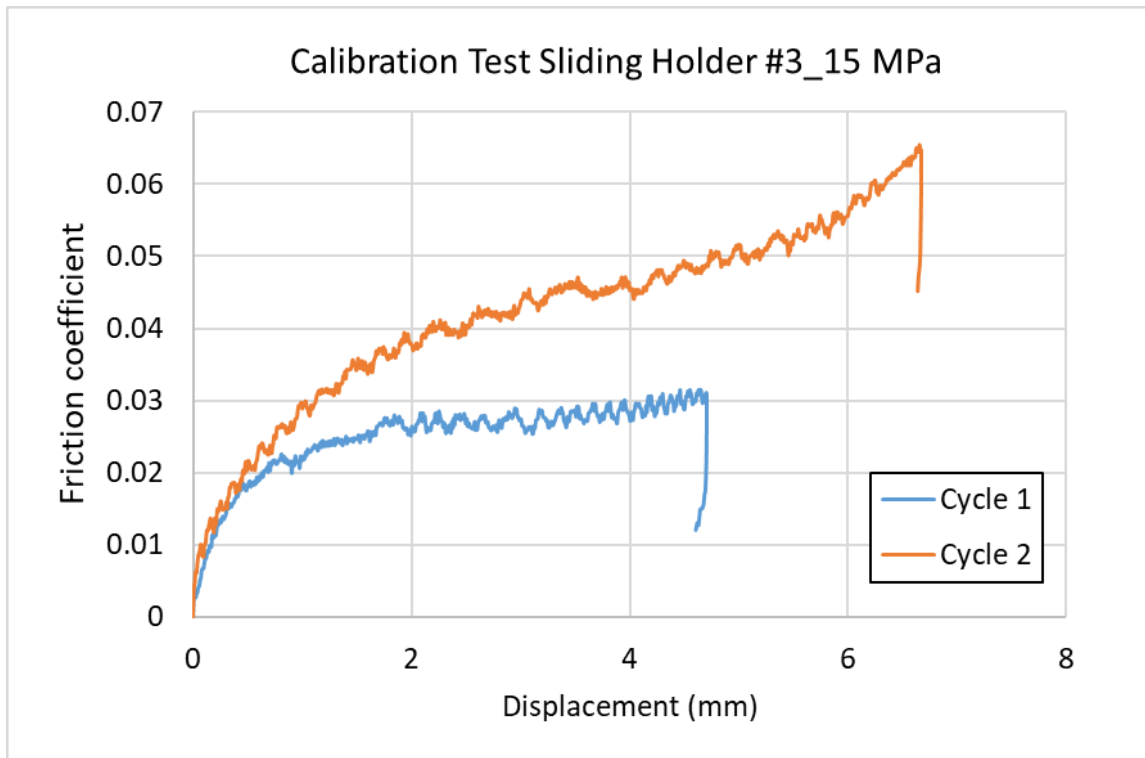


**Figure 3.25.** Results for the calibration test of sliding holder #3. The test were run using two Teflon sheets of 1 mm thickness each, and an applied confining pressure of 15 MPa. In cycle 1, the friction coefficient reached a maximum of  $0.03 \mu$  at 4.70 mm displacement, while in cycle 2 it reached a maximum of  $0.065 \mu$  at 6.63 mm displacement.

It is interesting to note how the friction coefficient was increasing during the cycle 2. The post experiment investigation revealed that the applied confining pressure is enough to compress the two Teflon sheets one against the other and enough for them to be superficially indented by the grooves. However, this calibration test proved that the assemblage is creating minimum resistance to the shear (i.e.  $< 0.1 \mu$ ), therefore this contribution was not counted as affecting the frictional data.

### 3.6.2.5 Calibration results with simulated gouge and silicone

The last calibration test, cycle 4, was built to mimic a real experiment, using a layer of powder as sample, the assemblage described beforehand, and an additional jacket (i.e. elastomer tubing, Viton-like) used as extra-precaution to assure no leaking in case of failure (i.e. Teflon jacket being cut and oil, used as pressure medium, infiltrating and invalidating the experiment). Confining pressure was applied at 25 MPa and the powder selected was the quartz-sandstone gouge. Friction coefficient results are below in figure 3.26. The powder was used wet, to assure an initial cohesion during sample preparation.

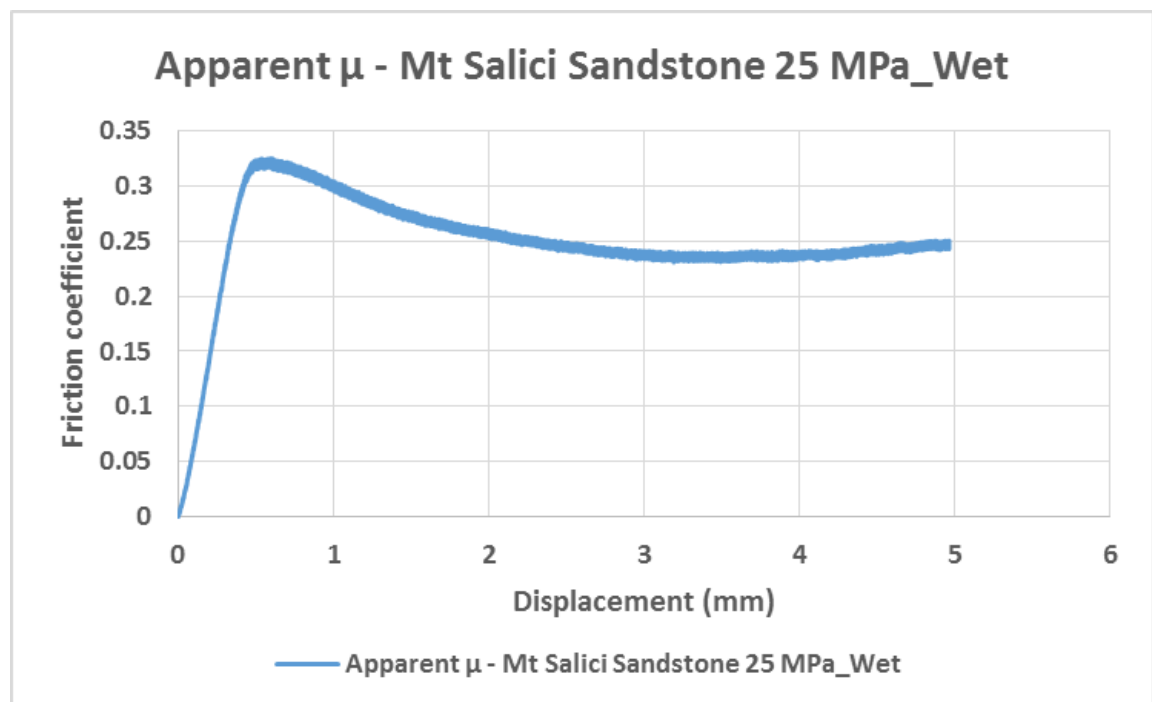


**Figure 3.26.** Calibration test with a layer of powder, two jackets (inner Teflon and outer rubber) and silicon stoppers. The experiment was run with  $P_c=25$  MPa. Friction coefficient showed an initial increase up to a peak of  $0.32 \mu$ , followed by a decreasing trend and a slight recover before 5 mm displacement, when experiment was stopped.

The friction coefficient showed to increase to a maximum peak of  $0.32 \mu$ , followed by a descending trend (Figure 3.26). The value for quartz-sandstone were quite low (i.e. average friction coefficient for quartz  $0.5-0.6 \mu$ , e.g. [Crawford et al., 2008](#)), probably because the powders were spread wet onto the surface to assure cohesion during test preparation. The test stopped at 5 mm of axial displacement, when the friction coefficient was showing a mild increase. Subsequent investigations after the test showed that the silicon stoppers are behaving without excess of extrusion and, most importantly, the second rubber jacket was definitely necessary to protect the entire assemblage from oil intrusion, because of the presence of signs of wearing in correspondence of the gouge layers.

### 3.6.3 Procedure for the final assemblage

The gouges layers were prepared using a metal rig designed to suite half cylinder and equipped with a top screw that allowed stopping the half sliding holder to rotate (Figure 4.27 and 4.28 a). The rig allowed spreading either a layer of 1 or 2 mm on top of the surface by the use of removable separate bars of 1 mm thickness. A T-shape platens was used to press and level the gouge.



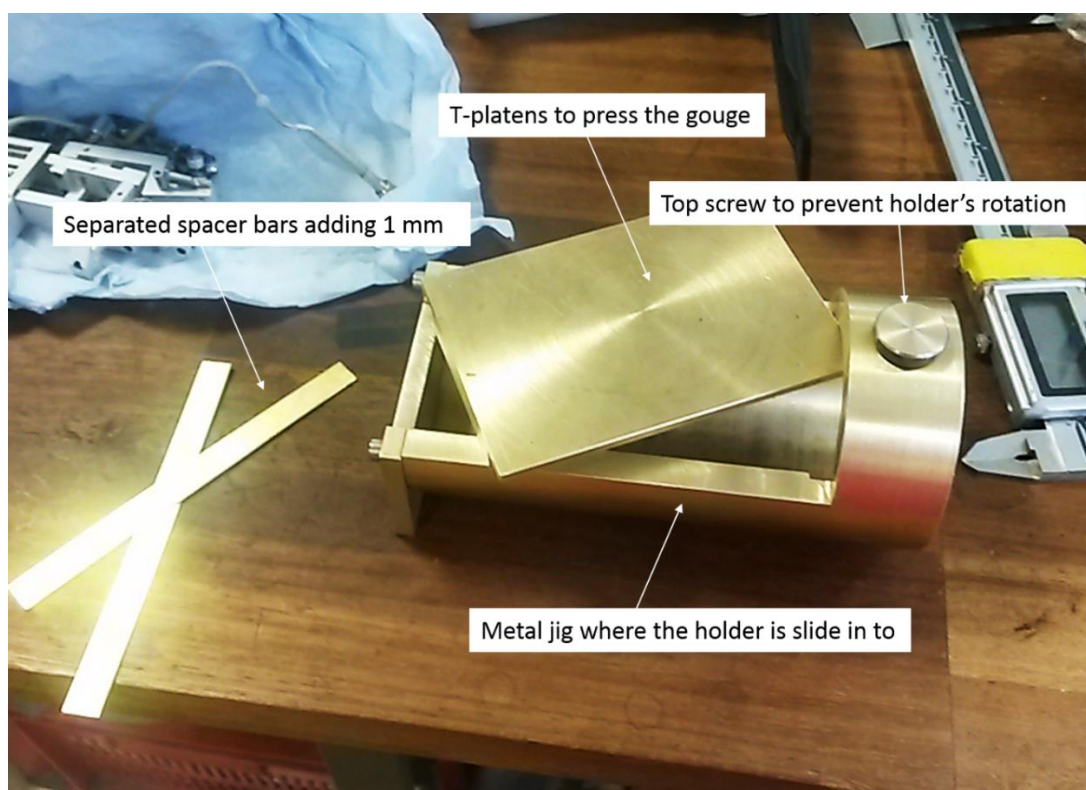


**Figure 4.27.** Metal rig designed to host half cylinder to spread an even layer of synthetic powders of 1 or 2 mm. the metal rig is provided with a top screw to avoid the cylinder to rotate.

The gouges were combined with water at the first attempt. Few drops of water were added until a ‘creamy’ texture was reached. This helped to spread uniformly the powder onto the sliding holder before being pressed with the ‘T-shape’ metal bar. The assemblage (i.e. the metal rig containing the half cylinder with the gouge) was placed in a hoven at 40°C for at least 1 hour (i.e. for limestone and sandstone) or 1 day (i.e. for clay) to assure a complete evaporation of the water. Unfortunately, the combination with water resulted in a hardened and extremely brittle soil when dry. Therefore, following the same procedure, a 2-Propanol – ACS reagent,  $\geq 99.5\%$  pure (or isopropanol alcohol,  $C_3H_8O$ . Sigma-Aldrich Company Ltd.) was used. Isopropanol showed a quicker evaporation (i.e. less than 1 hour for limestone), and when dry, the samples consisted of a soft, consolidated gouge layer (Figure 3.28 d). Carefully, the silicon stoppers were placed at the end of each half-cylinder and the second half-cylinder was then positioned on top of the other, and all together rotated vertically (Figure 3.28 b and c). The recompleted cylinder (i.e. the two sliding holders with the sandwiched sample), was then encased in a 0.5 mm Polytetrafluoroethylene (PTFE) heat shrink tubing; rubber membranes were added at the ends of the cylinder to create

a better grip for sealing between the holders and the PTFE layer to prevent further oil infiltration (Figure 3.28 b). An additional thick (i.e. 2 mm) elastomer tubing (i.e. Viton-like) was slide over the entire assemblage. The full seal was then provided with locking wires (Figure 3.28 c).

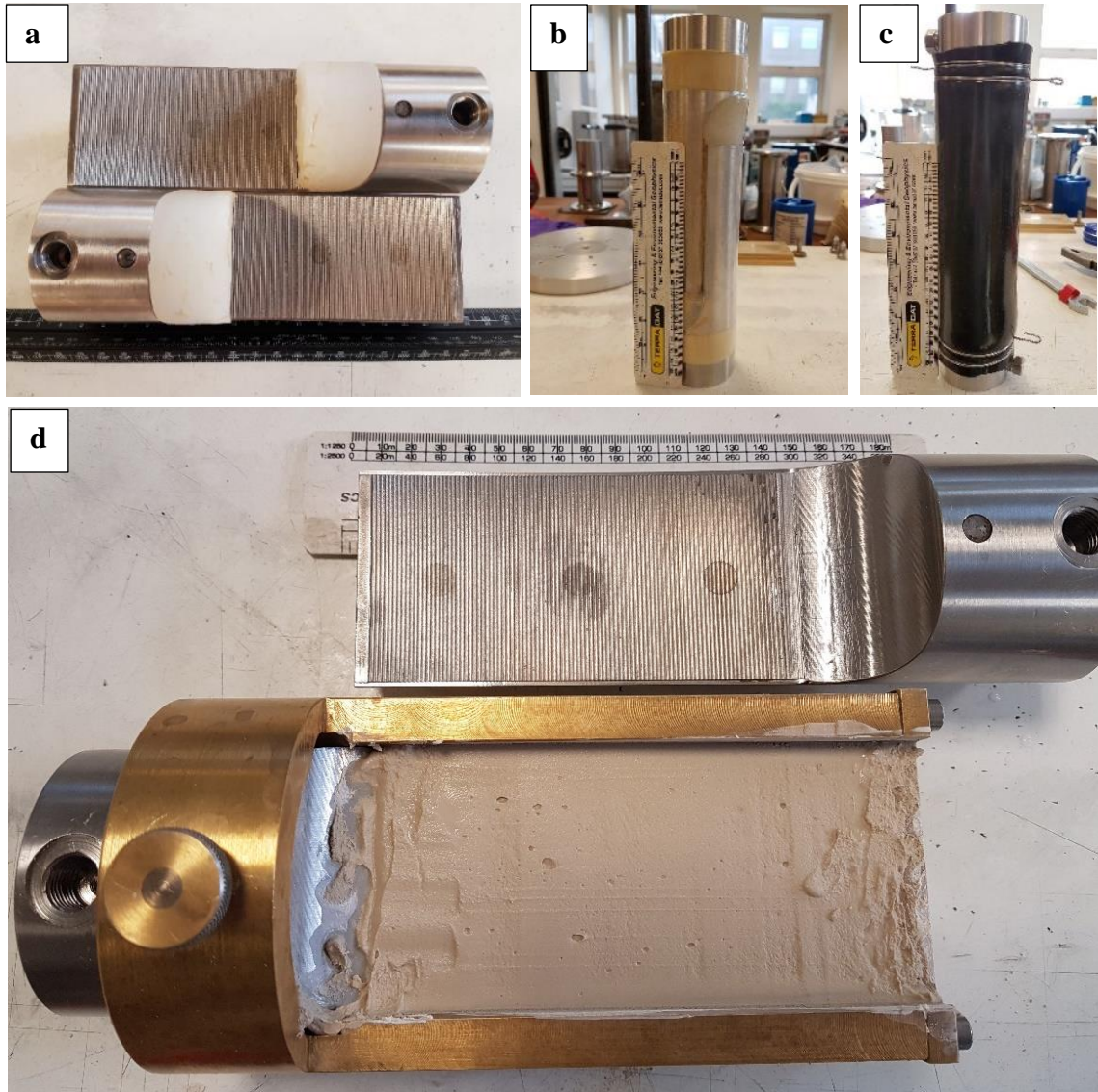


**Fig. 3.28** a) The two half cylinders showing the contact areas provided with grooves and the two stoppers used to avoid collisions during tests. b) The assemblage was jacketed with a heat-shrinking Teflon jacket, two membranes were added between the slider and the jacket to assure a better isolation from the confining pressure medium. c) The entire assemblage was then jacketed again with a black rubber jacket and provided with locking wires. d) Metal jig with one sliding holder and a simulated gouge spread and compressed.

Simulated gouges were tested both pure and then combined with an increasing amount of clay to measure the changes in frictional properties. To assure the correct

proportion of clay and gouges, the volume of the gap between the two half cylinders was calculated as follows (Figure 3.29):

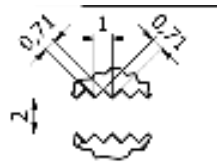


**Figure 3.29.** Sketch of the measure of one groove covering the contact surface of the sliding holder, in millimetres.

Volume of one groove:  $(0.71 \times 0.71)/2 \times 53.92 = 13.590 \text{ mm}^3$

Volume of all grooves:  $13.590 \times 2 \times 98$  (number of grooves) =  $2663.75 \text{ mm}^3$

Volume of the gap between the surfaces:  $2 \times 98 \times 53.92 = 10568.32 \text{ mm}^3$

Total volume:  $2663.75 + 10568.32 = 13232.07 \text{ mm}^3$

Along with the particle densities calculated in section 3.3.3.1, this chapter, it was possible to obtain the weight of each powder combined to clay, the latter varying in increasing percentages of: 0%, 10%, 25 % and 50% (Table 3.4).

**Table 3.4.** Example of percentage calculation based on powders' densities to obtain each powder fraction to be used in the experiments.

Gravimetric clay fraction (g)			Volumetric clay fraction			Density g/cm <sup>3</sup>		
32.48427	100%		11899			Clay	2.73	0.00273
24.3632	75%		8924.25			Sand	2.5	0.0025
16.24214	50%		5949.5			Limestone	2.73	0.00273
8.121068	25%		2974.75					
3.248427	10%		1190					
Gravimetric sand fraction (g)			Volumetric sand fraction			Density=weight/volume		
29.7475	100%		11899					
22.31063	75%		8924.25			Weight=density*volume		
14.87375	50%		5949.5					
7.436875	25%		2974.75			Volume=weight/density		
2.97475	10%		1190					

### 3.6.4 Experimental procedures

Two experimental procedures were designed to investigate the properties of the three natural end-members selected, and the binary mixtures of them. A first series of

tests was done at a constant displacement rate of 0.001  $\mu\text{m/s}$  and three confining pressures (i.e. 10, 30, 50 MPa). The three confinements of 10, 30, and 50 MPa investigated represent, considering an average density of 2.615  $\text{g/m}^3$ , an increasing depth into the Etnean basement of 390 m, 1170 m and 1950 m, respectively. A second series of tests was done at a fixed confining pressure of 50 MPa but with variable displacement rates (i.e. velocity steps for rate-and-state analyses). Table 3.5 summarizes the experiments conducted: experiments conducted with the first sliding holder are shown in orange, of which the results are presented but not discussed because of the uncertainty about the quality of the data. Note that the percentages reported are indicating the increasing amount of natural quaternary clay mixed with the two end-members of quartz-sand and limestone. Successful experiments are reported in green, with the data presented in the following sections. In red are the experiments missing, due to lack of time within this study. Purple signifies that the experiments failed.

**Table 3.5.** List of the experiments, divided into standard and rate and state, lithologies used and confining pressures. In green experiments done, in red experiments missing, in purple experiments failed.

Type of test	Confining Pressure [MPa]	Monte Salici (quartz-sandstone)	Quaternary natural clays	Comiso limestone (limestone)
Constant Strain Rate, dry	10	100%	100%	100%
	30	100%	100%	100%
	50	100%	100%	100%
		90%	10%	10%
		75%	25%	25%
		50%	50%	50%
Rate and state, dry	50	100%	100%	100%
		90%	10%	10%
		75%	25%	25%
		50%	50%	50%



### Experimental procedure for Constant Strain Rate

Similarly than for the calibration tests, the samples assembly were mounted inside the triaxial cell. The axial piston was brought as close to the assemblies as possible without entering in contact. Then the cell was closed and filled in oil. Confining pressure was applied in hydrostatic conditions until the desired value is reached, and then the experiments began: the axial piston started to move at the applied constant strain rate of 0.001 mm/s and maintained throughout the entire experiments. Following this procedure meant that the samples deformed only when the axial piston was entering in contact with them. Confining pressure was kept constant. The tests were terminated once 9.5 mm of axial displacement was reached, as 0.5 mm were kept for safety to avoid any contact between the cylinders (Figure 3.30).

Time, axial displacement, axial pressure, differential stress, confining displacement, confining pressure and temperature were recorded all along the tests.

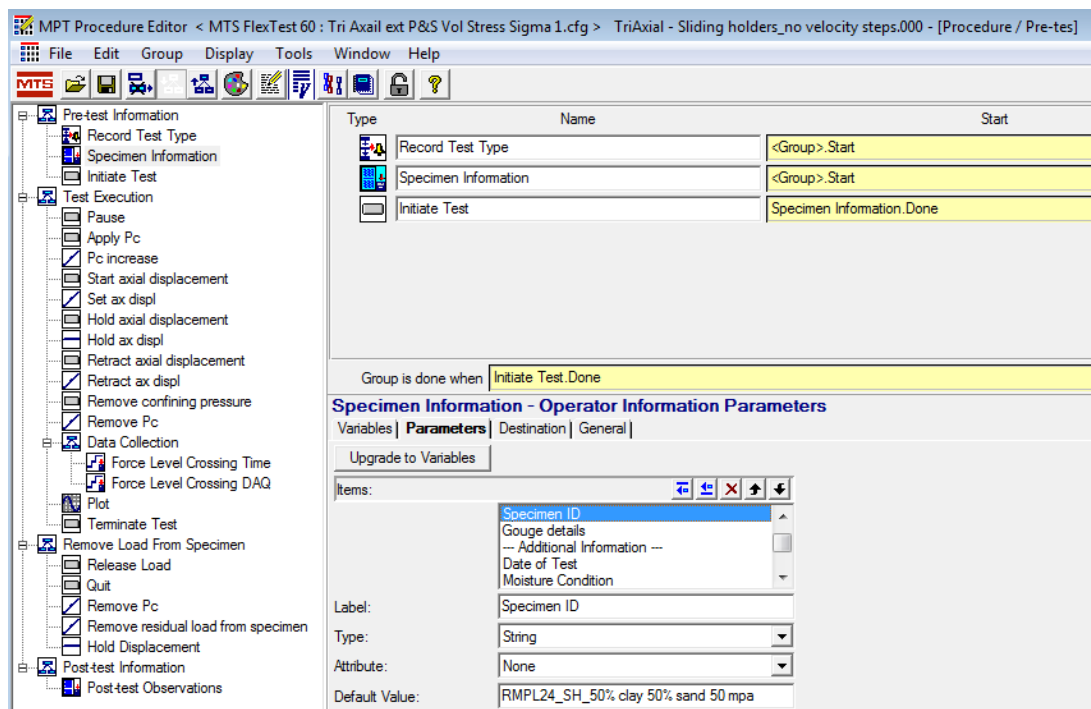


**Figure 3.30.** Screenshot of the interface showing the procedure followed for the constant strain rate experiments with MTS.

## Experimental procedure for velocity steps

The Velocity Steps procedure was thought to run at a constant strain rate of 0.001 mm/s up to 5 mm displacement, then a series of velocity changes were applied (Figure 3.31). The initial set-up of the experiment follows the same steps as specified beforehand. The velocity steps were:

From 0.001 mm/s to 0.01 mm/s – up-step at 5 mm displacement;

From 0.01 mm/s to 0.001 mm/s – down-step at 5.5 mm displacement;

From 0.001 mm/s to 0.1 mm/s – up-step at 6 mm displacement;

From 0.1 mm/s to 0.001 mm/s – down-step at 6.5 mm displacement;

From 0.001 mm/s to 0.01 mm/s – up-step at 7 mm displacement;

From 0.01 mm/s to 0.001 mm/s – down-step at 7.5 mm displacement;

From 0.001 mm/s to 0.1 mm/s – up-step at 8 mm displacement;

From 0.1 mm/s to 0.001 mm/s – down-step at 8.5 mm to 9 mm displacement.

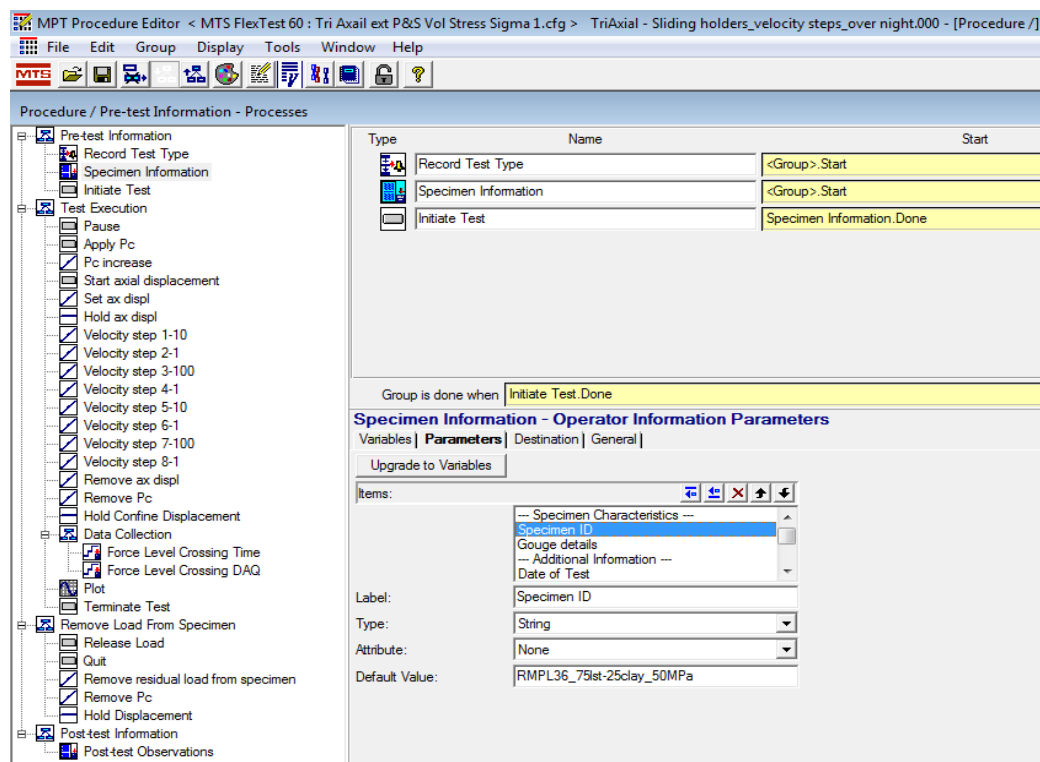


**Figure 4.24.** Screenshot of the PC interface showing the procedure followed for the dynamic friction experiments with MTS.

### Data correction and elaboration

As for the calibration tests calculations explained in section 3.6.2, this chapter, raw data obtained from each test need to be corrected. At the beginning of the test, the piston was retracted to not entering in contact with the sample and so to avoid undesired modification in the sample (i.e. accidental shearing if the piston touches the holder). When the vessel was closed and filled with the confining medium, the experiment began and the piston started to move down towards the assemblage. The computer was therefore registering an increasing displacement even if the true deformation stage was not started. For this reason, the zero point was set when the axial force values become positive digits, hence when the piston contacted the sample. Once the starting point was selected, the values for time, axial force, and displacement were subsequently corrected. The apparent friction coefficient  $\mu$  was calculated considering the ratio between the tangential force  $\tau$  and the normal load applied (e.g. [Lafaye et al., 2005](#)), considering zero initial cohesion. As mentioned previously, in this configuration the normal stress was  $\sigma_3$  and  $\tau$  was the axial load. The tangential force  $\tau$  was calculated dividing the axial load by the contact area, the latter calculated considering the time interval and the displacement recorded by the PC to obtain a true value of area displaced. For the analyses of the rate and state parameters (i.e.  $a$  and  $b$  respectively), each step of velocity is analysed using the MatLab code RsFit3000. The code is an interactive graphic user interface (GUI) created by [Skarbek and Savage, \(2019\)](#) that allows the calculation of the best fit for the values of  $a$ ,  $b$  and  $D_c$  (i.e. the latter is the critical slip distance required for steady state sliding). Introduced by [Dieterich, 1979](#) and [Ruina, 1983](#), the rate and state friction law is widely used to describe how friction coefficient  $\mu$  is dependent from velocity ( $v$ ) perturbations and other *internal* variables  $\theta_i$  (e.g. [Skarbek and Savage, 2019](#); [Marone, 1998](#)). In particular,  $a$  and  $b$  express the direct and evolution effect that is happening when the velocity is changed, hence how the friction coefficient responds to the change ( $a$ ) and how is the new steady state ( $b$ ), and  $D_c$  is the slip distance needed to attain a new steady state. Hence the friction coefficient is:

$$\mu = \mu_0 + a \ln (v/v_0) + \sum_i b_i \ln(\frac{v_0 \theta_i}{d_{ci}}) \quad (3.1)$$

To describe the evolution of the state variables, two equations are usually used. The aging law (1.5, Chapter 1, Section 1.4) (i.e. [Dieterich, 1979](#)), and the slip law (1.6,



Chapter 1, Section 1.4) (i.e. [Ruina, 1983](#)). RsFit3000 allows both the equations to be resolved (i.e. [Skarbek and Savage, 2019](#)).

### 3.7 Discussion: Advantages and Limitations

Direct shear configuration has been previously tested showing its efficiency (e.g. [Samuelson and Spiers, 2012](#); [Verberne et al., 2013](#)). However, usual dimensions for sliding holders are smaller than the dimensions required for the MTS Triaxial apparatus. It required the development of three generations of sliding holders to upscale properly the problems encountered. Here after, a list of advantages and limitations connected to the design.

#### Advantages

- MTS triaxial machine is capable to host samples of considerable size, and thanks to this characteristic, the machine can test contact surface larger than usual surfaces built for the direct shear setup.
- The size allows up to 10 mm of total displacement.
- The machine is equipped to be instantaneously responding to every change in confining pressure, and keeping a constant confining pressure throughout an experiment with increasing axial load with this configuration, is much easier than to do the same with a saw-cut configuration. Therefore, the values of  $\sigma_1$  and  $\sigma_3$  are more reliable in this configuration. As shown by [Samuelson and Spiers, 2012](#), the direct shear allows considering the confining pressure  $\sigma_3$  as the axial pressure  $\sigma_1$ , and the new  $\sigma_1$  remains constant throughout the experiments, without the continuous changes that the saw-cut configuration is experiencing.
- There is no surface loss as the experiments are progressing.
- The bigger size allows collection of considerable quantities of gouges for subsequent tests aimed to analyse microstructures and chemical variations.

#### Limitations

Being the first time in testing the direct shear configuration for MTS apparatus, few issues arose during calibration tests, gouges preparation and experiments.

- Silicone proved to be the best material to create the stoppers at the end of each slider, but it had a long cure time, requiring two weeks of preparation for each stopper. Two Teflon gasket were built to have the possibility to prepare two stoppers contemporaneously, and 10 stoppers were made to have enough of them in case of substitution.
- Natural samples of clay were sieved manually to avoid mechanical sieving, which could destroy clay minerals. The amount of clay gouges for each experiment was in the range from 3 g to 32 g, depending the mixture. Clay preparation was particularly time-consuming.
- Experiments containing 100% clay or a minor amount of clay, required long time to dry before the test. Every test containing clay took at least one day of preparation plus one day for the test.
- The entire assemblage was heavy, being each half cylinder  $\pm 1760$  g. When the gouges were positioned and pressed with the metal rig and oven dried, the sliding holder was closed with the other half cylinder and then manually rotated vertically in order to slide the entire assemblage inside the heat shrinking Teflon and keep everything together. The vertical position was mandatory to avoid imperfections in the heat-shrinking jacket, that could work as weak point when confining pressure was raising and therefore failure was more probably to occur. Unfortunately, this procedure was not the best approach and several times it caused loss of powder, despite the cohesion given by the alcohol and the initial pressure.
- A better transition from the gouge spreading to the closure of the assemblage was needed, and a vacuum chamber where to put the assembly and shrink the Teflon jacket without rotational movements it was the best solution but not applicable for there was no time to build a proper vacuum chamber.
- The procedure itself required time and numerous attempts to find the best way to handle the sliding holder, from the right material to use to build it, to how manage the powders in a way to not lose too much samples during preparations. This is normal when approaching a new procedure. Despite the great attention paid in each step, several times the procedure had to be stopped and began again in case of errors, to improve each time. The first chosen material used to build the sliding holder, even if with good mechanical properties, showed to be not

resistant enough in case of inconvenience, (i.e. grooves interlock). The second stainless steel revealed to be a better alloy, but again it failed the calibration test for the presence of the sintered disk chosen to cover the contact surface.

- The first sliding holder required nearly one year to be ready, the second six months and the third one, not provided of the pore fluid system and therefore less complicated, required only one month.

---

## ***Chapter 4 Results of Thermal Damage and Pore Pressure Effects on Comiso Limestone***

---

### **4.1 Introduction**

*Note: the following chapter reports the results obtained from the triaxial experiments on thermally treated and natural carbonate rocks, presented in a peer-to-peer published paper: Castagna, A., et al., Thermal Damage and Pore Pressure Effects of the Brittle-Ductile Transition in Comiso Limestone. Journal of Geophysical Research: Solid Earth, 2018, 123.9: 7644-7660. See Appendix D for the cover page and abstract.*

This chapter presents the results of the tests on ‘as-collected’ samples of CL, where nor pore fluid pressure or temperature treatment were applied. The first group of experiment was used as proxy to evaluate the deformation induced by pore fluid pressure and temperature on CL specimens heated and cooled before mechanical testing at room temperature (i.e. here called as ‘thermally treated sample’).

### **4.2 Results of the Thermal Treatment with High Temperature Furnace: Acoustic Emission and Ultrasonic Wave Velocities**

Figure 4.1 a shows the radial P-wave velocity ( $V_p$ ) of each specimen as a function of the increasing thermal treatment. Concentric reduction in specimen radial-velocities shows that the carbonate specimens remained isotropic even after the thermal treatment, and that overall velocities decreased with increasing maximum temperature. ‘As collected’ CL specimen had a radial P-wave velocity of 4.60 km/s (+/- 0.17 km/s) and was essentially isotropic (i.e. anisotropy < 4 %). The change in P-wave velocity following the 150 °C thermal test was negligible, and it remained at approximately 4.60 km/s overlapping the room-temperature specimen curve, therefore it was not reported.

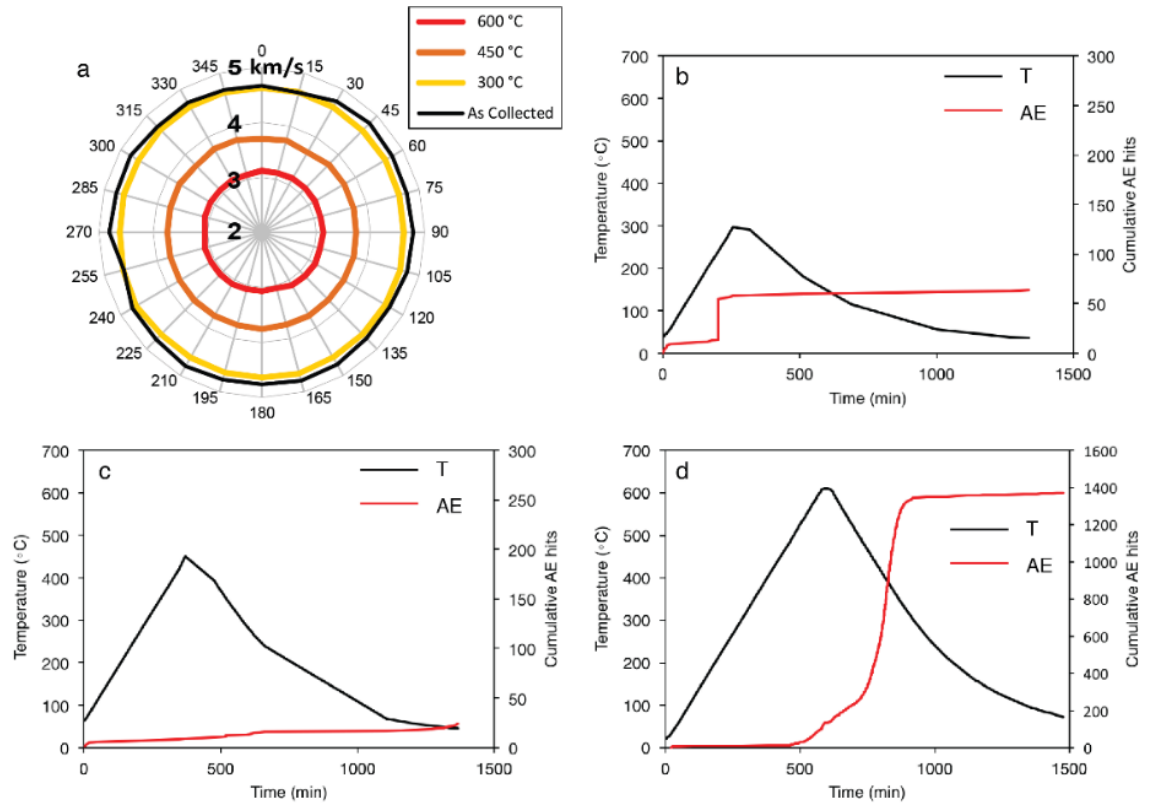


**Figure 4.1.** a) Radial ultrasonic P-wave velocities (km/s) as measured across the diameter of a cylindrical specimen at 15° increments. The thick black line represents the untreated (i.e., as-collected) specimen, reporting a P-wave velocity of 4.60 km/s. Lines represent the P-wave velocities as measured with increasing thermal temperature treatment. (b), (c) and (d) represent the contemporaneous acoustic emission output recorded during the thermal treatment at 300 °C, 450 °C and 600 °C respectively. Note the change of scale in cumulative AE hits in part d.

P-wave velocities decreased by approximately 5% to 4.26 km/s following heat treatment to 300 °C, and by 22 % to 3.55 km/s, following heat treatment to 450 °C. Following the 600 °C thermal stressing test, P-wave velocities decreased by approximately 37 % to 2.83 km/s (i.e. red line, Figure 4.1 a). Figure 4.1 b, c and d show AEs outputs for tests heated to 300 °C, 450 °C and 600 °C. AEs output was negligible in the 150 °C test and therefore it was not added. In tests performed to maximum temperatures of 300 °C and 450 °C, the AEs output was similar in terms of amplitude (i.e. size of individual AE hits) and number of AEs hits. In both cases the total amount of AEs hits is low (i.e. <1000 events). Tests with a maximum temperature of 600 °C show substantial AEs output (Figure 4.1 c). The rate and amplitude of AEs hits increased substantially at approximately 480 minutes and 500 °C in heating, and

continued to produce AEs at a similar rate and size on cooling. The total AEs hits recorded in the 600 °C test exceeded 1000 events.

#### 4.2.1 Triaxial test: dry conditions on ‘as collected’ specimens

Figure 4.2 a, b and c shows the results from deformation experiments conducted on ‘as collected’ specimens of CL under dry conditions, at room temperature (22°C), with increasing levels of  $P_{\text{eff}}$  (i.e. 7 MPa, 15 MPa, 30 MPa, 50 MPa) representing increasing depth.

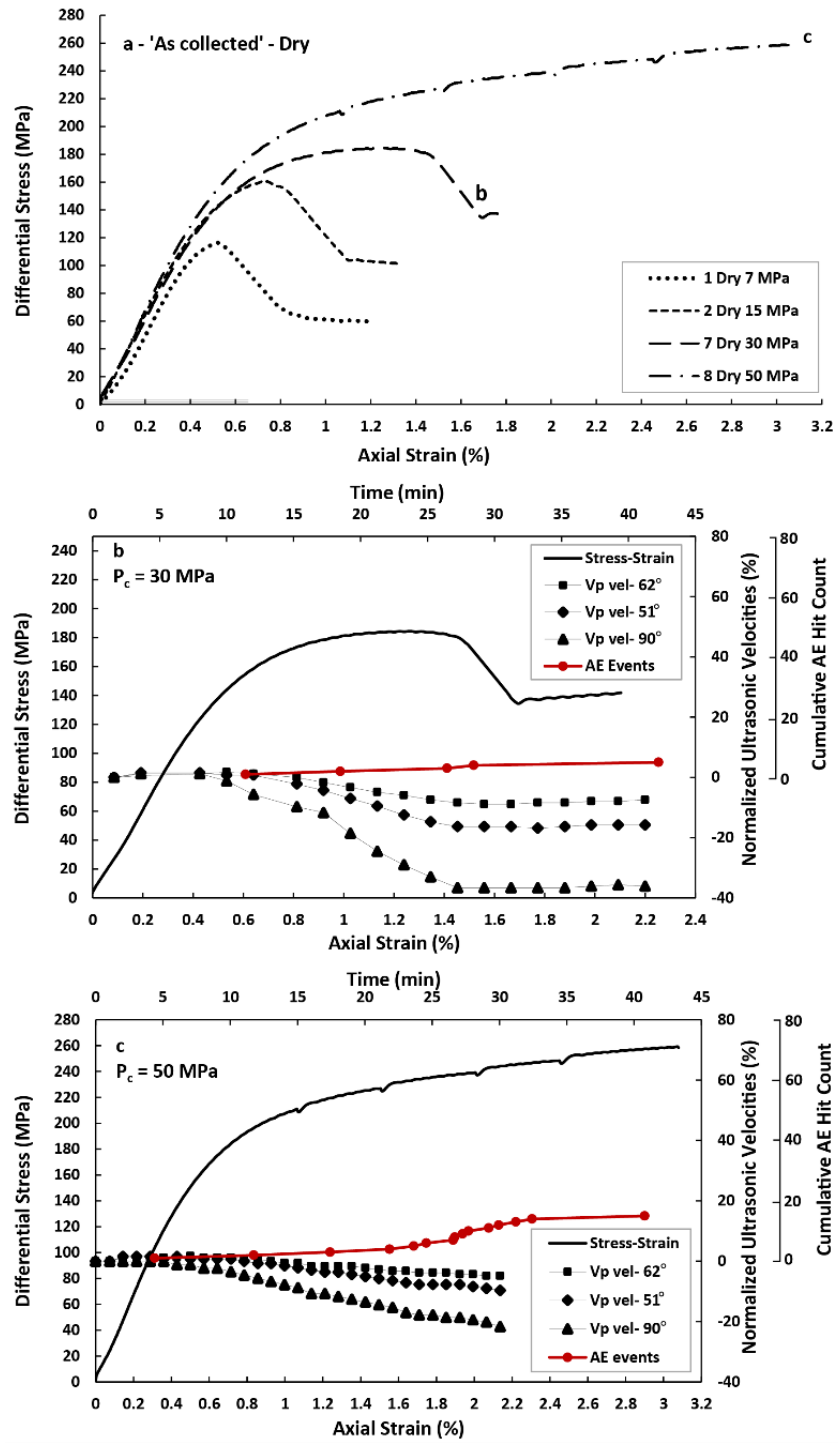


**Figure 4.2.** (a-b-c). Triaxial test results in dry conditions, for non-thermally-treated specimens. (a) Differential stress versus axial strain, as a function of increasing confining pressure. (b) and (c) are stress-strain plots with corresponding, normalized, ultrasonic velocities along three representative directions, and cumulative AEs hit count (red line) for the test conducted at (b) 7 dry, 30 MPa and (c) 8 Dry, 50 MPa effective pressure, respectively. In 4.2 c,  $P_c$  increased in steps of 5 MPa in the attempt to check for changing behaviour in the ductile response as a



*function of burial depth, using the same experimental setup. The increasing  $P_c$  steps resulted in small differential stress ‘bumps’ in the stress-strain curves, but no changes.*

In the mechanical data it was present a typical evolution from the brittle to the ductile regime as effective pressure increased beyond 30 MPa. Ductile behaviour was clearly present at 50 MPa, here defined as the capacity of the rock to undergo substantial strain without developing a microscopic fracture (i.e. [Paterson and Wong, 2005](#)) or loss of strength (i.e. [Bakker et al, 2015](#)). The two tests conducted at 50 MPa confining pressure exhibited small ‘bumps’ in the stress-strain curve. These represented steps of increasing confining pressure (i.e. each step an increase of 5 MPa). In all cases and across higher effective pressures, the specimens attained substantial strain without the development of a macroscopic shear fracture. All tests showed an initial stage of strain hardening due to the closure of pre-existing cracks and/or pores (e.g. [Baud et al 2000a](#); [Nicolas et al, 2016](#)) followed by linear elastic behaviour. Experiments 1, 2 and 7 dry attained peak stresses at 116.23 MPa, 160.59 MPa and 184.41 MPa, respectively, followed by strain softening and brittle failure (Figure 4.2 a and Table 3.3, Chapter 3, Section 3.5). To understand better the accommodation of deformation at the brittle to plastic (BP) transition, figures 4.2 b and c additionally plot the details of experiment 7 Dry at 30 MPa, and experiment 8 Dry at 50 MPa, respectively. Normalized  $V_p$  and cumulative AEs hit rates are added to the graphs.

At  $P_c = 30$  MPa (Figure 4.2 b), the  $V_p$  velocities increased up to 1.52 % at 0.2 % axial strain. Then, they started to decrease at the onset of inelastic deformation at 0.4 % axial strain leading towards failure where the velocities reached a minimum. The most marked decreases in velocity were in the 3N-3S and 3E-3W directions, both at 90° respect to  $\sigma_1$ , corresponding to the directions travelling through the centre of the specimens. After failure, velocities remained steady between -8 to -35% below initial values; this directional variation in  $V_p$  represented a significant anisotropy. AEs cumulative hit rate increased steadily during deformation and strain accommodation, showing a marked increase from the time of stress drop (i.e. dynamic failure), although only a small number of AEs events was recorded.

At 50 MPa of  $P_c$  (Figure 4.2 c), a ductile behaviour set the BD transition somewhere between 30 and 50 MPa. The elastic-wave velocity data showed dependence with the orientation of the travelling directions. It was present an initial increase up to 1.55 % in the direction at  $62^\circ$  and  $51^\circ$  to  $\sigma_1$  at 0.2 % axial strain, whereas there was no increase for the ray-path at  $90^\circ$ . For the first two ray-paths, the velocities started to decrease after the elastic accommodations reached values of -5 % and -10 %, respectively. The ray-path at  $90^\circ$  showed a continuous decreasing velocity to a minimum of -21.7 %. The  $V_p$  velocities presented a lower anisotropy than test at 30 MPa  $P_c$ . Cumulative AEs data showed a slow increase initially, which accelerated towards the end of the experiment.

#### 4.2.2 Triaxial test: drained saturated conditions on ‘as collected’ specimens

Figure 4.3 d, e and f presents data in drained saturated conditions. There are several notable differences in stress-strain accommodation compared to tests in dry conditions. Experiment 1 and 2 Sat attained a peak stress at 105.09 MPa, 0.76 % axial strain, and at 133.49 MPa, 1.01 % axial strain, respectively, followed by strain softening. The peak stresses were lower, between 5% and 20% MPa less when compared to dry conditions at equivalent effective pressure (cf. Figure 4.2 a). Young’s modulus values were also lower in saturated conditions (Table 3.3, Chapter 3, Section 3.5), and in general there was significantly more total strain accommodation before failure (i.e. such as the case of  $P_{eff}=7$  and  $P_{eff}=15$  MPa). At  $P_{eff}=30$  MPa, the specimen accommodated strain hardening up to 1.5% axial strain, where a small stress drop was recorded. At 50 MPa the specimen was dominated by ductile deformation. The BD transition was again between 30 MPa and 50 MPa  $P_{eff}$ . AEs data were not reported for the experiments in figures 4.3 e and f, as the number of events was negligible.

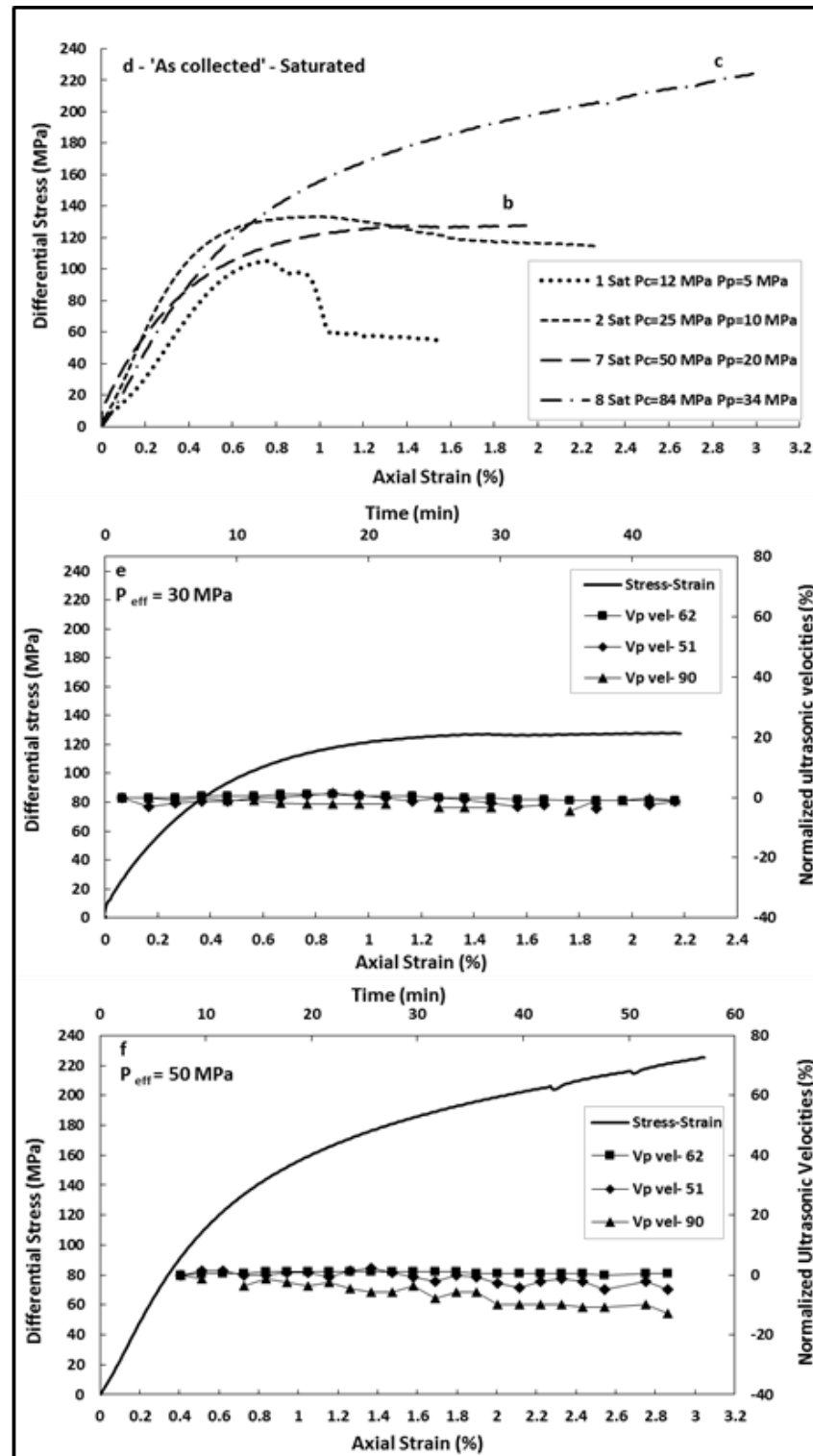


**Figure 4.3.** (d-e-f) are the triaxial test results in drained, saturated conditions, for non-thermally-treated specimens. AE hit count it is not reported as the event rate is too low. In the final tests (Figure 4.3 f),  $P_c$  increased in steps of 5 MPa in the attempt to check for changing behaviour in the ductile response as a function of burial depth, using the same experimental setup. The increasing  $P_c$  steps resulted in small differential stress 'bumps' in the stress-strain curves.

The transition from brittle to ductile behaviour along with normalized  $V_p$  was reported in figure 4.3 e and f using data from experiment 7 Sat,  $P_{eff} = 34$  MPa, and experiment 8 Sat,  $P_{eff} = 54$  MPa, respectively. At  $P_{eff} = 30$  MPa the behaviour was characterized by strain hardening until brittle failure but the stress drop was barely discernible but present at 1.5 % strain. Post-mortem macroscopic inspections revealed the presence of wedge splitting along with several conjugate fractures (see supporting material). The P-wave elastic velocity data remained essentially constant throughout the experiment. The level of velocity anisotropy was low, with a range from -1 % to -5 % velocity decreasing towards the end of the experiment.

At higher  $P_{eff} = 50$  MPa (Figure 4.3 f), the divergence from elastic to plastic behaviour started at 70 MPa differential stress or 0.3% strain, about 20 MPa less than the data reported in figure 4.2 c. Similar trends were seen with regards to  $V_p$  with in general small decreasing trends for the velocities oriented at  $62^\circ$  and  $51^\circ$  to  $\sigma_1$ , finally resulting in anisotropy values ranging between 0 % and -5 %. The ray-path travelling perpendicular to  $\sigma_1$  was the most affected decreasing of an amount of 13% The overall anisotropy was lower than the anisotropy recorded in the dry test (i.e. 8 Dry, Figure 4.2 c).

#### 4.2.3 Triaxial tests: dry conditions on thermally treated specimens

Figure 4.4 a shows mechanical results from triaxial experiments run at room temperature on previously thermally treated CL. Here, a constant confining pressure was maintained at 15 MPa to investigate only the influence of the heat treatment, ranging from untreated (i.e. ‘as collected’) to 600 °C. All the specimens reached the same peak stress (i.e. 160-162 MPa) before failure regardless the thermal treatment with the exception of the specimen at 600 °C, which failed at 138 MPa peak stress. The stress-strain curves remained similar until experiment 5 Dry (i.e. treatment at 450 °C). At 600 °C, the behaviour started to be weaker and in fact the Young’s modulus was markedly lower compared to specimens treated at lower temperatures (see Table 3.3, Chapter 3, Section 3.5). The trend in total strain at failure was likewise tied to the thermal treatment, with a tentative increase in the percentage strain at failure with increasing temperature, but a clear behavioural variation was observed beyond 450 °C. Conversely, the stress drop itself appeared to be constant (i.e. between 60 to 80 MPa) with the thermal treatments.

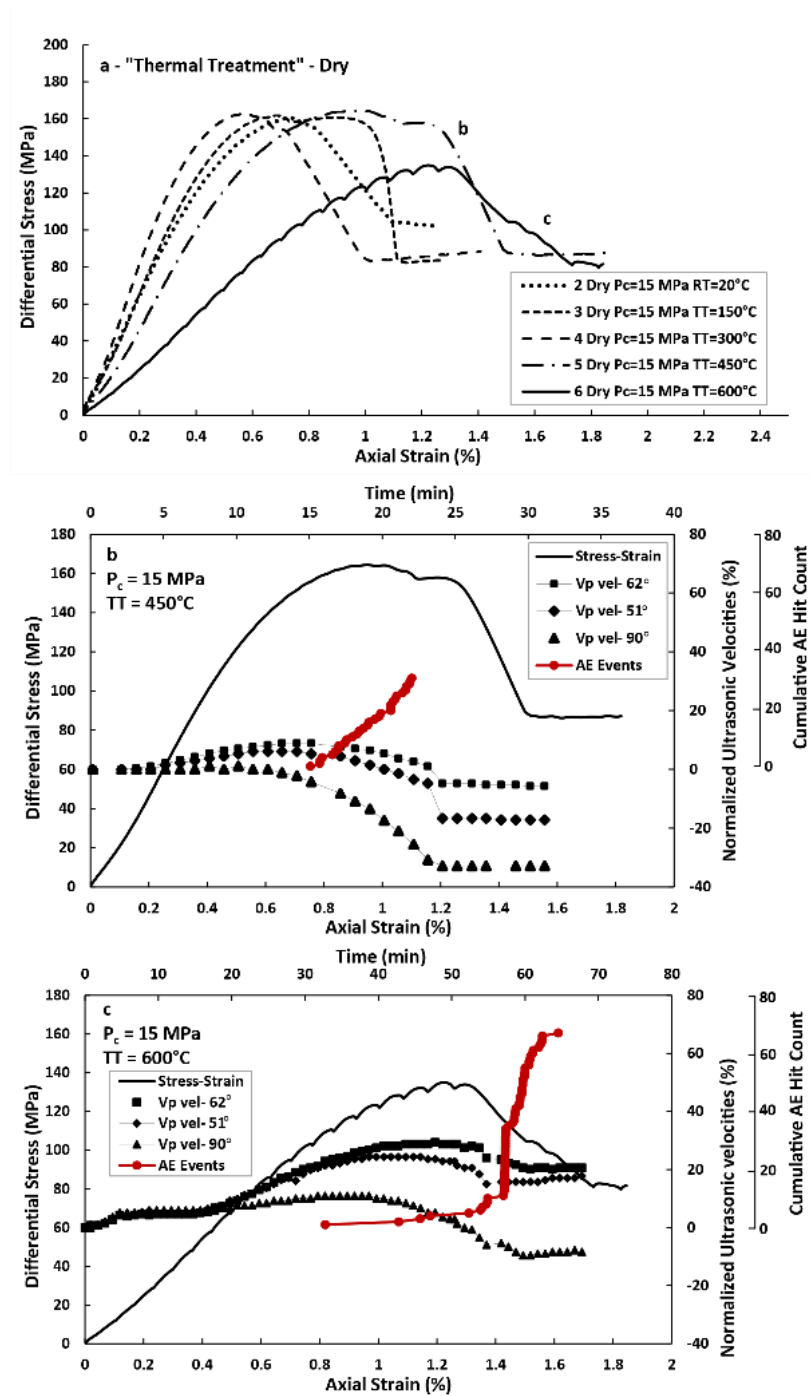


**Figure 4.4.** (a-b-c). Triaxial test results in dry conditions for thermally-treated specimens, at a constant 15 MPa effective pressure. (a) Differential stress versus axial strain, as a function of maximum thermal treatment temperature (see inset key). (b and c) Stress-strain plots with corresponding, normalized ultrasonic velocities along three representative directions, and cumulative AE hit count (red line) for the test conducted on specimens treated to (b) 5 Dry, 450°C and (c) 6 Dry, 600°C. Note the initial increase in ultrasonic velocities in c) across all raypaths likely indicating thermal induced micro-cracking, followed by velocities reduction corresponding to an increase in AEs hit count.

Figures 4.4 b and 4.4 c show details of normalized  $V_p$  and AEs hit rates for the highest thermal treated specimens at 450 °C and 600 °C. For experiment 5 Dry (i.e. 450 °C), the initial strain accommodation preceded elastic accommodation until approximately 80 MPa, 0.3 % axial strain. After the peak stress occurring at 0.9 %, the specimen entered a strain-softening phase, with a complex strain-softening behaviour. In comparison to the ‘as collected’ specimens, where ultrasonic velocities showed a small increment at the beginning of the experiments, here  $V_p$  data showed an overall trend of higher velocities for the dry experiments prior to failure. For the 450 °C treated specimen, velocity data indicated a significant velocity anisotropy developing prior to failure, with velocities ranging from +8 % to -4 %. The most affected ray-path once again was at 90° to  $\sigma_1$ , suggesting the formation of axial fractures opening perpendicular to  $\sigma_1$ . For the specimen treated to 600 °C, the behaviour appeared similar. However, specimens strength was affected by the prior thermal treatment. In the specimen treated to 600 °C, the peak stress occurred at 1.22 % axial strain and 134 MPa differential stress compared to the specimen treated at 450 °C, where the peak stress occurred at 0.94 % axial strain and 164 MPa differential stress (Figure 4.4 c). In both cases, the specimens developed a localized shear fracture. Also, in both cases, AEs hit rate started to increase dramatically when approaching the peak stress and failure, with a supra-exponential trend evident for the specimen treated to 600 °C, whilst the specimen treated to 450 °C had a more linear trend.

#### 4.2.4 Triaxial tests: drained saturated conditions on thermally treated specimens

Figure 4.5 a, b and c show the stress versus strain results for thermally-treated specimens in saturated, drained conditions.

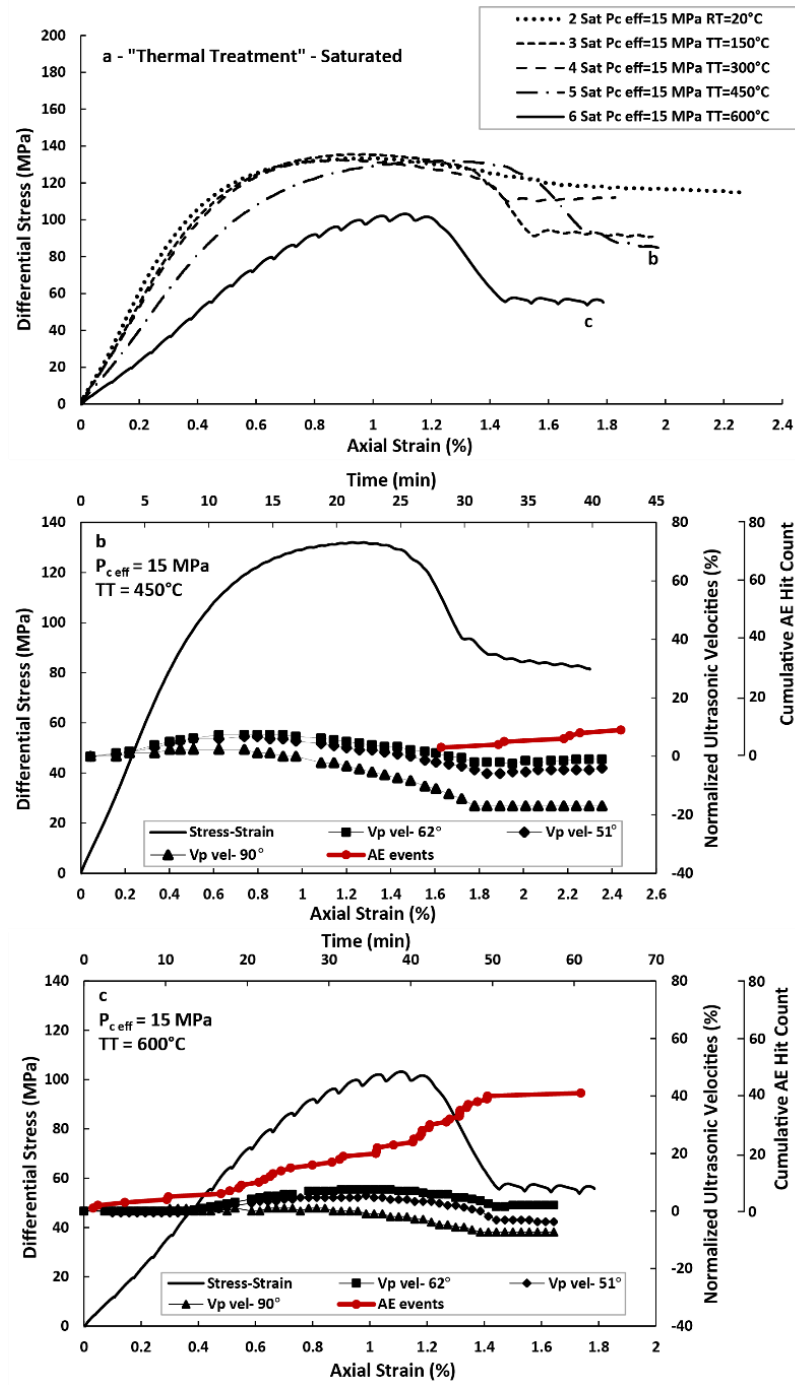


**Figure 4.5.** (a-b-c) are the triaxial test results in drained, saturated conditions for thermally-treated specimens, at a constant 15 MPa effective pressure.

Peak stresses were lower across all specimens of about -30 MPa in all the experiments compared to dry deformation (for comparison, see figure 4.4 a and table 3.3, Chapter 3, Section 3.5). The stress-strain paths were virtually identical with a maximum strain value of 1.4 % at failure. Saturated conditions for the thermal treatment at 450 °C showed an increase in the percentage of strain accumulated at failure of 1.5



% and a slightly lower peak stress of 130 MPa. The presence of pore fluid pressure along with the thermal treatment at 600 °C resulted in a significant change in peak stress and stress-strain path, with strain at failure of 1.2 % and peak stress of 100 MPa. In all cases, the strain accommodated before the peak stress and before failure resulted significantly increased relative to tests in dry conditions (Figure 4.4 a). Specimens showed a systematic decrease in the static Young's modulus with increasing thermal treatment temperature. Focusing on the transition from 450 °C (Figure 4.5 e) to 600 °C (Figure 4.5 f), in both experiments an initial increase in  $V_p$  was recorded followed by a decrease, occurring at approximately 0.8 % strain for 450°C and approximately 1 % for 600 °C. As was the case for dry experiments, the normalised velocity increased initially with deformation from 0% to +7% in both cases, and ultimately giving anisotropy values ranging from -4 % to -16 % (i.e. 5 Sat, 450 °C) and +2 % to -10 % (i.e. 6 Sat, 600 °C). For experiment 5 Sat, AEs cumulative hit rate showed few events before yield and failure whereas the AEs hit rate for experiment 6 Sat showed a significant AEs hit count compared to the previous experiment from the beginning of the deformation, which increased discontinuously until the stress drop occurs.

### 4.3 Discussion

#### 4.3.1 Mechanical behaviour of dry and saturated specimens 'as collected'

For dry, 'as collected' specimens it is evident that a classical brittle to ductile behaviour started to evolve when crossing a threshold confining pressure of approximately 30 MPa. The transition is a steadily flattening and widening pre- and post-peak behaviour in the stress-strain curve. For dry experiments at 30 MPa, the amount of strain accommodated at peak stress is 1.26 %, considerably higher than that at 15 MPa (i.e. registered at 0.73 %). At 50 MPa, the behaviour is in ductile regime and the experiments show that strain hardening is generally insensitive to confining pressure increases (i.e. the jumps in the differential stress due to  $P_c$  increase). [Bakker et al., 2015](#) show that for CL at 50 MPa confinement and  $10^{-5} \text{ s}^{-1}$  strain rate, the specimen reaches peak stress at 370 MPa of differential stress sustaining 1.8 % axial strain, with strain softening behaviour before failure. However, reviewing the specimen descriptions of [Bakker et al., 2015](#), it is evident that they use a more dolomitic material, compared with CL specimens. At the same confining pressure, the specimens used in this study are already within the ductile regime. [Nicolas et al., 2016](#) conduct dry

experiments on Tavel Limestone, at the same constant axial strain rate and room temperature, which exhibits brittle behaviour for confining pressures up to 55 MPa. They find that for  $P_c \geq 70$  MPa the behaviour transitions to a semi-brittle regime, defined as a coupled plastic deformation and induced damage (i.e. [Evans et al., 1990](#)). The brittle-ductile transition is occurring at confining pressures above 30 MPa for the specimens here presented, tested at room temperature and without thermal treatment. The reason of such lower threshold for the BDT transition is likely due to the larger grain size of CL compared to Tavel limestone (see [Nicolas et al., 2016](#) and [Vajdova et al., 2004](#); [Vajdova et al., 2010](#) for more details about Tavel limestone). As porosity and grain size increase, the brittle to cataclastic flow transition can occur at lower confinement (e.g. [Wong and Baud, 2012](#)).

In saturated conditions, [Nicolas et al., 2016](#) find that water has a weakening effect lowering the peak stresses at which dilatancy occurred. In the water-saturated experiments here discussed, the response of CL changes already at  $P_{eff} < 30$  MPa: water lowers the mechanical strength, decreasing peak stresses and promoting strain softening as seen for experiments 1 and 2 Sat (Figure 4.3 d). [Baud et al., 2000b](#) explain the reduction of sandstone brittle strength in presence of water integrating the Orowan's generalization of the Griffith-Irwin equilibrium concept (i.e. [Lawn, 1993](#)) in a sliding wing crack model. This generalization sees the chemical influence of the fluids that weakens the rock through reduction of the free energy surface that is creating adhesion, or in other terms, fluid molecules enter the cracks and are adsorbed at the interface walls of the cohesion zone lowering the energy surface and promoting reduction of strength. Here most of the brittle damage measured is controlled by micro-mechanisms at the grain-scale, as demonstrated by the amount of AEs recorded during deformations. Water molecules can have lowered the micro-crack interface energy on entering and adsorbing onto the walls in the cohesion zones, diminishing the stress intensity in the saturated limestone samples compared to the dry conditions. Experiment 7 Sat at  $P_{eff} = 30$  MPa undergoes strain hardening until the deformation localized, resulting in wedge splitting and conjugate fractures localized in the upper part of the sample. At  $P_{eff} = 50$  MPa the behaviour of CL (experiment 8 Sat) is in the ductile regime, presenting strain hardening insensitive to increasing confining pressures (Figure 4.3 f). As highlighted by previous studies, ultrasonic wave velocities and AEs are both sensitive to inelastic damage, what could be crack nucleation and/or propagation under sufficiently high

differential stresses (e.g. [Browning et al., 2017](#) and reference therein).  $V_p$  velocities are decreasing as crack damage is increasing. The behaviour of the recorded ultrasonic velocities for the experiments here presented (Figure 4.2 a) is reflecting the previous findings. The  $V_p$  velocities increase at the beginning of the tests when differential stress is applied, because of closure of pre-existing micro-cracks (e.g. [Browning et al., 2017](#)). The change in velocities at the onset of inelastic accommodation depends on the direction of the considered ray-paths. In general, the most affected direction showing the higher anisotropy is the ray-path oriented at  $90^\circ$  respect to  $\sigma_1$ , where the travelling distance of the seismic waves is across newly generated fractures. Encountering a high density of micro-cracks at a high incidence angle is consistently demonstrated in the data set here presented, and it is in common with other studies (e.g. [Harnett et al., 2018](#)).

#### 4.3.2 Effects of thermal treatment on Comiso Limestone strength

Pre-deformation thermal treatment has an influence on the rock mechanical properties. XRPD analyses on powders of specimens treated at  $600^\circ\text{C}$  reveals the presence of Portlandite (Figure 4.6).

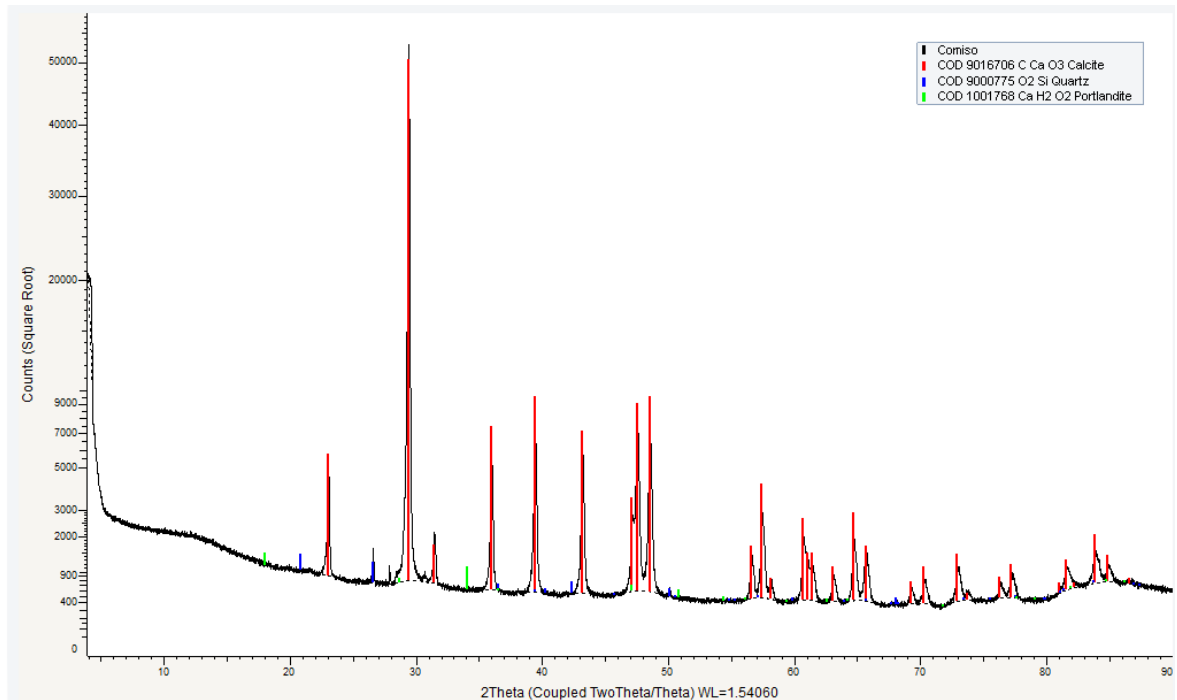


**Figure 4.6.** XRPD for CL sample after temperature treatment at  $600^\circ\text{C}$ . Portlandite was highlighted in green.

As reported by [Heap et al., 2013](#), Portlandite is a calcium hydroxide which is the result of the combination of CaO (i.e. product of decarbonation) with water in the atmosphere after the thermal treatment, according to the formula  $\text{CaO} + \text{H}_2\text{O} = \text{Ca}(\text{OH})_2$ . As this is an exothermic reaction, it provokes an increase in volume that affects the specimens even further. Decarbonation is therefore reported to be one of the cause of strength weakening (e.g. [Heap et al., 2013](#); [Mollo et al., 2011](#)). A collection of SEM images of the thermally treated specimens is in Figure 4.7 below, showing a positive correlation between porosity and increasing temperature.

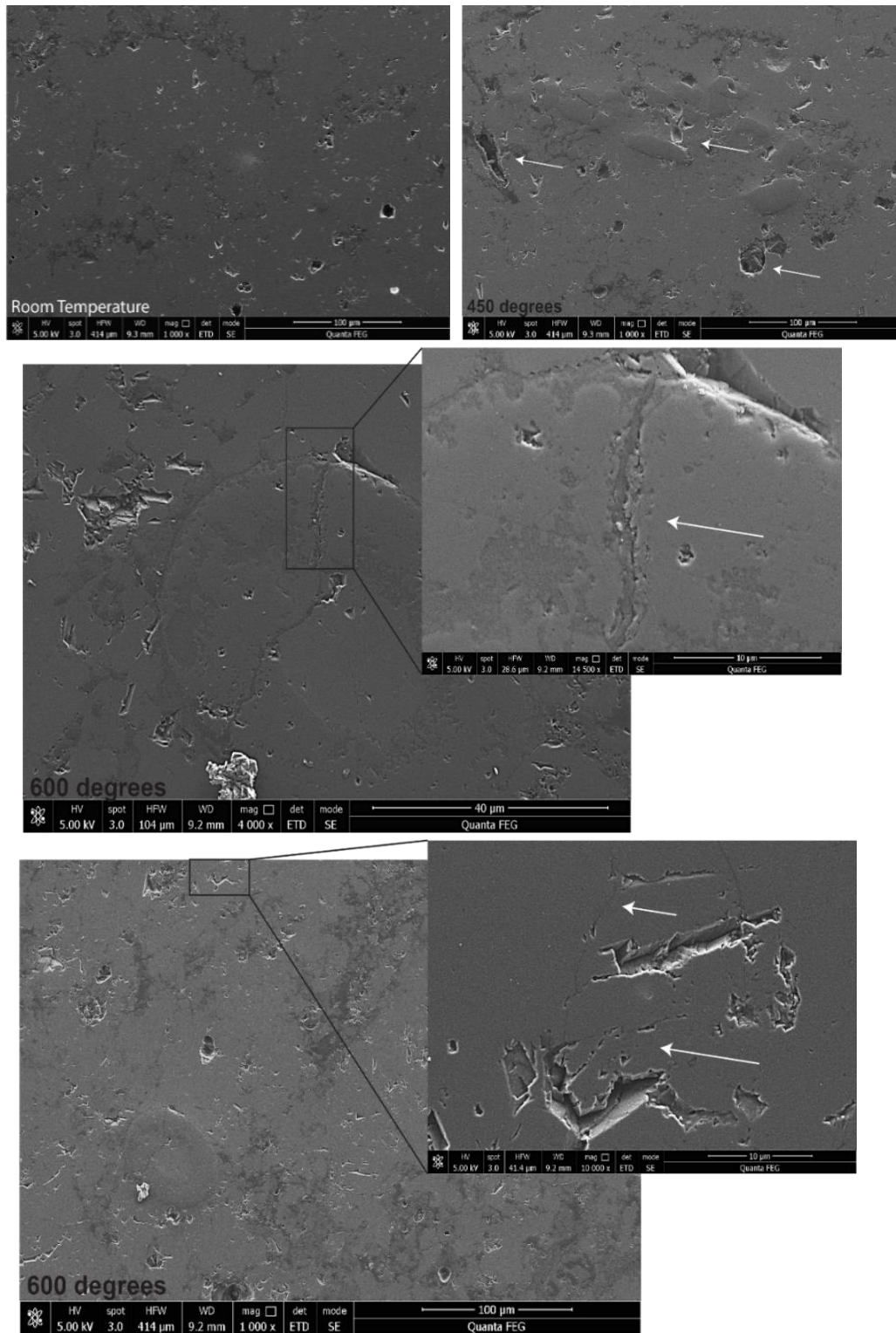


**Figure 4.7.** SEM-SE images of CL at increasing thermal treatment, from a) room temperature, b) 450 °C to c)-d) at 600 °C. a) At room temperature the SEM inspection highlights the presence of numerous pores of few microns and only few up to  $\leq 50 \mu\text{m}$ . b) At 450 °C, a trend is visible showing an increased pore sizes, with numerous pores at  $30 \leq \mu\text{m} \leq 50$ . At 600 °C c) and d) micro-cracks radiates from the pores connecting newly-formed/existing pores.

Amongst the results found by [Heap et al., 2013](#), a few comparisons can be made between CL and MCL (Monte Climiti Limestone - 100% calcite). In uniaxial compression tests, the MCL specimens that are previously thermally treated up to 800 °C, show no variation in strength up to 500 °C, with a peak stress at 0.3 % axial strain, the latter kept constant at  $1.0 \times 10^{-5} \text{ s}^{-1}$ . For  $500 \text{ °C} < T < 650 \text{ °C}$ , the strength shows no variation but the specimens attains the peak stress at 0.6 % axial strain. As [Heap et al., 2013](#) highlight, the addition of  $P_c$  results in a reduction of the temperature required to switch to a ductile flow. [Bakker et al., 2015](#) and [Nicolas et al., 2016](#) perform triaxial experiments on CL and Tavel Limestone respectively, and both apply *in situ* temperatures while deforming. [Bakker et al., 2015](#) find the Young Modulus to be insensitive of  $P$ , but sensitive to  $T$ , decreasing from 34 GPa at 20 °C to 16 GPa at 600 °C. The CL specimens here tested show a decrease from 28.7 GPa at 20 °C to 12 GPa in the samples pre-treated at 600 °C. [Nicolas et al., 2016](#) conduct experiments of Tavel Limestone at 70 °C, finding an overall reduced strength, but with the brittle to semi-brittle transition occurring at a lower confinement: between 35 and 55 MPa, in dry conditions. Conversely, the experiments run at  $P_c = 50 \text{ MPa}$  of [Bakker et al., 2015](#), show a BD transition at  $350 \pm 50 \text{ °C}$ . The collected data, although at different pressure and temperature conditions, support the idea that the presence of elevated temperatures can impress the limestone microstructure (i.e. thermal damage) by lowering its mechanical strength; this is true either when elevated temperatures are present during mechanical deformation or when elevated temperatures are present before.

The pre-test thermal treatment on CL illustrates an underlying thermal damage that is only partially characterised by AEs output: at 150 °C, CL does not show any significant AEs output or damage, supported by unchanged P-wave velocities. Low AEs counts in the 300 °C – 450 °C thermal stressing tests would also, apparently, indicate the absence of significant damage, however P-wave velocities decrease by up to 17 % over this temperature range (Figure 4.1 a, b and c), indicating indeed that thermal damage is present. The interpretation is that these temperatures induce thermal damage but, likely, the low AEs output is indicative of the natural variability of these carbonate rocks. At 600 °C (Figure 4.1 a and d), the number of AEs increases dramatically along with a consistent  $V_p$  decrease. At this temperature, different mechanisms of thermal damage can be activated, such as decarbonation and quartz  $\alpha$  to quartz  $\beta$  transition (i.e. 573 °C, ambient  $P$ : [Tuttle, 1949](#)) the latter corresponding to



increasing volume. Elastic P-wave anisotropy measurements further confirm the development of a pervasive fracture damage, extended and promoted by the thermal treatment. The consistent nature of the peak strength of the thermally treated materials results obtained during the triaxial tests at room temperature is thought to be due to the previous heat treatment, which promotes inter-granular cracking (e.g. [Fredrich and Wong, 1986](#)). This consistent inter-granular cracking locks the overall specimens to give a consistent strength, but with additional heating, it allows a higher total strain at failure, as seen in the data (Figure 4.2 a). This influence extends in dry and saturated conditions, where the peak strength is at 160 MPa, between 0.57 % and 0.91 % axial strain and 130 MPa and 0.67 % to 1.22 % axial strain, respectively. Whilst the seismic anisotropy reaches a maximum of 15 % (i.e. span ranging from -3 % to -18 %) for dry untreated specimens, this increases to 30 % (i.e. span +10 % to -20 %) after thermal treatment to 600 °C. The effect is subdued when water is present, increasing from 10 % (i.e. 0 % to -10 %) to 17 % (i.e. +7 % to -10 %) due to thermal stressing, with the lower anisotropy providing further evidence of crack fabric, but this time filled with pore fluid that seek to lower the effective elastic wave speed (e.g. [Mavko et al., 1998](#)). The AEs trend shows indeed an increment in the final output for the thermally treated specimens, whereas for the as collected specimens the trend is slightly flat and homogeneous throughout the experiments. Overall, with respect to the previous triaxial experiments run with *in situ* temperature, the pre-test thermal treatment assumes here a different point of view. An *in situ* experiment aims to reproduce either a condition in depth or the presence of a magmatic body close to the rocks at the same time of the deformation. On the other hand, triaxial tests at room temperature run on specimens previously treated and confined at modest pressures to represent depth aim to reproduce a common situation in volcanic environment: the intrusion of magma bodies that causes deterioration of the country rocks in the shallower level of the basement. Once deteriorated, these rocks would be more prone to fail and accommodate structural deformation that are of fundamental importance in the overall stability of the edifice.

#### 4.3.3 Brittle-ductile transition

To provide a macroscopic description of the brittle-ductile transition, the data from all the tests are plotted in strength versus  $P_c$  space (e.g. [Kohlstedt et al., 1995](#)) (Figure 4.8). For those experiments that produce ductile behaviour, the strength is taken



consistently at a threshold of 2 % axial strain. Byerlee's Rule (i.e. black solid line) and the Goetze's Criterion (i.e. black dotted line) delimit the brittle region from the semi-brittle region (Figure 4.8).

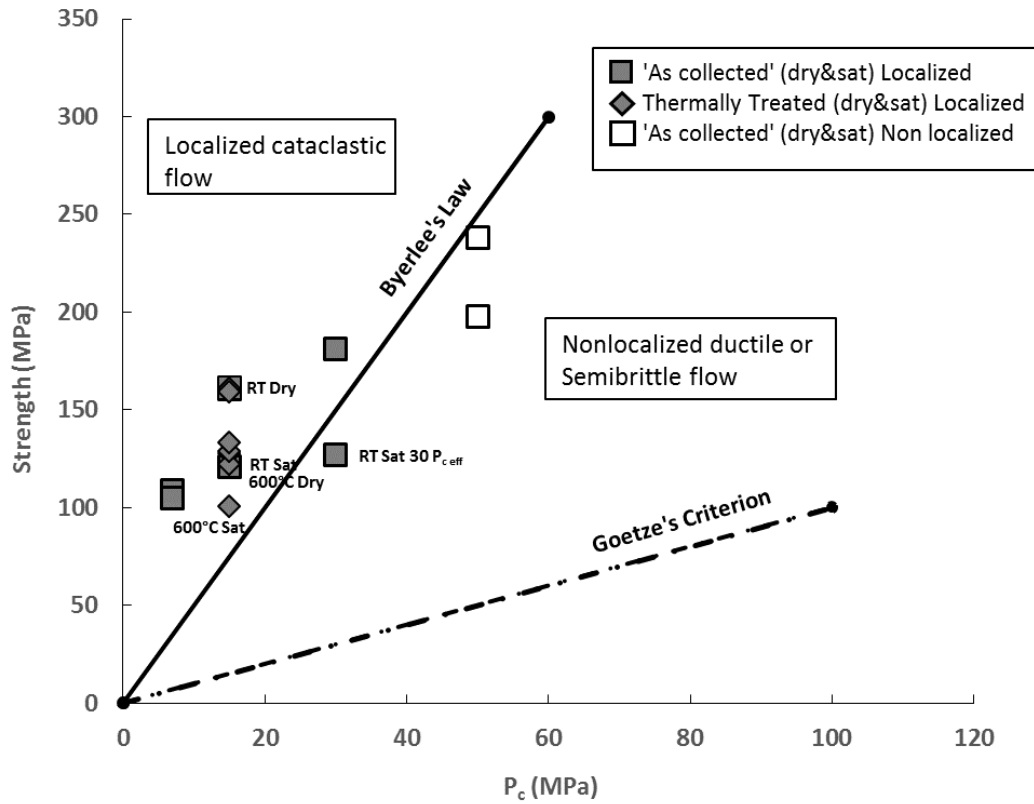


**Figure 4.8.** Experimental results plotted on a strength vs  $P_c$  plot. In this graph, the end-member results for dry ‘as collected’ and dry, thermally treated at the maximum temperature (i.e. grey square), as well as saturated ‘as collected’ and saturated, thermally treated at the maximum temperature (i.e. grey diamond) are reported with a label. As these experiments are run at the same confining pressure (i.e.  $P_{c\text{ eff}} = 15$  MPa), it is possible to note as both temperature and water have a weakening effect on the strength of CL. As the temperature of the thermal treatment increase and water is present, the CL is moving closer towards the transition from brittle to semi-brittle behaviour. In this graph it is labelled the experiment 7 Sat, that is characterized by a marked overall semi-brittle behaviour with a barely discernible brittle failure. White square indicates the experiments 8 Dry and 8 Sat, run at the maximum confinement pressure chosen (i.e.  $P_{c\text{ eff}} = 50$  MPa) and falling into the ductile region.

Most of the experiments concentrate in the brittle region, which is characterized by localized cataclastic flow. In figure 4.8, the end-members dry ‘as collected’ and dry thermally treated (i.e. 600°C) samples (i.e. grey square in figure 4.8), as well as

saturated ‘as collected’ and saturated, thermally treated (i.e. 600°C) samples are reported (i.e. grey diamond in figure 4.8). The experiment 6 Dry (i.e. labelled 600 °C Dry, grey diamond in figure 4.8) attains a strength comparable to that of experiment 8 Sat (i.e. labelled RT Sat, grey square in figure 4.8), run at the maximum confinement here considered in saturated condition, indicating that both water and thermal cracking has a strong influence on strength. It is highlighted the experiment 7 Sat (i.e. ‘as collected’ at  $P_{c\text{ eff}}=30$  MPa) that exhibits a strain hardening behaviour typical of the semi-brittle regime but which eventually reaches failure (Figure 4.3 e). The two experiments, 8 Dry and 8 Sat on ‘as collected’ samples run at the maximum confinement pressure chosen (i.e.  $P_{c\text{ eff}}=15$  MPa), fall in the transitional region (i.e. white square in figure 4.8), as confirmed from the macroscopic inspection of the post-mortem specimens. According to [Evans and Kohlstedt, 1995](#), these experiments transition to a failure mode from localized to pervasive ductile deformation, into the mechanism class from brittle to semi-brittle, involving both brittle and plastic mechanisms. These results explore only a single strain rate whilst the sensitivity of rock strength to strain rate is known to be very pronounced in the semi-brittle and ductile domain, especially in presence of continuous high temperature and/or creep conditions.

#### 4.3.4 Application of results to the Etna basement

At Mount Etna, previous studies locate the presence of shallow magma reservoirs between 3-5 km depth, within the sedimentary basement (e.g. [Aloisi et al., 2011](#); [Bonaccorso et al., 2010](#); [Gambino et al., 2016](#)): this provides one of the key motivations for this study. Magmatic intrusions generate high temperature gradients that significantly affect the mechanical, chemical, and physical properties of the surrounding rocks. Sedimentary rocks are more prone to the effect of temperature and fluids circulation, promoting micro-cracking development and enhancing inelastic behaviour (e.g. [Rutter, 1972](#); [Rutter, 1974](#); [Yavuz et al., 2010](#); [Mollo et al., 2011](#); [Heap et al., 2013](#); [Nicolas et al., 2016](#)). As carbonate rocks have a tendency to exhibit ductile behaviour already at laboratory temperature and strain rate (e.g. [Baud et al., 2000a](#)), the addition of fluids and thermal cracking, as shown here, lead to ductile behaviour even at lower boundary conditions of pressure and pore fluid pressure for CL. Magma reservoirs in the Etna’s sedimentary basement feed both central and lateral conduits as well as numerous dykes and sills (e.g. [Aloisi et al., 2011](#), [Bonaccorso et al., 2010](#),

[Gambino et al., 2016](#), [Bonforte et al., 2008](#)). In general, dykes at Etna can be classified into two main types: a) horizontally propagating dykes that originated from a central conduit to the point of eruption (i.e. [Sigmundsson et al., 2010](#)) and b) vertically propagating dykes fed from a shallow magma reservoir that bypass the central conduit and intrude through the entire basement towards the surface. This latter type is the more typical for the Etna's basement (e.g. [Aloisi et al., 2009](#); [Gambino et al., 2016](#); [Bonaccorso et al., 2010](#); [Gudmundsson, 2002](#)). The volume of sedimentary substratum that is thermally affected by shallow magma reservoirs (i.e. 3-5 km depth) at Mount Etna is approximately 6 km<sup>3</sup>, with a temperature gradient from 1200 °C to 300 °C at a radial distance of 1.5 km (i.e. [Mollo et al., 2011](#) and reference therein). Magmatic intrusions, whether dykes or sills, or sub-spherical pressure sources, produce substantial heat that likely affects the basement rocks of Mt Etna, and the same situation is present in other volcanoes with sedimentary substratum. A 2D finite element model using COMSOL Multiphysics relates the laboratory data to a physical model considering the proximity to a dyke intrusion (Figure 4.9).

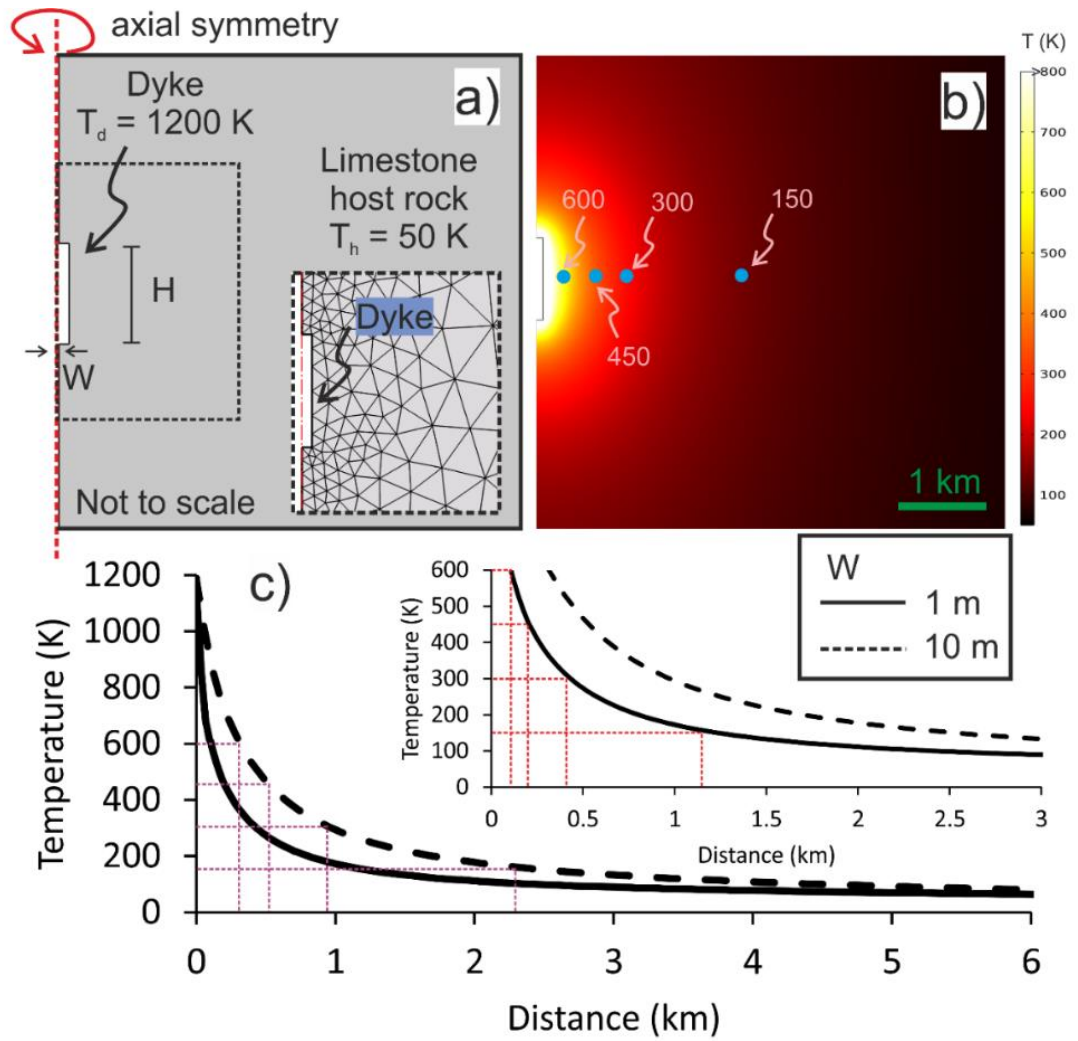


**Figure 4.9.** 2D finite element model representing a dyke as heat source of  $1200^{\circ}\text{C}$  embedded in a cooler carbonate host rock of  $50^{\circ}\text{C}$ . (a). Model set-up and parameters. (b) Model results showing temperature decay away from a 1 m thick dyke. (c) Temperature versus distance plot for a 1 m thick dyke, and for a 10 m thick dyke. Inset shows zoomed view up to  $600^{\circ}\text{C}$ , for a distance up to 3 km. Thin-dashed lines show representative temperatures as per the thermal treatment experiments. Data are summarised in Table 2.

**Table 4.1.** the table reports the modelled proximity of the rocks interested by temperature gradients for a size of dyke of 1 m and 10 m.

Dyke thickness (m)	Proximity to dyke (km)	Temperature (°C)
10	0.3	600
10	0.5	450
10	0.95	300
10	2.5	150
1	0.1	600
1	0.2	450
1	0.43	300
1	1.2	150

Here, the thermal effects on a carbonate host rock is considered from the intrusion of a vertical basaltic dyke with a temperature of 1200 °C (Figure 4.9 a). Using the heat transfer module in COMSOL, an axisymmetric 2D representation is built of a 1 m and 10 m thick dyke intruding into a cooler carbonate host rock with an average calcite thermal conductivity ( $k$ ) of 2.5 W K<sup>-1</sup> m<sup>-1</sup>, and a base temperature of 50 °C (Fig. 4.9 a). A finite element mesh is created around the intrusion with a maximum resolution of 0.5 m. The model then solves the heat transfer equation (4.1) for conduction throughout the 20 km<sup>2</sup> domain to calculate the resultant temperature field of the host rock following intrusion (Figure 4.9 b) as follows:

$$\rho C_p \cdot \Delta T + \Delta \cdot (-k\Delta T) = Q \quad (4.1)$$

where  $\rho$  is density,  $C_p$  is specific heat capacity and  $Q$  is heating power per unit volume. This is a first order model that calculates the instant temperature field ( $\Delta T$ ) in an isotropic dry host rock and so does not consider time dependant effects or preferred pathways for convective heat transfer or fluid rock interactions. The model therefore does not fully characterise the complexities of a thermal regime surrounding an intruded dyke but instead provides insights of the effect of temperature with proximity to a heat source. Applying this model to the heat-treated laboratory specimens suggests the expected approximate distance from the two different thicknesses of dykes that each specimen represents. In the case of a 1 m thick dyke intrusion, our four heat treated specimens represent a proximity to the dyke of 0.1 km at 600 °C, 0.2 km at 450 °C, 0.43 km at 300 °C, and 1.2 km at 150 °C. For a dyke of 10 m thickness, which is an extreme case for Etna, but commonly found at other volcanoes (e.g. [Gudmundsson, 1995](#)), the temperature field is much hotter as it is entirely as expected. Increasing dyke thickness reduces the temperature decay at distance from the heat source: for a 10 m

dyke, the 600 °C heat treatment would now be experienced at 0.3 km, 450 °C at 0.5 km, 300 °C at 0.95 km and 150 °C at 2.5 km from the dyke (Figure 2.13c and Table 2.3).

Although being a quite simple model, when combined to laboratory analysis, it is possible to observe that a dyke 1 m thick can already exert a critical influence on the mechanical properties of large volumes of rocks present at few hundreds of metres away. This scenario may easily be extended across the depths where dykes and sedimentary rocks are present. In particular, the transition from brittle to ductile deformation induced by temperature is influencing the permeability (e.g. [Baud et al., 2000a](#); [Violay et al., 2012](#)), and in this case, along with the presence of fluids in the basement, the CO<sub>2</sub> produced by decarbonation can be prevented from escaping. A consequence of a reduced permeability is likely promoting local increments of pore pressure, resulting in an overall lower strength of the basement.

## 5.1 Introduction

The results obtained from the direct shear tests are presented for all the experiments conducted but the failed, therefore this chapter includes the results obtained with the first sliding holder that are subjected of uncertainty: these data will be presented but not discussed. The main reason of uncertainty is that those results can be altered by the contribution of any bending in the holder. Even if the results obtained with the first holder show agreement with previous findings in literature regarding limestone and quartz-sand, clay's friction coefficient values are too high to be considered correct (e.g.  $\mu \sim 0.7$ ), therefore these data are invalidated.

## 5.2 Results for Constant Sliding Velocity: end-members

Table 5.1 below summarizes the results obtained with the two generation of sliding holders. In orange are the results obtained with sliding holder #1, subjected to uncertainties. In black are the results obtained with sliding holder #3, and here discussed.



**Table 5.1.** Detailed description of the experiments conducted. The steady-state apparent friction coefficient,  $\mu_{ss}$ , is taken at 2 mm displacement for each experiment. In orange the experiments with uncertainties that are not discussed here.

Experiment	Gouge composition	T °C	Pc	Pf	Strain Rate (mm/s)	$\mu_{ss}$ (2 mm)	(a-b)	Sliding Behaviour	Note
1_ClayCSR	100% Clay	20	10	0	0.0003	0.69	N/A	Strain weakening	Values of friction coefficient too high
2_ClayCSR	100% Clay	20	30	0	0.0003	0.66	N/A	Strain weakening	
3_ClayCSR	100% Clay	20	50	0	0.0003	0.68	N/A	Steady state	
1_SandCSR	100% Sand	20	10	0	0.0002	0.64	N/A	Strain hardening/weakening	
2_SandCSR	100% Sand	20	30	0	0.0003	0.59	N/A	Strain hardening/steady state	
3_SandCSR	100% Sand	20	50	0	0.0003	0.62	N/A	Strain weakening	
1_LimeCSR	100% Lime	20	10	0	0.001	0.83	N/A	Strain weakening	
2_LimeCSR	100% Lime	20	30	0	0.00099	0.8	N/A	Strain weakening	
3_LimeCSR	100% Lime	20	50	0	0.00097	0.78	N/A	Strain weakening	
1_Lime90CSR	90%Lime-10%Clay	20	50	0	0.001	0.765	N/A	Strain weakening	Stick-slip
2_Lime75CSR	75% Lime-25%Clay	20	50	0	0.00099	0.61	N/A	Strain weakening/hardening	Stick-slip
3_Lime50CSR	50% Lime-50%Clay	20	50	0	0.00099	0.623	N/A	Strain hardening/weakening	Stick-slip
100ClayVS	100% Clay	20	50	0	variable	0.49	N/A	Strain hardening	
100LimeVS	100% Lime	20	50	0	variable	0.67	Velocity strenghtening	Strain weakening	
75LimeVS	75% Lime-25%Clay	20	50	0	variable	0.66	Velocity strenghtening	Strain hardening	
50LimeVS	50% Lime-50%Clay	20	50	0	variable	0.61	Velocity strenghtening	Strain hardening	

### 5.2.1 Quartz-sand Synthetic Gouge

Figure 5.1 reports the results for quartz-sandstone friction coefficients at increasing confining pressures. The samples were partially wet to assure initial cohesion during samples preparation. The three experiments with quartz-sand showed almost identical curves for the three confining pressures tested (i.e. 10, 30 and 50 MPa). They were characterized by an initial sudden quasi-linear increase in friction coefficient at 1 mm displacement. After the elastic deformation and the achievement of the yield point, an initial state of strain hardening was present in all the tests, followed by strain weakening.

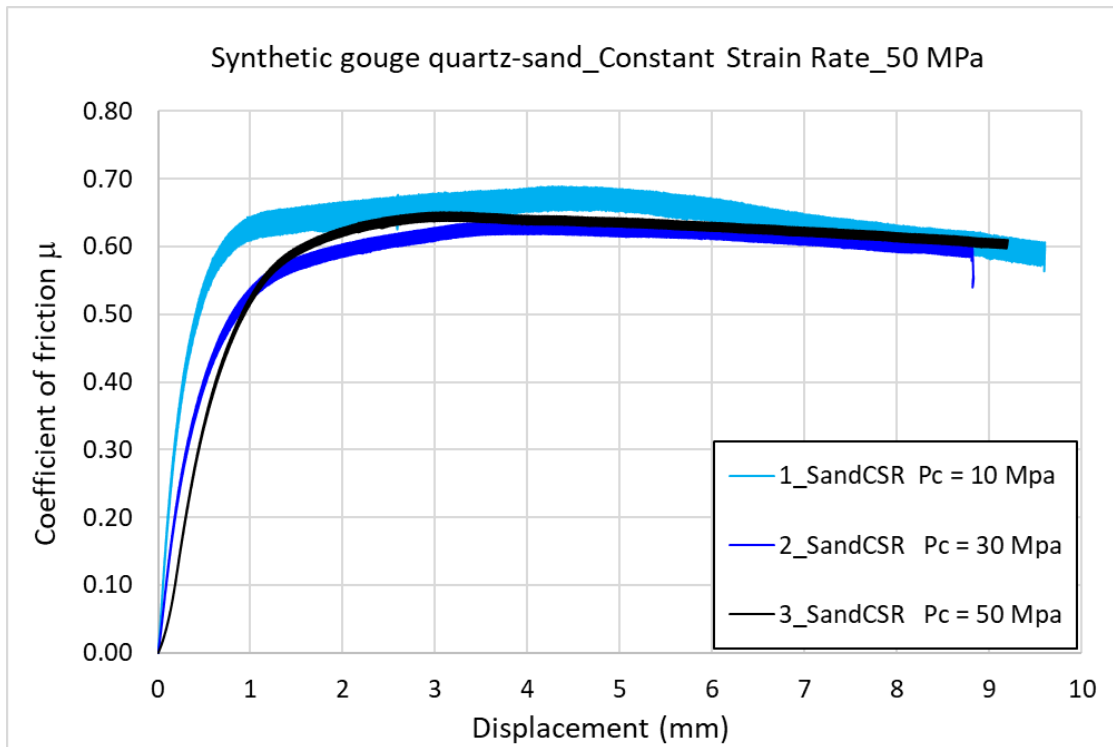


**Figure 5.1.** Friction coefficient VS displacement for the results of the end-member containing quartz-sand at increasing confining pressure.

For 1\_SandCSR at 10 MPa (i.e. light blue line, figure 5.1), the strain hardening was continuing up to 4.5 mm displacement, after that it was becoming strain weakening. For 2\_SandCSR at 30 MPa (i.e. dark blue line, figure 5.1), a consistent strain hardening to a maximum friction coefficient of 0.62 was present before a mild strain weakening persisted until the end of the experiment. 3\_SandCSR at 50 MPa (i.e. black line, figure 5.1) showed strain hardening after the yield point, which it was becoming strain weakening until the end of the experiment with a trend matching 2\_SandCSR. The effect of varying the confining pressures up to 50 MPa had little effect on these synthetic gouges.

### 5.2.1 Quaternary Clay Synthetic Gouge

Clay end-members (i.e. 100% clay) showed an anomalous high friction coefficient, in the range of 0.70 coefficient of friction. The three experiments showed steady initial elastic and linear increase until they reached a yield point approximately at 1 mm displacement. Test 1\_ClayCSR at 10 MPa (i.e. light blue line, figure 5.2) and test 2\_ClayCSR at 30 MPa (i.e. dark blue line, figure 5.2) presented a steady strain weakening until they reached a value of 0.55 and 0.60 friction coefficient, respectively.

Test 3\_ClayCSR at 50 MPa (i.e. black line, figure 5.2) was maintaining a steady frictional strength until 9 mm displacement. The results are presented in Figure 5.2.

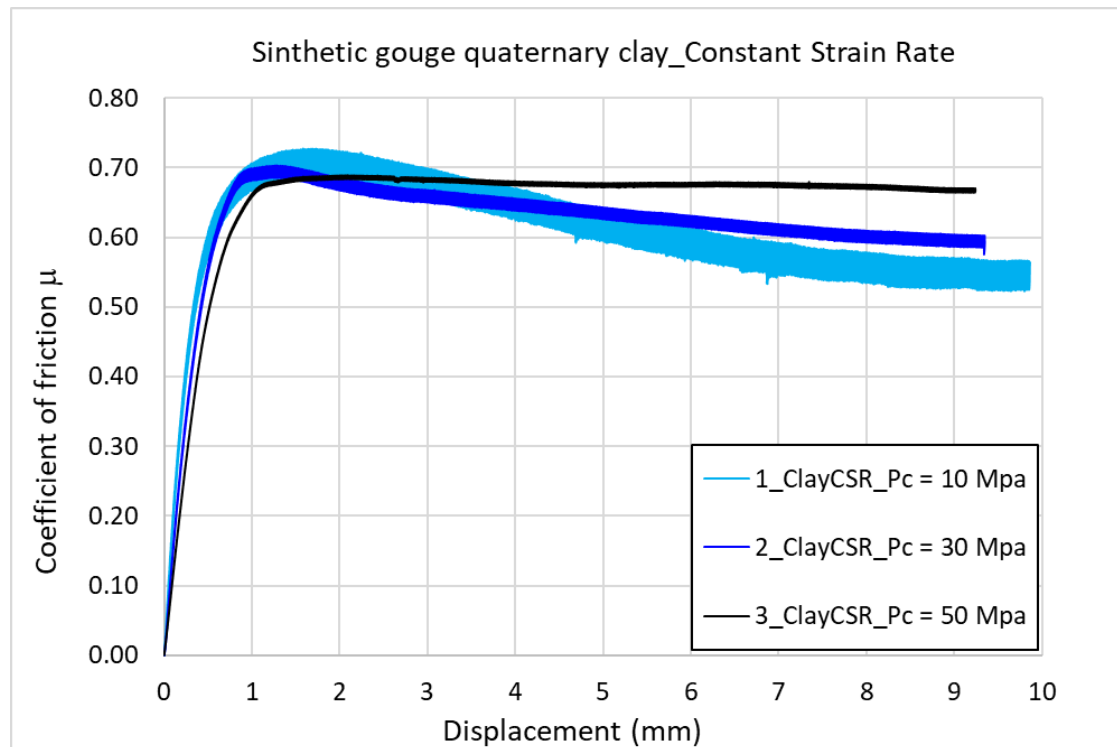


**Figure 5.2.** Increasing confining pressures at constant strain rate for the experiments with quaternary clay synthetic gouges.

The increasing confining pressure was markedly stabilizing the behaviour from strain weakening to steady-state. From 1\_ClayCSR (i.e. light blue) to 3\_ClayCSR (i.e. black line) the trend stabilized, especially in 3\_ClayCSR where the black line showed no variations in friction coefficient. The maximum value of  $\mu$  obtained at the yield point for the three experiments was around 0.70  $\mu$ . Unfortunately, as mentioned beforehand in the introduction of this chapter, these values of friction coefficient for natural clays were anomalous and generally too high to be considered as valuable.

### 5.2.1 Limestone Synthetic Gouge

For the CL synthetic gouges the general behaviour was strain weakening (Figure 5.3) with values decreasing from 0.80  $\mu$  for 1\_LimeCSR (i.e. light blue line), to 0.78  $\mu$  for 2-LimeCSR (i.e. dark blue line) and to 0.75  $\mu$  for 3\_LimeCSR (i.e. black line). These values for limestone synthetic gouges were in the range of values found in previous studies on carbonate gouges (e.g. [Chen 2015](#)). As in the previous experiments presented

here, the frictional strength was following a steady increase until a yield point within 1 mm displacement. For 1\_LimeCSR at 10 MPa (i.e. light blue line) and 2\_LimeCSR (i.e. dark blue line) at 30 MPa, the friction coefficient is slightly increasing up to 0.82  $\mu$  and 0.80  $\mu$ , respectively, before starting to decrease in a matching ‘strain weakening mood’ until the end of the experiments. For experiment 3\_LimeCSR at 50 MPa (i.e. black line), the friction coefficient was maintaining a stable behaviour up to 5 mm displacement without notable increment, followed by strain weakening until the end of the experiment.

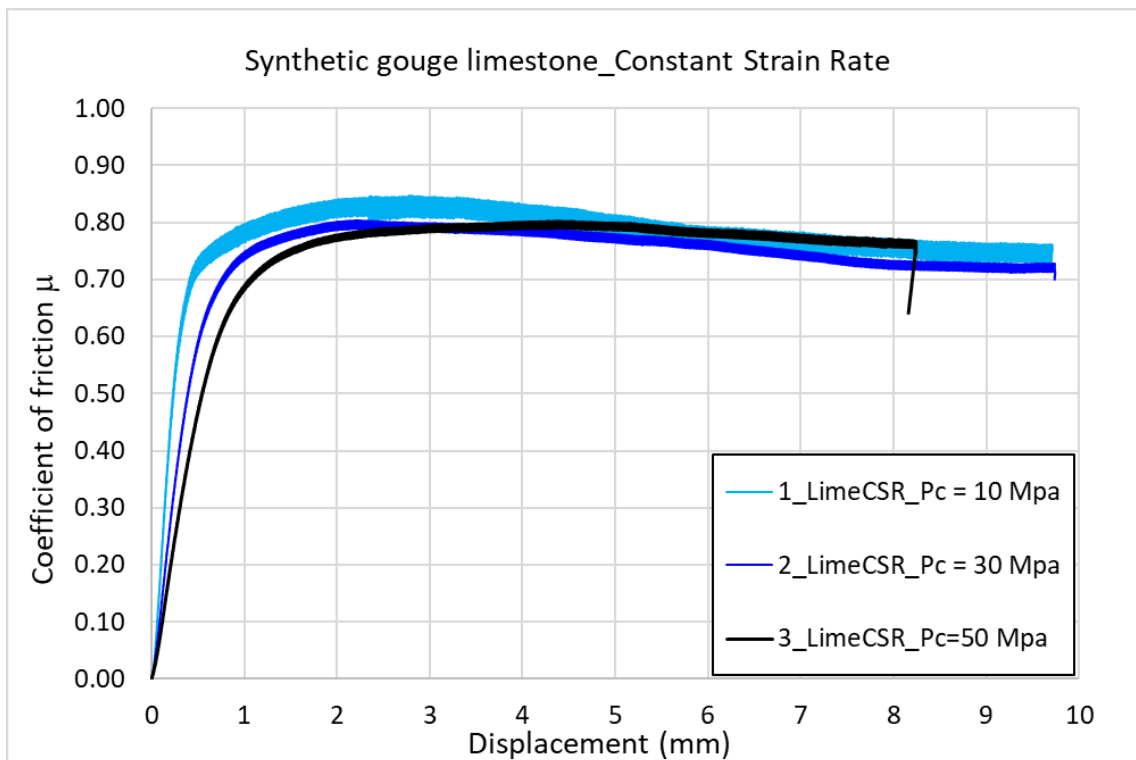


**Figure 5.3.** Friction coefficient versus displacement for the three experiments with 100% limestone synthetic gouge at increasing confining pressure.

### 5.3 Results for Constant Sliding Velocity: Binary Mixtures

The binary mixtures combined synthetic gouges of quartz-sand and limestone with increasing amount of quaternary clay, specifically the quantity of clay was increasing from 0%, to 10%, 25% and 50%. This set of experiments run at constant 50 MPa of confining pressure and constant strain rate at 0.001 mm/s. The tests here presented were performed with sliding holder #3, and because the results of the calibration tests proved to be reliable, they are presented and discussed here.

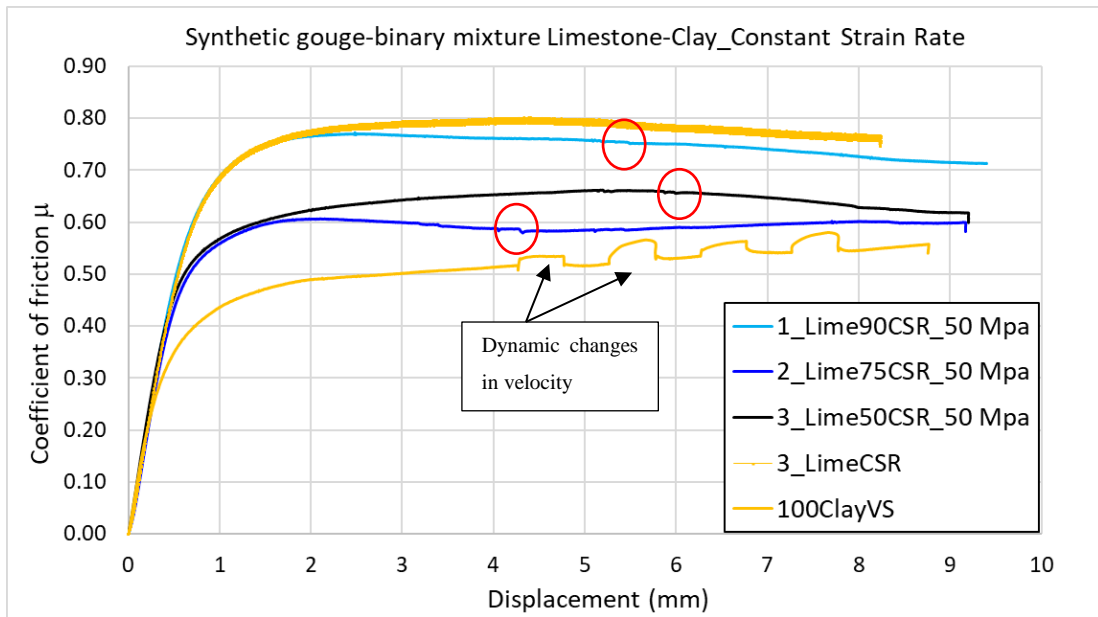


**Figure 5.4.** Results for the synthetic binary mixtures of limestone with increasing clay content. In yellow are reported the two end-member for comparison.

The binary mixtures showed to be sensitive to the clay content (Figure 5.4). Few common features in frictional experiments were present: a) after a quick increase in frictional strength, the samples attained a constant value of  $\mu$  before 2 mm displacement, followed by a linear weakening (i.e. 1\_Lime90CSR, light blue line) or hardening (i.e. 3\_Lime50CSR, black line) response; b) the sliding behaviour presented few stick slip events (i.e. red circles in figure 5.4); c) the friction coefficients attained by the samples of binary mixtures fell between the friction coefficient of the two end-members (i.e. yellow lines in Figure 5.4). Regarding experiments 3\_LimeCSR and 100ClayVS here reported as end-members for comparison (i.e. yellow lines in figure 5.4) few considerations were needed. The friction data for 100% Limestone (i.e. experiment 3\_LimeCSR) were taken only for comparison, as they were part of the data considered as not reliable. For the same reason, instead of reporting data of experiment 3\_ClayCSR that was the obvious end-member for these group of constant strain experiments, here were reported the results for 100ClayVS instead (i.e. the result of the velocity steps experiment run with sliding holder #3). In experiment 100ClayVS the friction coefficient was maintaining a value of 0.5  $\mu$  before the onset of dynamic changes in velocity (i.e. the ‘bumps’ in the curve). In detail, experiment 1\_lime90CSR (i.e. light blue line) showed a steady increment up to 0.77 friction coefficient at 2 mm displacement, followed by a mild strain weakening which was becoming more pronounced towards the end of the experiment. The increment of clay at 25% was

decreasing the friction coefficient at 0.60 in the experiment 2\_Lime75CSR (i.e. dark blue line). It was followed by strain weakening to a value of 0.58  $\mu$  at 4.5 mm displacement and a mild strain hardening to the end of the experiment. At 50% clay, experiment 3\_Lime50CSR (i.e. black line) was showing an increasing shear resistance consistently matching experiment 2\_Lime75CSR (i.e. dark blue line) until the yield point, then started to diverge becoming strain hardening and reaching the maximum friction coefficient value of 0.66 at 5.3 mm displacement followed by strain weakening until the end of the test.

#### 5.4 Results for Dynamic Sliding Velocity: End-members

##### 5.4.1 Clay Synthetic Gouge

Data for the velocity steps are presented in the typical graph displaying the friction coefficient versus the displacement, and figure 5.5 reports the experiment 100ClayVS. The friction coefficient was showing a steady increase until a yield point from which departed a strain hardening behaviour. At 2 mm displacement, the value of friction was of 0.49. The general trend was of strain hardening until the end of the experiment, regardless the velocity changes.

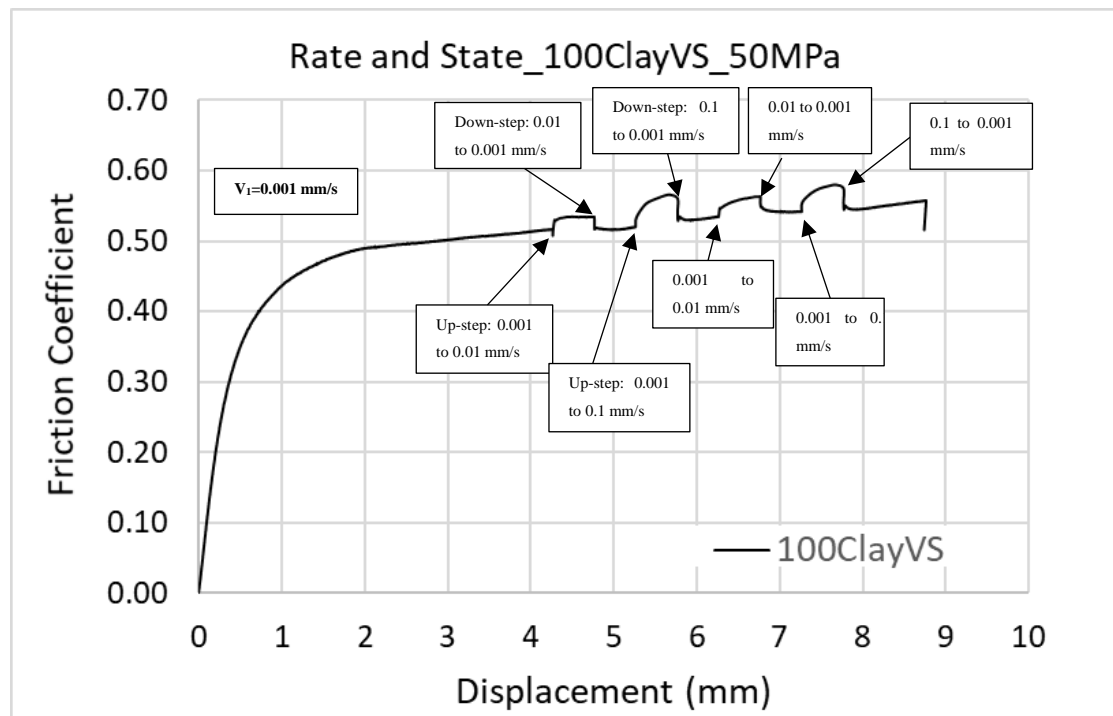


**Figure 5.5.** Result for the experiment of the end-member containing 100% clay.

The state parameters (a-b) showed to be positive for the steps analysed, so that the synthetic gouge is velocity strengthening (see Table 5.2).

#### 5.4.2 Limestone Synthetic Gouge

The experiment 100LimeVS showed to reach a maximum value of friction coefficient of 0.70 at 1.3 mm displacement (Figure 5.6), after a steady increase in strength from the beginning of the test. The maximum value attained was followed by strain weakening behaviour until the end of the experiment. The (a-b) values were showing that this lithology was velocity strengthening, showing positive results at each velocity change.

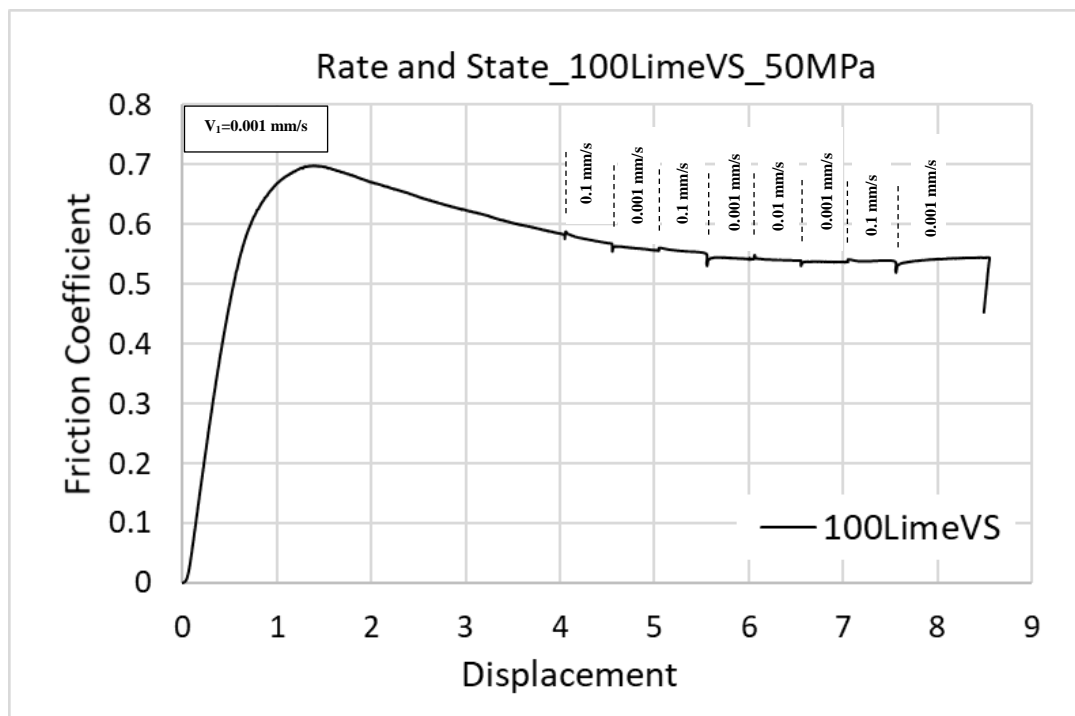


**Figure 5.6.** Friction coefficient versus displacement for the test 100LimeVS. The trend was strain weakening.

#### 5.5 Results for Dynamic Sliding Velocities: Binary Mixtures

Experiments 75LimeVS (i.e. dark blue) and 50LimeVS (i.e. black line) showed a mineralogy dependence at increasing clay content (Figure 5.7).



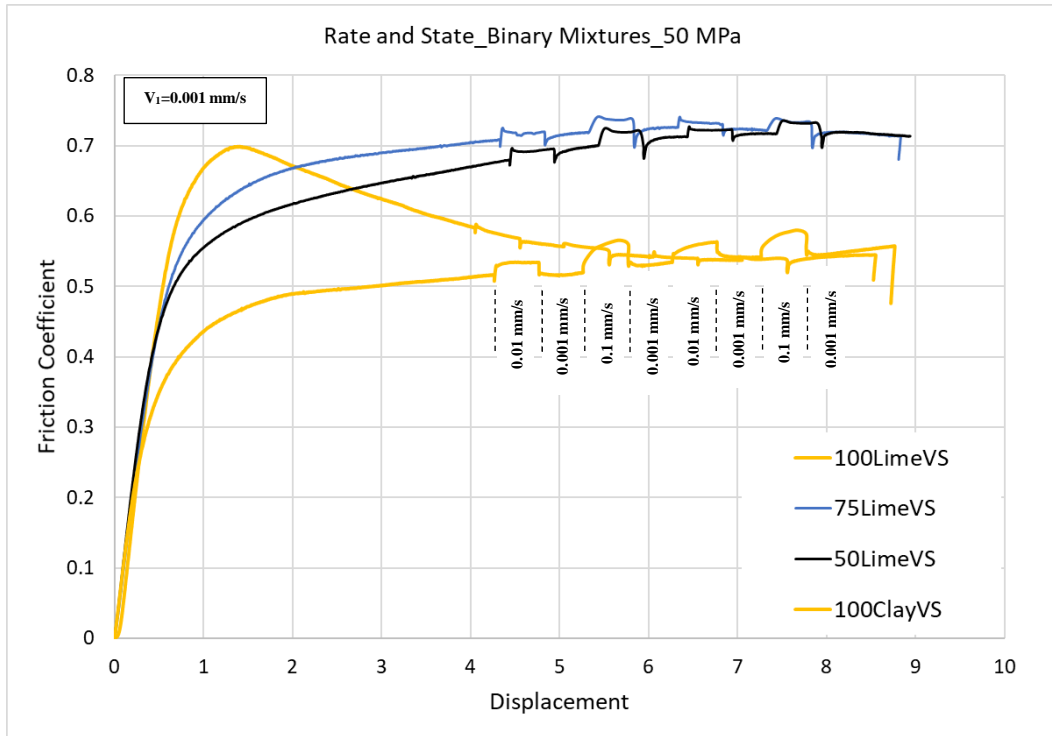


**Figure 5.7.** Friction coefficient versus displacement for the experiments with binary mixtures. In yellow are reported the results of the two end-members for comparison.

From 100LimeVS (i.e. yellow line) to 75LimeVS (i.e. light blue line) the yield point reached was, respectively, of  $0.7 \mu$  and  $0.63 \mu$  at 1.3 mm displacement. Experiment 75LimeVS showed to be strain hardening, with an increasing strength until the end of the experiment, while the end-member 100LimeVS was markedly strain weakening. 50LimeVS (i.e. black line) was again showing a strength decrease, with the friction coefficient at the yield point of  $0.58 \mu$  and showing, also in this case, a sustained strain hardening until the end of the experiment. When the clay content raised up to 100%, the strength was reduced at  $0.45 \mu$  at 1.3 mm displacement in experiment 100ClayVS (i.e. yellow line). The binary mixtures showed values of friction coefficient contained between the two end-members, even if 100LimeVS is decreasing in strength after the yield point. The rate and state parameters ( $a$ - $b$ ) summed in Table 5.2 showed a velocity dependence such as velocity strengthening at increasing clay content.

**Table 5.2.** (a-b) parameters, reported from the slip law, or Ruina law, obtained from RsFit3000.

	(a-b)			
	100% Limestone	100% Clay	75% Limestone	50% Limestone
<b>step1</b>	-3.263e05 ± 6.644e-04	0.005 ± 1.16e-04	-8.35e-04 ± 0.001	0.003 ± 2.11e-04
<b>step2</b>	0.001 ± 7.049e-05	0.006 ± 7.58e-05	0.002 ± 1.07e-04	0.001 ± 5.02e-05
<b>step3</b>	2.407e-04 ± 10.671	0.007 ± 0.001	0.002 ± 2.99e-04	0.003 ± 1.92e-04
<b>step4</b>	0.001 ± 1.955e-05	0.005 ± 3.56e-05	0.003 ± 5.30e-05	0.001 ± 2.52e-05
<b>step5</b>	-1.369e-04 ± 1.4799e-04	0.008 ± 6.79e-04	-0.012 ± 0.04	0.002 ± 1.165e-04
<b>step6</b>	4.272e-04 ± 3.2863e-05	N/A	0.003 ± 3.51e-05	0.002 ± 2.89e-05
<b>step7</b>		N/A	N/A	
<b>step8</b>	0.0015 ± 4.346e-05	0.005 ± 2.20e-05	0.003 ± 5.18e-05	0.001 ± 1.64e-05

In 100LimeVS (i.e. 100% limestone), velocity steps were for the majority positive values, showing a negative result in the first up-step from 1 µm/sec to 10 µm /sec and up-step 5, which is again from 1 to 10 µm /sec. Negative values were present at the same up-steps for experiment 75LimeVS (i.e. 75% limestone), where the clay content was increased of 25%. The behaviour was becoming completely velocity strengthening in 50LimeVS (i.e. 50% limestone) and 100ClayVS (i.e. 100% clay), hence increasing amount of clay content was a factor of stabilization.

## 5.5 Discussion

Of the actual available data on direct shear, [Hunfeld et al., 2017](#) present data on simulated gouges obtained by ‘crush and sieve’ method with the aim of studying the frictional properties of rocks belonging to a gas field under P-T conditions, pore fluid pressure applied and varying fluid salinity. However, even if saturated experiments, in their work they report results for a mixture of carbonate and claystone simulated gouge, which somehow it is comparable to the mixture presented here. [Leclere et al., 2016](#) present data of permeability at increasing confining pressures for dehydrated gypsum gouges. Also [Pluymakers et al., 2014](#) collect data on anhydrite gouges at fixed confining pressure and increasing temperature. On carbonate simulated gouges, [Chen et al., 2015](#) present results on simulated gouges obtained with the ‘crush and sieve’ method from carbonate fault breccia, at a fixed confining pressure of 50 MPa and varying the temperature range, both in dry and saturated conditions. In this case, it is

possible to compare the data here presented with their rate and state experiments run at 20°C. Another study collecting data on simulated calcite and limestone gouges is from [Verberne et al., 2013](#). The direct shear experiments are run at 50 MPa confining pressure varying the temperature and it is possible to refer to their data at ~20°C. A wealth of data regarding the evolution of the frictional properties from pure clay to mixtures combining increasing clay content is found in literature when different techniques are applied, such as the double direct shear or the saw-cut configuration (e.g. [Crawford et al., 2008](#); [Ikari et al., 2009](#); [Collettini et al., 2009](#); [Tembe et al., 2010](#); [Tesei et al., 2012](#); [Zhang and He, 2013](#)).

The tests presented in section 5.2 are run at constant strain rate, showing to be dependent on clay content, as highlighted in many previous studies (e.g. [Ikari et al., 2009](#); [Tembe et al., 2010](#); [Zhang and He, 2013](#)). The friction coefficient shows to decrease sensibly from a content of clay of 10% to 25% and again from 50% to 100%, while almost no difference is found between 75% and 50%. The behaviour shows mainly strain weakening for the experiment 1\_Lime90CSR, while at 75% and 50% it is somehow contrasting: strain hardening then weakening for experiment 3\_Lime50CSR and strain weakening then hardening for experiment 2\_Lime75CSR. The end-member reporting the result for 100% clay shows a steady strain hardening regardless the slip rate changes. These results are in agreement with previous findings: [Hunfeld et al., 2017](#) test some synthetic gouges obtained from natural samples in direct shear. Their samples of Basal Zechstein is a mixture of anhydrite (48%) and carbonates (32%) showing a lower friction coefficient attained ( $0.63 < \mu_{ss} < 0.66$  between 1 and 2 mm displacement), probably because wet, and a strain weakening behaviour. [Verberne et al., 2013](#) report a friction coefficient's peak of 0.7-0.8 attained at 1-2 mm displacement followed by a near-constant, slight decrease strain weakening behaviour. [Chen et al., 2015](#), who report a friction coefficient attained of 0.63-0.7  $\mu$  followed by a quasi-linear steady state regardless increasing temperature and sliding velocities, obtain other comparable results. The examples here reported are experiments run with the direct sliding holder technique, using carbonate synthetic gouges. To the actual knowledge, the only study using a combination of 50-50 natural carbonate and clay (i.e. the latter obtained by a sample of claystone) is the mixture experiment presented in [Hunfeld et al., 2017](#). Their brine experiments show to reach a maximum peak of  $\mu=0.5$  at 1 mm displacement, followed by a rapid decrease in strength and slight weakening

until the end of the experiment. Experiment 3\_Lime50CSR here presented, considering that is dry, shows to reach a yield point after a linear increase in strength, followed by a strain hardening until 5 mm displacement, followed by strain weakening. Regarding the little instability recorded in experiments 1\_Lime90CSR, 2\_Lime75CSR and 3\_Lime50CSR, the decrease in strength is of minor entity, probably due to particle reorganization or compaction rather than repetitive stick-slip instability. The experiment 100ClayVS shows to reach a point of yield deviating from the initial linear increase, with a measured  $\mu=0.49$  at 2 mm displacement, followed by a sustained strain hardening regardless the velocity changes. The result show to be in the range of the many previous findings (e.g. [Crawford et al., 2008](#); [Hunfeld et al., 2017](#); [Tembe et al., 2010](#)), despite resulting quite high for clay mineralogy.

In [Tembe et al., 2010](#), the experiments are run with pure illite samples obtain by gravity settling in water, which is not the case of this study. They highlight the difference in their results of a friction coefficient lower than the results obtained by [Morrow et al., 1992](#), who run experiments with illite gouges obtained by ‘crush and sieve’ procedure. As [Tembe et al., 2010](#) report, the difference it can be cast in the different method of samples preparation. As highlighted previously in this thesis, the quaternary clay used for the tests are obtained using the ‘crush and sieving’ method, being the necessary quantity too high to be collected using the gravity settling in water. By the use of this procedure, the fraction of fine silt it is not removed, and the presence of coarser grains might result in a higher friction coefficient.

A similar trend of oscillation between strain weakening and strengthening is found in the rate and state experiments (Figure 5.7). Only the experiment 100LimeVS (i.e. yellow line) is showing a marked strain weakening after reaching the maximum point of frictional strength at  $0.70 \mu$ . The response to the velocity perturbation in this experiment is in line with [Hunfeld et al., 2017](#)’s results, showing both velocity strengthening and velocity weakening, but they are not, for example, in agreement with [Verberne et al., 2013](#), who find velocity strengthening in their (*a-b*) response for limestone gouges. Experiments 75LimeVS and 50LimeVS (Figure 5.7, light blue line and black line, respectively) show again a similar strengthening trend in comparison to the constant strain rate experiments with the same clay percentage reported in Figure 5.4. However, in this case, the friction coefficient is slightly decreasing with the

increasing amount of clay. At 75 % clay, the rate and state parameters show to have negative values in two up-steps (see Table 5.2), while the behaviour is becoming totally velocity strengthening at 50% clay, denoting that the presence of clay has the function of stabilize the frictional sliding.

Tembe et al., 2010 present their friction data of binary (i.e. quartz-montmorillonite, quartz-illite) and ternary (i.e. quartz-montmorillonite-illite) mixtures according to the transitional regime proposed by Lupini et al., 2009. The transitional regime proposes that a first increase of 25% in clay content provokes a moderate decrease in frictional strength in a phase called ‘turbulent shear’; at 70% clay content the frictional strength is significantly decreased entering in the ‘transitional regime’; finally, at 100% clay content, the frictional strength is at its minimum, entering the ‘sliding shear’ phase. As highlighted in the paper, few differences might to be taken into account: results from Lupini et al., 2009 concern data obtained at low stresses (i.e. 1 MPa) while results from Tembe et al., 2010 are at higher stress (i.e. 41 MPa). The active mechanisms during the shear slide are different, moving towards grain-on-grain slip rather than grain crushing. In fact, data obtained at higher stresses often present a sustained strain hardening which it is not present at lower stresses. Further, the third ‘sliding shear’ flow it might not to be achieved for the total displacement allowed in triaxial apparatus respect to ring shear apparatus. However, despite the intrinsic differences given by different gouges investigated and different stresses applied, the increasing content of clay consistently decreases the friction coefficient (e.g. Crawford et al., 2008; Takahashi et al., 2011; Tembe et al., 2010). In Figure 5.8 are reported the friction coefficients measured at 8 mm displacement for the constant axial displacement experiments, which is near the end of the maximum displacement allowed in this study (i.e. 9 mm), and where a stable sliding is almost attained.

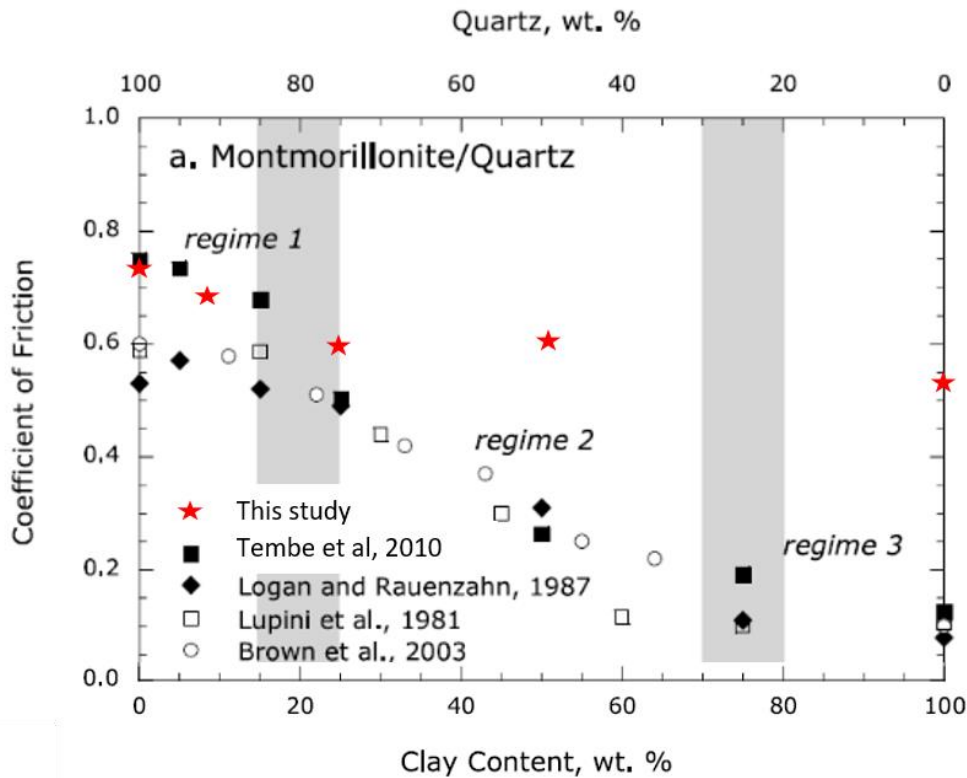


**Figure 5.8.** Modified after [Tembe et al, 2010](#). In the graph friction coefficient results are reported for experiments at high stress, such as this study, [Tembe et al, 2010](#) and [Logan and Rauenzahn, 1987](#) (red star, black square and black diamond respectively), and results for low stress, such as [Lupini et al, 1981](#) and [Brown et al., 2003](#) (white square and white circle respectively).

The coefficients of friction collected during this part of the project fall into regime 1 and 2 moving from a composition of pure clay (i.e. 100% clay) to 75% clay, with a frictional strength that is slightly higher than previous studies. As highlighted in Figure 5.8, in this study the composition at 50% clay is strengthening respect to the composition at 75%, and the end-member at 100% clay is higher than results reported here. Following the subdivision in three regime proposed here, the results are not falling in regime 2 and 3, denoting that the simulated gouges here used are behaving in a different, strong manner. In this case, apart for experiment 100LimeVS which is showing a marked strain weakening behaviour, all the others are strain hardening or a combination of both. However, the clay used for this study are not pure clay, such as the montmorillonite powder commercially purchased by [Tembe et al, 2010](#), but indeed a natural gouge containing different amount of clay minerals. Furthermore, they cannot be considered as pure clay from the granulometric point of view, as they are hand-

sieved at the minimum diameter allowed of 40  $\mu\text{m}$  that consents the passage of fine silt. Bearing this in mind, the strain hardening observed in the experiments can be interpreted as angular grains self-organization in force chain through the layer, combined with the presence of rough boundary surfaces, which are found to increase the frictional strength respect to friction coefficient measured with non-angular grains and smooth boundary surface (e.g. [Anthony, 2005](#)). These force chains fail as the sliding continue, creating compaction in the layer: this is also the interpretation for the few small events of strength drop recorded into the constant strain experiments (see Figure 5.4, red circles). Carbonate-rich gouges presented in [Hunfeld et al., 2017](#) present strongly fractured angular grains in contact. The augmented clay content is decreasing the frictional strength, even if remaining at high values. In this case, the interpretation is that the frictional strength is moving from a stress-supporting framework of grains to a fabric where grains are embedded into a clay matrix, probably characterized by the development of preferential shear zone, in which shear localization occurs (e.g. [Hunfeld et al., 2017](#); [Ikari et al., 2011](#); [Tembe et al., 2010](#); [Tesei et al., 2012](#)).



### 6.1 Conclusions

This thesis research aims to study the frictional and mechanical behaviour of the Etnean lithologies subjected to simulated *in-situ* environmental effects, such as changes in presence of temperature gradient and pore fluid pressure, at representative conditions to mimic the overload. The results obtained during this research significantly improve the current understanding on the working mechanisms underpinning the volcano flank instability of Mount Etna. The datasets produced are unique and contain a wealth of information only partially analysed within the scope of this work. The experimental procedure followed during this project show to be achievable and applicable for other research's topics, for instance fault stability, geothermal research and in particular for investigations of mechanical stability at other volcanoes lying on sedimentary basements.

In the first part of the project, the new experimental results obtained within the context of dyke emplacement simulation on carbonate rocks (i.e. CL - Comiso Limestone) considered as the main component for the Etna's basement, strongly support the coupled effect of temperature and water in promoting micro-cracking development and enhancing the inelastic behaviour of macroscopic deformation. In particular, this study shows the strength and strain accommodation dependence of the carbonate rock related to the proximity to magmatic bodies and the presence of pore fluid, both as a function of burial depths (i.e. confining pressure) and fracture damage. Medium and high temperatures used to create thermal damage in the specimens prior to the mechanical testing mimic the thermal gradient of a distant heat source or the influence of a "recently cooled" magma body into the host carbonate rock.

Based on these results, the conclusion is that even a modest temperature of 450 °C can affect the carbonate strength, which is relevant for the units present in the substratum underlying Mount Etna. At 600 °C, CL definitely become weaker, so below the decarbonisation point identified in previous studies (i.e. [Bakker et al., 2015](#)). Triaxial experiments confirm that CL does not generate significant acoustic emissions, at least up to 450 °C of thermal treatment. However, a substantial development of new

micro-cracks between 300 °C to 450 °C is detected by the recording of ultrasonic wave velocities after the thermal treatment, which decrease from 4.26 km/s to 3.55 km/s and up to 2.83 km/s at 600 °C. Additionally, the study highlights that the marked decrease in mechanical strength of CL due to thermal damage or presence of water (i.e. pore fluid pressure) enhances inelastic strain accommodation without dynamic failure by promoting the brittle-ductile transition regime of deformation at shallower depths. Finally, our modelling results indicate that the critical aseismic temperature zone in relation to the CL unit is likely to extend as far away as 2.5 km away from a 10 m thick dyke, a distance encompassing a large thickness of sub-Etnean pile if applicable, thus suggesting a very ductile substratum.

Considering the particular seismic/aseismic behaviour registered at the Pernicana Fault System, the results suggest that the portion of basement interested by the BDT transition lies at relatively low depth (i.e. about 2 km b.s.l.). The presence of fluids is found in Mount Etna's basement down to few kilometres below the sea level (i.e. [Siniscalchi et al., 2010](#); [Mattia et al., 2015](#)) and in this study the relevance of pore fluid pressure in lowering the mechanical strength and enhance a semi-brittle to ductile deformation at relatively modest confining pressure is evident. The presence of fluids at the BDT transition is also highlighting a reduced AE's rate and ultrasonic velocities, the latter suggesting a low seismic anisotropy. The passage from brittle to ductile deformation is accompanied by the transition from a dilatant to a compactant mode, relevant for fluid transport (e.g. [Violay et al., 2012](#); [Baud et al., 2000](#)). The application of a thermal gradient able to induce consistent micro cracking is of particular influence on the strength of CL, promoting lower mechanical strength in dry conditions and even lower strength in saturated conditions. The application of thermal gradient is therefore crucial for enhancing porosity and therefore for promoting fluid transport, even if the temperature is applied before the deformation, which is the case of a distant volume rock respect to a dike intrusion considered here. A reduced fluid transport can eventually lead to local increase of pore fluid pressures, leading to an overall reduced strength of the basement and likely affecting new portion of basement's rocks. In light of this, this study reveals that thermal gradients can affect heavily the integrity of large portion of basement, along with local changes of stress field, new intrusions and/or magma movements, tectonic processes, and presence of water not necessarily

happening at the same time, as suggested by previous studies investigating the role of *in-situ* high temperatures during deformation.

The second part of the project quantifies, for the first time at the actual knowledge, the frictional properties of some representative members of the sedimentary basement of Mount Etna. The design and fabrication of new sliding holders capable to fit the size required by the MTS 815 – Mechanical Testing System triaxial apparatus bring an unforeseen engineering aspect in addition to the project. When a new tool is developed, a mandatory series of calibration tests are required to evaluate the reliability of the assemblage. The use of a stainless steel capable of sustaining the deformation, the material chosen to complete the assemblage (i.e. silicone, Teflon jacket, rubber jacket), the calibration procedure, the sample preparation, all of these aspect require several revisions to upscale properly the final assemblage. During the preliminary tests, the first generation of sliding holder experiences deformation, revealing compulsory improvements. The second generation fails during the initial calibration, because of the presence of sintered material too weak to sustain the strain imposed by the presence of a gouge layer onto the slider's contact surface. A third and last generation, improved and finally fabricated without weak points, allows the completion of the experimental plan. Even if a lesser amount of experiments respect to the original plan are successful, the data reported shed light on significant aspects of the frictional properties of the selected simulated gouges. When the amount of percentage of clay inside the binary mixtures increases, the frictional strength decreases. This pattern is observed also when velocities changes are applied: at increasing clay content, the sliding behaviour is stable, as the rate and state parameters ( $a-b$ ) result positive, hence indicating velocity strengthening and stable sliding. Projected to the Mount Etna case and in particular to seismic/aseismic transition at the Pernicana Fault System, these results provide a first insight on the condition at which stable sliding is promoted.

The underline guideline for this part of the project is the presence of a mature fault cutting through the sedimentary basement, juxtaposing various and with variable frictional properties lithologies, such as those encountered at Mount Etna: quaternary clay strata, carbonate, sandstone and claystone. In particular, taking into account the contribution of various minerals during sliding experiments and therefore avoiding much heterogeneities for the sake of simplicity, the experiments are run testing three

lithologies considered as representative of the variability of the basement: 1) sandstone, 2) carbonate, 3) clay. The evidence is that both clay and carbonate gouges are behaving in a stable manner, for the boundary conditions here used and considered. Transposing in a very speculative manner these results to the PFS transitional behaviour, the lack of clear seismicity in the section of fault considered as ‘silent’ can be due to the fact that the frictional resistance of this portion is affected by the presence of the quaternary clay layer and clayish terms of the basement. This results, that still can be improved by future experiments testing the influence of pore fluid pressure during sliding, find agreement with the conclusion proposed by Mattia et al., 2015, in which the influence of the layer of quaternary clay plays a fundamental role in the sliding of the unstable flank.

## 6.2 Concluding remarks

The development of the sliding holder required much of the project time to be invested in its development rather than on effective laboratory experiments. This is something normal when a new piece of tools needs to be prepared and verified in order to conduct precise analyses. At the actual state, it was not possible to recover intact samples of powders at the end of the experiments, as most of the powders were destroyed while trying to collect them from the contact surfaces, therefore not microstructures analyses were performed. A proper procedure aimed to collect intact chips of powder needs to be developed. Furthermore, the actual experimental setting can be developed inserting radial strain measurements, to obtain a quantitative measure of layer compaction, along with the use of acoustic emissions transducer to reveal the presence of noises indicating grain micro-fracturing. A new piece of equipment allowing test with pore fluid pressure would be a great improvement for experiments considering also permeability.

## 6.3 Future developments

The possibilities to expand investigations on the topic of edifice stability are numerous. Regarding Mount Etna, which is the main focus of this work, there are several areas of research that may contribute to better understanding of volcano stability, including: (1) constraining the role of basement foliation on failure, and patterns and character of deformation and seismicity in the basement; (2) the mechanical properties of the layered cover of basaltic rocks; (3) the transmission of

strains and style of structures passing from the basement to cover, and vice versa; (4) the role of fluids and fluid pressures in controlling gouge frictional properties, and host rock intact strength in the cover and basement.

### *1. Constraining the role of basement foliation on failure, and patterns and character of deformation and seismicity in the basement*

In outcrop, basement foliations within the AMC are generally E-W striking, following the structural grain of N-S shortening. Fold and thrust systems show an overall southward vergence, with thrusts and reverse faults dipping at a range of angles towards the north. The strike of these structures is therefore at a low angle to the Pernicana Fault System, but at a high angle to the Timpe Faults System. Questions remain, therefore, how these two orthogonal structures variably interact with the basement foliations: (a) Does the PFS sole into foliations in the basement, or across the foliation to join the Timpe Fault System? (b) Does the basement foliation impose a control on the geometry of the Timpe fault (i.e. does it affect the length and or continuity of the fault plane?), and/or the kinematics of the fault system?

- Future work could focus on triaxial testing of intact samples of the foliated basement rocks, seeking to perform tests at a range of orientations relative to the foliation. Collection of samples presenting bedding and/or tectonic foliation (e.g., cleavage and/or shear planes) can present variable strength depending on the orientation of these structures to the applied stress. Mount Etna's basement is composed by several units of sedimentary rocks highly deformed and therefore probably retaining intrinsic strength variability.

### *2. The mechanical properties of the layered cover of basaltic rocks*

Current studies of the Etnean covers focus on the use of the eponymous “*Etna Basalt*”; a basalt collected from the massive core zone of a thick lava on the south flank of Etna. *Etna basalt* is low porosity (~3%), and mechanically strong, with a UCS strength of 475 MPa. Typically, the core zone of simple sheet lavas may account for >50% of the lava total thickness. Relatively high porosity flow unit tops, and intermediate-porosity flow unit bases, can account for ~1/3 of the total thickness. In addition, lavas are commonly interlayered with volcanoclastic and pyroclastic units of conglomeratic through to finely-granular material. The basal sequence of pre-Etnean

volcanic rocks is dominated by subaqueous volcanic deposits, including hyaloclastites, pillow breccias, and pillow lavas. Subaerial lavas, such as the *Etna Basalt* lava, are therefore emplaced in places onto a pile of fine-grained volcanic glasses that are likely to be highly altered by low to high temperature fluids. *Etna Basalt*, therefore, should not be considered as the only representative material for the layered and heterogeneous composition of the Etna edifice, but as a strong end-member of the system.

- To gain a more detailed overview of the overall strength of the volcanic terms, a set of UCS and triaxial tests on intact rocks collected from the top and basal units of lava flows should be taken into consideration to describe the edifice strength. Further, the edifice is constrained in its north-western sector by the presence of the AMC, while its south-eastern sector is free to slide towards the Ionian Sea. The edifice is emplaced onto altered layers of volcanic glasses, and highly degraded lava products can be found today in outcrops along the coast, and inland around Palagonia, but presumably the entire south-eastern sectors is lying on top of weak materials, besides the quaternary clays used in this project. It would be of great interest to perform a series of triaxial experiments both on intact rocks (depending on the weakness of the altered samples) and/or on simulated gouges, at *in situ* boundary condition, to obtain more data on their strength and frictional properties.

3. *Faults that cut the basement and cover.* Both the edifice and the basement are intersected by several fault systems, starting from the surface dipping into the basement and/or viceversa: these faults are reasonably juxtaposing volcanic terms against the sedimentary lithologies of the basement.

- Using the direct shear sliding holder, investigations of the frictional properties on binary and ternary mixtures containing basalt-clay, and basalt-clay-limestone at increasing percentage of wt% of clay and carbonate should be taken into consideration.

4. *The role of fluids and fluid pressure combined with thermal gradient in controlling gouge frictional properties, and host rocks intact strength in the cover and basement.*

- Application of pore fluid pressure, along with *in situ* temperature to mimic the conditions at which the Etna rocks are subjected during magma emplacement

in order to answer the following questions: a) How is the frictional strength changing in presence of water and pore fluid pressure at relevant pressure conditions? and b) How is it degrading at hydrothermal condition?

Finally, the results obtained from these future developments could be useful in modelling the actual instability of Mount Etna.

## Appendix A. Fiumefreddo Quaternary Clay – XRF Investigation

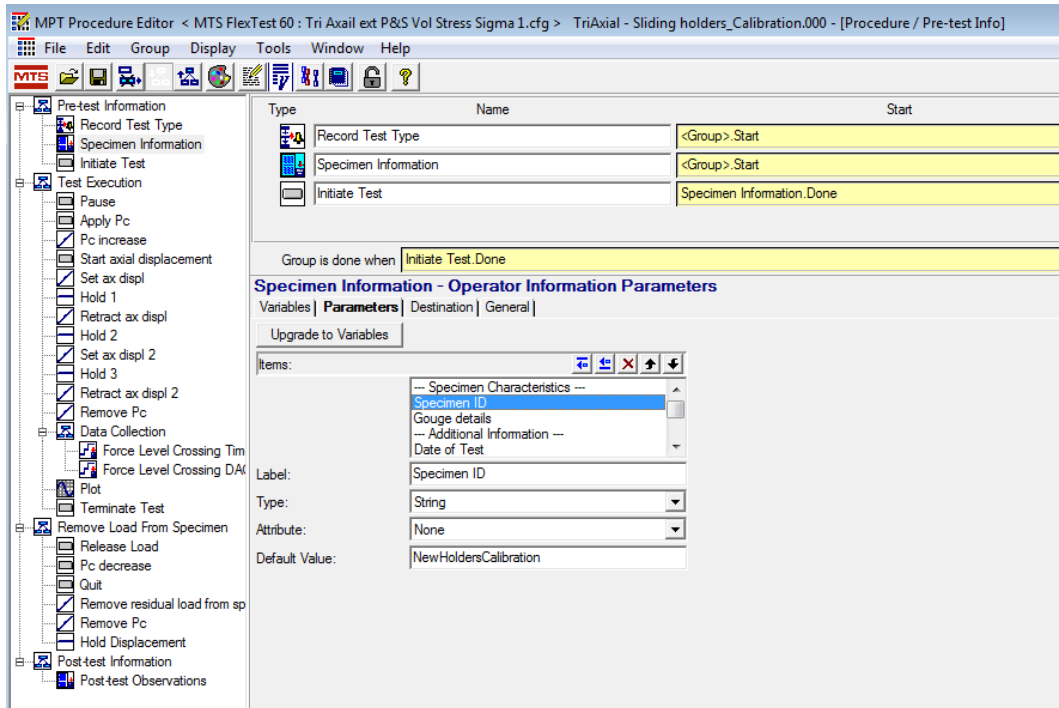
As reported in Chapter 1, the edifice is resting on a top of a complex sedimentary basement: during the Quaternary Period, the area actually occupied by the edifice was a gulf where clays have been deposited (e.g. [Rittmann A., 1973](#)). The initial submarine volcanism shifted to subaerial volcanism starting to build the actual edifice, accompanied by a regional uplift (i.e. [Rittmann A., 1973](#)). The edifice is then lying on top of layer of quaternary clays, which can play a fundamental role in promoting flank instability (e.g. [Groppelli and Tibaldi, 1999](#); [Mattia et al, 2015](#)). The clay are outcropping around the feet of the volcano, for instance in Misterbianco village (i.e. southern sector of Mount Etna), and sometimes they are outcropping as isolated spots where volcanic covers are missing. This is the case of Fiumefreddo clays (i.e. north-eastern sector), here collected to test their quantitative chemical composition to be confronted with Misterbianco clays, here used as simulated gouges for the tests.

Name	Bead	SiO2	TiO2	Al2O3	Fe2O3	MnO	MgO	CaO	Na2O	K2O	P2O5	SO3	LOI	Total
Grey-Blue Clay	LF40341	52.70	0.80	15.15	6.06	0.09	2.84	6.80	1.12	2.26	0.15	0.49	11.42	99.88
Fiumefreddo	LF41517	51.88	0.74	14.91	5.94	0.123	2.63	8.56	0.86	2.147	0.158	0.072	11.69	99.71

From XRF analyses reported, it is possible to note that the two sample of clays collected are showing nearly the same composition, and therefore the results obtained in this study can be considered valuable at least for the lithologies present below the north-eastern sector of the edifice.



## Appendix B. Calibration Procedure



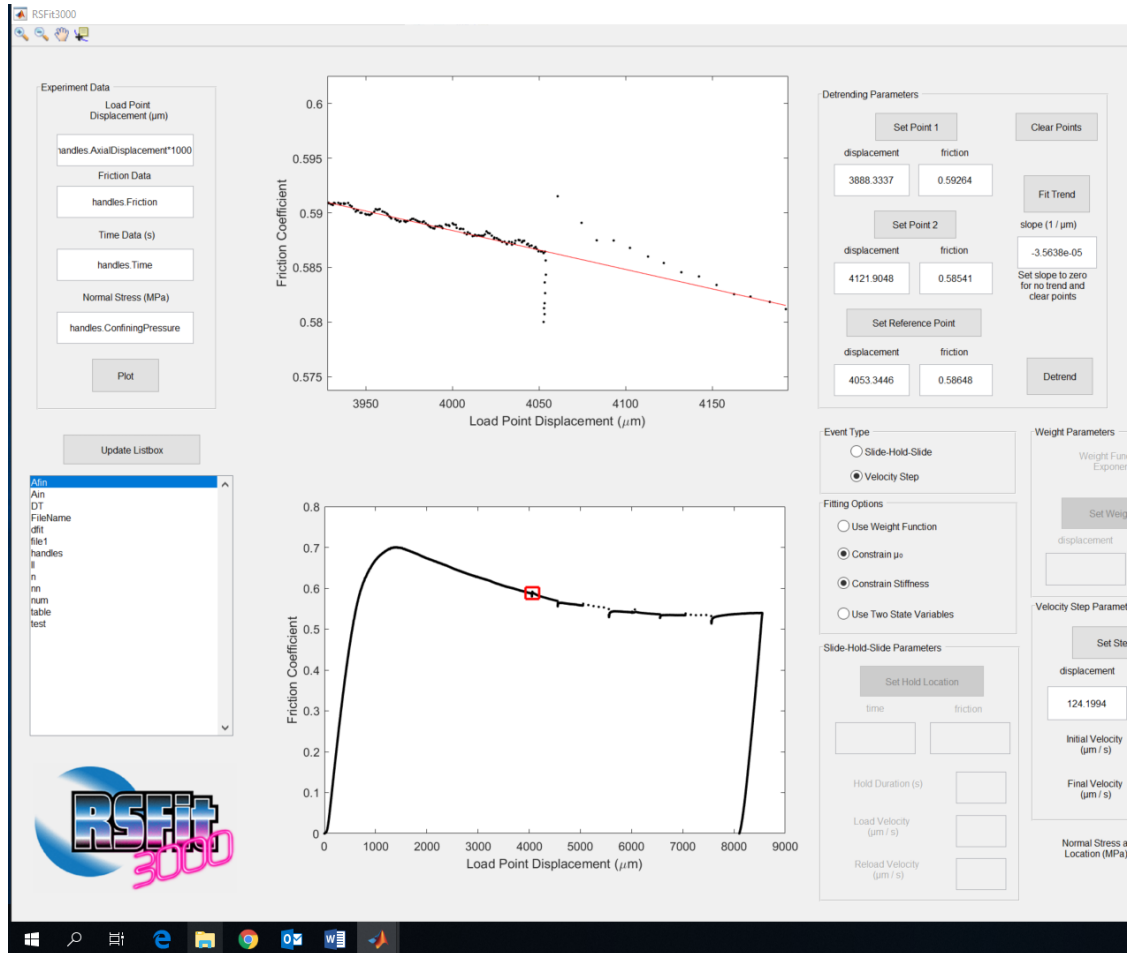
The MTS computer interface allows to create a procedure *a priori*, hence it is not possible to change the procedure while the test begins: every step needs to be thought in advance. In the screenshot here reported, the procedure used for calibration tests with applied confining pressure is reported. The procedure followed is:

- Sample positioned inside the cell;
- The cell is closed and filled in oil;
- All the relevant information about test conditions and sample are saved into the Pc interface;
- The procedure is activated;
- The first operation is to apply confining pressure until the desired value (i.e. hydrostatic pressure conditions);
- The axial piston is activated, but not being in contact with the sliding holder it requires a while to start to apply axial load;
- The axial piston enters in contact with the assemblage (i.e. differential pressure is applied) and the test begins.
- First displacement until 5 mm;

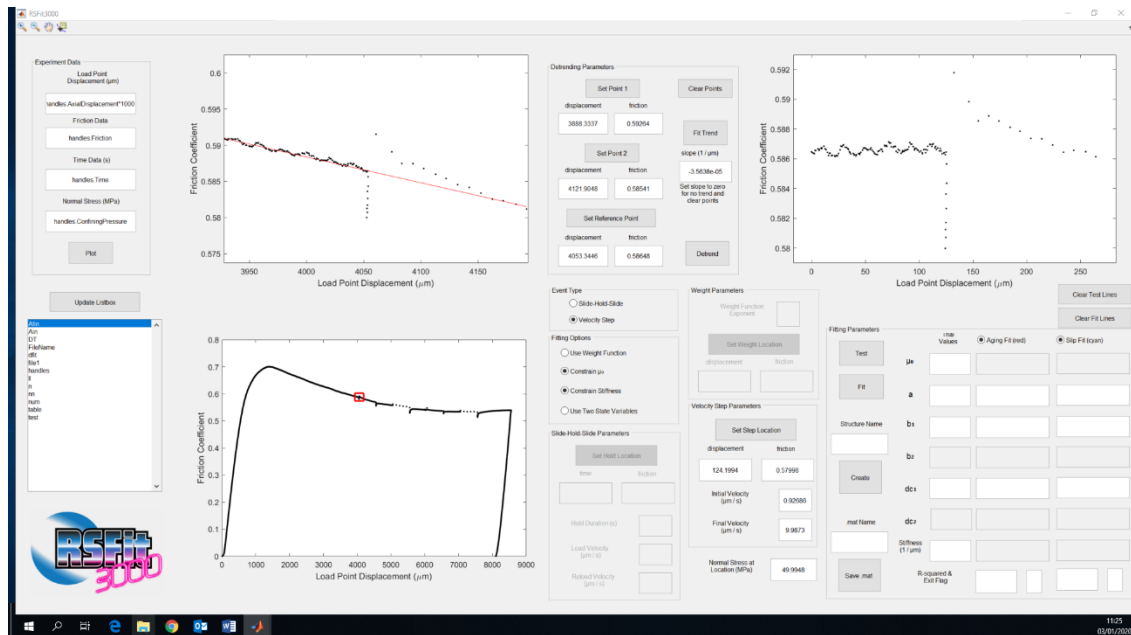
- At 5 mm displacement, the axial load is removed to check the recovery properties of the material used as stoppers;
- Apply again axial load;
- Displaced the full capacity of the sliding holder up to 10 mm;
- Retract the axial piston and unload the sample completely.

The same procedure is followed for samples tested without confining pressure (e.g. Cycle 1 and 2).

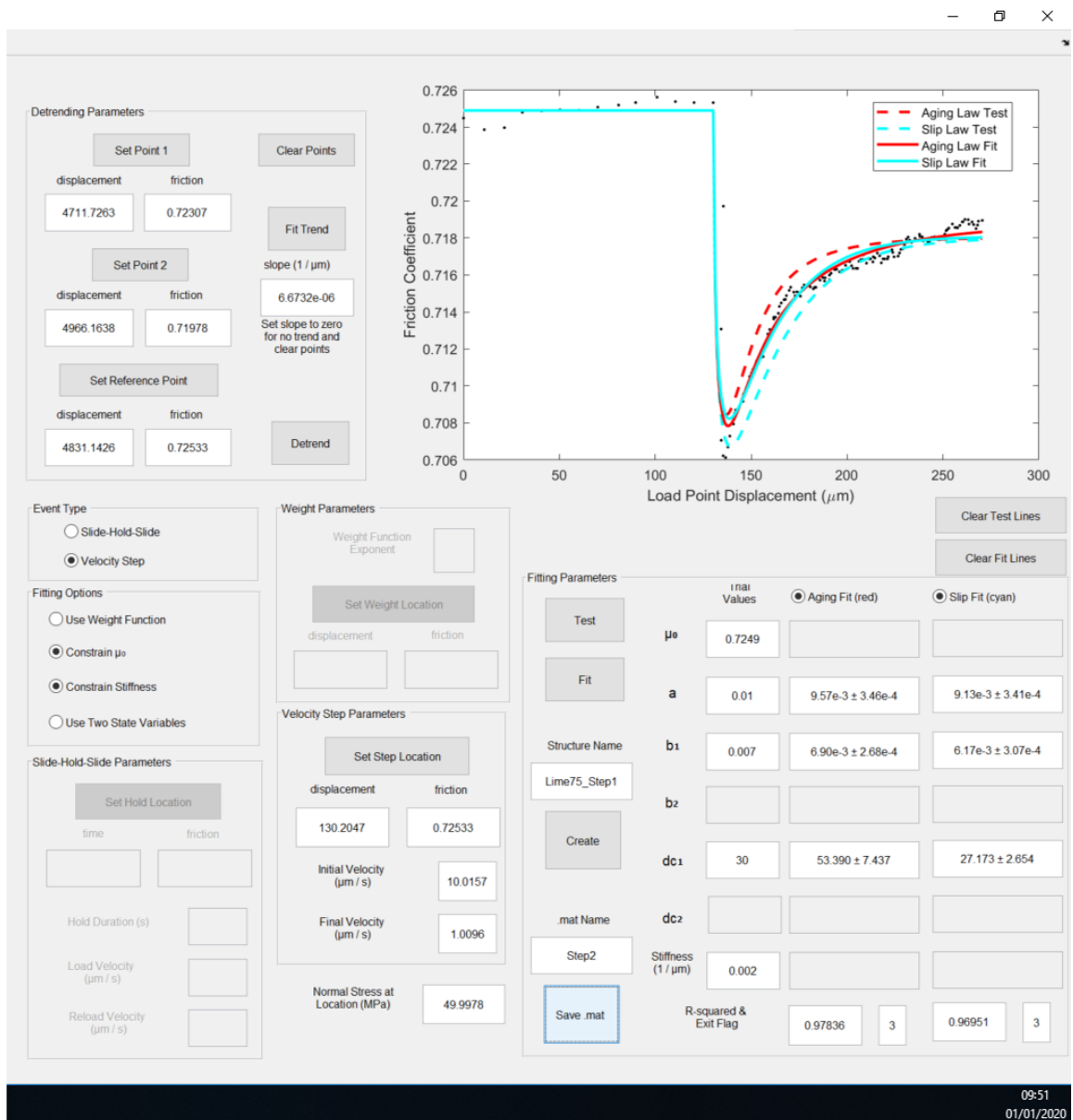
## Appendix C. RsFit3000



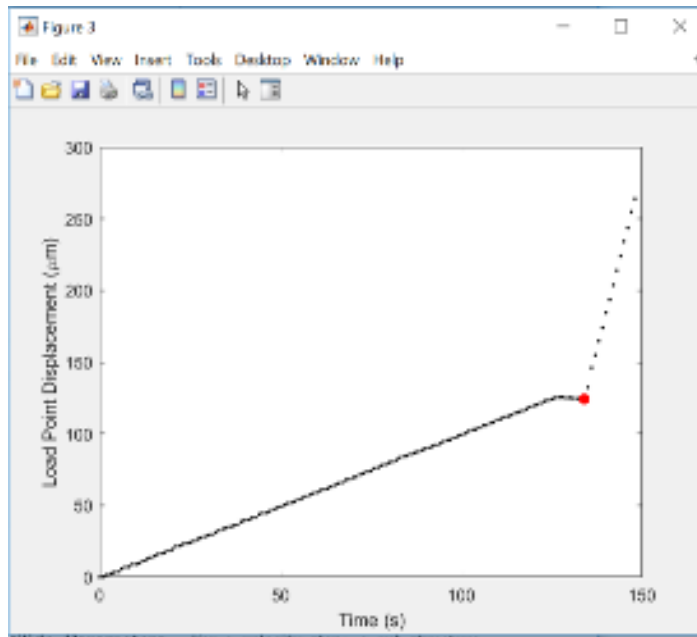
RsFit3000 is a graphical user interface (GUI) created by [Sharbek and Savage, 2019](#). This GUI uses the aging and slip laws to calculate the evolution of the state parameters  $a$ ,  $b$  and  $D_c$  by fitting the velocity change events in rate and state experiments. The GUI allows detrending the weakening/hardening trends sometimes present in experiments dataset. When the right fit is found, they are saved in MatLab structures reporting all the relevant values, such as  $a$ ,  $b$ ,  $D_c$ , stiffness along with their calculated errors.



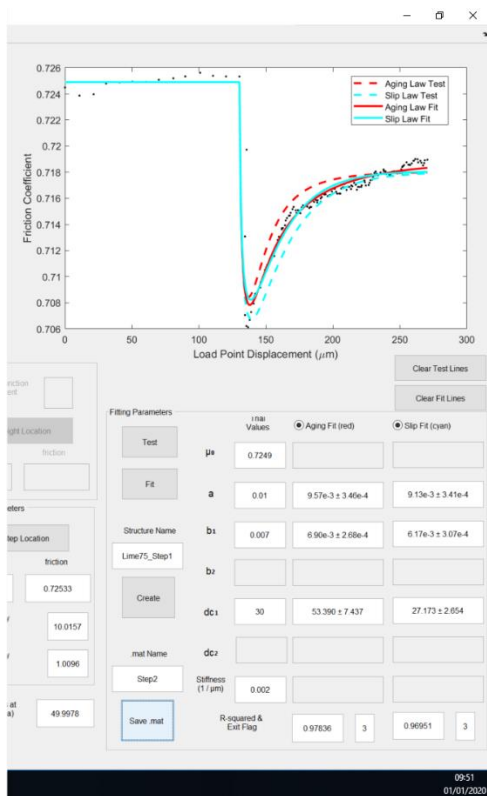
The original datasets (e.g. axial displacement, time, confining pressure, friction) are uploaded into the GUI, which is plotting the curve in the first window on the left side. By zooming into the first step, it is possible to select the first step and start the procedure to detrend the curve: the GUI allows to select Point 1 (before the jump), Point 2 (after the jump) and a reference point (usually right before the event). The detrended velocity step is plotted into the third window on the right side.



Once the selected velocity step has been detrended, it is possible to select the point at which the velocity step takes place, determining the change in the velocity. A picture is provided to check that the selected point it is actually at the beginning of the step.



The last part of the procedure is to insert guessed values for friction coefficient,  $a$ ,  $b$ ,  $D_c$  and stiffness. It is possible to change as many values as necessary, of friction coefficient and stiffness, until the procedure is returning a good fit. Once the values are inserted, the GUI calculates the results. This first result is just giving a visual report of the fitting curves obtained with the guessed values of the parameters. If the curves are not fitting well, it is possible to modify again the values and recalculate the fit. Once a good fit is found, the values are saved in MatLab files.





## Journal of Geophysical Research: Solid Earth

### RESEARCH ARTICLE

10.1029/2017JB015105

#### Key Points:

- Mechanical tests with ultrasonic data of heat-treated, dry and saturated limestones
- Results revealed water and temperature dependence at the brittle-ductile transition
- Integrated in a 2D model, results highlight broad impacts for some volcanic basements

#### Supporting Information:

- Supporting Information S1

#### Correspondence to:

A. Castagna,  
ac605@ac.le.uk

#### Citation:

Castagna, A., Ougier-Simonin, A., Benson, P. M., Browning, J., Walker, R. J., Fazio, M., & Vinciguerra, S. (2018). Thermal damage and pore pressure effects of the brittle-ductile transition in comiso limestone. *Journal of Geophysical Research: Solid Earth*, 123, 7644–7660. <https://doi.org/10.1029/2017JB015105>








Received 12 OCT 2017

Accepted 12 JUN 2018

Accepted article online 26 JUN 2018

Published online 27 SEP 2018

## Thermal Damage and Pore Pressure Effects of the Brittle-Ductile Transition in Comiso Limestone

A. Castagna<sup>1</sup> , A. Ougier-Simonin<sup>2</sup> , P. M. Benson<sup>3</sup> , J. Browning<sup>4</sup> , R. J. Walker<sup>1</sup> ,  
M. Fazio<sup>3,5</sup> , and S. Vinciguerra<sup>6</sup> 

<sup>1</sup>Department of Geology, University of Leicester, UK, <sup>2</sup>Rock Mechanics and Physics Laboratory, British Geological Survey, Nottingham, UK, <sup>3</sup>Rock Mechanics Laboratory, University of Portsmouth, UK, <sup>4</sup>Rock and Ice Physics Laboratory, Department of Earth Sciences, UCL, UK, <sup>5</sup>Department of Applied Geology, University of Göttingen, Germany, <sup>6</sup>Department of Earth Sciences, University of Turin, Italy

**Abstract** Volcanic edifices are commonly unstable, with magmatic and non-magmatic fluid circulation, and elevated temperature gradients having influence on the mechanical strength of edifice and basement rocks. We present new mechanical characterization of the Comiso limestone of the Mount Etna Volcano (Italy) basement to constrain the effects of regional ambient conditions associated with the volcanic system: the effects of pore fluid on rock strength and the effects of distal magmatic heating (~20 °C to 600 °C) at a range of simulated depths (0.2 to 2.0 km). The presence of water promotes ductile behaviour at shallow depths and causes a significant reduction in brittle rock strength compared to dry conditions. Thermal stressing, in which specimens were heated and cooled before mechanical testing at room temperature, has a variable effect for dry and saturated cases. In dry conditions, thermal stressing up to 450 °C homogenizes the strength of the specimen such that the majority of the specimens exhibit the same peak stress; at 600 °C, the brittle failure is promoted at lower differential stress. The presence of water in thermally-stressed specimens promotes ductile behaviour and reduces peak strength. Acoustic emission monitoring suggests that accumulated damage is associated with the heating-cooling sequence, particularly in the 300–450–600 °C. Based on conduction modeling, we estimate this temperature range could affect basement rocks up to 300 m away from minor sheet intrusions and much further with larger bodies. Considering the dyke spacing beneath Etna, these conditions may apply to a significant percentage of the basement, promoting ductile behaviour at relatively shallow depths.

**Plain Language Summary** Volcanoes can collapse as a result of underground magma, gas and/or water flows, and temperature effects on its basement rock's strength. We did laboratory experiments to further test the strength of surface samples of a limestone present beneath Mount Etna Volcano (Italy). We kept some samples 'as-collected' and heated and cooled the others at different temperatures (up to 600 °C) prior to their deformation as if some magma bodies had flown in the vicinity of these rocks. We then water saturated a sample of each temperature condition applied and compared their strengths at different simulated depths ranging about 0.2 to 2.0 km (i.e. confinement ranging between 7 and 50 MPa) to the ones of the corresponding samples kept dry. Our results show that water presence lowers the limestone strength compared to dry conditions but also the conditions of pressure at which the failure behaviour transitions between brittle and ductile regimes. For temperature up to 450 °C, the strength of this limestone seems to be independent of the treatment's temperature with the maximum strength values being higher in dry conditions than in water saturated conditions. The rock fails only in the brittle regime when thermally treated prior deformation at all temperatures, saturation and confinement applied. Considering the dyke spacing beneath Mount Etna, these combinations of water, temperature and pressure conditions may apply to a significant percentage of the basement, promoting weaker and ductile behaviour at relatively shallow depths.



## **BIBLIOGRAPHY**

- Accaino, F., Catalano, R., Di Marzo, L., Giustiniani, M., Tinivella, U., Nicolich, R., Sulli, A., Valenti, V., and Manetti, P., 2011, A crustal seismic profile across Sicily: *Tectonophysics*, v. 508, no. 1-4, p. 52-61.
- Acocella, V., 2003, Link between major flank slip and 2002–2003 eruption at Mt. Etna (Italy): *Geophysical Research Letters*, v. 30, no. 24.
- Acocella, V., Puglisi, G., and Amelung, F., 2013, Flank instability at Mt. Etna Preface: *Journal of Volcanology and Geothermal Research*, v. 251, p. 1-4.
- Allard, P., Behncke, B., D'Amico, S., Neri, M., and Gambino, S., 2006a, Mount Etna 1993–2005: Anatomy of an evolving eruptive cycle: *Earth-Science Reviews*, v. 78, no. 1-2, p. 85–114.
- Allard, P., Behncke, B., D'Amico, S., Neri, M., and Gambino, S., 2006b, Mount Etna 1993–2005: Anatomy of an evolving eruptive cycle: *Earth-Science Reviews*, v. 78, no. 1-2, p. 85–114.
- Aloisi, M., Bonaccorso, A., Cannavò, F., Gambino, S., Mattia, M., Puglisi, G., and Boschi, E., 2009, A new dyke intrusion style for the Mount Etna May 2008 eruption modelled through continuous tilt and GPS data: *Terra Nova*, v. 21, no. 4, p. 316-321.
- Aloisi, M., Mattia, M., Ferlito, C., Palano, M., Bruno, V., and Cannavo, F., 2011, Imaging the multi-level magma reservoir at Mt. Etna volcano (Italy): *Geophysical Research Letters*, v. 38, no. 16, p. n/a-n/a.
- Alparone, S., Cocina, O., Gambino, S., Mostaccio, A., Spampinato, S., Tuvè, T., and Ursino, A., 2013, Seismological features of the Pernicana–Provenzana Fault System (Mt. Etna, Italy) and implications for the dynamics of northeastern flank of the volcano: *Journal of Volcanology and Geothermal Research*, v. 251, p. 16-26.
- Anthony, J. L., 2005, Influence of particle characteristics on granular friction: *Journal of Geophysical Research*, v. 110, no. B8.
- Aydin, A., and Basu, A., 2005, The Schmidt hammer in rock material characterization: *Engineering Geology*, v. 81, no. 1, p. 1-14.

Azzaro, R., Bonforte, A., Branca, S., and Guglielmino, F., 2013, Geometry and kinematics of the fault systems controlling the unstable flank of Etna volcano (Sicily): *Journal of Volcanology and Geothermal Research*, v. 251, p. 5-15.

Azzaro, R., Branca, S., Gwinner, K., and Coltelli, M., 2012, The volcano-tectonic map of Etna volcano, 1:100.000 scale: an integrated approach based on a morphotectonic analysis from high-resolution DEM constrained by geologic, active faulting and seismotectonic data: *Italian Journal of Geosciences*, v. 131, no. 1, p. 153-170.

Azzaro R., M. M., Puglisi G, 2001, Fault creep and kinematics of the eastern segment of the Pernicana Fault (Mt Etna, Italy) derived from geodetic observation and their tectonic significance: *Tectonophysics*, v. 333.

Accaino, F., Catalano, R., Di Marzo, L., Giustiniani, M., Tinivella, U., Nicolich, R., Sulli, A., Valenti, V., and Manetti, P., 2011, A crustal seismic profile across Sicily: *Tectonophysics*, v. 508, no. 1-4, p. 52-61.

Acocella, V., 2003, Link between major flank slip and 2002–2003 eruption at Mt. Etna (Italy): *Geophysical Research Letters*, v. 30, no. 24.

Acocella, V., Puglisi, G., and Amelung, F., 2013, Flank instability at Mt. Etna Preface: *Journal of Volcanology and Geothermal Research*, v. 251, p. 1-4.

Allard, P., Behncke, B., D'Amico, S., Neri, M., and Gambino, S., 2006a, Mount Etna 1993-2005: Anatomy of an evolving eruptive cycle: *Earth-Science Reviews*, v. 78, no. 1-2, p. 85-114.

Aloisi, M., Bonaccorso, A., Cannavò, F., Gambino, S., Mattia, M., Puglisi, G., and Boschi, E., 2009, A new dyke intrusion style for the Mount Etna May 2008 eruption modelled through continuous tilt and GPS data: *Terra Nova*, v. 21, no. 4, p. 316-321.

Aloisi, M., Mattia, M., Ferlito, C., Palano, M., Bruno, V., and Cannavo, F., 2011, Imaging the multi-level magma reservoir at Mt. Etna volcano (Italy): *Geophysical Research Letters*, v. 38, no. 16, p. n/a-n/a.

Alparone, S., Cocina, O., Gambino, S., Mostaccio, A., Spampinato, S., Tuvè, T., and Ursino, A., 2013, Seismological features of the Pernicana–Provenzana Fault System (Mt. Etna, Italy) and implications for the dynamics of northeastern flank of the volcano: *Journal of Volcanology and Geothermal Research*, v. 251, p. 16-26.

- Anthony, J. L., 2005, Influence of particle characteristics on granular friction: *Journal of Geophysical Research*, v. 110, no. B8.
- Aydin, A., and Basu, A., 2005, The Schmidt hammer in rock material characterization: *Engineering Geology*, v. 81, no. 1, p. 1-14.
- Azzaro, R., Bonforte, A., Branca, S., and Guglielmino, F., 2013, Geometry and kinematics of the fault systems controlling the unstable flank of Etna volcano (Sicily): *Journal of Volcanology and Geothermal Research*, v. 251, p. 5-15.
- Azzaro, R., Branca, S., Gwinner, K., and Coltelli, M., 2012, The volcano-tectonic map of Etna volcano, 1:100.000 scale: an integrated approach based on a morphotectonic analysis from high-resolution DEM constrained by geologic, active faulting and seismotectonic data: *Italian Journal of Geosciences*, v. 131, no. 1, p. 153-170.
- Bakker, R., Benson, P., and Vinciguerra, S., Deforming Etna's Basement: Implications for Edifice stability, *in Proceedings EGU General Assembly Conference Abstracts 2013, Volume 15*.
- Bakker, R., Fazio, M., Benson, P., Hess, K.-U., and Dingwell, D. B., 2016, The propagation and seismicity of dyke injection, new experimental evidence: *Geophysical Research Letters*.
- Bakker, R. R., Violay, M. E. S., Benson, P. M., and Vinciguerra, S. C., 2015b, Ductile flow in sub-volcanic carbonate basement as the main control for edifice stability: New experimental insights: *Earth and Planetary Science Letters*, v. 430, p. 533-541.
- Barbera, G., Barone, G., Crupi, V., Longo, F., Maisano, G., Majolino, D., Mazzoleni, P., Raneri, S., Teixeira, J., and Venuti, V., 2014, A multi-technique approach for the determination of the porous structure of building stone: *European Journal of Mineralogy*, v. 26, no. 1, p. 189-198.
- Baud, P., Schubnel, A., and Wong, T.-f., 2000a, Dilatancy, compaction, and failure mode in Solnhofen limestone: *Journal of Geophysical Research*, v. 105.
- Baud, P., Zhu, W., and Wong, T.-F., 2000b, Failure mode and weakening effect of water on sandstone: *Journal of Geophysical Research: Solid Earth*, v. 105, no. B7, p. 16371-16389.
- Beckhoff, B., Kanngießer, B., Langhoff, N., Wedell, R., and Wolff, H., 2007, *Handbook of practical X-ray fluorescence analysis*, Springer Science & Business Media.

- Benson, P. M., Thompson, B. D., Meredith, P. G., Vinciguerra, S., and Young, R. P., 2007, Imaging slow failure in triaxially deformed Etna basalt using 3D acoustic-emission location and X-ray computed tomography: *Geophysical Research Letters*, v. 34, no. 3.
- Benson, P. M., Vinciguerra, S., Meredith, P. G., and Young, R. P., 2010, Spatio-temporal evolution of volcano seismicity: A laboratory study: *Earth and Planetary Science Letters*, v. 297, no. 1-2, p. 315-323.
- Bonaccorso, A., Cianetti, S., Giunchi, C., Trasatti, E., Bonafede, M., and Boschi, E., 2005, Analytical and 3-D numerical modelling of Mt. Etna (Italy) volcano inflation: *Geophysical Journal International*, v. 163, no. 2, p. 852-862.
- Bonaccorso, A., Currenti, G., Del Negro, C., and Boschi, E., 2010, Dike deflection modelling for inferring magma pressure and withdrawal, with application to Etna 2001 case: *Earth and Planetary Science Letters*, v. 293, no. 1-2, p. 121-129.
- Bonforte, A., Bonaccorso, A., Guglielmino, F., Palano, M., and Puglisi, G., 2008, Feeding system and magma storage beneath Mt. Etna as revealed by recent inflation/deflation cycles: *Journal of Geophysical Research-Solid Earth*, v. 113, no. B5.
- Bonforte, A., and Puglisi, G., 2006, Dynamics of the eastern flank of Mt. Etna volcano (Italy) investigated by a dense GPS network: *Journal of Volcanology and Geothermal Research*, v. 153, no. 3-4, p. 357-369.
- Borgia, A., Ferrari, L., and Pasquare, G., 1992, Importance of gravitational spreading in the tectonic and volcanic evolution of Mount Etna, *Nature*.
- Branca, S., Coltelli, M., De Beni, E., and Wijbrans, J., 2007, Geological evolution of Mount Etna volcano (Italy) from earliest products until the first central volcanism (between 500 and 100 ka ago) inferred from geochronological and stratigraphic data: *International Journal of Earth Sciences*, v. 97, no. 1, p. 135-152.
- Branca, S., Coltelli, M., and Groppelli, G., 2004, Geological evolution of Etna volcano: Washington DC American Geophysical Union Geophysical Monograph Series, v. 143, p. 49-63.
- Branca, S., Coltelli, M., Groppelli, G., and Lentini, F., 2011, Geological map of Etna volcano, 1:50,000 scale: *Italian Journal of Geosciences*, v. 130, no. 3, p. 265-291.

- Brown, K. M., Kopf, A., Underwood, M. B., and Weinberger, J. L., 2003, Compositional and fluid pressure controls on the state of stress on the Nankai subduction thrust: A weak plate boundary, v. 214, no. 3-4, p. 589-603.
- Browning, J., Meredith, P., and Gudmundsson, A., 2016, Cooling-dominated cracking in thermally stressed volcanic rocks: *Geophysical Research Letters*, v. 43, no. 16, p. 8417-8425.
- Browning, J., Meredith, P., Stuart, C. E., Healy, D., Harland, S., and Mitchell, T., 2017, Acoustic characterization of crack damage evolution in sandstone deformed under conventional and true triaxial loading: *Journal of Geophysical Research*.
- Bubeck, A., Walker, R. J., Healy, D., Dobbs, M., and Holwell, D. A., 2017, Pore geometry as a control on rock strength: *Earth and Planetary Science Letters*, v. 457, p. 38-48.
- Byerlee, J. D., 1978, Friction of rocks: *Pageoph*, v. 116.
- Byerlee, J. D., and Brace, W. F., 1968, Stick slip, stable sliding, and earthquakes-Effect of rock type, pressure, strain rate, and stiffness: *Journal of Geophysical Research*, v. 73, no. 18, p. 6031-6037.
- Carbone, S., Branca, S., and Lentini, F., 2009, Note Illustrative della Carta Geologica d'Italia alla scala 1:50.000 - Foglio 634 Catania.
- Chapple, W. M., 1987, STRENGTH OF ROCKS, Strength of rocks, Structural Geology and Tectonics: Berlin, Heidelberg, Springer Berlin Heidelberg, p. 746-748.
- Chen, J., and Spiers, C. J., 2016, Rate and state frictional and healing behavior of carbonate fault gouge explained using microphysical model, v. 121, no. 12, p. 8642-8665.
- Chen, J., Verberne, B. A., and Spiers, C. J., 2015, Interseismic re-strengthening and stabilization of carbonate faults by “non-Dieterich” healing under hydrothermal conditions, v. 423, p. 1-12.
- Chester, D. K., Duncan, A. M., and Guest, J. E., 1987, The Pyroclastic deposits of Mount Etna volcano, Sicily, v. 22, no. 3, p. 225-243.
- Chiocci, F. L., Coltelli, M., Bosman, A., and Cavallaro, D., 2011, Continental margin large-scale instability controlling the flank sliding of Etna volcano: *Earth and Planetary Science Letters*, v. 305, no. 1-2, p. 57-64.

- Cocina, O., Neri, G., Privitera, E., and Spampinato, S., 1997, Stress tensor computations in the mount Etna area (Southern Italy) and tectonic implications, v. 23, no. 2, p. 109-127.
- Collettini, C., Niemeijer, A., Viti, C., and Marone, C., 2009, Fault zone fabric and fault weakness.
- Crawford, B. R., Faulkner, D. R., and Rutter, E. H., 2008, Strength, porosity, and permeability development during hydrostatic and shear loading of synthetic quartz-clay fault gouge, *Journal of Geophysical Research*.
- Cristofolini, R., 1979, Integrazione di dati geologici, geofisici e petrologici per la stesura di un profilo crostale in corrispondenza dell'Etna.
- Dautriat, J., Gland, N., Dimanov, A., and Raphanel, J., 2011, Hydromechanical behavior of heterogeneous carbonate rock under proportional triaxial loadings: *Journal of Geophysical Research*, v. 116, no. B1.
- Day, S. J., 1996, Hydrothermal pore fluid pressure and the stability of porous, permeable volcanoes: Geological Society, London, Special Publications, v. 110, p. 77-93.
- De Paola, N., 2013, Nano-powder coating can make fault surfaces smooth and shiny: implications for fault mechanics?: *Geology*, v. 41, no. 6, p. 719-720.
- De Paola, N., Hirose, T., Mitchell, T., Di Toro, G., Viti, C., and Shimamoto, T., 2010, Fault lubrication and earthquake propagation in thermally unstable rocks: *Geology*, v. 39, no. 1, p. 35-38.
- De Vries, B. V. W., and Borgia, A., 1996, The role of basement in volcano deformation: Geological Society, London, Special Publications, v. 110, no. 1, p. 95-110.
- De Vries, B. V. W., and Francis, P., 1997, Catastrophic collapse at stratovolcanoes induced by gradual volcano spreading: *Nature*, v. 387, no. 6631, p. 387-390.
- Delaney, P. T., and Pollard, D. D., 1982, Solidification of basaltic magma during flow in a dike, v. 282, no. 6, p. 856-885.
- Di Toro, G., Han, R., Hirose, T., De Paola, N., Nielsen, S., Mizoguchi, K., Ferri, F., Cocco, M., and Shimamoto, T., 2011, Fault lubrication during earthquakes: *Nature*, v. 471, no. 7339, p. 494-498.

- Dieterich, J. H., 1979, Modeling of rock friction: 1. Experimental results and constitutive equations: *Journal of Geophysical Research*, v. 84, no. B5, p. 2161.
- Dieterich, J. H., 1988, Growth and persistence of Hawaiian volcanic rift zones: *Journal of Geophysical Research: Solid Earth*, v. 93, no. B5, p. 4258-4270.
- Dogliani, C., Innocenti, F., and Mariotti, G., 2001, Why Mt Etna?: *Terra Nova*, v. 13, p. 25-31.
- Elsworth, D., and Day, S. J., 1999, Flank collapse triggered by intrusion: the Canarian and Cape Verde Archipelagoes: *Journal of Volcanology and Geothermal Research*, v. 94, p. 323-340.
- Elsworth, D., and Voight, B., 1992, Theory of dike intrusion in a saturated porous solid, v. 97, no. B6, p. 9105.
- Engelder, J. T., 1974, Cataclasis and the Generation of Fault Gouge: *Geological Society of America Bulletin*, v. 85.
- Evans, B., Fredrich, J. T., and Wong, T.-f., 1990, The brittle-ductile transition in rocks: Recent experimental and theoretical progress, v. 56, p. 1-20.
- Evans, B., and Kohlstedt, D. L., 1995, Rheology of rocks, v. 3, p. 148-165.
- Faulkner, D. R., Mitchell, T. M., Behnken, J., Hirose, T., and Shimamoto, T., 2011, Stuck in the mud? Earthquake nucleation and propagation through accretionary forearcs: *Geophysical Research Letters*, v. 38, no. 18, p. n/a-n/a.
- Faulkner, D. R., Sanchez-Roa, C., Boulton, C., and Hartog, S. A. M. d., 2018, Pore Fluid Pressure Development in Compacting Fault Gouge in Theory, Experiments, and Nature, *Journal of Geophysical Research: Solid Earth*.
- Fazio, M., Benson, P. M., and Vinciguerra, S., 2017, On the generation mechanisms of fluid-driven seismic signals related to volcano-tectonics: *Geophysical Research Letters*, v. 44, no. 2, p. 734-742.
- Finetti, I., 1984, Geophysical study of the Sicily Channel rift zone.
- Finetti, I., Lentini, F., Carbone, S., Del Ben, A., Di Stefano, A., Forlin, E., Guarnieri, P., Pipan, M., and Prizzon, A., 2005, Geological outline of Sicily and lithospheric tectono-dynamics of its Tyrrhenian margin from new CROP seismic data: CROP Project: deep seismic exploration of the central Mediterranean and Italy, p. 319-375.

- Fortin, J., Stanchits, S., Vinciguerra, S., and Guéguen, Y., 2011, Influence of thermal and mechanical cracks on permeability and elastic wave velocities in a basalt from Mt. Etna volcano subjected to elevated pressure: *Tectonophysics*, v. 503, no. 1-2, p. 60-74.
- Fredrich, J. T., and Wong, T.-f., 1986, Micromechanics of thermally induced cracking in three crustal rocks: *Journal of Geophysical Research: Solid Earth*, v. 91, no. B12, p. 12743-12764.
- Gambino, S., Cannata, A., Cannavò, F., La Spina, A., Palano, M., Sciotto, M., Spampinato, L., and Barberi, G., 2016, The unusual 28 December 2014 dike-fed paroxysm at Mount Etna: Timing and mechanism from a multidisciplinary perspective: *Journal of Geophysical Research: Solid Earth*, v. 121, no. 3, p. 2037-2053.
- Garduno, V., Neri, M., Pasquarè, G., Borgia, A., and Tibaldi, A., 1997, Geology of the NE-Rift of Mount Etna (Sicily, Italy): *Acta Vulcanologica*, v. 9, p. 91-100.
- Griffiths, L., Lengliné, O., Heap, M., Baud, P., and Schmittbuhl, J., 2018, Thermal cracking in Westerly Granite monitored using direct wave velocity, coda wave interferometry, and acoustic emissions: *Journal of Geophysical Research: Solid Earth*, v. 123, no. 3, p. 2246-2261.
- Groppelli, G., and Tibaldi, A., 1999, Control of rock rheology on deformation style and slip-rate along the active Pernicana Fault, Mt. Etna, Italy, v. 305, no. 4, p. 521-537.
- Groppelli, T., 2011, Volcano-tectonic activity along structures of the unstable NE flank of Mt. Etna (Italy) and their possible origin: *Italian Journal of Geoscience*.
- Gudmundsson, A., 1995, Infrastructure and mechanics of volcanic systems in Iceland: *Journal of Volcanology and Geothermal Research*, v. 64, no. 1-2, p. 1-22.
- Gudmundsson, A., 2002, Emplacement and arrest of sheets and dykes in central volcanoes: *Journal of Volcanology and Geothermal Research*, v. 116, no. 3-4, p. 279-298.
- Guéguen, Y., and Palciauskas, V., 1994, *Introduction to the Physics of Rocks*, Princeton University Press.
- Harnett, C. E., Benson, P. M., Rowley, P., and Fazio, M., 2018, Fracture and damage localization in volcanic edifice rocks from El Hierro, Stromboli and Tenerife: *Scientific Reports*, v. 8, no. 1.
- Heap, M. J., Mollo, S., Vinciguerra, S., Lavallée, Y., Hess, K. U., Dingwell, D. B., Baud, P., and Iezzi, G., 2013, Thermal weakening of the carbonate basement under Mt. Etna volcano



(Italy): Implications for volcano instability: *Journal of Volcanology and Geothermal Research*, v. 250, p. 42-60.

Heap, M. J., Vinciguerra, S., and Meredith, P. G., 2009, The evolution of elastic moduli with increasing crack damage during cyclic stressing of a basalt from Mt. Etna volcano: *Tectonophysics*, v. 471, no. 1-2, p. 153-160.

Hunfeld, L. B., Niemeijer, A., and Spiers, C. J., 2017, Frictional properties of simulated fault gouges from the seismogenic Groningen gas field under in situ P-T-Chemical conditions, *Journal of Geophysical Research: Solid Earth*.

Ikari, M. J., Kopf, A. J., Hüpers, A., and Vogt, C., 2018, Lithologic control of frictional strength variations in subduction zone sediment inputs, *Geosphere*.

Ikari, M. J., Niemeijer, A. R., and Marone, C., 2011, The role of fault zone fabric and lithification state on frictional strength, constitutive behavior, and deformation microstructure: *Journal of Geophysical Research-Solid Earth*, v. 116.

Ikari, M. J., Saffer, D. M., and Marone, C., 2009, Frictional and hydrologic properties of clay-rich fault gouge, v. 114, no. B5.

Jenkins, R., and Snyder, R. L., 1996, *Introduction to X-ray powder diffractometry*, Wiley New York.

Kanamori, H., 1994, Mechanics of Earthquakes: *Annual Review of Earth and Planetary Sciences*, v. 22, p. 207-237.

Kohlstedt, D. L., Evans, B., and Mackwell, S. J., 1995, Strength of the lithosphere: Constraints imposed by laboratory experiments: *Journal of Geophysical Research: Solid Earth*, v. 100, no. B9, p. 17587-17602.

Lafaye, S., Gauthier, C., and Schirrer, R., 2005, A surface flow line model of a scratching tip: apparent and true local friction coefficients, v. 38, no. 2, p. 113-127.

Lawn, B., 1993, *Fracture of brittle solids*, Cambridge university press.

Leclere, H., Faulkner, D. R., Wheeler, J., and Mariani, E., 2016, Permeability control on transient slip weakening during gypsum dehydration: Implications for earthquakes in subduction zones, *Earth and Planetary Science Letters*.

Lentini, 2014, *Geologia della Sicilia: Memorie Descrittive della Carta Geologica d'Italia*.

Lentini, F., and Carbone, S., 2014, *Geologia della Sicilia-Introduzione: Memorie Descrittive Carta Geologica Italiana*.

Lentini, F., Carbone, S., and Guarnieri, P., 2006, Collisional and postcollisional tectonics of the Appenninic-Maghrebian Chain (southern Italy): *Geological Society of America* v. 409.

Lockner, D. A., and Beeler, N. M., 2002, Rock failure and earthquakes, v. *International Geophysics Series*, no. 81A.

Logan, J. M., and Rauenzahn, K. A., 1987, Frictional dependence of gouge mixtures of quartz and montmorillonite on velocity, composition and fabric.

Lupinl, J., Skinner, A., and Vaughan, P., 2009, The drained residual strength of cohesive soils, *Selected papers on geotechnical engineering by PR Vaughan*, Thomas Telford Publishing, p. 88-120.

Mair, K., Frye, K. M., and Marone, C., 2002, Influence of Grain Characteristics on the friction of granular shear zones, *Journal of Geophysical Research*.

Marone, C., 1998, Laboratory-derived friction laws and their application to seismic faulting: *Annual Review of Earth and Planetary Sciences*, v. 26, p. 643-696.

Marone, C., Hobbs, B. E., and Ord, A., 1992, Coulomb Constitutive Laws for Friction: Contrasts in Frictional Behavior for Distributed and Localized Shear.

Marone, C., and Kilgore, B., 1993, Scaling of the Critical Slip Distance for Seismic Faulting with Shear Strain in Fault Zones: *Nature*, v. 362, no. 6421, p. 618-621.

Marone, C., Raleigh, B. C., and Scholz, C. H., 1990, Frictional Behaviour and Constitutive Modeling of Simulated Fault Gouge.

Mattia, M., Bruno, V., Caltabiano, T., Cannata, A., Cannavò, F., D'Alessandro, W., Di Grazia, G., Federico, C., Giammanco, S., La Spina, A., Liuzzo, M., Longo, M., Monaco, C., Patanè, D., and Salerno, G., 2015, A comprehensive interpretative model of slow slip events on Mt. Etna's eastern flank: *Geochemistry, Geophysics, Geosystems*, v. 16, no. 3, p. 635-658.

Mathieu, L., Kervyn, M., and Ernst, G. G., 2011, Field evidence for flank instability, basal spreading and volcano-tectonic interactions at Mt Cameroon, West Africa: *Bulletin of Volcanology*, v. 73, no. 7, p. 851-867.

- Mavko, G., Mukerji, T., and Dyorkin, J., 1998, *The rock physics handbook: tools for seismic analysis in porous media*: Cambridge University Press, p. 329.
- McCarroll, D., 1994, *The Schmidt hammer as a measure of degree of rock surface weathering and terrain age: Dating in Exposed and Surface Contexts*. University of New Mexico Press, Albuquerque, v. 29, p. 45.
- McGuire, W. J., 1996, *Volcano instability: a review of contemporary themes*: Geological Society, London, Special Publications, v. 110, p. 1-23.
- Mollo, S., Vinciguerra, S., Iezzi, G., Iarocci, A., Scarlato, P., Heap, M. J., and Dingwell, D. B., 2011, Volcanic edifice weakening via devolatilization reactions: *Geophysical Journal International*, v. 186, no. 3, p. 1073-1077.
- Monaco, C., 2012, *Note Illustrative della Carta Geologica d'Italia alla scala 1:50.000 - Foglio 624 Monte Etna*.
- Morrow, C., Radney, B., and Byerlee, J., 1992, Chapter 3 *Frictional Strength and the Effective Pressure Law of Montmorillonite and Illite Clays*, Elsevier, p. 69-88.
- Munn, S., Walter, T. R., and KLÜGEL, A., 2006, Gravitational spreading controls rift zones and flank instability on El Hierro, Canary Islands: *Geological Magazine*, v. 143, no. 3, p. 257-268.
- Nicolas, A., Fortin, J., Regnet, J. B., Dimanov, A., and Guéguen, Y., 2016, Brittle and semi-brittle behaviours of a carbonate rock: influence of water and temperature: *Geophysical Journal International*, v. 206, no. 1, p. 438-456.
- Obrizzo, P., Troise, De Natale, 2001, Coseismic displacement and creeping along the Pernicana fault (Etna, Italy) in the last 17 years: a detailed study of a tectonic structure on a volcano: *Journal of Volcanology and Geothermal Research*, v. 109.
- Ohnaka, M. and Mogi, K., 1982, Frequency characteristics of acoustic emission in rocks under uniaxial compression and its relation to the fracturing process to failure, *J. Geophys. Res.*, 87, 3873– 3884.
- Patane', D., Aliotta, M., Cannata, A., Cassisi, C., Coltelli, M., Di Grazia, G., Montalto, P., and Zuccarello, L., 2011, *Interplay between Tectonics and Mount Etna's Volcanism: Insights into the Geometry of the Plumbing System - At the Midst of Plate Convergence*.

Paterson, M., and Wong, T.-f., 2005, *Experimental Rock Deformation - The Brittle Field*: 2nd ed Springer-Verlag.

Pluymakers, A. M. H., Samuelson, J. E., Niemeijer, A. R., and Spiers, C. J., 2014, Effects of temperature and CO<sub>2</sub> on the frictional behavior of simulated anhydrite fault rock, *Journal of Geophysical Research:Solid Earth*.

Poland, M. P., Peltier, A., Bonforte, A., and Puglisi, G., 2017, The spectrum of persistent volcanic flank instability: A review and proposed framework based on Kīlauea, Piton de la Fournaise, and Etna: *Journal of Volcanology and Geothermal Research*, v. 339, p. 63-80.

Puglisi, G., Briole, P., and Bonforte, A., 2004, Twelve years of ground deformation studies on Mt. Etna volcano based on GPS surveys: *Washington DC American Geophysical Union Geophysical Monograph Series*, v. 143, p. 321-341.

Reid, M. E., Sisson, T. W., and Brien, D. L., 2001, Volcano collapse promoted by hydrothermal alteration and edifice shape, Mount Rainier, Washington: *Geology*, v. 29, p. 779-782.

Rittmann, A., 1973, Structure and Evolution of Mount Etna: *Philosophical Transactions of the Royal Society a-Mathematical Physical and Engineering Sciences*, v. 274, no. 1238, p. 5-16.

Roknuzzaman, M., Hossain, M. B., Mostazid, M. I., and Haque, M. R., 2017, Application of rebound hammer method for estimating compressive strength of bricks: *Journal of Civil Engineering Research*, v. 7, no. 3, p. 99-104.

Roure, F., Howell, D., Müller, C., and Moretti, I., 1990, Late Cenozoic subduction complex of Sicily: *Journal of Structural Geology*, v. 12, no. 2, p. 259-266.

Ruch, J., Pepe, S., Casu, F., Solaro, G., Pepe, A., Acocella, V., Neri, M., and Sansosti, E., 2013, Seismo-tectonic behavior of the Pernicana Fault System (Mt Etna): A gauge for volcano flank instability?: *Journal of Geophysical Research: Solid Earth*, v. 118, no. 8, p. 4398-4409.

Ruch, J., Pepe, S., Casu, F., Acocella, V., Neri, M., Solaro, G., and Sansosti, E., 2012, How do volcanic rift zones relate to flank instability? Evidence from collapsing rifts at Etna: *Geophysical Research Letters*, v. 39, no. 20, p. n/a-n/a.

Ruch, J., Acocella, V., Storti, F., Neri, M., Pepe, S., Solaro, G., and Sansosti, E., 2010, Detachment depth revealed by rollover deformation: An integrated approach at Mount Etna: *Geophysical Research Letters*, v. 37, no. 16, p. n/a-n/a.

Ruina, A., 1983, Slip instability and state variable friction laws, v. 88, no. B12, p. 10359.

Rutter, E. H., 1972, The influence of interstitial water on the rheological behaviour of calcite rocks: *Tectonophysics*, v. 14, p. 13-33.

Rutter, E. H., 1974, The influence of temperature, strain rate and interstitial water in the experimental deformation of calcite rocks: *Tectonophysics*, v. 22, p. 311-334.

Rutter, E. H., MADDOCK, R. H., HALL, S. H., and WHITE, S. H., 1986, Comparative Microstructures of Natural and Experimentally Produced Clay-Bearing Fault Gouges, v. 1-2.

Sammonds, P. R., 1999, Understanding the fundamental physics governing the evolution and dynamics of the Earth's crust and ice sheets: *Philosophical Transactions of the Royal Society A: Mathematical, Physical and Engineering Sciences*, v. 357, no. 1763, p. 3377-3401.

Samuelson, J., and Spiers, C. J., 2012, Fault friction and slip stability not affected by CO<sub>2</sub> storage: Evidence from short-term laboratory experiments on North Sea reservoir sandstones and caprocks.: *International Journal of Greenhouse Gas Control*.

Scarascia, S., Cassinis, R., Lozej, A., and Nebuloni, A., 2000, A seismic and gravimetric model of crustal structures across the Sicily Channel Rift Zone: *BOLLETTINO-SOCIETA GEOLOGICA ITALIANA*, v. 119, no. 1, p. 213-222.

Scholz, C. H., 1968, The frequency-magnitude relation of microfracturing in rock and its relation to earthquakes: *Bulletin of the seismological society of America*, v. 58, no. 1, p. 399-415.

Scholz, C. H., 1987, *Wear and Gouge Formation in Brittle Faulting*.

Scholz, C. H., 1998, Earthquakes and friction laws: *Nature*, v. 391, no. 6662, p. 37-42.

Shanmugam, G., 1997, The Bouma Sequence and the turbidite mind set: *Earth-Science Reviews*, v. 42, no. 4, p. 201-229.

Siegesmund S., U. K., Weiss T., Tschegg E.K., 2000, Physical weathering of marbles caused by anisotropical thermal expansion: *International Journal of Earth Sciences*, v. 89, no. 1, p. 170-182.

Sigmundsson, F., Hreinsdottir, S., Hooper, A., Arnadottir, T., Pedersen, R., Roberts, M. J., Oskarsson, N., Auriac, A., Decriem, J., Einarsson, P., Geirsson, H., Hensch, M., Ofeigsson, B. G., Sturkell, E., Sveinbjornsson, H., and Feigl, K. L., 2010, Intrusion triggering of the 2010 Eyjafjallajokull explosive eruption: *Nature*, v. 468, no. 7322, p. 426-430.

- Siniscalchi, A., Tripaldi, S., Neri, M., Balasco, M., Romano, G., Ruch, J., and Schiavone, D., 2012, Flank instability structure of Mt. Etna inferred by a magnetotelluric survey: *Journal of Geophysical Research-Solid Earth*, v. 117, no. B3, p. n/a-n/a.
- Siniscalchi, A., Tripaldi, S., Neri, M., Giammanco, S., Piscitelli, S., Balasco, M., Behncke, B., Magri, C., Naudet, V., and Rizzo, E., 2010, Insights into fluid circulation across the Pernicana Fault (Mt. Etna, Italy) and implications for flank instability, *Journal of Volcanology and Geothermal Research*.
- Skarbek, R. M., and Savage, H. M., 2019, RSFit3000: A MATLAB GUI-based program for determining rate and state frictional parameters from experimental data: *Geosphere*, v. 15, no. 5, p. 1665-1676.
- Takahashi, M., Uehara, S.-I., Mizoguchi, K., Shimizu, I., Okazaki, K., and Masuda, K., 2011, On the transient response of serpentine (antigorite) gouge to stepwise changes in slip velocity under high-temperature conditions: *Journal of Geophysical Research*, v. 116, no. B10.
- Tembe, S., Lockner, D. A., and Wong, T.-F., 2010, Effect of clay content and mineralogy on frictional sliding behavior of simulated gouges: Binary and ternary mixtures of quartz, illite, and montmorillonite, v. 115, no. B3.
- Tesei, T., Collettini, C., Carpenter, B. M., Viti, C., and Marone, C., 2012, Frictional strength and healing behavior of phyllosilicate-rich faults: *Journal of Geophysical Research: Solid Earth*, v. 117, no. B9, p. n/a-n/a.
- Tibaldi, A., and Groppelli, G., 2002, Volcano-tectonic activity along structures of the unstable NE flank of Mt. Etna (Italy) and their possible origin, v. 115, no. 3-4, p. 277-302.
- Tomás, F. G., Kojdecki, M., Pardo, P., Ibañez, R., Larena, A. Á., and Bastida, J., 2016, X-ray Diffraction Microstructural Analysis of Swelling by Ethylene Glycol in Two Reference Clay Minerals: *Acta Physica Polonica A*, v. 4, no. 130, p. 876-879.
- Tuttle, O., 1949, The variable inversion temperature of quartz as a possible geologic thermometer: *American Mineralogist: Journal of Earth and Planetary Materials*, v. 34, no. 9-10, p. 723-730.
- Ulusay, R., and Hudson, J., 2007, The complete ISRM suggested methods for rock characterization, testing and monitoring: ISRM Turkish National Group, Ankara, Turkey.

- Vajdova, V., Baud, P., and Wong, T.-f., 2004, Compaction, dilatancy, and failure in porous carbonate rocks: *Journal of Geophysical Research: Solid Earth*, v. 109, no. B5.
- Vajdova, V., Zhu, W., Natalie Chen, T.-M., and Wong, T.-f., 2010, Micromechanics of brittle faulting and cataclastic flow in Tavel limestone: *Journal of Structural Geology*, v. 32, no. 8, p. 1158-1169.
- Van Wyk De Vries, B., and Borgia, A., 1996, The role of basement in volcano deformation: Geological Society, London, Special Publications, v. 110, p. 95-110.
- Verberne, B. A., de Bresser, J. H. P., Niemeijer, A., and Spiers, C. J., 2013, Nanocrystalline slip zones in calcite fault gouge show intense crystallographic preferred orientation: Crystal plasticity at sub-seismic slip rates at 18 – 150 °C, *Geology*.
- Vinciguerra, S., Trovato, C., Meredith, P. G., and Benson, P. M., 2005, Relating seismic velocities, thermal cracking and permeability in Mt. Etna and Iceland basalts: *International Journal of Rock Mechanics and Mining Sciences*, v. 42, no. 7-8, p. 900-910.
- Violay, M., Gibert, B., Mainprice, D., Evans, B., Dautria, J.-M., Azais, P., and Pezard, P., 2012, An experimental study of the brittle-ductile transition of basalt at oceanic crust pressure and temperature conditions: *Journal of Geophysical Research: Solid Earth*, v. 117, no. B3.
- Voight, B., and Elsworth, D., 1997, Failure of volcano slopes: *Geotechnique*, v. 47.
- Walsh, J. B., and Brace, W., 1984, The effect of pressure on porosity and the transport properties of rock: *Journal of Geophysical Research: Solid Earth*, v. 89, no. B11, p. 9425-9431.
- Walter, T. R., Troll, V. R., Cailleau, B., Belousov, A., Schmincke, H.-U., Amelung, F., and Vd Bogaard, P., 2005, Rift zone reorganization through flank instability in ocean island volcanoes: an example from Tenerife, Canary Islands: *Bulletin of Volcanology*, v. 67, no. 4, p. 281-291.
- Wiesmaier, S., Heap, M. J., Branca, S., Gilg, H. A., Kueppers, U., Hess, K. U., Lavallee, Y., and Dingwell, D. B., 2015, Variability in composition and physical properties of the sedimentary basement of Mt Etna, Italy: *Journal of Volcanology and Geothermal Research*, v. 302, p. 102-116.
- Wong, T.-f., and Baud, P., 2012, The brittle-ductile transition in porous rock: A review: *Journal of Structural Geology*, v. 44, p. 25-53.

Yavuz, H., Demirdag, S., and Caran, S., 2010, Thermal effect on the physical properties of carbonate rocks: *International Journal of Rock Mechanics and Mining Sciences*, v. 47, no. 1, p. 94-103.

Zhang, L., and He, C., 2013, Frictional properties of natural gouges from Longmenshan fault zone ruptured during the Wenchuan Mw7.9 earthquake, v. 594, p. 149-164.